Microengineered Biomaterials and Biosystems for Systems Immunology, Cancer Biology, and Stem Cell-based Regenerative Medicine

by

Weiqiang Chen

A dissertation proposal submitted in partial fulfillment
of the requirements for the degree of
Doctor of Philosophy
(Mechanical Engineering)
in the University of Michigan
2014

Doctoral Committee:

Assistant Professor Jianping Fu, Chair
Professor Katsuo Kurabayashi
Professor Sofia D. Merajver
Professor Thomas P. Shanley
Professor Shuichi Takayama

2014

Acknowledgments

I am indebted to innumerable people for their help and guidance during my time at University of Michigan. First and foremost, I would like to extend my sincere gratitude to Prof. Jianping for his constant encouragement and immerse support throughout the years of my doctoral studies. His guidance and inspiration have given me a unique opportunity to explore all sorts of different ideas without restriction. I also would like to thank Prof. Katsuo Kurabayashi and Prof. Shuichi Takayama for their kindly advice and continuous support for my research and career. I owe special thanks to Prof. Sofia D. Merajver, Prof. Thomas P. Shanley and Prof. Timothy T. Cornell from medical school, for their instruction, insights and supervision of my PhD research at Michigan. I would like to thank Dr. Raymond Hiu-Wai Lam, Dr. Nien-Tsu Huang, Dr. Pengyu Chen, Dr. Luis G. Villa-Diaz, Steven G. Allen, Liwei Bao and Walker M. McHugh for their kindly help for my reaseach. Finally, I wish to express my thanks and admiration to all the members in the Fu Lab and a great many friends and colleagues at Michigan who have helped me along my path through the years. The support and friendship have meant a great deal to me, and I hope that our paths will cross again in the coming years.

Table of Contents

List of Figures

List of Appendices

Abstract

Many exciting topics exist at the interface between biology and micro/nanotechnology. This dissertation will discuss interdisciplinary researches that leveraging the engineering advances in biomaterials, microfluidics and advanced manufacturing for new and better solutions for emerging problems in cancer biology, systems immunology, and stem cell-based regenerative medicine. First, this dissertation will discuss the potential of integrated microfluidic immunophenotyping assay device to perform rapid, accurate, and sensitive functional cellular immunophenotyping assays for target subpopulations of immune cells isolated directly from patient blood. This dissertation will also explore the possible technique using nanotopographic substrates for efficient capture of circulating tumor cells regardless of surface protein expression and cancer type, critical for early cancer diagnosis and for fundamental understanding of cancer metastasis. This dissertation will also provide a comprehensively profiling of the biophysical characteristics of inflammatory breast cancer stem cells at the single-cell level using multiple microengineered tools to delineate the live cell phenotypic characteristics of the model of the most metastatic breast cancer subtype. Last, this dissertation will further explore synthetic micro/nanoscale *ex vivo* cellular microenvironment for study and regulating human embryonic stem cell behaviors that are desirable for functional tissue engineering and regenerative medicine. These novel micro/nanoengineered functional biomaterials and biosystems will not only permit advances in engineering but also greatly contribute to improving human health.

Chapter 1

Introduction

1.1 Micro/nanoengineered Biomaterials an Biosystems for Medicine

Micro/nanotechnologies including advanced nanofabrication and functional nanomaterials have provided new opportunities for many biological and medical applications. Biological sample processing and analysis are of great importance for both medical and science applications, and hold a central role in the diagnosis of many physiologic and pathologic conditions, such as immune system dysfunction and cancer. However, tapping into the wealth of biological information, for clinical and scientific applications, requires not only the understanding of the biology involved but also adequate technologies. Therefore, this dissertation will discuss interdisciplinary researches that leveraging the engineering advances in biomaterials, microfluidics and advanced manufacturing for new and better solutions for emerging problems in cancer biology, systems immunology, and stem cell-based regenerative medicine. This dissertation will particularly discuss the potential of integrated microfluidics to perform

rapid, accurate, and sensitive functional cellular immunophenotyping assays for target subpopulations of immune cells isolated directly from patient blood, and their potential to provide an unprecedented level of information depth on the distribution of immune cell functionalities on a patient-by-patient basis. This dissertation will also explore the possible techniques for efficient isolation and informative analysis of circulating tumor cells (CTCs) and cancer stem cells (CSCs) from animal models and cancer patients, critical for accurate diagnosis and prognosis of cancer and for fundamental understanding of cancer metastasis. In addition to the applications for systems biology and cancer biology, this dissertation will further explore synthetic micro/nanoscale *ex vivo* cellular microenvironment for study and regulating human embryonic stem cell behaviors that are desirable for functional tissue engineering and regenerative medicine. These novel micro/nanoengineered functional biomaterials and biosystems will not only permit advances in engineering but also greatly contribute to improving human health.

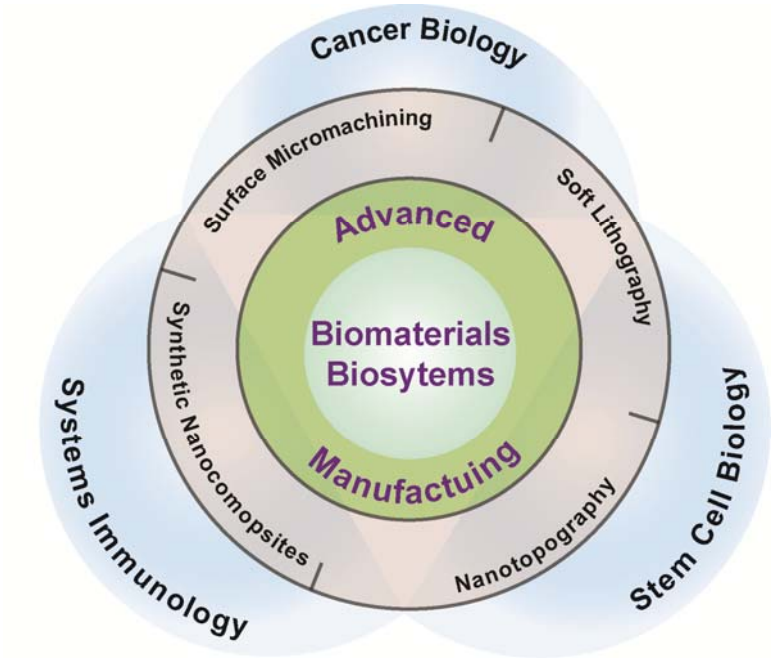

Figure 1-1 Micro/nanoengineered Biomaterials and Biosystems for Medicine.

1.2 Research Topics and Dissertation Outline

1.2.1 Integrated Microfluidic Immunophenotyping Platform for Functional Cellular Immunophenotyping

The immune status of patients with infectious diseases and immune dysfunctions are dynamic and patient-specific, and such complex heterogeneity has made effective immunomodulatory therapies challenging in the clinic [1, 2]. An accurate and real-time measurement of the immune status of patients is critical in disease diagnosis and prognosis, evaluating efficacy of immunotherapeutics, and tailoring drug treatments [2]. As such, there is an urgent need for new immunomonitoring technologies that can perform rapid and accurate cellular functional assays on patient immune cells in order to define and characterize the "immune phenotype" of patients.

Quantitative characterization of functional signature and diversity of immune cells from patient blood is currently challenging, owing to the intrinsic limitations of conventional methods, despite its promise to drastically improve clinical knowledge and

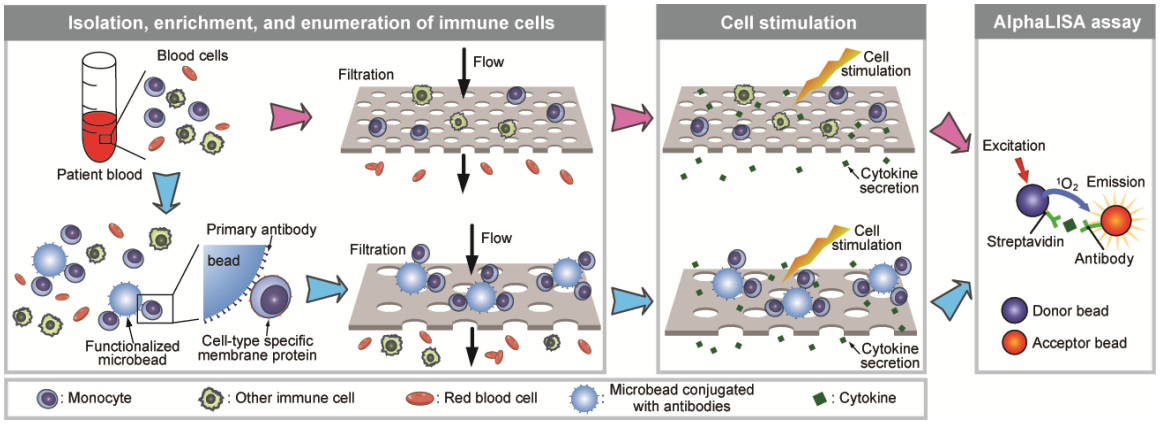

Figure 1-1 Isolation, enrichment, enumeration and functional immunophenotyping of immune cells using integrated microfluidics. Using functionalized microbeads with a microfiltration membrane, PBMCs and monocytes can be isolated for downstream functional immunosensing using the AlphaLISA assay.

practice for many immune and infectious diseases. Several approaches currently exist for assessment of immune status of patients; however, all these approaches have significant limitations that prevent their broad applications in the clinical setting. Enzyme-linked immunosorbent assay/spot (ELISA/ELISpot), for example, is a gold standard for quantifying cellular cytokine production while enabling multiplexed, highly sensitive analyses [3-5]. However, the ELISA/ELISpot technique usually requires numerous reagent manipulation processes that involve multiple staining, washing, blocking, and sample transfer steps, which are laborious and time-consuming, prohibitive for standardization and practical utility in real-time clinical decision making. In addition, the ELISpot method requires isolation and purification of desired subpopulations of immune cells prior to analysis, necessitating extensive sample preparation of blood specimens. Functional cellular immunoassays can also be performed using intracellular cytokine staining (ICS) flow cytometry [6]. However, ICS flow cytometry has so far only enabled detection of up to five cytokines, providing only a partial picture of the functional immune system. ICS flow cytometry also requires a large number of cells in suspension ($> 1 \times 10^7$ cells in 1 mL solution) and is sample destructive, thus precluding downstream functional assays that require live cells. ICS flow cytometry has so far remained highly variable with regard to sample handling, reagents, instrument setup, and data analysis, thus standardization of ICS flow cytometry has proved difficult if not impossible. The limitations associated with the conventional approaches to define the functional immune status of patients need to be fully addressed to realize rapid and accurate analysis of the immune phenotype of patients, a key step that provides crucial information relating to

staging, treatment choice, monitoring of efficacy, safety and dose adjustment of immunomodulation, as well as biological assessment of remission.

In Chapter 2, I will discuss a promising application of microfluidics for immune monitoring of patients with minimum sample requirement and rapid functional immunophenotyping capability. Here using a surface micromachining technique, I developed a integrated microfluidics-based immunophenotyping assay (MIPA) device capable of integrating all the immunophenotyping assay operations on a single chip, including cell isolation / enrichment / enumeration, cell stimulation, and cytokine secretion detection [7-9]. This integrated microfluidic platfom permits rapid, accurate, and sensitive cellular functional immunophenotyping assays on subpopulations of immune cells, potentially can provide an unprecedented level of information depth on the distribution of immune cell functionalities.

1.2.2 Micrengineered Nanorough Surfaces for Efficient Capture of Circulating Tumor Cells

Circulating tumor cells (CTCs) detached from both primary and metastatic lesions represent a potential alternative to invasive biopsies as a source of tumor tissue for the detection, characterization and monitoring of cancers. Over the last decade, there has been a great interest in utilizing the peripheral blood CTCs to predict response to therapy and overall survival of patients with overt or incipient metastatic cancers [10, 11]. It has been demonstrated that an elevated CTC level is negatively correlated with prognosis in patients with metastases of the breast [12-17], prostate [18-23], lung [24, 25], and colon [26]. Clinical evidence further suggests that cancer cells disseminate at a much earlier

stage in tumorigenesis than previously recognized and that the presence of CTCsmay be a marker of successful tumor vascular invasion, having occurred a considerable period of time before the establishment of viable distant metastases [27]. The concept of CTCs as a marker of very early metastases is a radical departure from current approaches for cancer detection, which are based on either radiographic screening or at the development stage on serum proteomics [28]. Neither of these approaches captures a living cell in the process of metastatic progression and thus, testing for the presence of bona fide CTCs constitutes a potentially very powerful tool for cancer diagnosis and prognosis, and by studying the alterations of these captured live cancer cells, for tailoring cancer treatments on a single patient basis.

Despite the clinical and pathophysiologicalimportance of CTCs, the current molecular and cellular understanding of CTCs is extremely poor, largely owing to the

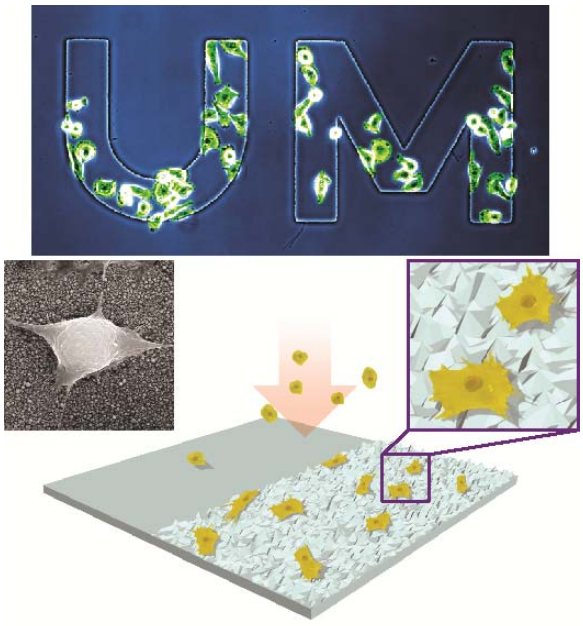

Figure 1-2 Intrinsic nanotopological sensing for capture of cancer cells. Inserts show a SEM (left) and a zoom-in (right) images of cancer cells captured on nanorough glass surfaces.

fact that the current techniques to isolate and characterize these rare cells are limited by low yield and purity, complex techniques, and expensive proprietary equipments, compounded by yielding little phenotypic and molecular information about the CTCs themselves. As such, there is still little knowledge about timing of CTC release fromprimary tumors, their heterogeneity and molecular and cellular properties, and the degree to which they are representative of either primary or metastatic tumor deposits.

Nanotechnologies including advanced nanofabrication and functional nanomaterials have provided new opportunities for many biological and medical applications. My doctoral study has leveraged novel nanofabrication techniques to develop synthetic nanotopographical biomaterial to address specifically these broad challenges in understanding the CTC biology. I introduced a simple yet effective microfabrication strategy for precise control and patterning of the local nanoroughness on glass surfaces using photolithography and reactive ion etching (RIE) which are well-established processes used in semiconductor microfabrication. Incorporating this nanotopographic surface into a microfluidic platform, I have proven a new approach that can efficiently isolate, enrich, realse and potentially informative molecular and cellular analysis of live CTCs at the single-cell level. This novel CTC capture strategy uniquely utilized the intrinsic differential adhesion preference of cancer cells to nanorough surfaces when compared to normal blood cells and thus did not depend on their physical size or surface protein expression, which is a significant advantage as compared to other existing CTC capture techniques (Figure 1-2) [29]. I envision that this CTC capture and analysis platform which can provide a superior performance for efficient isolation of rare and viable CTCs, permit potentional informative analysis of live CTCs for accurate

diagnosis and prognosis of cancer and help understand the crucial early metastatic process of cancer and hopefully discover new targets or phenotypes in the CTCs that can aid in the design of more effective molecular treatments.

1.2.3 Biophysical Phenotyping of Cancer Stem Cells

Cancer stem cells (CSCs), as defined through specific marker expression methods, have been shown to initiate tumorigenesis, have the capacity to self-renew, and initiate cancer metastasis in many cancer types. Although identification of CSCs through marker expression helps separate and define the CSC compartment, it does not directly provide information on how or why this cancer cell subpopulation is more metastatic or tumorigenic. In this Chapter 4, I will provide a comprehensively profiling of the functional as well as biophysical characteristics of inflammatory breast cancer (IBC) CSCs at the single-cell level using multiple microengineered tools and traditional *in vitro* studies to delineate the live cell phenotypic characteristics of the model of the most metastatic breast cancer subtype. IBC is the most aggressive and lethal form of breast cancer with two-thirds of patients presenting with axillary lymph node involvement and up to one-third of patients having distant metastases at initial diagnosis [30, 31]. Why

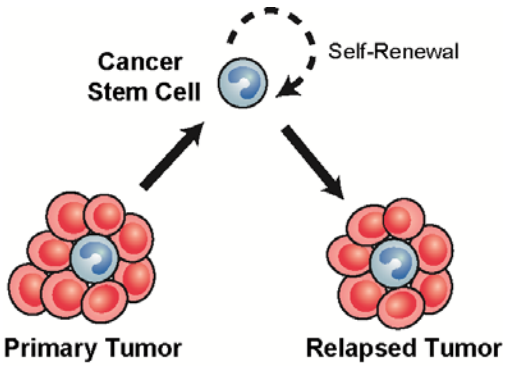

Figure 1-3 Concept of cancer stem cells.

IBC is so much more aggressive and metastatic than other breast cancers though is not definitively known. Previous studies have identified ALDH+ IBCs as key mediators of tumorigenesis and metastasis, and they are negatively correlated with survival [32]; however, the how and why have been left unstudied. Characterizing the functional behaviors of IBC CSCs such as cell migration, growth, adhesion, invasion, self-renewal, and differentiation is a direct approach to describe and understand IBC CSCs based upon their intrinsic properties, thus paving the way to determine therapeutic approaches to this most lethal subpopulation within IBC. Distinct biophysical properties of IBC CSCs such as cell deformability, adhesion strength, and traction force provide physical insights into why IBC has an enhanced propensity to metastasize compared to other breast cancers. The multiparametric cellular phenotyping of functional and biophysical characteristics of IBC CSCs yields a new understanding of IBC's metastatic properties and how they might develop and be targeted for therapeutic interventions.

1.2.4 Nanotopography-mediated Mechanoseing of Human Embryonic Stem Cells

During developmental processes within an embryo and the tissue maintenance and repair occurring in an adult organism, a myriad of stem cells are regulated by their extracellular matrix (ECM) enriched with tissue/organ-specific nanoscale topographical cues, and thus adopt different fates and functions specifically tuned by the microenvironment they reside in. Attributed to their capability of either self-renewal or differentiation into most types of somatic cells, stem cells are promising cell sources for future regenerative medicine. However, a major challenge still remains as to achieve stem cell fate control *in vitro* with high specificity as well as high yield.

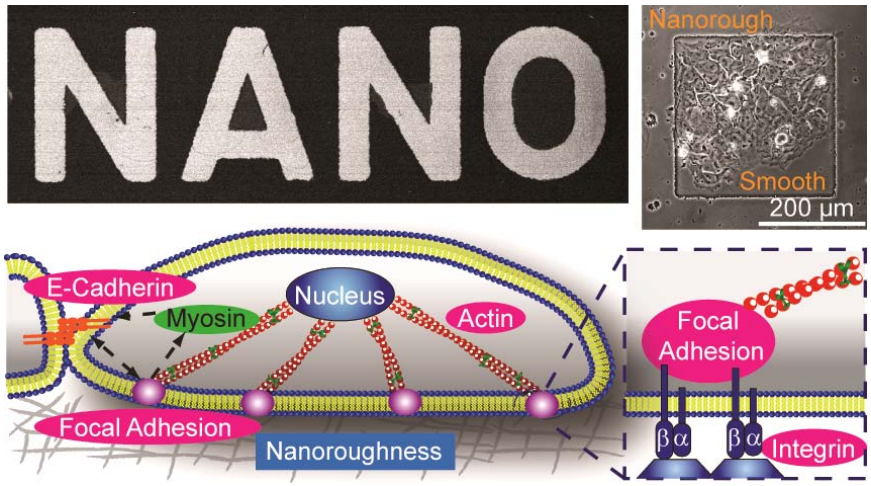

Figure 1-4 Nanotopography regulates stem cell behaviors.

In Chapter 5, I will demonstrate regulation of stem cell fates and functions via ECM nanotopography that enables versatile, robust and large-scale stem cell engineering *in vitro* through the development of synthetic nanotopographical biomaterials mimicking stem cell niches. In this study, I demonstrated that nanoscale topolographic features can provide a potent regulatory signal over a diverse array of hESC behaviors, including cell morphology, adhesion, proliferation, clonal expansion, self-renewal and fate. In addition, I explored underlying mechanism by which hESCs sense the biophysical cues and transduce them into intracellular biochemical signals and behavioral responses ('mechanotransduction'). Indeed, understanding these fundamental questions of mechanobiology in hESCs is of great current interest, as the results generated from such research will provide important insights and practical design guidelines for the synthetic stem cell microenvironment to direct hESC behaviors that are desirable for functional tissue engineering and regenerative medicine.

Chapter 2

Integrateded Microfluidics for Functional Immunophenotyping

2.1 Introduction

The immune system plays a critical role in protecting a living organism against invasions of viruses, bacteria, and parasitic worms, and distinguishes diseased tissue from healthy one [33-36]. Leukocytes (white blood cells) are important blood constituents that play a major role in innate and adaptive immune responses against pathogenic infections, allergic conditions, and malignancies. Leukocytes are a heterogeneous mixture of multiple cell subsets (granulocytes, lymphocytes, and monocytes) defined by their morphology, surface antigen expression, and production of cytokines - small proteins for intercellular communications between leukocytes of the same type (homotypic) or different types (heterotypic) [37-40]. The numbers, proportions and functional responses of leukocyte subsets change drastically in the presence of infections, malignancies, and autoimmune disorders, making analysis of leukocyte subpopulations particularly valuable in the diagnosis and monitoring of diseases [36, 41]. For example, human

immunodeficiency virus (HIV) infection causes depletion of CD4+ T cells in peripheral blood and other lymphoid tissues [33, 42-44]. As a result, the absolute counts of CD4+ T-cells and the ratio of CD4+ / CD8+ T-cells are commonly used as indicators of the onset of the acquired immunodeficiency syndrome (AIDS) and as benchmarks for the initiation of antiviral therapy to treat AIDS.

Leukocytes orchestrate immune responses by releasing cytokines [3, 34, 41, 45-48]. Given the heterogeneity of leukocytes and different roles played by different subpopulations of leukocytes in the immune response, measurements of capacity to produce cytokines from different subpopulations of leukocytes become critically important in clinical diagnosis. Production of interferon gamma (IFN-γ) by T-cells, for example, correlates with the body's ability to mount a vigorous immune response and is used to identify antigen-specific T cells in diseases such as HIV and tuberculosis.[34, 48, 49] Sepsis is another serious clinical condition that results from dysregulation of the immune response to infection [1, 3, 50-52]. One hallmark of sepsis commonly reported is the decreased capacity of monocytes to release pro-inflammatory cytokines such as tumor necrosis factor-alpha (TNF-α) in response to *ex vivo* lipopolysaccharide (LPS) challenge [3].

The immune status of patients with infectious diseases and immune dysfunctions are dynamic and patient-specific, and such complex heterogeneity has made effective immunomodulatory therapies challenging in the clinic [1, 2]. An accurate measurement of the immune status in patients with immune system disorders is critical in evaluating the stage of diseases and tailoring drug treatments. As such, there is an urgent need for new technologies that can perform rapid and accurate functional cellular

immunophenotyping for quantitative analysis of the cytokine secretion profiles on patient immune cells in order to define and characterize the "immune phenotype" of patients.

A significant challenge in profiling cytokine secretion in a heterogeneous cell suspension such as blood is the fact that the same cytokines can be produced by several different subpopulations of leukocytes. For example, IFN-γ is commonly secreted by CD4+ T-cells. However, IFN-γ can also be produced by CD8+ T-cells, macrophages and neutrophils. In addition, the numbers and proportions of subpopulations of immune cells may vary in individuals and at different stages of diseases. The conventional whole blood stimulation assay routinely used in the clinical setting involve measurements of the capacity of the whole population of leukocytes to produce pro-inflammatory cytokines when stimulated *ex vivo*. However, this 'bulk' assay may not be informative enough pinpoint the phenotype or real identity of the reactive immune cells involved, and is insufficient to accurately define and characterize the immune status of patients.

To address this need, an integrated microfluidic immunophenotyping device was developed to achieve rapid and efficient isolation, enrichment, stimulation and functional immunophenotyping of subpopulations of immune cells directly from blood specimens. This microfluidics-based innovative technology can serve as a comprehensive and standardized immune monitoring platform to define and characterize the "immunotype" of healthy individuals and patients with immune dysfunctions before, during, and after targeted immunomodulation, thus leading to interventions that can significantly reduce or eliminate symptoms, side effects, disease progression, recurrence, and ultimately immune dysfunction-associated mortality.

2.2 Overview of the Current Techniques

2.2.1 Conventional Functional Cellular Immunophenotyping Assays

Several approaches currently exist for assessment of immune status of patients. Enzyme-linked immunosorbent assay/spot (ELISA/ELISpot), for example, is a gold standard for quantifying cellular cytokine production while enabling multiplexed, highly sensitive analyses (Figure 2-1) [53]. ELISA/ELISpot has been commonly adapted for identifying immune status of patients infected by malaria [54], HIV [55, 56] and mycobacterium tuberculosis [57] patients and monitoring immune response of cancer patients undergoing immuno-therapeutic treatment [58, 59]. However, the ELISA/ELISpot technique usually requires numerous reagent manipulation processes that involve multiple staining, washing, blocking, and sample transfer steps, which are laborious and time-consuming. The complexity in implementing ELISA/ELISpot has been prohibitive for their standardization and has significantly reduced their practical utility in real-time clinical decision making. In addition, the ELISpot method requires isolation and purification of desired subpopulations of immune cells prior to analysis, necessitating extensive sample preparation of blood specimens.

Functional cellular immunophenotyping assays can also be performed using intracellular cytokine staining (ICS) flow cytometry - a flow cytometry based assay that detects the production and accumulation of cytokines (Figure 2-1) [6]. For example, the multiple parameter ICS flow cytometry can be used for understanding the functional capacity of effector and memory T-cells response, which can provide detailed information for vaccine development [6]. ICS flow cytometry has also been widely used

for study of sepsis [3], HIV [60, 61] and tuberculosis [62, 63] cancer immunotherapy [5]. Although ICS flow cytometry can perform the high-throughput (>10,000 cells/sec) single-cell based cytokine production measurement, it has so far only enabled detection of up to five cytokines, providing only a partial picture of the functional immune system. ICS flow cytometry also requires a large number of cells in suspension (> 1×10^7 cells in 1 mL solution) and is sample destructive, thus precluding downstream functional assays that require live cells. ICS flow cytometry has so far remained highly variable with regard to sample handling, reagents, instrument setup, and data analysis, thus standardization of ICS flow cytometry has been proved difficult if not impossible. The limitations associated with the conventional approaches to define the functional immune status of patients need to be fully addressed to realize rapid and accurate analysis of the immune phenotype of patients, a key step that provides crucial information relating to staging, treatment choice, monitoring of efficacy, safety and dose adjustment of immunomodulation, as well as biological assessment of remission.

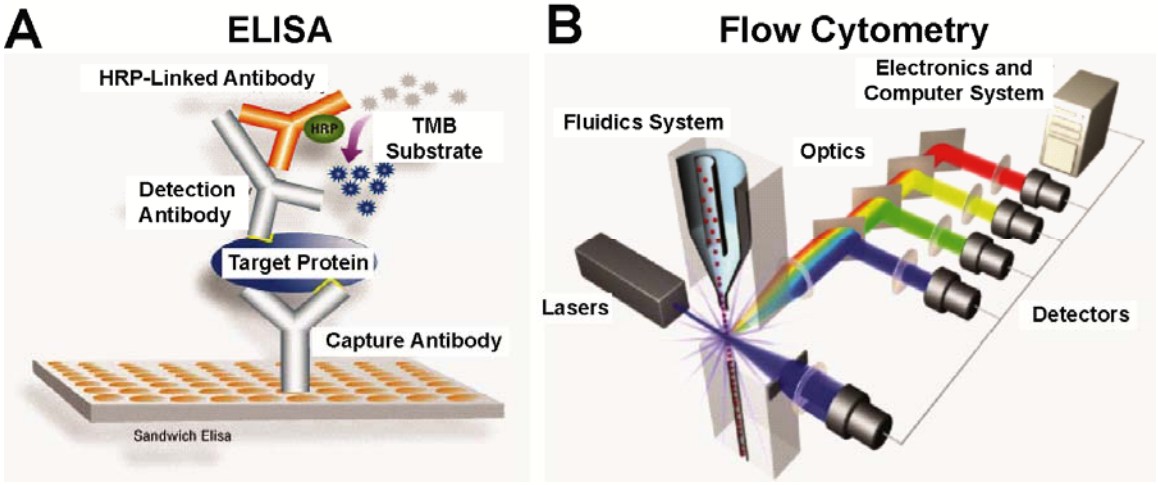

Figure 2-1 Schematics of ELISA (A) and flow cytometry (B).

2.2.2 Microfluidic Cellular Immunophenotyping of Whole Blood

Recent advances in integrated microfluidics have made possible miniaturization and integration of biosample preparative and analytical techniques on a single chip to enable rapid, sensitive, and multiplexed high-throughput cell-based assays. Some of these microfluidic tools have been demonstrated as promising immune monitoring technologies with cell trapping and analysis functionalities and a minimum sample requirement to achieve rapid functional immunophenotyping analysis (Figure 2-2).

Whole blood immunoassay is one of the most commonly used methods to determine patient immune status, which provides useful information for diagnosis [3, 4], prognosis [64], and deepening biological understanding of immune and infectious diseases [65, 66]. Conventional whole-blood immune tests are based on proteomic identification of biomarkers in blood, relying on antibody-based heterogeneous or homogeneous immunoassays (e.g., ELISA) to capture soluble biomarkers in blood specimens. Recently, to achieve rapid on-chip immunoassays with a minimum amount of blood, several microfluidics-based whole blood immunoassay devices have been successfully developed and implemented for disease biomarker detection using patient blood. A notable example is the integrated blood barcode chip recently reported by Fan et al. [67] that can achieve on-chip plasma separation from microliter quantities of whole blood and rapid in-situ multiplexed protein biomarker measurements (Figure 2-2A). The blood barcode chip consists of two components: (1) a plasma separation structure as the plasma-skimming channel based on the Zweifach-Fung effect; (2) a protein detection region using a patterned DNA-encoded antibody library (DEAL) barcode immobilized on the surface of the plasma-skimming channel. The blood barcode chip has been reported

to be capable of detecting picomolar concentrations of human chorionic gonadotropin (hCG), cancer biomarkers such as prostate-specific antigen (PSA), and more than ten cytokines in blood samples simultaneously from cancer patients.

A key enabling technology used in the blood barcode chip for multiplexed bio-sensing and -detection is the DEAL technology involving DNA-directed immobilization of antibodies to convert a prepatterned ssDNA barcode microarray into an antibody array, thus providing a powerful means for spatial encoding. Specifically, in the DEAL assay, each capture antibody is tagged with multiple copies of an ssDNA oligomer that is complementary to ssDNA oligomers that have been surface-patterned into a microscopic barcode within the immunoassay region of the blood barcode chip. Flow-through of the DNA-antibody conjugates transforms the DNA microarray into an antibody microarray for subsequent surface-bound immunoassays. Because DNA patterns are robust to dehydration and can survive elevated temperatures, the DEAL approach circumvents denaturation of antibodies often associated with typical microfluidics fabrication. Compared with conventional whole blood immunoassays such as those using ELISA, which require a large blood volume and extensive sample preparations, the microfluidics-based blood barcode chip enables rapid on-chip blood separation and multiparametric measurements of a panel of plasma proteins from a finger prick of whole blood.

More recently, the same research group has further extended the antibody barcode technique to establish an automated, self-powered microfluidic chip for rapid and multiplexed protein detection from whole blood [68]. The blood plasma separation and subsequent immunoassays are sequentially driven by the capillarity of a filter paper coupled with the hydrophilic nature of microfluidic channel surfaces. This inexpensive

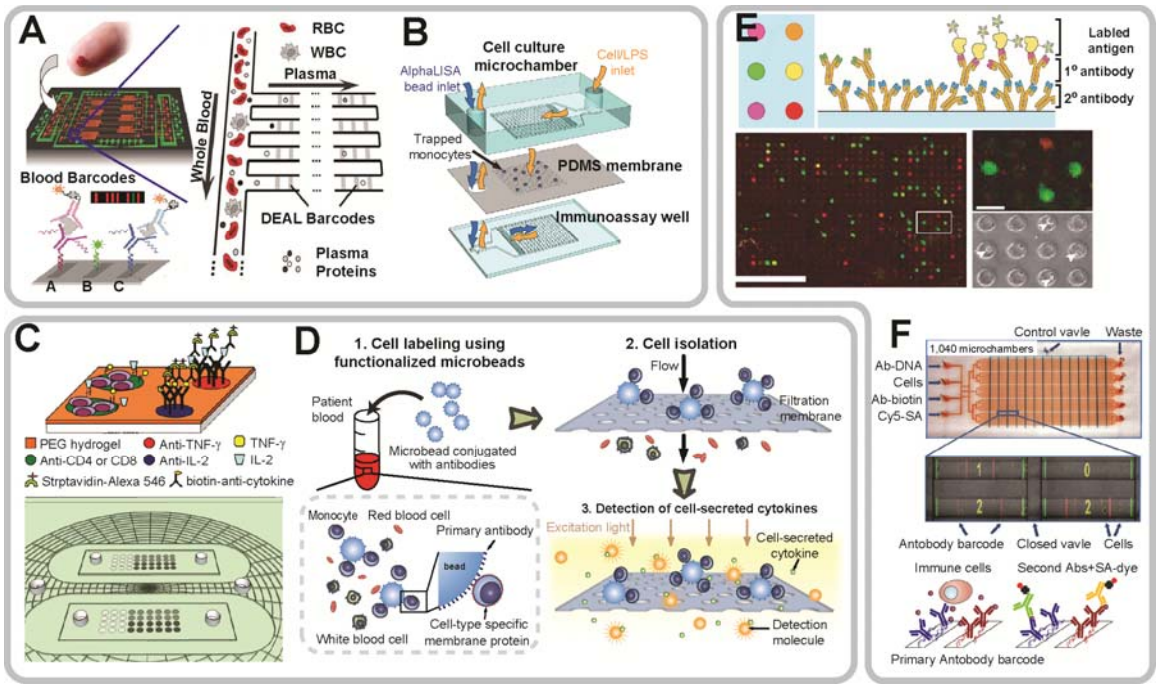

Figure 2-2 Intgrated microfluidic devices for functional immunophenotyping of immune cells in whole blood (A-B), subpopulations of immune cells (C-D) and single immune cells (E-F). (A) Design of the integrated blood barcode chip (IBBC). Adapted from reference [67], Copyright © 2008, with permission from Nature Publishing Group. (B) Schematic of a multi-layered MIPA device consisting of a cell culture chamber, a PDMS microfiltration membrane (PMM), and an immunoassay chamber. Reproduced from reference [8]. (C) Conceptual design of an antibody-coated microarray for detection of cytokines secreted by CD4+ or CD8+ T-cells. Reproduced from reference [69], by permission of The Royal Society of Chemistry. (D) Schematic of isolation and immunophenotyping of subpopulations of immune cells from blood specimens by a combined use of both PMM and functionalized microbeads. Reproduced from reference [9]. (E) Working principle of the microengraving array for capture and immunomonitoring of single immune cells. Adapted from reference [70], Copyright © 2006, with permission from Nature Publishing Group. (F) Photograph and working principle of the single-cell barcode chip for polycytokine analysis of single immune cells. Adapted from reference [71], Copyright © 2011, with permission from Nature Publishing Group

subsequent immunoassays are sequentially driven by the capillarity of a filter paper coupled with the hydrophilic nature of microfluidic channel surfaces. This inexpensive and self-powered whole blood immunoassay chip can provide a cost effective platform for point-of-care diagnosis in a resource limited environment.

Several microfluidics-based label-free, real-time detection techniques have also been developed recently for immunosensing. Development of real-time immunosensing techniques allows detailed examination of temporal dynamics of cytokine secretion from

immune cells, which may provide informative and unique signature about the functional status of patient immune system [36]. The ability to assess dynamic cytokine secretion from immune cells, for example, can allow detection of onset of the signaling process and study of intercellular communications via cytokine-mediated paracrine / autocrine signaling. Monitoring both the location and timing of cytokine secretion events among a heterogeneous population of individual immune cells can also potentially allow identification of which individual cells initiate the immune response and which cells are then activated by such initial immune response. In clinical diagnosis such as tuberculosis detection, pathogen biomarkers (e.g., pathogen-specific antibodies) are not yet available. As a result, cytokine production by T-cells is commonly used as a diagnostic marker for tuberculosis. If detection of dynamic response of antigen-specific T cells becomes available, it will enable early pathogen detection before pathogen biomarkers are produced or the pathogen proliferates in the host.

A noteworthy microfluidic label-free immunodetection method has been recently reported by Stern et al. [72], who have developed CMOS-compatible semiconducting nanowires for real-time measurements of antibodies and early signals responsible for T-cell activation that involve clustering of CD3 receptors. Another label-free biosensing technique reported by Endo et al. [73] has applied immobilized antibodies and localized surface plasmon resonance (LSPR) to continuously monitor concentration levels of IL-2 secreted by concanavalin-A (Con-A) stimulated mouse thymus cells. The LSPR-based biosensor provides a promising platform with attractive advantages for real-time detection of cellular responses in a simplified experimental set-up with a low sample volume requirement. Overall, label-free cellular immunophenotyping techniques permit

real-time quantifications of dynamic cytokine secretion processes, providing unique functional signature of immune cells such as how fast and strong immune cells secrete cytokines in response to antigen stimulations.

2.2.3 Microfluidic Cellular Immunophenotyping of Subpopulations of Immune Cells

Microfluidic whole-blood immunoassays measure the overall capacity of the whole population of leukocytes in blood to produce cytokines. The numbers, proportions and capacity to produce cytokines of leukocyte subsets actively respond to the presence and status of infections, malignancies, and autoimmune disorders, making analysis of leukocyte subpopulations critically important in clinical diagnosis [36, 41]. Thus, microfluidic whole-blood immunoassays may not be informative enough to accurately reveal the immune status of patients, as in these 'bulk' assays it is difficult to pinpoint the phenotype or real identity of the reactive immune cells involved. Recently, there are concerted efforts from different research groups to integrate immune cell separation procedures into microfluidic immunoassay devices and systems to achieve accurate and rapid cellular functional analysis on specific subpopulations of immune cells isolated from blood specimens. Zhu et al., for example, have recently developed a microarray device uniformly coated with both T-cell capture antibodies (anti-CD4 and anti-CD8) and cytokine capture antibodies (anti-IFN-γ and anti-IL-2) on top of a poly(ethylene glycol) (PEG) hydrogel layer (Figure 2-2C) [69]. To enable capture and positioning of single CD4+ and CD8+ T-cells, the antibody-coated microarray was covered with photolithographically patterned PEG hydrogel microwells on top of the antibody

containing hydrogel layer. The antibody-coated microarray can directly process red blood cell (RBC) depleted human whole blood samples for capture of individual CD4+ and CD8+ T-cells and subsequent functional examination of IFN-γ and IL-2 secretion from single CD4+ T-cells. To capture CD4+ and CD8+ T-cells, RBC- depleted whole human blood was simply introduced into the microfluidic device and the target T-cells were immobilized on their respective Antibody spots while the unwanted cells were washed away at a pre-defined shear stress. As the cytokine capture antibody (anti-IFN-γ and anti-IL-2) spots were designed to localize next to the isolated T-cells, following mitogenic activation and immunofluorescent staining of the captured T-cells revealed concentration gradients of surface-bound cytokine molecules.

The antibody-based microarray platform reported by Zhu et al. has simplified sample preparation process and also reduced the required sample volume. Although immobilized antibodies offer a heightened cell isolation purity and cytokine measurement sensitivity, it still suffers from several limitations, including the need of multiple washing and blocking steps and the difficulty to achieve real-time dynamic cytokine secretion measurement. To address these limitations, the same research group have recently applied DNA and RNA-based aptamers as an alternative to antibodies and immobilized aptamers on an array of micropatterned gold electrodes [74, 75]. The aptamers have been thiolated for assembly on gold and functionalized with methylene blue redox reporter for electrochemical signal transduction and detection with gold electrodes. Instead of using fluorescence-based biosensing methods, the authors have demonstrated electrochemical measurements to access the dynamic nature of cytokine secretion from activated human monocytic cell and T-cell lines with a detection sensitivity of ~ ng/mL [74, 75].

2.2.4 Microfluidics to Study Functional Heterogeneity of Single Immune Cells

Functional and phenotypic variation among individual single cells, or single-cell functional heterogeneity, is a common feature for hematopoietic cells including immune cells. Thus, quantitative analysis of cytokine secretion profiles of individual immune cells is required for precise assessment of subtle variations in the functional immune status across different subsets of immune cells. The most commonly used methods for single-cell cytokine secretion analysis are ICS flow cytometry and ELISpot [53, 76]. As discussed earlier, quantitative functional assessment of individual leukocytes by ICS flow cytometry requires detection of cytokines accumulated inside fixed and permeabilized cells. The need for such cell fixation in ICS flow cytometry prohibits assessments of dynamic cytokine secretion from the same single immune cell or post-detection functional characterization requiring live cells. ELISpot assay allows enumeration of single immune cells secreting cytokines in response to antigen stimulation. However, ELISpot cannot quantify the amount of cytokine secretion. Further, ELISpot requires removal of immune cells from the substrate coated with capture antibodies upon completion of the assay and only allows for tracing cytokine spots left behind on the substrate surface, which prevents identification of which individual single cells secrete what cytokines on the antibody-coated substrate. In addition, ELISpot requires isolation of desired cell subsets prior to analysis by extensive preprocessing of blood samples.

Over the last decade, significant research efforts have been directed toward applying microfluidics for manipulation of single immune cells and massively parallel, high-throughput analysis of cell-secreted soluble molecules, such as antibodies, cytokines

and metabolites, at the single-cell level. One of the most notable example entails plating and stimulating single immune cells in an array of microfabricated wells, transferring soluble molecules secreted from immune cells onto a secondary solid surface coated with capture antibodies, and labeling captured molecules with fluorescently tagged proteins (e.g., antigens for antibody detection and secondary antibodies for antigen detection) prior to subsequent optical detection. For example, Love et al. [70] have pioneered the development of engraved microarrays made in PDMS using soft lithography to monitor cytokines secreted from single immune cells (Figure 2-2E). The engraved microarray can consist of 25,000 microwells (50-100 μm in diameter), each of which can confine single immune cells in a nanoliter volume (~ 0.1-1 nL). After individual immune cells trapped and stimulated in the microwell array, the engraved microarray can be flipped against an antigen- or secondary antibody-immobilized glass slide to capture primary antibodies secreted from cells. Compared to ELISpot, the engraved microarray enables a rapid (< 12 hr) and high-throughput (> 10,000 individual cells) system for identification, recovery and clonal expansion of single immune cells producing antigen-specific antibodies. More recently, follow-up studies from the same research group have demonstrated the capability of the engraved microarray for characterization of dynamic cytokine secretion from individual primary human T-cells after activation ex vivo [77, 78].

In addition to the microengraving method developed by Love et al., Jin et al. have independently developed a similar functional immunosensing technique called 'immunospot array assay on a chip' (or ISAAC) to detect production of monoclonal antibodies by blood lymphocytes [79]. The ISAAC method offers a rapid and high-

throughput system for screening and analysis of antigen-specific antibody-secreting cells (ASCs) on a single-cell basis. Similar to the microengraving assay, the ISAAC also includes an array of microwells for trapping of single live immune cells. The top surface of ISAAC is functionalized with antibodies against immunoglobulin, and antibodies secreted by individual ASCs trapped in the wells are captured and bound to the device surface around the well. The ISAAC method is useful for detecting ASCs in response to different antigens as well as for selection of ASCs secreting high-affinity antibodies. Although both the microengraving and ISAAC methods have used a high-density array of microwells to trap and isolate single immune cells, the two methods utilize quite different detection techniques. Fundamentally, the microengraving method pioneered by Love, at al. is based on ELISA [70], whereas the ISAAC is based on ELISPOT [79].

Ma et al. [71] have recently implemented a novel integrated microfluidic approach called the "single-cell barcode chip" for high-content assessment of functional heterogeneity of antigen-specific T-cells at the single-cell level (Figure 2-2F). The single-cell barcode chip consists of 1,040 microchambers with a nanoliter volume, and each microchamber can trap single or a small number of immune cells. On the bottom surface of each microchamber, a spatially encoded antibody barcode array is pre-printed to capture cytokine molecules secreted from immune cells trapped in the microchamber. Protein concentrations are measured with immunosandwich assays from the spatially encoded antibody barcode. A full barcode from each microchamber represents a complete panel of multiple cytokine species produced by a single immune cell (or a few cells). The single-cell barcode chip permits highly multiplexed (more than ten proteins) on-chip detection of a few thousand proteins or less from thousands of immune cells

simultaneously. The single-cell barcode chip reported by Ma et al. represents an exciting and very informative microfluidic single-cell immunophenotyping tool for analyzing functional signatures of immune cells with high sensitivity, throughput, multiplicity and small sample size, which can be used in a wide range of fundamental and clinical applications.

All of the microfluidic devices and systems discussed in this section can clearly provide a promising potential for high-throughput study of functional heterogeneity of single immune cells. However, one critical issue common with these approaches is that they require off-chip isolation and purification of target cells from whole blood prior to on-chip analysis. As such, there is still an unmet need for highly integrated microfluidic technology platform for efficient isolation and informative systems-level cellular characterization of immune cells down to the single-cell level and using unprocessed or minimally processed blood samples.

2.3 Methods and Materials

2.3.1 Surface Micromachining of Polydimethylsiloxane (PDMS)

Polydimethylsiloxane (PDMS) is one of the most frequently used structural materials in microfluidics, due to its great biocompatibility, optical transparency, gas permeability, mechanical elasticity, and electrical insulation [80]. The complexity of PDMS-based microfluidic systems is also increasing rapidly as sophisticated functions have being integrated into single microfluidic devices [81]. Just as the surface patterning techniques using lithography and etching processes have been the major drivers for the

successful development of micro-electro-mechanical systems (MEMS), there is an increasing demand in the field of microfluidics for highly reliable, repeatable and precise surface micromachining techniques to pattern PDMS for different practical microfluidic and bioengineering applications.

However, till now, PDMS has been largely considered incompatible with conventional lithography, due to its low surface energy resulting in dewetting of photoresist on the PDMS surface [82]. Soft lithography is a popular micromachining technique for rapid fabrication of PDMS structures [80]. Yet, soft lithography is a bulk micromachining technique, and it largely relies on replica molding, which often leaves behind a thin residual PDMS layer on top of the mold features. Through holes in bulk PDMS are typically achieved by punching through the PDMS structures, which can only generate macroscopic openings in PDMS and is far from a precise patterning method. High fidelity PDMS surface micromachining so far remains a major technical hurdle for the microfluidics research.

Several approaches for surface patterning of PDMS have been reported recently, even though each of these methods has its intrinsic constraints that have limited the scopes of their applications in microfluidics. Ryu *et al.* have reported a simple PDMS patterning method by mechanically removing excessive PDMS prepolymer from a pre-patterned mold using a traversing blade [82]. However, this mechanical scrapping method could limit the achievable minimum PDMS film thickness and its pattern resolution and uniformity. Another example is the photo-patternable silicone introduced by Dow Corning [83, 84]. This photosensitive silicone can be conveniently patterned as traditional negative photoresists. However, it also suffers with the drawbacks associated

with negative photoresists in terms of their high cost and limited resolution. Bhagat *et al.* and some others have proposed another photo-patterning approach by addition of photoinitiators such as benzophenone or 2,2-dimethoxy-2-phenyl acetophenone (DMAP) into PDMS prepolymer to make it photosensitive and thus directly photo-patternable [85, 86]. Yet, during UV exposure, the photomasks need to be kept at a minimum distance (~80 μm) from the PDMS prepolymer to avoid their direct contact. Thus, pattern resolution achieved using these photosensitive PDMS was significantly limited as compared to conventional photolithography operated in the contact mode. The cytotoxic effects of benzophenone or DMAP have not been well characterized yet and thus could present potential problems for biological applications. More recently, a rapid prototyping technique using direct UV-lithography followed by chemical development for pre-cured PDMS was introduced [87]. Although this technique does not introduce undesirable chemical components into PDMS, its pattern resolution is still limited by the required chemical development. Researchers have also recently attempted using intermediary adhesion layers, such as metal or polydimethyl-glutarimide (PMGI), to permit high-resolution lithography on PDMS [88, 89]. Still, these methods unavoidably require complex processing steps, and introduce undesirable alterations of the surface and mechanical properties of PDMS. For example, the spontaneous buckling of the metal film could result in a permanent deformation of PDMS during thermal curing [90].

To address the unguent need for surface patterning of PDMS, I have developed an easily-implementable wafer-level surface micromachining method to generate different planar PDMS microstructures using direct photolithography followed by reactive-ion etching (RIE). This new PDMS fabrication technique does not induce undesired

chemical components into PDMS and can be conveniently integrated with conventional silicon (Si)-based surface and bulk micromachining techniques and other PDMS-based soft lithography methods. The PDMS surface micromachining technique permits high fidelity lithographic patterning of PDMS structures with a resolution comparable to conventional photolithography (~2 μm). As a proof of its general applicability, this PDMS surface micromachining technique has been applied to generate different planar microstructures, such as patterned PDMS microfiltration membranes and free-standing beam structures, with their thickness ranging from sub-microns to tens of microns.

The fabrication process for surface micromachining of PDMS is illustrated in Figure 2-3 (details see Appendix A). A Si wafer was first silanized with (tridecafluoro-1,1,2,2,-tetrahydrooctyl)-1-trichlorosilane (United Chemical Technologies, Bristol, PA) for 1 hr under vacuum to facilitate subsequent release of patterned PDMS layers. PDMS prepolymer (Sylgard-184, Dow Corning, Midland, MI) was prepared by thoroughly mixing the PDMS curing agent with the PDMS base monomer (wt : wt = 1 : 10). PDMS prepolymer was then spin coated on the silanized Si wafer and completely cured at 110°C for 4 hrs. The thickness of the PDMS layer, ranging from hundreds of microns down to ~2 μm, could be controlled easily by the spin speed. To achieve ultra-thin PDMS layers with a sub-micron thickness, the PDMS prepolymer could be further diluted with hexane (Fisher Scientific, Pittsburgh, PA) to reduce its viscosity [91]. It has been reported that this strategy could generate PDMS layers with a thickness as thin as ~70 nm [91]. Similarly, with a weight ratio of PDMS curing agent:base:hexane as 1:10:20, PDMS thin films with a thickness of 500 nm were achieved by spin coating the diluted PDMS prepolymer at 5,000 rpm for 2 min. A surface profilometer (Dektak 6M surface profiler,

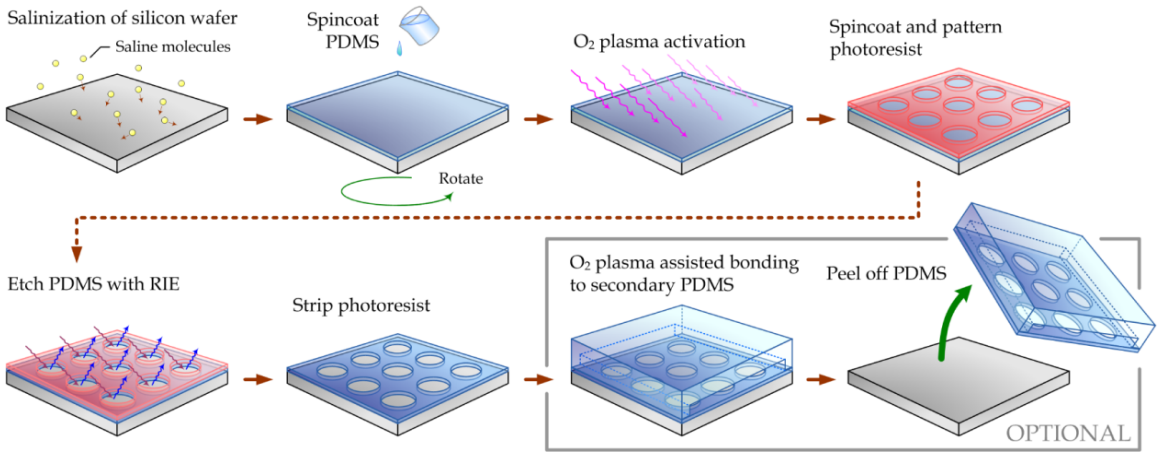

Figure 2-3 Schematic of photolithographic surface micromachining of PDMS.

Veeco Instruments, Plainview, NY) was then used to measure thickness of the PDMS.

The PDMS surface was then activated using a gentle treatment of O_2 plasma (Plasma Cleaner PDC-001, Harrick Plasma, Ithaca, NY) for 5 min to change the PDMS surface from hydrophobic to hydrophilic, in order to allow uniform coating of photoresist in the following step. Immediately following the O_2 plasma activation, photoresist such as AZ 9260 (AZ Electronic Materials, Branchburg, NJ) or SPR 220 (Rohm and Haas, Philadelphia, PA) was spin-coated uniformly on PDMS, soft baked at 80ºC for 10 min in oven, and then patterned using conventional contact or projection photolithography. It should be noted that sudden temperature changes should be avoided after soft bake of photoresist, as cracks in the photoresist layer might develop owning to the known issue of a mismatch of the coefficient of thermal expansion (CTE) between PDMS and photoresist. The Si wafer was then processed with RIE (LAM 9400, Lam Research, Fremont, CA) using SF_6 and O_2 gas mixtures to transfer patterns from the photoresist to the underlying PDMS layer. During the RIE process, the reactive gas ions would etch anisotropically the exposed PDMS regions where the photoresist had been previously developed and dissolved. (Details of the RIE process are discussed in the following

paragraphs.) Photoresist was then striped using solvents or O_2 plasma, leaving patterned PDMS thin films attaching on the Si wafer (Figure 2-4).

Our photolithographic method for surface micromachining of PDMS could be easily integrated with other conventional microfabrication techniques to generate functional microfluidic devices for different biomedical applications. As shown in Figure 2-4A & Figure 2-5A-E, large PDMS microfiltration membranes with arrays of through holes of different diameters were generated using our photolithographic PDMS surface micromachining method. These PDMS microfiltration membranes had a thickness of 2-20 μm, and they contained hexagonally spaced or square arrays of through holes with the hole diameter and center-to-center (c.t.c.) distance precisely defined by photolithography (the hole diameter of 4-20 μm and c.t.c. distance of 6-200 μm). Using the O_2 plasma-assisted PDMS bonding process, the PDMS microfiltration membrane was further transferred onto a secondary bulk PDMS, whose surface contained square-shaped support microstructures fabricated using soft lithography, to provide a superior mechanical strength for the large microfiltration membrane. As another example, free-standing thin PDMS beam structures (with a thickness of 500 nm) were successfully fabricated using XeF_2-based bulk Si dry etching (Xetch X4 series, XACTIX, Pittsburgh, PA) after surface pattering of PDMS on the Si wafer (Figure 2-4B and Figure 2-5F-I). Using contact photolithography, the minimum beam width along these free-standing PDMS beam structures was as small as 2 μm.

In this new fabrication method, a simple O_2 plasma treatment is introduced to address the major technical hurdle for wafer-level surface machining of PDMS: dewetting of photoresist on the intrinsically hydrophobic PDMS surface. The difficulty

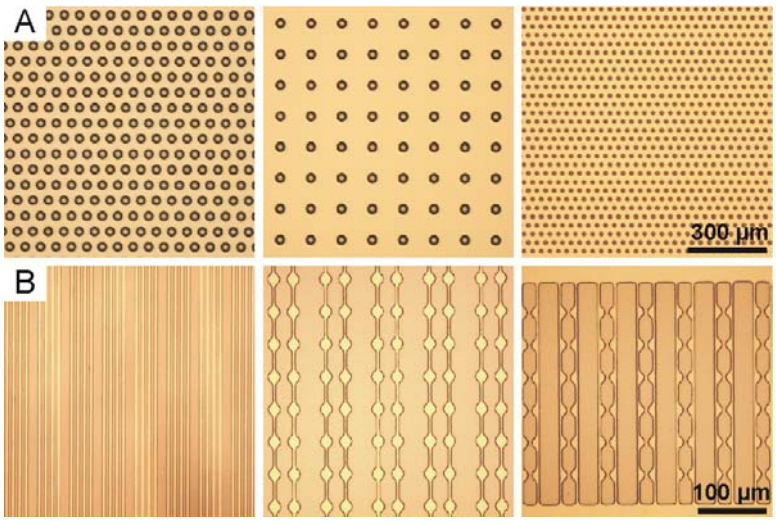

Figure 2-4 Bright-field images of patterned PDMS layers on Si wafers. (A) Arrays of through holes with the hole diameters of 20 µm (*left* and *middle*) and 8 µm (*right*). (B) PDMS strips of different line widths.

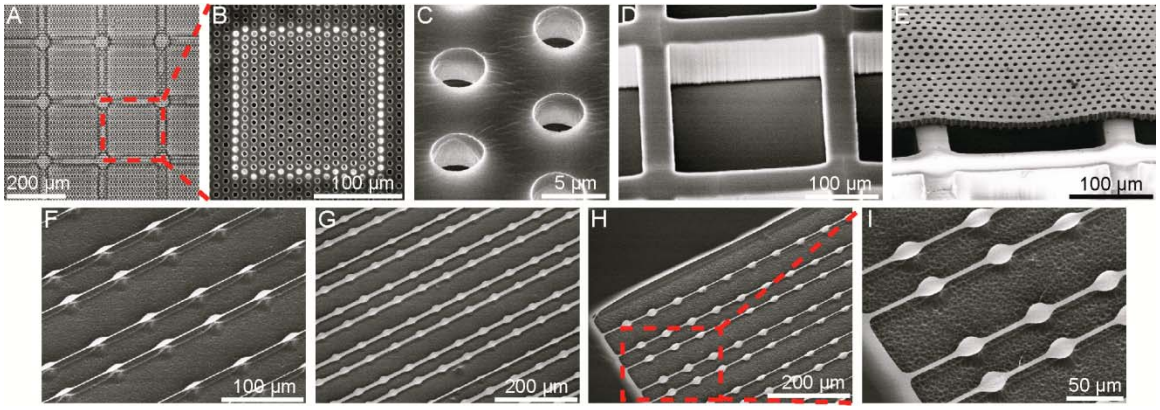

Figure 2-5 Photolithographic surface micromachining of free-standing PDMS microfiltration membranes and beam structures. (A-E) Bright-field (A) and SEM (B-E) images of a PDMS microfiltration membrane, bonded to a PDMS support structure (D). The microfiltration membrane had a thickness of 10 µm and it contained an array of hexagonally spaced through holes (with a hole diameter of 4 µm). (F-I) Free-standing PDMS beam structures on Si wafers, with the beam thickness of 500 nm and total beam length of 800 µm. The minimum beam widths were 2 µm (F), 10 µm (G), 5 µm (H & I), respectively.

in spin coating photoresist directly onto the untreated PDMS surface is because of its low surface energy (~23 mN m^{-1}), which is originated from the shielding effect of the nonpolar methyl groups (carbon and hydrogen containing groups) on the polar siloxane backbone, resulting in a tendency for photoresist to dewet on PDMS [89, 92]. It is showed that a brief treatment of O_2 plasma for the PDMS surface could create super-

hydrophilicity on the PDMS surface, by stripping methyl groups from the PDMS surface which could then form silanols [80, 89, 93] (Figure 2-6A). As evidence of this super-hydrophilicity on the PDMS surface after the O_2 plasma treatment, the contact angle of a water droplet was dramatically reduced from about 100º (on untreated PDMS; Figure 2-6B, *left*) to <5º (on plasma-treated PDMS; Figure 2-6B, *right*). After the O_2 plasma activation of PDMS, a uniform photoresist layer could be successfully spin-coated onto the PDMS surface (Figure 2-6C, *right*), which could be difficult to achieve for the untreated PDMS surface (Figure 2-6C, *left*). It should be noted that the effect of O_2 plasma treatment was not permanent and would decay within a few hours as the low molecular weight siloxane chain in the bulk PDMS could migrate to its surface [89, 94]. Hence, the O_2 plasma treatment of the PDMS surface could temporarily establish a hydrophilic surface suitable for spin coating photoresist uniformly, and this O_2 plasma treatment will not introduce permanent alterations of the PDMS surface property.

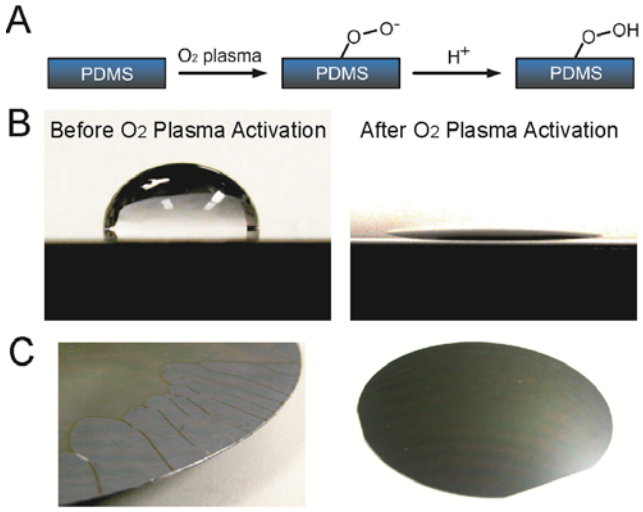

Figure 2-6 Effect of O_2 plasma treatment on coating photoresist on Si wafer. (A) Surface hydrophilization of PDMS using O_2 plasma treatment. (B) Contact angles of water drops on PDMS before (100º, *left*) and after (<5º, *right*) 5 min treatment of O_2 plasma. (C) Images of photoresist layer spin-coated on PDMS surface with (*right*) and without (*left*) treatment O_2 plasma. Photoresist could not be spread out uniformly on the PDMS surface without O_2 plasma treatment (*left*), while after O_2 plasma treatment, the photoresist could be uniformly spin-coated on PDMS.

The RIE process was further optimized for anisotropic dry etching of PDMS using SF_6 and O_2 gas mixtures and achieved a maximum PDMS etch rate of ~0.8 μm/min with a vertical etch profile and a smooth etched surface. After 15-min etching of PDMS, the root-mean-square (RMS) surface roughness of the etched PDMS surface measured by atomic force microscopy (AFM, Digital Instruments, Tonawanda, NY) was about 1 nm, comparable to the intrinsic surface roughness of unprocessed PDMS (data not shown). It has been reported that reactive plasma generated using CF_4 and O_2 gases could also etch PDMS, yet I observed that RIE process using such gases could result in a large surface roughness (~μm) for the etched PDMS surface (data not shown) [95]. To further examine the anisotropic etch profile for PDMS after the RIE process using SF_6 and O_2 gas mixtures, cross-sectional scanning electron microscopy (SEM) images of the PDMS microfiltration membrane were taken, and indeed vertical sidewalls of the through holes in the PDMS microfiltration membrane were observed (Figure 2-5C), indicating our RIE process using SF_6 and O_2 gas mixtures achieved anisotropic dry etching of thick PDMS layers.

For RIE process using SF_6 and O_2, the etch rate of PDMS increased with the plasma power and the bias voltage but decreased with increasing chamber pressure, consistent with previous reports [93]. A sufficiently low chamber pressure was required to ensure a short resident time for the reactive ions on the PDMS surface and rapid renewal of the reactive species inside the plasma, both contributing to rapid etching of PDMS. SF_6 is the main resource for reactive fluorine (F) ions to etch PDMS and these fluorine ions could break the Si-O bond and thus etch PDMS. In addition, the partial pressure of O_2 in the plasma also affected the PDMS etch rate, which decreased with

increasing the partial pressure of O_2. Adding a small fraction of O_2 could facilitate this fluorine-assisted PDMS etching process, even though the detailed mechanism is not well understood yet [92]. The RIE process conditions used in our fabrication were: gas (SF_6 (90 sccm) and O_2 (6 sccm)), chamber pressure (0.67 Pa), bias voltage (100 V) and RF power (500 W). Under this RIE condition, the etch rate for photoresist such as SPR220 was about 0.41-0.46 μm/min, leading to an etch selectivity between PDMS and photoresist of about 2:1. It is also worth noting that the RIE RF power and etching time could affect the anisotropic etching profile of PDMS, as excessive RF power or etching time often leaded to a slanted sidewall of the PDMS structures.

This new photolithographic surface micromachining technique can achieve wafer-level fabrication of different planar PDMS structures with their thickness covering a very broad size range from submicron to tens of micrometers. Similar to surface micromachining for processing microelectronics and MEMS devices, our PDMS surface micromachining technique involved deposition or spin coating and dry etching of PDMS layers on top of the Si substrate. Further, our PDMS surface micromachining technique was compatible with Si-based surface and bulk micromachining techniques, enabling the possibility of realizing different monolithic microscale devices and systems in which PDMS structures and other electronic and MEMS components could be integrated on the same substrate.

Using the PDMS surface micromachining technique, wafer-level fabrication of different planar PDMS microstructures was performed to elucidate its simplicity and versatile applications. The PDMS microfiltration membranes contained a large array of closely packed through holes with the hole diameter of 4-20 μm and the hole c.t.c.

distance of 8-200 μm (Figure 2-4A & Figure 2-5A-E). These PDMS microfiltration membranes could potentially be utilized for size-based separation of blood cells. For instance, there is a great current interest in devising efficient techniques to isolate and enrich the rare live circulating tumour cells (CTCs) from cancer patient blood as surrogates to understand the crucial early cancer metastatic process and discover new targets or new phenotypes in the CTCs that need to be targeted [10, 11]. The surface micromachined PDMS microfiltration membranes could be easily integrated onto PDMS support structures to improve its mechanical strength, which would be important for PDMS microfiltration membranes with a large surface area. Our PDMS microfiltration device could potentially be applied as a low-cost innovative technology for achieving isolation of live CTCs without the requirement for large and expensive apparatus.

Our PDMS surface micromachining technique could be further combined with Si surface or bulk micromachining to generate submicron-scale free-standing planar PDMS structures (Figure 2-5F-I). Free-standing thin PDMS structures could potentially be utilized as sensitive mechanical biosensors based on mass- or force-based methods [96]. These PDMS mechanical biosensors could open new exciting opportunities to seamlessly integrate such biosensors with upstream or downstream PDMS-based microfluidic sample preparation and bioanalytical components. In addition, the low density and mechanical flexibility of PDMS provided additional desirable advantages for mass- or force-based sensing.

In summary, a PDMS surface micromachining strategy was demonstrated using a combination of photolithography, RIE, and convenient thin film releasing techniques (O_2 plasma assisted PDMS bonding or XeF_2 Si etching). By using a gentle treatment of O_2

plasma for the PDMS surface prior to spin coating the photoresist, the long-standing challenge of photolithography on the PDMS surface was successfully addressed. Our PDMS surface micromachining technique was compatible with existing Si-based surface and bulk micromachining techniques, thus opening promising opportunities for generating different novel hybrid devices for highly integrated bio-sensing and -analytical applications. Our PDMS surface micromachining method could provide an efficient tool for fabricating well-defined PDMS microstructures, fulfilling the current technical demands of PDMS surface micromachining in microfluidic and bioengineering applications.

2.3.2 Integrated Microfluidic Immunophenotyping Device

Using the above-mentioned surface micromachining technique for soft materials, we have developed a highly integrated microfluidic immunophenotyping assay (MIPA) device that can perform efficient isolation and rapid and accurate functional immunophenotyping of subpopulations of immune cells from patients with immunodysfunctions [7-9]. The new immunophenotyping platform employed a combined use of a surface micromachined PDMS microfiltration membrane (PMM) in the MIPA device and antibody-conjugated polystyrene microbeads for isolation, purification, and functional immunophenotyping of different subpopulations of immune cells directly from blood specimens (Figure 2-7). Immobilized on the microbead surface were monoclonal antibodies against cell surface antigens specific to the desired subpopulation of immune cells. When mixed with a blood specimen, the microbeads could selectively capture the desired subpopulation of immune cells by recognizing and

binding covalently to the specific surface proteins of the cells. The diameter of the through holes in the PMM, which solely defined the effective size cutoff for microfiltration, was designed to be smaller than the size of the microbeads but larger than normal blood leukocytes. Thus when the blood specimen was introduced into the microfiltration device and forced to pass through the PMM, the cell/microbead conjugates were readily trapped and isolated on the PMM, whereas other untargeted leukocytes and erythrocytes (red blood cells) unbound to microbeads could freely pass through the PMM. Owing to its large surface area and high porosity, the PMM permitted a heightened volume throughput (> 5 mL min^{-1}) for processing blood specimens without causing clogging of the PMM, a common problem in microfiltration membrane filters.

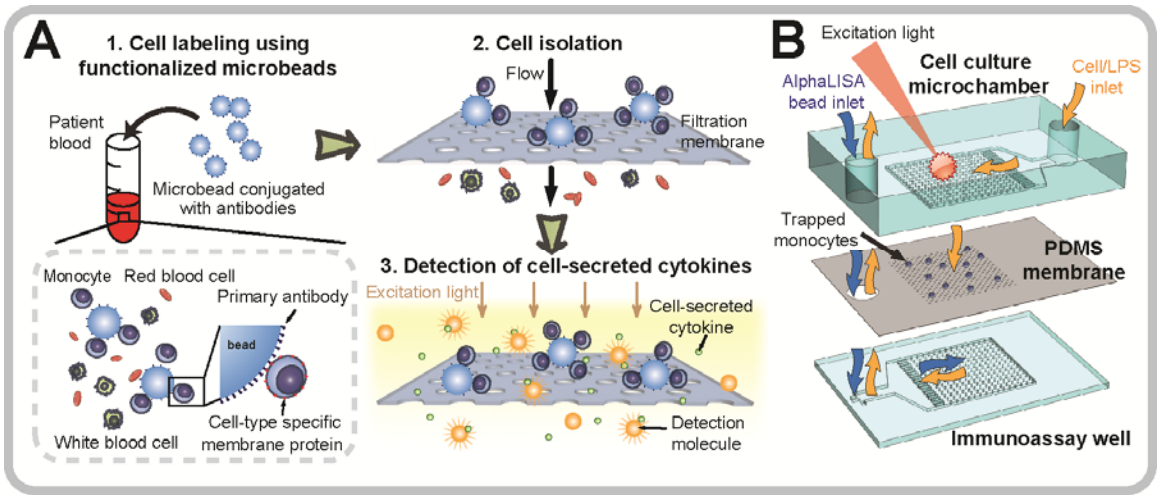

Figure 2-7 Microfluidic device for isolation and immunophenotyping of subpopulations of immune cells. (A) Schematic of isolation and immunophenotyping of subpopulations of immune cells from blood specimens. Subpopulations of immune cells were recognized and captured by microbeads conjugated with monoclonal antibodies against specific cell surface antigens. Owing to the increased size of cell-microbead conjugates, the desired subpopulation of immune cells was retained on the PDMS microfiltration membrane (PMM) upon loading of the blood sample, while the other blood cells including undesired immune cells could pass freely through the PMM. On-chip functional immunophenotyping was then performed to examine the capacity of this subpopulation of immune cells to produce pro-inflammatory cytokines following stimulation. (B) Schematic of a multi-layered MIPA device consisting of a cell culture chamber, a PMM, and an immunoassay chamber.

The MIPA device further allowed *in situ* quantitative immunosensing of cell-secreted cytokines by detecting optical signals resulted from a no-wash homogeneous sandwich chemiluminescence assay. In this homogeneous immunoassay, so called "AlphaLISA" [97-99], the analyte of interest (*i.e.*, cytokine) binds simultaneously to primary antibody-coated donor and acceptor beads, which brings the beads into a close proximity to each other. In this bead proximal state, singlet oxygen generated by laser excitation (λ = 680 nm) from the donor bead will transfer to the acceptor bead, eliciting a shorter wavelength emission (λ = 615 nm) from the acceptor bead. The AlphaLISA assay provides an efficient way for quantitative detection of cytokine production, without involving complex reagent loading and washing steps as in the conventional fluorescence-based immunoassays (*e.g.*, enzyme-linked immunosorbent assay (ELISA)) [53, 100].

In addition, the miniaturized size of the PMM-integrated microfiltration device required only a sample volume as small as 5 μL for each assay. The MIPA device, permitting the homogenous AlphaLISA immunoassay in a microfluidic chamber, could reduce the entire assay time comprising the time for pretreatment, process, and detection down to a few hrs, a nearly 10-fold reduction in total assay time as compared to the conventional whole blood stimulation assay using ELISA or the enzyme-linked immunosorbent spot (ELISpot) assay [53, 100]. Given the shortened assay time, enhanced sample efficiency, and the ability to determine the functional status of different subpopulations of immune cells, our microfluidic immunophenotyping technology promises to provide a new approach to diagnosing infectious and inflammatory diseases across a broad patient spectrum.

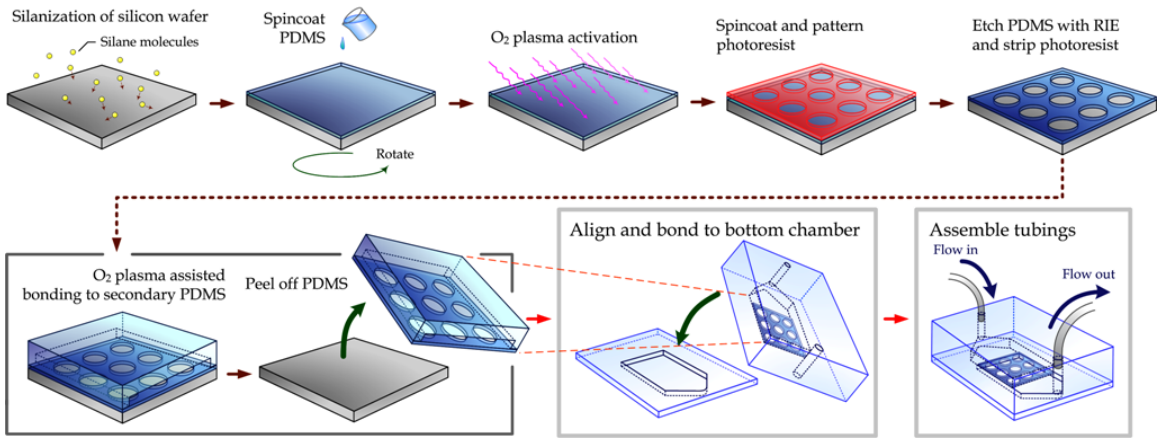

Figure 2-8 Schematic of fabrication process of the PMM-integrated microflitration device.

The structure of the MIPA device consists of three different PDMS layers (Figure 2-7). The top and bottom PDMS chambers are the cell culture and immunoassay chambers, respectively. Embedded between the top and bottom layers is the PMM, which serves (1) for isolation, enrichment, and enumeration of immune cells, and (2) for allowing cytokines secreted by immune cells to diffuse rapidly into the bottom immunoassay chamber for quantitative immunosensing.

In last section, a wafer-scale surface micromachining method have been demonstrated to generate different PDMS thin film microstructures, with their critical dimensions ranging from sub-microns to tens of microns, using a combination of photolithography, RIE and convenient thin film releasing techniques [7]. This method to achieve surface patterning of PDMS applies an O_2 plasma treatment to PDMS to activate its surface to overcome the challenge of poor photoresist adhesion on PDMS for photolithography. Utilizing this newly developed PDMS surface micromachining technique, we have achieved wafer-scale batch fabrication of large PMMs containing a regular array of micron-scale through holes with high porosity (Figure 2-8 and Appendix A for the detailed fabrication procedure). Specifically, using our PDMS surface

micromachining technique, We successfully fabricated PMMs with an effective membrane area of 3 cm × 3 cm and porosity up to 30%; both factors could contribute to a heightened volume throughput for processing unprocessed blood specimens without causing clogging of the PMM, a common problem in microfiltration membrane filters. For comparison, conventional track-etched polycarbonate filters, which have been used for isolation of blood cells and circulating tumor cells, has porosity of less than 2%, and the other more recently developed parylene-based micropore membrane has porosity of 7% - 15% [101-103]. Since the through holes in the PMM were defined by photolithography, the size and pattern of the through holes in the PMM could be precisely controlled. The PMMs used in this work had a thickness of about 10 μm and contained a regular array of hexagonally arranged through holes with a hole diameter of 6 - 60 μm and a center-to-center distance of 10 - 100 μm (Figure 2-9A-C). By

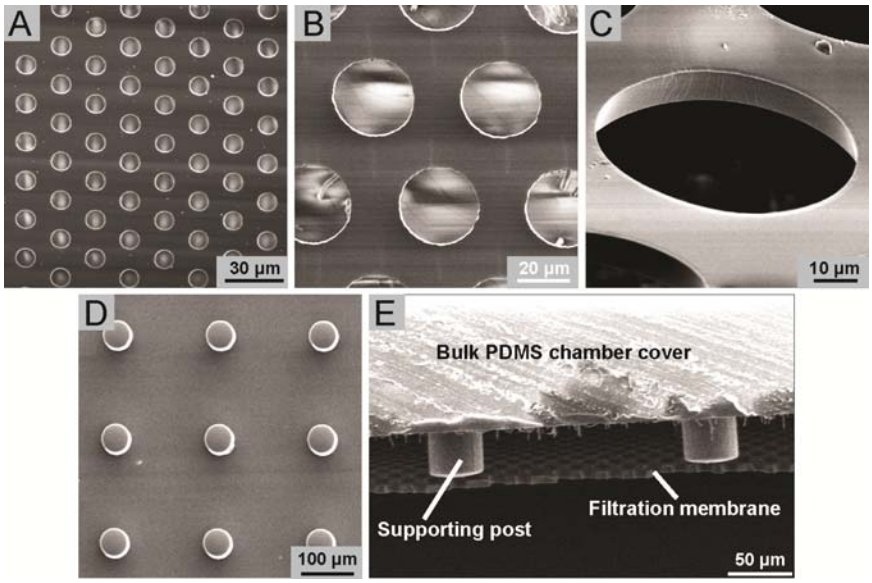

Figure 2-9 SEM images showing free-standing PMMs with high porosity. (A-C) Top (A&B) and tilted (C) view SEM images showing PMMs containing a regular array of hexagonally arranged through holes with the hole diameter of either 6 μm (A), 30 μm (B), or 60 μm (C). The PMMs had a thickness of 10 μm. (D) Top view SEM image showing PDMS supporting pillars with a height of 100 μm and a diameter of 60 μm. (E) SEM image showing a cross-section view of a free-standing PMM bound to PDMS supporting posts. In E, the diameter of the PMM through hole was 30 μm.

controlling anisotropic etching of PDMS using RIE, the through holes of the PMM had a near vertical sidewall profile (Figure 2-9C). The transparent nature of PDMS permitted imaging and enumeration of cells captured on the PMM using standard clinical histopathological stains, in addition to immunofluorescence-conjugated antibodies.

Our PDMS surface micromachining technique is compatible with soft lithography techniques and other silicon-based microfabrication methods. Thus, the PMM can be easily integrated with PDMS supporting structures and other PDMS-based molecular and cellular analysis components while maintaining a large surface area and high porosity. In this study, using O_2 plasma-assisted PDMS-PDMS bonding, the PMM was assembled with two structured PDMS layers serving as the top cell culture chamber and the bottom immunoassay chamber to form a completely sealed PMM-integrated microfiltration device (Figure 2-8). The cell culture and immunoassay chambers in the microfiltration devices contained supporting pillar structures to provide the aforementioned mechanical strength for the PMM during cell filtration process (Figure 2-9E).

2.4 Results and Discussions

2.4.1 Capture of Subpopulation of Immune Cells Using Microbeads Conjugated with Antibodies

Surface functionalized micro/nano scale beads and particles are widely used for isolations of cells and proteins (see Appendix B for details). Leukocytes are known to produce specific antigens on their surfaces. By using the biotin-streptavidin conjugation chemistry to coat polystyrene microbeads with antibodies directed against specific cell

surface antigens, these microbeads could recognize and capture desired subpopulations of immune cells expressing specific surface proteins.

The cell capture efficiency of on microbeads was first characterized using functionalized microbeads with a diameter of 32 μm and conjugated with monoclonal antibodies directed against CD14, a unique surface protein marker of monocytes. Well-controlled quantities of the microbeads were mixed with known quantities of fluorescence-tagged CD14+ THP-1 cells, a human acute monocytic leukemia cell line as a model for human monocytes. THP-1 cells were suspended in either blank culture media, culture media spiked with known quantities of peripheral blood mononuclear cells (PBMCs) mimicking blood leukocytes, or lysed blood that was pre-stained with DiI to label blood leukocytes (the concentrations of THP-1 cells and microbeads were 2×10^6 mL^{-1} and 4×10^5 mL^{-1}, respectively). Well-controlled quantities of the microbeads were also mixed directly with lysed blood that was pre-stained with Calcein AM to label blood leukocytes at a concentration of 10×10^6 mL^{-1}. The mixture of the microbeads and immune cells were incubated for 1 hr on a roller mixer before they were examined under florescence microscopy (Figure 2-10A-C).

The results in Figure 2-10D&E showed that for THP-1 cells spiked in growth media or lysed blood, on average, there were about 4 THP-1 cells bound to a single microbead following cell-bead mixing and incubation. Similar to results for THP-1 cells, on average, there were about 4 CD14+ monocytes from lysed blood bound to a single microbead following cell-bead mixing and incubation (Figure 2-10F). The overall capture efficiency of the microbeads for THP-1 cells (defined as the ratio between the total number of THP-1 cells captured by microbeads and the total number of THP-1 cells

in the sample) was further quantified to validate the capture performance. The results in Figure 2-10G showed that for THP-1 cells spiked in culture media or lysed blood, the capture efficiency of the microbeads conjugated with anti-CD14 antibodies was all greater than 70%. Together, our data in Figure 2-10 strongly supported the utility of functionalized microbeads for efficient recognition and capture of desired subpopulations of immune cells from a complex mixture of background cells, such as blood leukocytes.

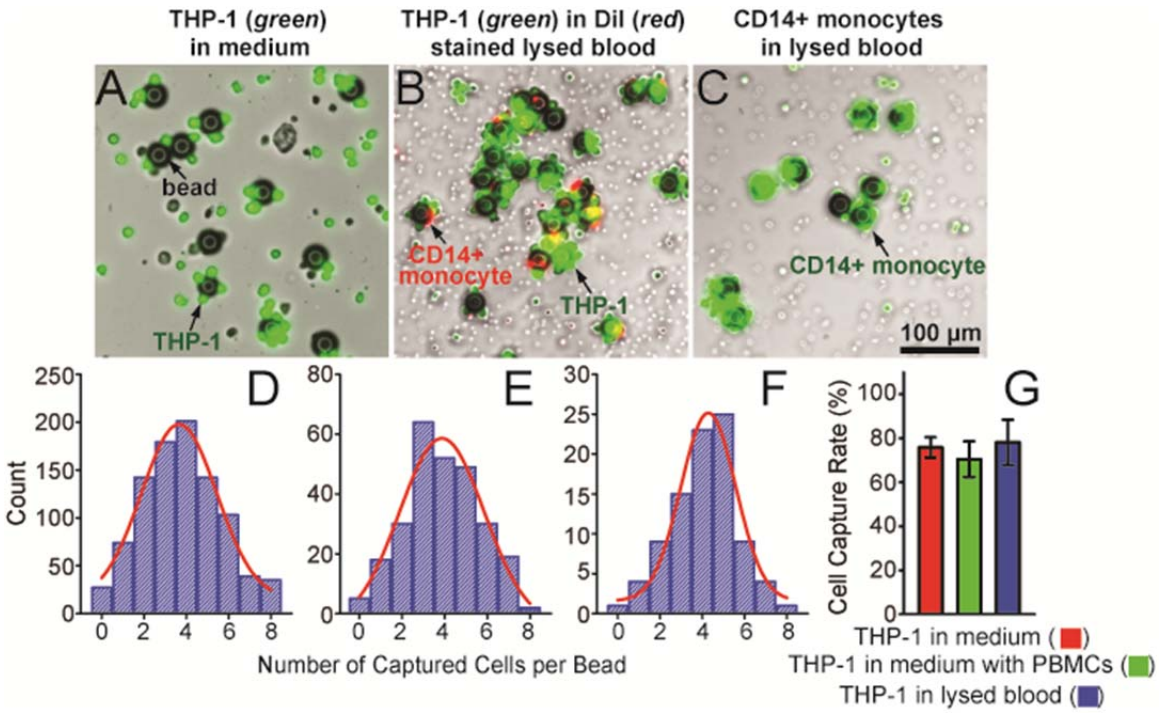

Figure 2-10 Capture of immune cells using microbeads conjugated with anti-CD14 antibodies. (A-C) Representative merged brightfield and fluorescence images showing THP-1 cells (green; A&B) and CD14+ monocytes (green; C) captured by microbeads in either culture media (A) or lysed blood (B&C). The microbeads with a diameter of 32 µm were conjugated with anti-CD14 monoclonal antibodies. THP-1 cells were pre-stained with CellTracker Green. Blood leukocytes in B&C were pre-stained with DiI (B) or CellTracker Green (C). (D-F) Distributions of the number of cells captured per bead for THP-1 cells (D&E) and CD14+ monocytes (F) in either culture media (D) or lysed blood (E&F). For D&E, 2×10^6 THP-1 cells were mixed with 4×10^5 microbeads in 1 mL cell culture media (D) or lysed blood (E). For F, 2 mL lysed blood containing about 2×10^7 leukocytes was mixed with 3×10^5 microbeads. Gaussian functions (red curves) were used for fitting in D-F. (G) Capture rate of functionalized microbeads for THP-1 cells spiked in growth media, in growth media with PBMCs, and in lysed blood as indicated. Error bars represent ± standard error of the mean (s.e.m; $n = 4$).

2.4.2 Capture Efficiency Characterization

After capturing the taget immune cells on the microbeads, the bead-lable cells can be further filted and isolated on PMM in the MIPA device. Owing to the significant physical size difference between the microbeads and leukocytes, when the blood sample was passing through the PMM, the desired subpopulation of immune cells that were bound to functionalized microbeads could be efficiently isolated by the PMM, while the other blood cells including undesired immune cells would pass freely through the PMM.

To validate the isolation performance of the PMM, the capture efficiency of the PMM was first characterized using well-controlled quantities of fluorescence-tagged polystyrene microbeads spiked in PBS (Figure 2-11). The PMM used in these assays contained a regular array of through holes with a hole diameter of 13 μm and a center-to-center distance of 20 μm. The porosity of the PMM was about 25%. Two different sized polystyrene microbeads were assayed with the means of their diameters of 6 μm and 15 μm. The microbeads at a concentration of 2×10^4 mL^{-1} in the PBS were injected into the PMM-integrated microfiltration device using a syringe infusion pump under a constant flow rate of 100 μL min^{-1}. The fluorescence-tagged microbeads trapped on the PMM could be visually examined and enumerated under bright-field and fluorescence microscopy (Figure 2-11A). Since the diameter of the through holes in the PMM was 13 μm, smaller than the 15 μm microbeads but larger than the 6 μm ones, the PMM would capture virtually all the 15 μm microbeads while letting all the 6 μm ones passing through. The quantitative results in Figure 2-11B-D demonstrated an extremely high efficiency of the PMM to separate the two different sized microbeads, as evidenced by a capture yield (defined as the ratio of the number of beads captured on the PMM to the

total number of beads injected) and purity of 97.2% and 98%, respectively, for the 15 µm microbeads.

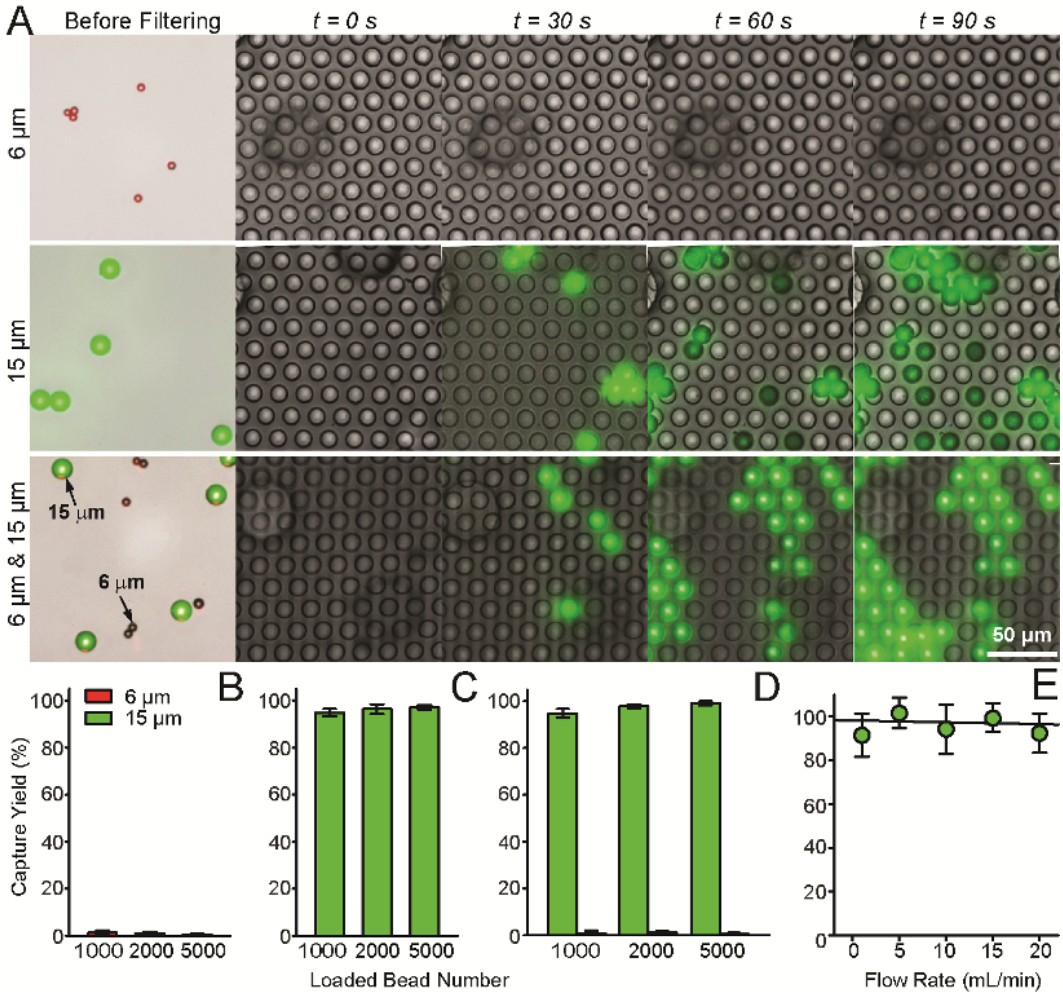

Figure 2-11 Characterization of capture efficiency of the PMM using florescence-tagged microbeads. (A) Temporal sequence of merged brightfield and fluorescence images showing isolation of 6 µm (top), 15 µm (middle), and a mixture of 6 µm and 15 µm (1:1 ratio; bottom) florescence-tagged microbeads on a PMM with the through hole diameter of 13 µm. The microbead concentration was 2×10^4 mL^{-1}, and they were injected through the PMM with a volume flow rate of 100 µL min^{-1}. Virtually all 15 µm beads were trapped on the PMM while all 6 µm beads passed through the PMM. (B&C) Captured yield of 6 µm (B) and 15 µm (C) microbeads as a function of the total number of microbeads injected through the PMM. Data was calutlated from the top and middle panels of images shown in A. (D) Captured yield of 6 µm and 15 µm microbeads from a mixture of 6 µm and 15 µm microbeads, as a function of the total number of microbeads injected through the PMM. Data was calculated from the bottom panel of images shown in A. (E) Capture yield of 15 µm microbeads as a function of the volume flow rate. The microbead concentration was 2×10^4 mL^{-1}, and they were injected through the PMM with a varied volume flow rate. Error bars in B-E represent ± s.e.m. ($n = 4$).

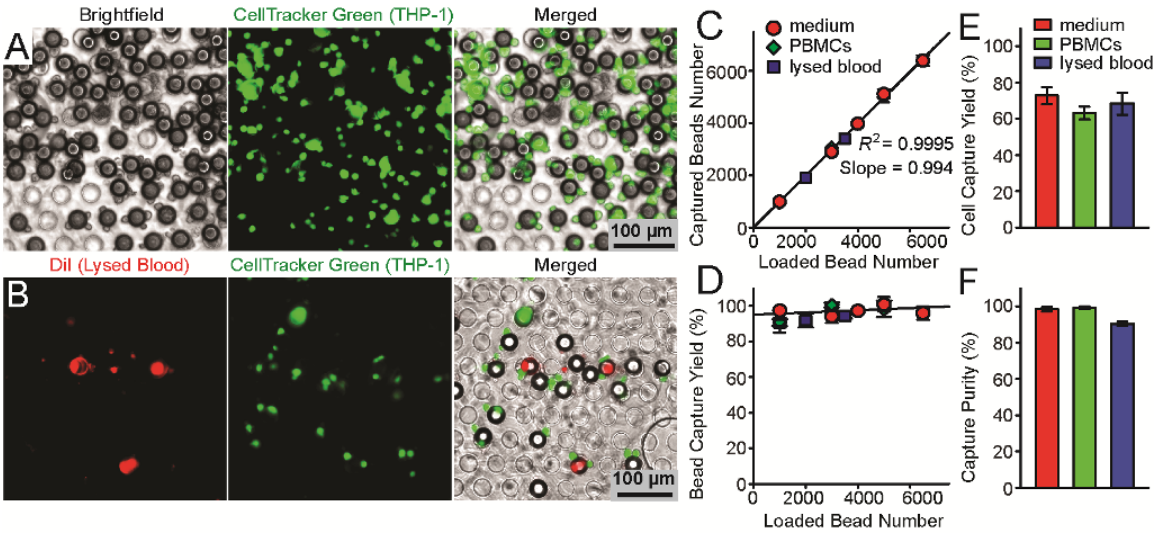

Figure 2-12 Characterization of capture efficiency of the PMM using samples spiked with THP-1 cells. (A&B) Representative brightfield, fluorescence, and merged microscopic images showing fluorescence-tagged THP-1 cells bound to microbeads isolated on the PMM. THP-1 cells labeled with CellTracker Green were spiked in either cell culture media (A) or lysed blood pre-stained with DiI to label blood leukocytes (B). The microbeads with a diameter of 32 μm were conjugated with anti-CD14 antibodies. The PMM had a through hole diameter of 30 μm. (C) Regression analysis of capture efficiency of the PMM for the functionalized microbeads used for capturing THP-1 cells. The plot represents the number of microbeads (bound with or without cells) captured on the PMM against the total number of microbeads (bound with or without cells) injected through the PMM. (D) Capture yield of microbeads (bound with or without cells) as a function of the total number of microbeads (bound with or without cells) injected through the PMM. (E&F) Capture yield (E) and purity (F) of THP-1 cells on the PMM. For C-F, known quantities of THP-1 cells (2×10^6) were mixed with microbeads (4×10^5) in 1 mL cell culture media (red symbols or bars), 1 mL cell culture media containing 5×10^6 mL^{-1} PBMCs (green symbols or bars), or 1 mL lysed blood containing about 6×10^6 mL^{-1} leukocytes (blue symbols or bars), as indicated. The volume flow rate was 1 mL min^{-1}. Solid lines in C&D represent linear fitting. Error bars represent ± s.e.m (n = 4).

The effect of flow rate on the capture efficiency of the PMM was further examined, by comparing the capture efficiency of the PMM for microbeads under different flow rate conditions (from 1 - 20 mL min^{-1}; Figure 2-11E). The results in Figure 2-11E suggested that the PMM was able to achieve extremely high capture efficiency for the microbeads even under a flow rate as high as 20 mL min^{-1}, without evidence showing plastic deformation or fracture of the PMM under the microscopy, which might be attributable to the PDMS supporting pillars integrated in the microfiltration device.

Then, the isolation performance of the PMM was characterized for the bead-labled THP-1 cells. In this study, the diameter of the through hole in PMM was 30 μm and THP-1 cells were bound to 32 μm microbeads functionalized with anti-CD14 antibodies as described before (Figure 2-12). Here known quantities of THP-1 cells (2×10^6) labeled with CellTracker Green were mixed and incubated with the functionalized microbeads (4×10^5) for 1 hrs in either 1 mL cell culture medium containing 5×10^6 mL^{-1} PBMCs or 1 mL lysed blood containing about 6×10^6 mL^{-1} leukocytes and 5×10^5 mL^{-1} CD14+ monocytes. Different volumes of the culture medium and lysed blood samples were injected into the PMM-integrated microfiltration device at a flow rate of 1 mL min^{-1}. The cells bound to the microbeads trapped on the PMM were examined under fluorescence microscopy to determine the capture efficiencies for the microbeads and THP-1 cells (Figure 2-12A&B). As expected, virtually all the 32 μm microbeads (> 99%), regardless whether bound with or without cells, were captured on the PMM (Figure 2-12C&D). The capture yield of THP-1 cells, defined here as the ratio between the number of THP-1 cells bound to microbeads captured on the PMM to the total number of THP-1 cells injected into the microfiltration device, was all greater than 70%, regardless whether THP-1 cells were spiked in culture media, culture media containing PBMCs, or lysed blood. In addition, capture purities of THP-1 cells, defined as the ratio between the number of THP-1 cells bound to microbeads captured on the PMM to the total number of cells captured on the PMM, was on average as high as 97%, regardless whether THP-1 cells were spiked in culture media, culture media containing PBMCs, or lysed blood. Together, our data in Figure 2-12 convincingly supported our approach of using functionalized microbeads and the PMM for efficient capture and isolation of

subpopulations of immune cells with a high purity. From our data in Figure 2-12, the overall capture yield of our method to isolate subpopulations of immune cells was largely determined by the yield of the cell capture process using the functionalized microbeads, not by the microbead isolation process using the PMM.

2.4.3 Isolation of Subpopulation of Immune Cells from Blood

Using the PMM coupled with functionalized microbeads, direct isolation, enrichment, and enumeration of CD14+ monocytes was demonstrated from both lysed as well as whole blood specimens (Figure 2-13A-C; see Appendix C for blood processing details). As a control, PMMs with the through hole diameter of 6 μm were used to isolate the whole population of leukocytes from lysed blood (Figure 2-13A). Leukocytes in the lysed blood were stained with Calcein AM for visualization. Lysed blood with the leukocyte concentration of 5×10^6 mL^{-1} or diluted lysed blood with the leukocyte concentration of 1×10^6 mL^{-1} was filtered by the PMM with the through hole diameter of 6 μm in the microfiltration device at a flow rate of 1 mL min^{-1}. The number of leukocytes trapped on the PMM increased lineally with the sample injection volume, and our regression analysis of capture efficiency of the PMM for leukocytes in Figure 2-13D revealed that about 93% of leukocytes in the lysed blood were captured on the PMM under a flow rate of 1 mL min^{-1}.

To isolate CD14+ monocytes from human blood, known quantities of functionalized 32 μm microbeads conjugated with anti-CD14 antibodies were added into blood samples. Prior to this, leukocytes in the blood sample were pre-labeled with Calcein AM. After 1-hr mixing and incubation, the blood specimens were injected

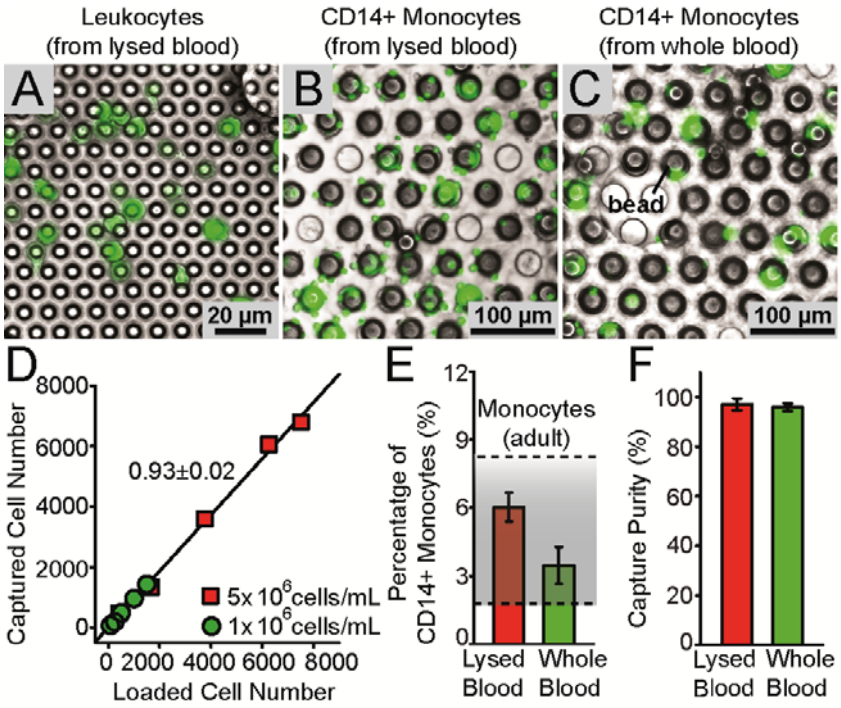

Figure 2-13 Isolation of CD14+ monocytes from blood specimens using the PMM. (A-C) Representative merged brightfield and fluorescence images showing flurescence-tagged leukocytes (A) and CD14+ monocytes (B&C) from lysed blood (A&B) or whole blood (C) isolated on the PMM. The PMM had a through hole diameter of 6 μm (A) or 30 μm (B&C). CD14+ monocytes were first captured by 30 μm microbeads conjugated with anti-CD14 antibodies before the cell-microbead conjugates were isolated on the PMM. Leukocytes in the blood samples were stained with Calcein AM for visualization. (D) Regression analysis of capture efficiency of the PMM with the through hole diameter of 6 μm for blood leukocytes, under a flow rate of 1 mL min^{-1}. The plot represents the number of leukocytes captured on the PMM against the number of leukocytes injected through the PMM, using undiluted (5×10^6 mL^{-1}) as well as diluted (1×10^6 mL^{-1}) lysed blood samples as indicated. Solid lines represent linear fitting. (E&F) Percentage (E) and purity (F) of CD14+ monocytes captured using functionalized microbeads and the PMM from lysed and whole blood. For E&F, known quantities of microbeads (3×10^5) were mixed with 2 mL lysed and whole blood (containing about 2×10^7 leucocytes). The shaded area in E indicates the normal percentage range of CD14+ monocytes in blood from healthy adults. Error bars represent ± s.e.m. ($n = 4$).

through a PMM with the through hole diameter of 30 μm. The results in Figure 2-13E showed that about 6.0% and 3.5% leukocytes from the lysed and whole blood samples, respectively, were bound to the 32 μm microbeads and subsequently captured by the PMM with the through hole diameter of 30 μm as CD14+ monocytes. These results are consistent with the fact that the normal percentage range of CD14+ monocytes in blood from healthy adults is from 2% - 8% [104, 105]. Compared to the results for lysed blood,

the capture yield of CD14+ monocytes from whole blood was slightly lower, likely due to the large number of erythrocytes (red blood cells) and other undesired leukocytes in whole blood blocking effective interactions between CD14+ monocytes and functionalized microbeads. Using microbeads conjugated with different antibodies, various subpopulations of the immune cells including CD4+ and CD8+ T-cells have also been successfully isolated on PMMs in the MIPA devices with high yield and purity.

2.4.4 Functional Cellular Immunophenotyping of Subpopulations of Immune Cells

After cell isolation, a rapid, no-wash, quantitative immunosensing method, the AlphaLISA [97-99], was further demonstrated to achieve on-chip functional immunophenotyping of subpopulations of immune cells using minute quantities of blood. The overall immunophenotyping assay protocol using the microfiltration device was shown in Figure 2-14A (see Appendix D for details). After the desired subpopulation of immune cells (*e.g.*, CD14+ monocytes) was captured and enriched by functionalized microbeads and the PMM from blood specimens (Step 1 in Figure 2-14A), the cells trapped on the PMM were stimulated and incubated with LPS loaded from the inlet of the top cell culture chamber of the microfiltration device (Step 2 in Figure 2-14A). LPS is a canonical endotoxin that can cause septic shock in the human body due to severely pronounced immune response. Pro-inflammatory cytokines secreted from LPS-stimulated immune cells would diffuse rapidly through the PMM to the bottom immunoassay chamber, where the AlphaLISA donor and acceptor beads were loaded and optically detected *in situ* for quantitative immunosening (Step 3 in Figure 2-14A). The

AlphaLISA signal detected could be converted to the cytokine concentration using standard curves generated using AlphaLISA with samples spiked with known concentrations of cytokines (Figure 2-15).

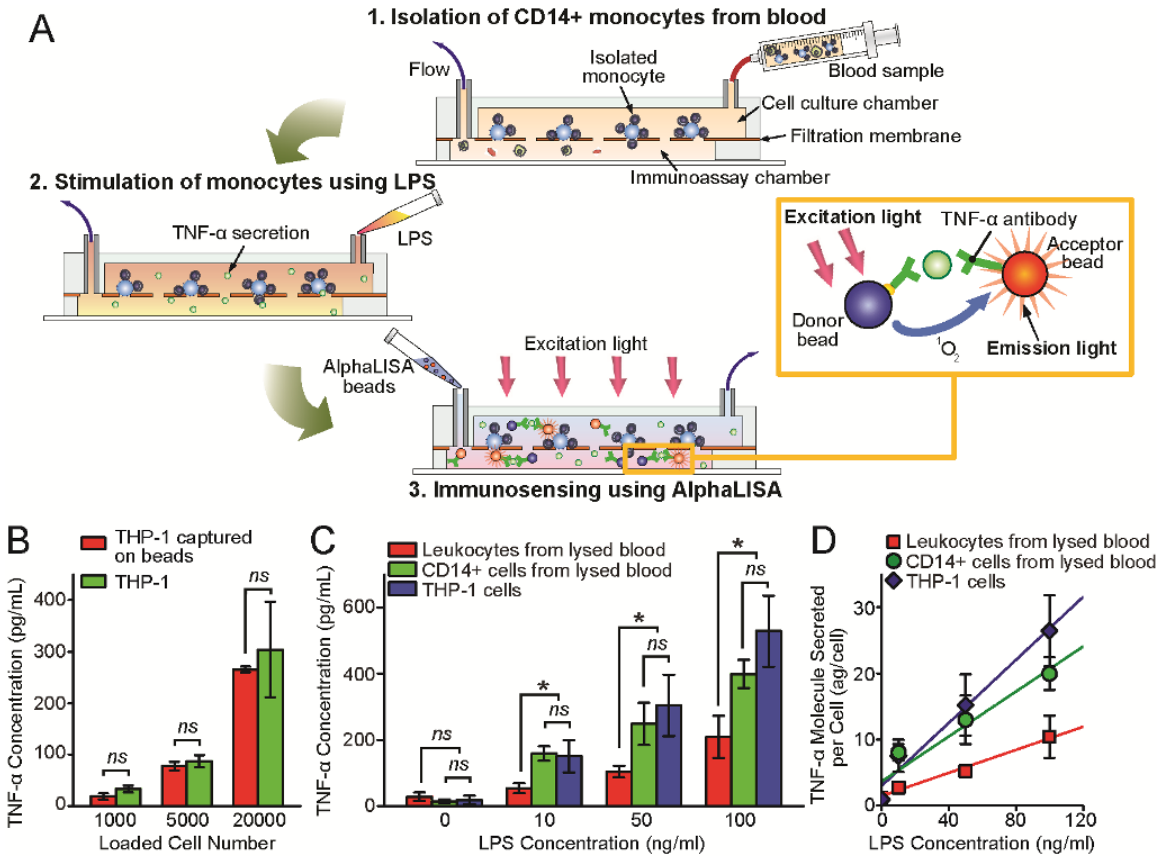

Figure 2-14 Immunophenotyping of subpopulations of immune cells isolated from human blood. (A) Schematic showing the immunophenotyping assay protocol using the PMM-integrated microfiltration device and the AlphaLISA: (1) isolation and enrichment of CD14+ monocytes on the PMM from blood samples; (2) LPS stimulation of CD14+ monocytes trapped on the PMM to release pro-inflammatory cytokines; (3) Loading and incubation of AlphaLISA beads in the immunoassay chamber; (4) Detection of TNF-α using the AlphaLISA, in which the streptavidin-coated donor (blue) and acceptor beads (orange) were both conjugated with TNF-α antibodies. The beads were brought into a close proximity (< 200 nm) through binding simultaneously to TNF-α. Using a 680 nm laser for excitation, the singlet oxygen released by the donor bead would diffuse to the nearby acceptor bead and trigger it to emit the 615 nm fluorescent light. Measurement of this emission light from the acceptor beads using our custom optical setup (**Fig. S3**) would allow a quantitative detection of TNF-α secretion. (B) Comparison of TNF-α secretions from LPS-stimulated free THP-1 cells and THP-1 cells bound to microbeads. (C&D) Comparative study of TNF-α secretion from LPS-stimulated THP-1 cells, leukocytes isolated directly from lysed blood, and CD14+ monocytes isolated from lysed blood. For C&D, about 2×10^4 THP-1 cells, leukocytes, and CD14+ monocytes were trapped on the PMM before quantitative immunosensing. C&D plot the bulk TNF-α concentration and TNF-α molecules secreted per cell, respectively, as a function of LPS concentration. Solid lines in D represent linear fitting. Error bars represent ± s.e.m. (n = 4). P-values were calculated using the paired student's t-test. *ns* ($P > 0.05$; not significant), * ($P < 0.05$).

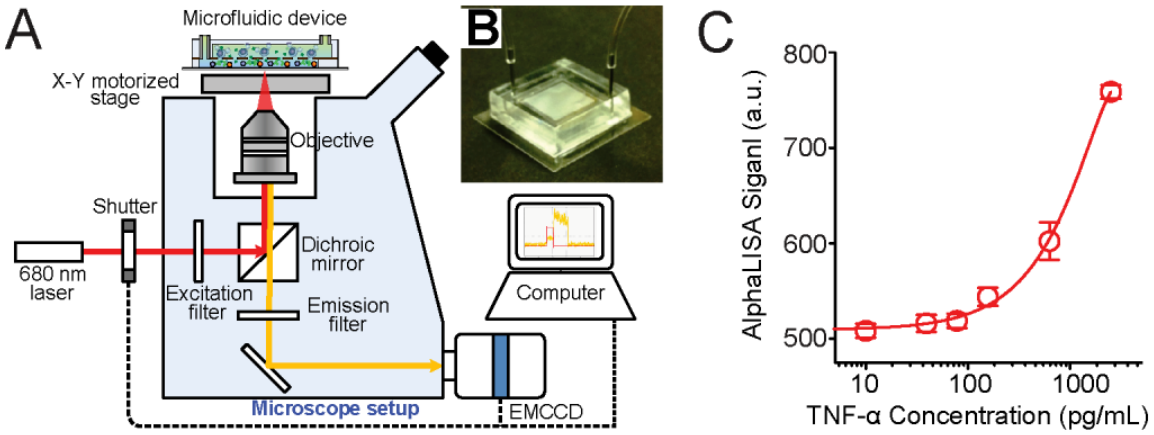

Figure 2-15 Optical setup for AlphaLISA detection. (A) Schematic of a custom optical setup for the on-chip AlphaLISA signal detection using the PMM-integrated microflitration device. (B) Photo of a MIPA device. (C) Standard curve for TNF-α detection using AlphaLISA. To generate the standard curve, cell growth media spiked with known concentrations of TNF-α (0-5,000 pg/mL) was assayed using AlphaLISA.

In this research, MIPA device and the AlphaLISA were applied to detect secretion of TNF-α from LPS-stimulated CD14+ monocytes isolated from blood specimens. TNF-α is a pro-inflammatory cytokine and a key biomarker associated with host defense and immunosurveillance. Secretion of TNF-α from LPS-stimulated monocytes has been shown to reflect the functional status of the innate immune response. The data in Figure 2-15B showed that TNF-α secretion from LPS-stimulated free THP-1 cells and THP-1 cells bound to microbeads were very similar, leading us to conclude that binding to anti-CD14 antibodies on microbeads would not significantly affect TNF-α secretion from CD14+ monocytes.

Next, MIPA device was applid for quantitative immunosensing of cytokines secreted from LPS-stimulated CD14+ monocytes isolated directly from lysed blood. The results were compared with cytokine secretions from LPS-stimulated leukocytes isolated directly from lysed blood and from LPS-stimulated THP-1 cells. In these assays, equal numbers of THP-1 cells, leukocytes and CD14+ monocytes (about 2×10^4) were trapped

on the PMM before quantitative immunosensing. The result in Figure 2-15C demonstrated that similar to THP-1 cells, TNF-α secreted by CD14+ monocytes isolated directly from lysed blood would increase with LPS concentration. Further, the amount of TNF-α secreted by CD14+ monocytes was very comparable to that from THP-1 cells but significantly higher as compared to TNF-α secretions from leukocytes isolated directly from lysed blood, confirming the functional heterogeneity between different types of immune cells.

2.4.5 Application of the MIPA Device for Patient Samples

After validating the system, MIPA device was futher applied for functional cellular immunophenotyping of pediatric patients with congenital heart defects (CHD) undergoing cardiopulmonary bypass (CPB) to prospectively validate the use of the MIPA device in predicting post-operative infections in pediatric patients following CPB. CHD are among the most common birth defects and are the leading causes of birth defect-related deaths [106]. Mortality associated with CHD accounts for up to 50% of pediatric deaths and nearly 6000 deaths each year [106]. Over 48% of these deaths occur in children less than 1 year of age [106]. Thus, mortality associated with CHD remains a serious public health problem necessitating the identification of risk factors and novel therapeutic strategies to decrease mortality, especially in high-risk populations.

Nearly all children with CHD require surgical correction of their lesions necessitating the use of CPB. However, post-operative infections contribute significantly to the mortality associated with pediatric patients undergoing cardiac surgery with CPB [107-110]. Pediatric studies have suggested an average incidence of post-operative

infections in pediatric patients following CPB around 20% and a mortality rate of nearly 25% associated with post-operative infections and infectious complications [109]. Pediatric patients who develop post-operative infections are significantly younger, have longer surgeries, extended intubations and longer lengths of stay - all attributes associated with complex cardiac repairs [109-111].

A pervading theory as to the reason for the development of the post-operative infections following cardiac surgery with CPB is that the hyper-inflammatory state created by CPB results in a compensatory anti-inflammatory immune response in the body leading to a hypo-inflammatory state rendering the patient immunosuppressed and susceptible to invading pathogens [1, 112]. This acquired immunosuppression has been termed immunoparalysis [113]. Recent study has shown that immunoparalysis in children following CPB increases the likelihood of developing a post-operative infection by nearly 6 times that of non-immunoparalyzed patients [4]. Allen and colleagues have also demonstrated that immunoparalysis following CPB can increase the risk for development of post-operative sepsis [114]. These clinical studies demonstrate a heightened risk for the development of post-operative infections for immunoparalyzed patients following CPB, hence it requires an accurate immunomonitoring and instant immunomodulatory therapy for these immunoparalyzed patients following CPB. Hall *et al.* have shown that immunoparalysis can be reversed in critically ill children by treating them with granulocyte macrophage colony-stimulating factor (GM-CSF), and thus reduce the risk of developing infections in children with multiple organ dysfunction syndrome [115]. However, current post-operative practices for pediatric patients following CPB do not address monitoring the function of the immune system, even though the clinical

presentations and consequences of post-operative infections that may develop are the result of the dysregulation of the immune response [1, 116]. This omission is a direct consequence of the current lack of standardized immunophenotyping tools in the clinical setting that can easily and rapidly determine the functional status of different subpopulations of immune cells involved in the immune response. Taken together, there is a critical need for accurate measurement of the immune status of children following exposure to CPB in order to identify those children who are immunoparalyzed and may benefit from the GM-CSF therapy. To address this need, we have applied our highly integrated microfluidics-based immunomonitoring platform for efficient isolation and rapid, accurate, and multiplexed functional immunophenotyping of subpopulations of immune cells from pediatric patients undergoing cardiac surgery with CPB, rapidly identify immunoparalysised pediatric patients and accordingly introduce effective and personalized immunomodulatory interventions and therapy.

The incidence of immunoparalysis as well as data on development of infections from any patient along with the functional status of the immune cells (PBMCs and CD14+ monocytes) have be collected and analyzed in relationship to the individual patient's immunophenotype (dichotomized as immunoparalyzed or non-immunoparalyzed). To immunophenotype the enrolled patients, 600-800 μL of patient blood (200 μL for each standard whole blood assay and 20 μL for each assay with the MIPA device; each assay was run in triplicate) were obtained as allowed by our currently approved IRB protocols right before and one day after (day 1) the CPB. TNF-α concentrations were measured and compared using the MIPA device for the whole blood leukocytes (PBMCs) as control as well as the CD14+ monocytes.

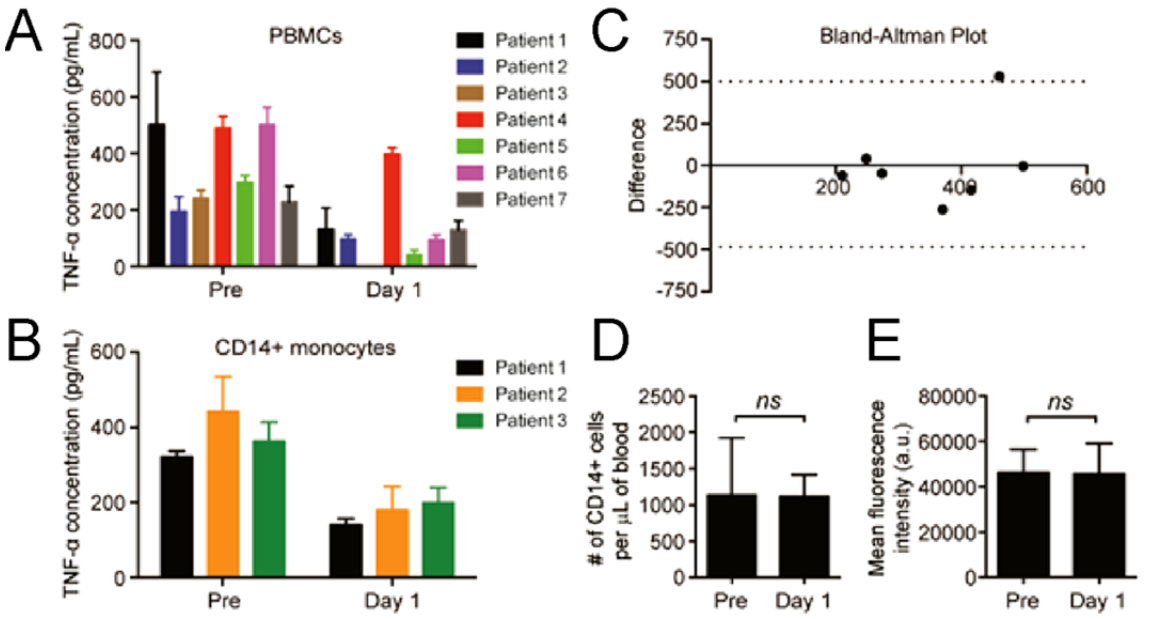

Figure 2-16 Feasibility of the MIPA device for immunophenotyping in pediatric patients following CPB. (A&B) TNF-α secretion from LPS-stimulated PBMCs (cell number: 20,000) and CD14+ monocytes (cell number: 20,000) isolated directly from whole blood samples of pediatric patients before and 1 day after CPB. (C) Bland-Altman plot of agreement between TNF-α values obtained with the MIPA device and values obtained using standard ELISA. Flow cytometry comparison of the number of cells expressing CD14 (D) and the density of CD14 (e) before and 1 day after CPB (n=7 patients). All Pre values were collected within one hour of initiation of CPB, while Day1 values were collected on the morning of the first post-operative day.

Our preliminary research investigating post-operative infections following CPB at the University of Michigan C.S. Mott Children's Hospital is consistent with published data reporting a 17% overall rate of infection with most occurring in younger patients undergoing longer surgeries [4]. Additionally, all of the children in our cohort who died (n = 3) had developed a post-operative infection. The whole blood stimulation assay determined that 42% of patients who developed a post-operative infection were immunoparalyzed whereas only 7% of the patients who did not develop any infection were classified as immunoparalyzed. These clinical data strongly argue for the need to identify pediatric patients following CPB as immunoparalyzed in order to performindividualized, immunomodulatory therapies to reverse the immunoparalysis.

More importantly, the highly predictable immunoparalysis characteristics of this cohort (time of initial insult [i.e. CPB], % incidence [~20%], and nearly universal depression at day 1 post-CPB) make this an ideal cohort to validate the MIPA platform as compared to less well characterized, though no less important cohorts, such as pediatric subjects with sepsis.

Preliminary data from patients support the feasibility of using the MIPA device on patient blood samples before and after CPB (Figure 2-16). A reduction of TNF-α production was detected using the MIPA device for LPS-stimulated PBMCs as well as CD14+ monocytes isolated directly from patient whole blood samples before and 1 day after CPB (Figure 2-16A&B). Our data further indicate a strong agreement between results generated from the MIPA and standard ELISA following whole blood stimulation (Figure 2-16C). We also observed no change in the number of immune cells expressing CD14 (Figure 2-16D) or in the density of the CD14 receptor (Figure 2-16E) on post-operative day 1 compared to pre-CPB values in this cohort. These preliminary data strongly support the feasibility of using the MIPA device to detect immunoparalysis in patients following CPB as well as using CD14 as a monocyte marker to isolate a subpopulation of leukocytes using the MIPA device.

2.5 Conclusion

Functional immunophenotyping of immune cells is a promising method for diagnosis of immune dysfunctions. The conventional functional immunophenotyping assay involves measurements of the capacity of peripheral blood mononuclear cells to produce cytokines when stimulated *ex vivo*. However, this 'bulk' assay measures the

overall reactivity of a population of immune cells, making it difficult to pinpoint the phenotype or real identity of reactive immune cells involved. In this work, an integrated microfluidic immunophenotyping device was developed for rapid and efficient isolation, enrichment, stimulation and functional immunophenotyping of subpopulations of immune cells directly from blood specimens. Owing to the high porosity and large surface area of the PMM, the PMM-integrated MIPA device could process lysed and whole blood samples with a high volume throughput (up to 20 mL min^{-1}). The MIPA device could achieve high capture yield (> 90%) and excellent capture purity (> 97%) for subpopulations of immune cells from blood samples. Further, the MIPA device could be directly integrated with the AlphaLISA biosensing technique and used for rapid, efficient on-chip immunophenotyping assays for subpopulations of immune cells isolated directly from minute quantities of blood samples. The total assay time including cell isolation, stimulation and cytokine detection only need 4 hours, 6 faster than the conventional ELISA method. The MIPA device can provide a very high sensitivity for cytokine measurement, about 75 pg mL^{-1}, which is comparable to ELISA. Because of the microfluidic environment, the MIPA device requires very small amount of sample (< 5 μL mL^{-1}) for the measurement. All together, the new integrated microfluidic functional immunophenotyping technology could perform rapid, accurate, and sensitive cellular functional assays on different types or subpopulations of immune cells, which could provide an unprecedented level of information depth on the distribution of immune cell functionalities. Such an innovative tool will potentially allow comprehensive and systems-level immunomonitoring to define and characterize the "immunotype" of healthy

individuals and patients, critical for clinical interventions and managements of patients with immune system disorders.

Chapter 3

Nanoroughened Surfaces for Capture of Circulating Tumor Cells

3.1 Introduction

Over the last decade, there has been great interest in utilizing peripheral blood circulating tumor cells (CTCs) to predict response to therapy and overall survival of patients with overt or incipient metastatic cancers [12, 117]. CTCs are shed by both primary and metastatic lesions and they are thought to contribute to hematogenous spread of cancer to distant sites [27, 118]. It has been demonstrated that the presence of elevated CTC levels is negatively correlated with prognosis in patients with metastases of the breast, prostate, lung, and colon [11, 119]. Despite the clinical and pathophysiological importance of CTCs, the current molecular and cellular understanding of CTCs is extremely poor, largely due to the fact that the current techniques to isolate and characterize these rare cells are limited by low yield and purity, complex techniques, and expensive proprietary equipments, compounded by the currently employed techniques yielding little phenotypic and molecular information about the CTCs themselves [10, 120].

So far, different approaches have been used to isolate CTCs, which can be divided into two groups: cell size-based isolation using membrane filters or microfluidic sieves [102, 103, 121] and immunoaffinity purification using immunomagnetic beads [12, 122] or microfluidic chips [117, 123-128] conjugated with antibodies against surface markers of cancer cells. Even though these approaches have been used to demonstrate the presence of CTCs in patients with metastatic cancer, each of these approaches has intrinsic major limitations. Briefly, size-based separation of CTCs is hampered by the fact that CTCs are not universally larger than all leukocytes and leukocytes clot filter pores or are collected along with CTCs thereby contaminating the isolate. For immunoaffinity purification, a monoclonal antibody against the epithelial cell adhesion molecule (EpCAM) is most commonly used because of its nearly universal expression on cells of epithelial origin and its absence from blood cells. However, surface expression of EpCAM on CTCs might be more heterogeneous than initially anticipated (*e.g.*, due to the epithelial-mesenchymal transition) and even absent altogether in some tumor types (such as melanoma) [129, 130]. Thus, positive isolation and enrichment of CTCs based on their EpCAM expression can potentially result in a substantial loss of informative CTCs [131, 132]. To avoid the biases of selecting cells based on their EpCAM expression alone, immunoaffinity-based negative depletion methods to remove CD45+ leukocytes and thereby enrich residual CTCs have also been employed [133, 134]. Although this strategy has the potential to purify CTCs regardless of cancer cell surface markers, the extremely low prevalence of CTCs can significantly limit the yields of purified CTC fractions achieved by negative selection [133, 134].

Herein, by taking advantage of the differential adhesion preference of cancer cells to nanorough surfaces when compared to normal blood cells, we demonstrated a simple, yet effective strategy for capturing CTCs regardless of their physical size and without using any capture antibody [29]. To this end, we have recently developed a simple yet precisely-controlled method to generate random nanoroughness on glass surfaces using reactive ion etching (RIE) [135, 136]. RIE-based nanoscale roughening of glass surfaces is consistent with a process of ion-enhanced chemical reaction and physical sputtering [137]. We had shown that bare glass surfaces treated with RIE for different periods of time could acquire different levels of roughness (as characterized by the root-mean-square roughness R_q; R_q = 1 - 150 nm) with a nanoscale resolution [135]. Integrating RIE with photolithography, spatially patterned nanorough islands could be generated on glass surfaces. Thus, by precisely controlling both techniques, photolithography and RIE, wecould specify the location, shape, area, and nanoroughness levels of different nanorough regions on glass surfaces. In this work, we successfully demonstrated that the RIE-generated nanorough surfaces could efficiently capture different kinds of cancer cells (*i.e.*, MCF-7, MDA-MB-231, Hela, PC3, SUM-149) without using any capture antibody. My cancer cell capture strategy with the nanorough glass surface uniquely utilized the differential adhesion preference of cancer cells to nanorough surfaces when compared to normal blood cells, and thus it did not depend on the cancer cells' physical size or surface protein expression, a significant advantage as compared to other existing CTC capture techniques.

3.2 Microfabrication of Nanorough Glass Surfaces

In this work, the surface nanoroughness on the silica-based glass wafers (Borofloat 33 glass) was generated with RIE, a well-established process used in semiconductor microfabrication (Figure 3-1A) [29, 135, 136]. The etching of the silica-based glass wafer was consistent with a process of the ion-enhanced chemical reaction and physical sputtering as reported by others [137, 138]. Specifically, during the RIE process, bombardment by the reactive ion species generated using the SF_6 and C_4F_8 gases disrupted the unreactive glass substrate and caused damage such as dangling bonds and dislocations, resulting in the glass surface reactive towards the etchant species. Interestingly, since small concentrations of impurities such as Al, K and Na (about 6% *w*/*w* in total) existed in the silica glass, these impurities resulted in accumulations of less volatile species (such as AlF_3, KF, NaF, *etc.*) on the glass surface during the RIE process [137, 138]. Thus, when the reactive plasma species approached the glass surface, these less-volatile compounds inevitably underwent numerous collisions with the plasma species. Some of these compounds were then backscattered onto the glass surface and formed randomly distributed small clusters that could shield the glass surface from bombardment and reaction with reactive ions. These compound clusters effectively generated the so-called "micro masking" effect that could randomly shadow the glass surface and thus result in nanoscale roughening of the glass surface during the RIE process [137]. Therefore, under the same RIE process conditions, the surface nanoroughness of the glass wafer could be precisely controlled in nanoscale by solely adjusting the RIE process duration (Figure 3-1B).

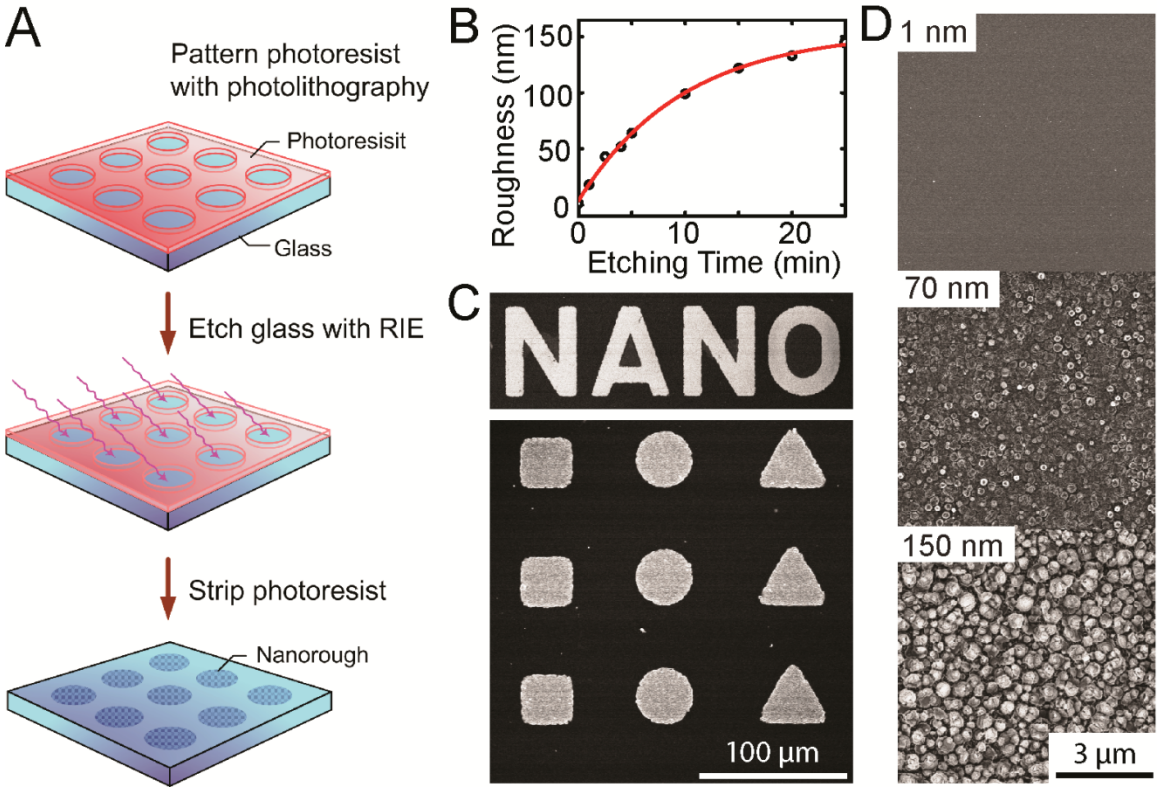

Figure 3-1 Microfabrication of nanotopographical glass surfaces. (A) Schematic of the fabrication process for patterned nanorough glass substrates using photolithography followed by RIE. (B) Nanoscale surface roughness generated on glass substrates using RIE as a function of the RIE process time, with a red fitting curve plotted for guidance. (C) SEM images of glass surfaces patterned with nanorough letters (NANO; top) and different shaped islands (bottom) using photolithography followed by RIE. (D) High-resolution SEM images of glass surfaces without (top) or with (middle and bottom) treatments of RIE-based surface roughening processes, with their RMS nanoroughness indicated.

The initial surface roughness of the unprocessed silica-based glass wafers, characterized by atomic force microscope (AFM) using the root mean square (RMS) roughness R_q (see Appendix F for details of fabrication and surface characterization of nanorough glass samples), was about 1 nm. The glass wafers were processed with RIE (LAM 9400, Lam Research, Fremont, CA) for different periods of time to generate nanorough surfaces with R_q ranging from 1 nm to 150 nm (Figure 3-1B), using SF_6, C_4F_8, He and Ar gas mixtures. To spatially pattern nanoroughness on the glass wafers, the glass wafers were first spin-coated with photoresist, and the photoresist layer was then patterned with photolithography to physically expose different glass regions of

various sizes and shapes for subsequent RIE etching. After the RIE process, photoresist was striped using solvents, and the glass wafers were cleaned using distilled water and a Piranha solution (4:1 H_2SO_4:H_2O_2) to remove organic residues from the glass substrates [139]. Thus, by precisely controlling photolithography and RIE, we could specify the location, shape, area, and nanoroughness level of different nanorough regions on glass substrates (Figure 3-1B&C).

3.3 Results and Discussion

CTCs detached from both primary and metastatic lesions represent a potential alternative to invasive biopsies as a source of tumor tissue for the detection, characterization and monitoring of cancers. Based on our nanotopograchic surfaces, we demonstrated a simple yet effective strategy for capturing CTCs without using capture antibodies [29]. This new capture method uniquely utilized the differential adhesion preference of cancer cells to nanorough surfaces when compared to normal blood cells and thus did not depend on their physical size or surface protein expression, a significant advantage as compared to other existing CTC capture techniques.

3.3.1 Nanotopographic Sensing of Cancer Cells

Using RIE-generated nanorough glass surfaces, we first examined the differential adherence preference of cancer cells to nanorough glass surfaces. Two breast cancer cell lines, MCF-7 (EpCAM-positive, or EpCAM+) and MDA-MB-231 (EpCAM-negative, or EpCAM-) were seeded as single cells on a glass surface patterned with nanorough islands or letters (R_q = 70 nm). Phase-contrast images of cancer cells taken 24 hrs after cell

seeding showed both cell types adhering selectively to patterned nanorough regions (Figure 3-2A). Quantitative analysis revealed that adhesion selectivity, defined as the ratio of the number of cells adhered to nanorough regions and the total number of cells attached to the whole glass surface, was 96.1% and 95.2% for MCF-7 and MDA-MB-231, respectively (Figure 3-2B), suggesting strong segregation of cancer cells for adherance to nanorough surfaces, regardless of their EpCAM expression status. We further performed the EdU proliferation assay for cancer cells, and our data suggested that proliferation rate of cancer cells increased with nanoroughness (Figure 3-2C).

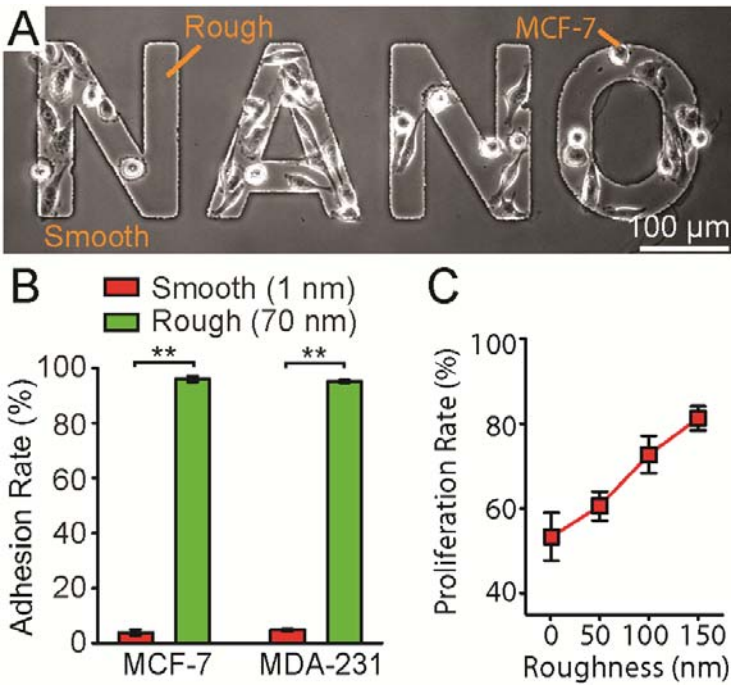

Figure 3-2 Adhesion selectivity of cancer cells to nanoroughness. (A) Phase-contrast microscopic image showing MDA-MB-231 cells selectively adhering to patterned nanorough letters (NANO; R_q = 70 nm) on the glass surface 24 hr after cell seeding. (B) Bar graph showing cell adhesion rates of MCF-7 and MDA-MB-231 cells on the smooth glass surface (R_q = 1 nm) and the patterned nanorough islands (R_q = 70 nm) of a glass substrate. Data was obtained 24 hr after cell seeding. Error bars represent ± s.e.m. (n = 3). ** (P < 0.01; Student's t-test). (C) Proliferation rates of MDA-MB-231 cells as a function of nanoroughness. Error bars represent ± s.e.m. (n = 3).

3.3.2 Capture of Cancer Cells without Using Capture Antibodies

To examine specifically whether the RIE-generated nanorough glass surfaces could achieve efficient capture of cancer cells without using any capture protein bait, we prepared two sets of unpatterned nanorough glass surfaces: one coated with anti-EpCAM antibody and the other unprocessed. MCF-7 and MDA-MB-231 cells spiked in 500 μL growth media were seeded at a concentration of 10^5 cells mL^{-1} on nanorough glass surfaces. After different periods of incubation (0.5 - 8 hrs), glass samples were rinsed gently to remove floating cells, and the remaining adherent cells were stained with DAPI for visulization and enumeration (Figure 3-3D & Figure 3-4A). Cancer cell capture yield, defined as the ratio of the number of cancer cells captured on glass surfaces to the total number of cells initially seeded, was quantified as a function of both incubation time and nanoroughness R_q.

The results in Figure 3-4 and Figure 3-3D-F revealed significant enhancements of cancer cell capture yield and speed by nanorough surfaces, and such improvements appeared to increase with nanoroughness R_q but were independent of anti-EpCAM antibody coating. For example, bare uncoated nanorough glass surfaces with R_q = 150 nm captured 80% MCF-7 and 73% MDA-MB-231 cells within 1 hr of cell incubation. In distinct contrast, only 14% MCF-7 and 10% MDA-MB231 cells were captured on bare smooth glass surfaces (R_q = 1 nm) over the same period of time. Importantly, the contribution to additional cancer cell capture using anti-EpCAM antibody coating was relatively insignificant, especially when R_q > 50 nm (Figure 3-3E-F). We further performed capture assays using other cancer cell lines, including Hela cervical cancer cells, PC3 prostate cancer cells, and SUM-149 inflammatory breast cancer cells, and

similar significant enhancements of cancer cell capture yield and speed by nanorough surfaces were observed (Figure 3-3G). Taken together, our results demonstrated that RIE-generated nanoroughness on glass surfaces enhances cancer cell capture yield up to 80% within 1 hr of cell incubation, regardless of EpCAM expression on cancer cell surfaces and without using any capture antibody coating.

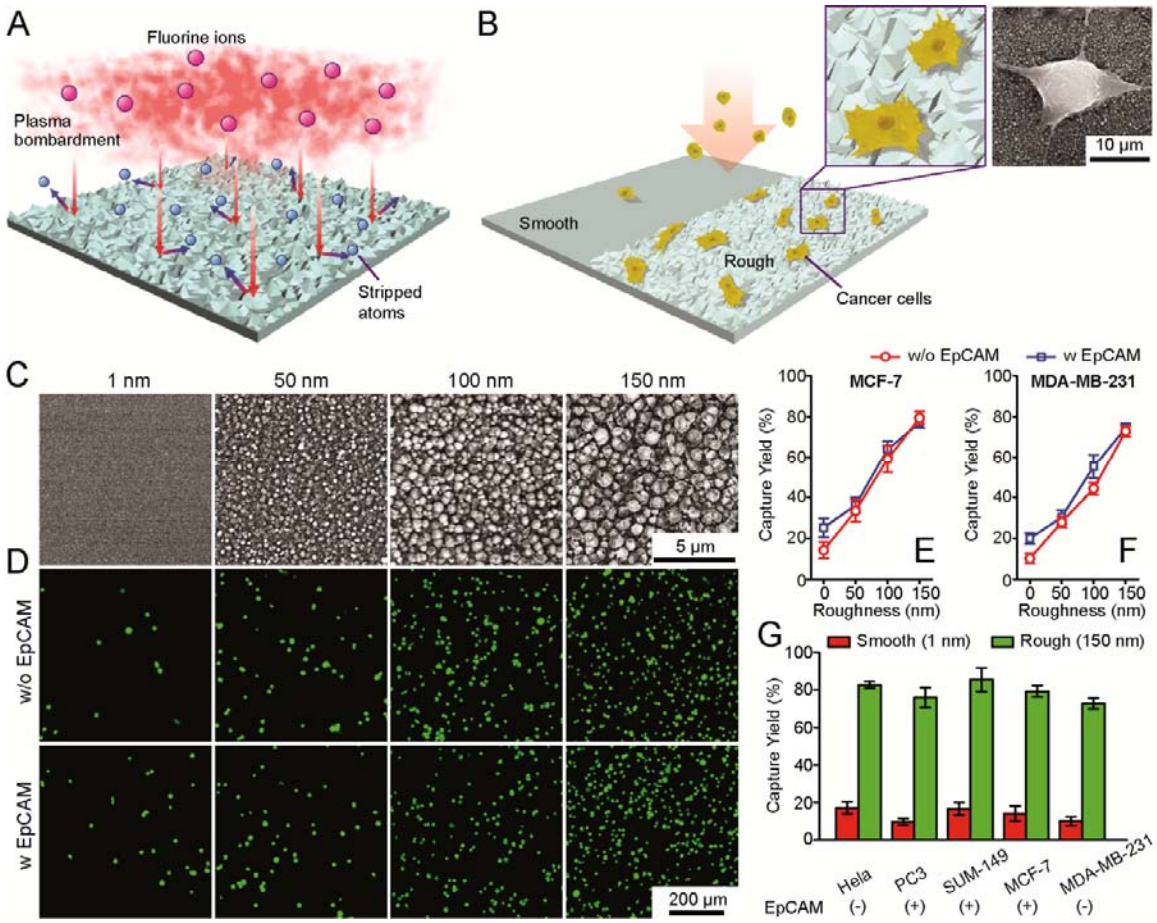

Figure 3-3 Intrinsic nanotopological sensing for capture of cancer cells. (A&B) Schematic of nanotopography generated by RIE on glass surfaces. Inserts show a zoom-in (left) and a SEM (right) images of cancer cells captured on nanorough glass surfaces. (C) SEM images of glass surfaces with their RMS nanoroughness indicated. (D-G) Cancer cells spiked in growth media at a concentration of 10^5 mL^{-1} captured on glass surfaces 1 hr after cell seeding. D shows fluorescence images of MCF-7 cells captured on glass surfaces coated with (bottom) or without (top) EpCAM antibodies. MCF-7 cells were stained for nuclei (DAPI; green) for visualization and enumeration. E-G plotted capture yields of MCF-7 (E), MDA-MB-231 (F), and other cancer cell lines (G) as a function of nanoroughness. Error bars represent ± standard error of the mean (s.e.m; $n = 4$).

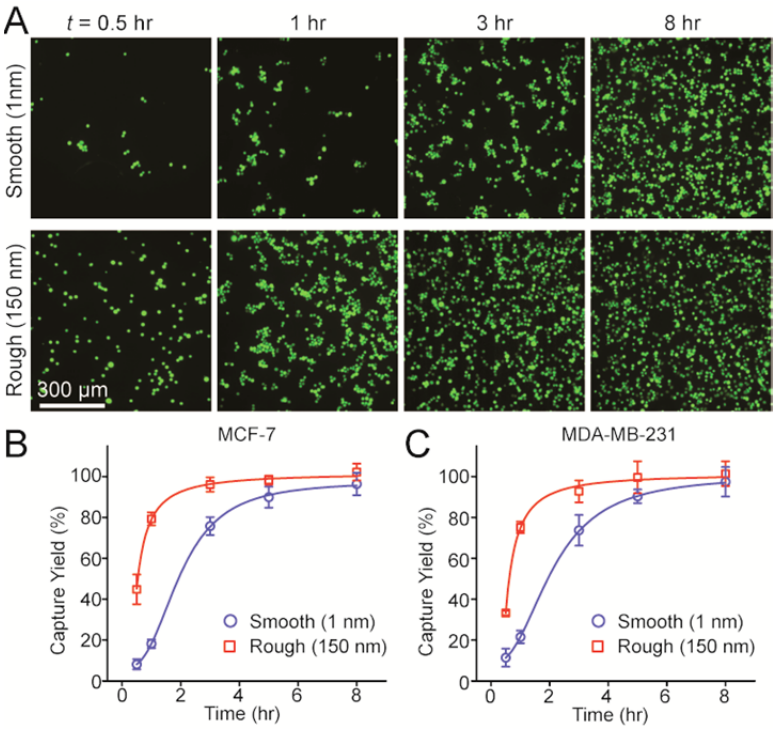

Figure 3-4 Temporal study of cancer celll adhesion behavors to the nanoroughness. (A) Representative fluorescence images showing temporal sequences of capture of CellTracker Green-labeled MDA-MB-231 cells on smooth (R_q = 1 nm; top) and nanorough (R_q = 150 nm; bottom) glass surfaces. These images were used for calculation of cell capture yields as a function of incubation time shown in B & C. (B&C) Capture yields of MCF-7 (B) and MDA-MB-231 (C) cells on smooth (R_q = 1 nm) and nanorough (R_q = 150 nm) glass surfaces as a function of incubation time, with fitting curves plotted for guidance using logistic functions. Error bars represent ± s.e.m. (n = 4). For A-C, cancer cells were spiked in growth media at a concentration of 10^5 mL^{-1}.

To evaluate the efficiency of our RIE-generated nanorough substrates for capturing rare CTCs from blood specimens without using capture antibody, we conducted capture assays for known quantities of MCF-7 and MDA-MB-231 cells (n = 10 - 1,000) spiked in 500 μL culture media containing peripheral blood mononuclear cells (PBMCs; cancer cells mixed with PBMCs at a ratio of 1:1) or 500 μL lysed human blood (Figure 3-5). Target cancer cells and background cells (PBMCs or leukocytes in lysed blood) were first labeled with CellTracker Green and Δ9-DiI, respectively, before they were mixed and used for 1-hr cell capture assays with nanorough glass surfaces (R_q = 150 nm).

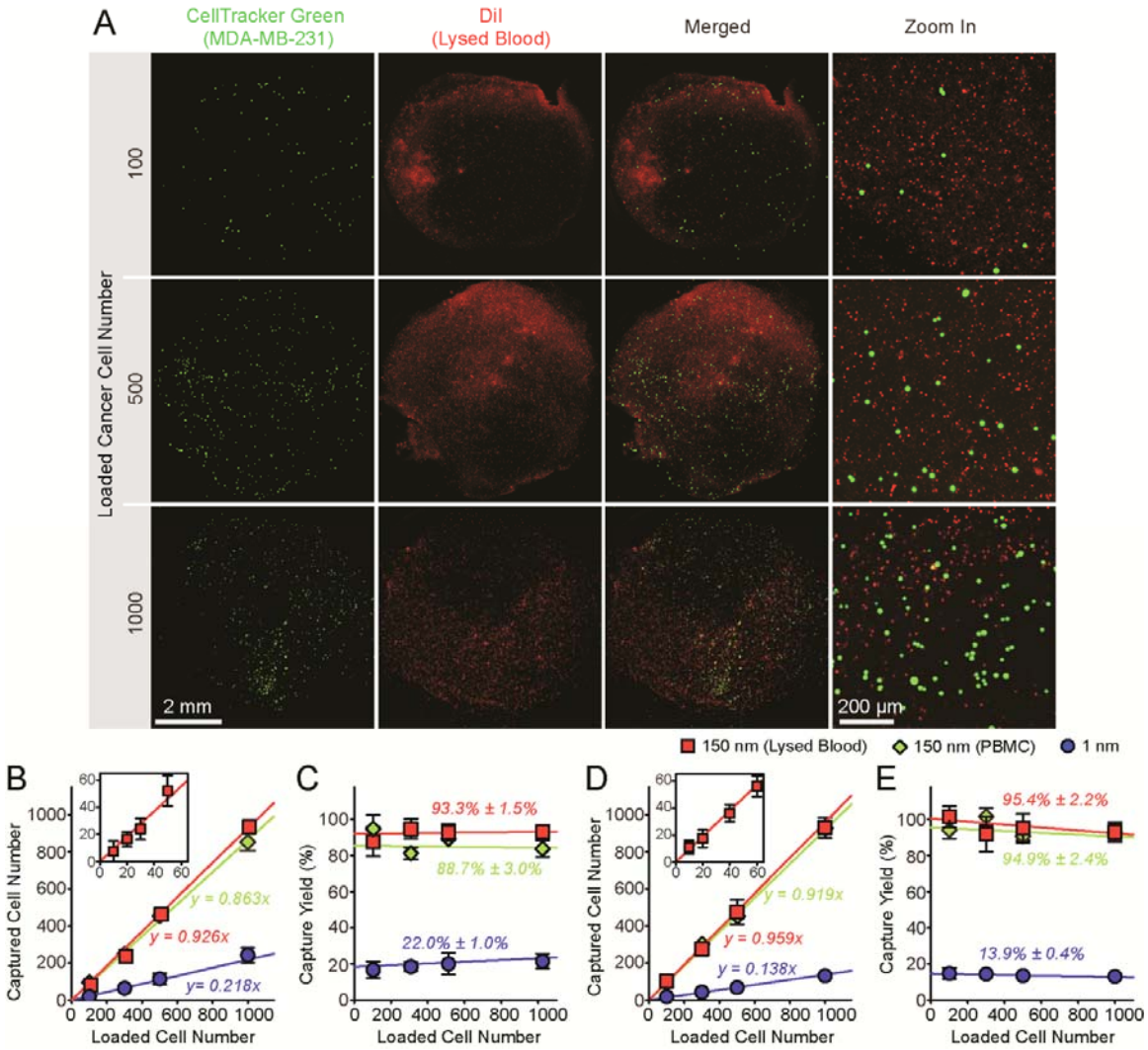

Figure 3-5 Capture and enumeration of cancer cells. (A) Representative fluorescence and merged microscopic images showing known quantities of MDA-MB-231 cells as indicated spiked in lysed blood captured on nanorough glass surfaces (R_q = 150 nm) 1 hr after cell seeding. Target MDA-MB-231 cells were labeled with CellTracker Green before spiked in lysed blood that was pre-stained with DiI. (B-E) Regression analysis of 1-hr capture efficiency for MCF-7 (B&C) and MDA-MB-231 (D&E) cells on smooth (R_q = 1 nm) and nanorough (R_q = 150 nm) glass surfaces. In A-E, known quantities of cancer cells (n = 10 - 1,000) were spiked in 500 mL growth media containing PBMCs or 500 mL lysed blood as indicated. For PBMC samples, cancer cells were mixed with PBMCs at a constant ratio of 1:1. Insets in B&D show correlations between captured cell number and loaded cell number for n = 10 - 60, indicating efficient capture of low abundant CTCs. Solid lines represent linear fitting. Error bars represent ± s.e.m. (n = 4).

As shown in Figure 3-5, high capture yields were achieved with nanorough glass surfaces for both EpCAM+ MCF-7 and EpCAM- MDA-MB-231 cells, even at low cancer cell concentrations and for both PBMC and lysed blood samples (Figure 3-5B-E).

On average, capture yields were 88.7% ± 3.0% and 93.3% ± 1.5% for MCF-7 cells mixed with PBMCs and spiked in lysed blood, respectively (Figure 3-5B&C), while for MD-MB-231 cells, capture yields were 94.9% ± 2.4% and 95.4% ± 2.2% for the PBMC and lysed blood samples, respectively (Figure 3-5D&E). In contrast, control experiments using smooth glass substrates (R_q = 1 nm) with cancer cells spiked in culture media showed much lower capture yields for both MCF-7 and MDA-MB-231 cells (22.0% ± 1.0% for MCF-7 and 13.9% ± 0.4% for MDA-MB-231) (Figure 3-5B-E), again confirming the efficiency of nanorough substrates for capturing cancer cells.

We further studied systematically the effect of admixtures of cancer cells with other background cells on the efficiency and purity of cancer cell capture on uncoated nanorough glass surfaces (R_q = 150 nm) by varying the ratio of MDA-MB-231 and PBMCs from 1:1 to 1:200, with the MDA-MB-231 cell number fixed at 1,000 (Figure 3-6A). Our 1-hr cell capture assay results in Figure 3-6 showed that capture yields of MDA-MB-231 were preserved with admixture and were as high as 93.6%. Thus, the capture yield was not affected strongly by the proportion of background PBMCs (Figure 3-6B&C). Interestingly, capture yields of PBMCs by uncoated nanorough glass surfces remianed low and were gradually decreased from 16.7% to 4.1% when the ratio of MDA-MB-231 and PBMCs decreased from 1:1 to 1:200 (Figure 3-6C). Not surprisingly, as the absolute numbers of PBMCs captured on nanorough glass surfaces increased when the ratio of MDA-MB-231 and PBMCs decreased from 1:1 to 1:200, capture purity of MDA-MB-231 cells was significantly decreased from 84% to 14% (Figure 3-6D).

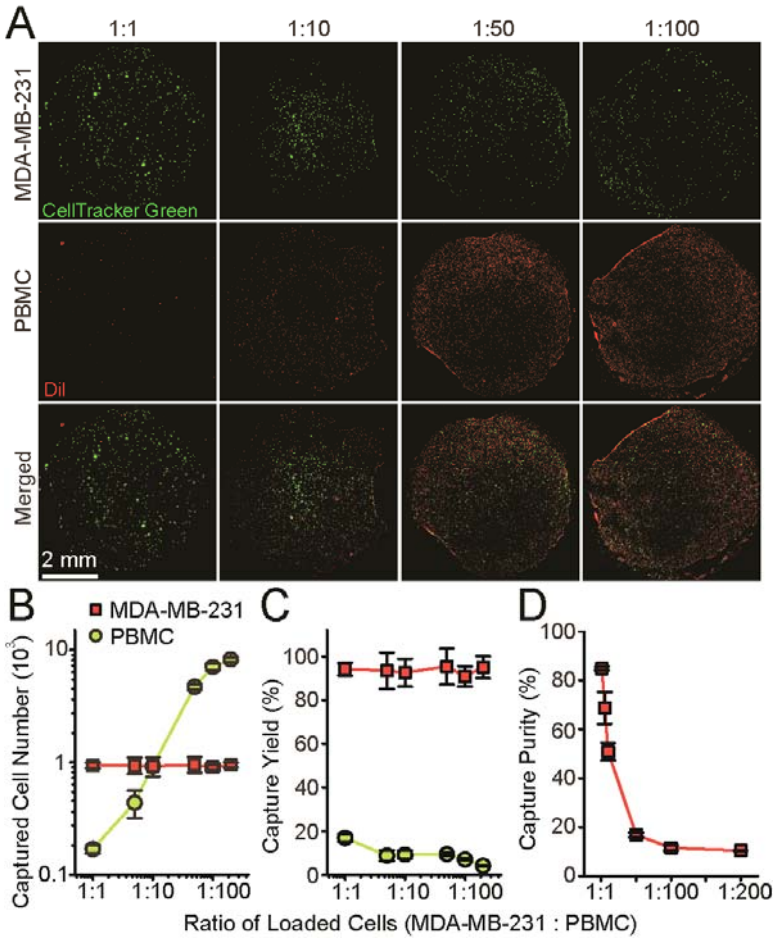

Figure 3-6 Effect of cellular background on capture yield and purity of cancer cells. (A) Fluorescence and merged microscopic images showing CellTracker Green-labeled MDA-MB-231 cells and DiI-stained PBMCs captured on nanorough glass surfaces (R_q = 150 nm) 1 hr after cell seeding. The ratio of cancer cells and PBMCs was varied as indicated. (B-D) Captured cell number (B), capture yield (C) and purity (D) of MDA-MB-231 cells on nanorough glass surfaces (R_q = 150 nm) as a function of the ratio of MDA-MB-231 cells to PBMCs. Results were obtained 1 hr after cell seeding. In A-D, a fixed number of cancer cells (1,000) were mixed with PBMCs in growth media to achieve cell ratios from 1:1 to 1:200. Error bars represent ± s.e.m. (n = 4).

The current concept of metastasis proposes that the process of epithelial-mesenchymal transition (EMT) occurs in the primary tumors [140, 141]. EMT could contribute to the generation of CTCs in the bloodstream, where phenotypic changes are very likely to occur. Tumor cells leave the primary site of cancer and enter the circulation after undergoing EMT. During the EMT process, tumor cells lose the epithelial features such as EpCAM, and acquire mesenchymal characteristics, which

include enhanced migratory capacity, invasiveness, elevated resistance to apoptosis, and greatly increased production of ECM components [142]. There have been many studies on their predictive, diagnostic or prognostic significance, including a recent study in breast cancer patients that demonstrated dynamic changes in the epithelial and mesenchymal composition of CTCs with disease progression [143]. However, the most current commenly used CTC isolation techniques based on EpCAM expression can potentially result in a substantial loss of these CTCs of mesenchymal phenotype after undergoing EMT [131, 132]. Expression of EpCam is very heterogeneous and it is significantly down regulated during EMT. Therefore, relying on EpCAM failed to capture mesenchymal-like CTCs as a result of EMT [143].

Our nanorough surface based method which can capture CTCs regardless of cancer cell surface markers, can efficiently capture both epithelial (non-EMT) and mesenchymal like (EMT) cells with equal high efficiency, a significant advantage as compared to other existing CTC capture techniques. To induce the EMT process, A549 lung caner cells (ATCC, Manassas, VA) were treated for 3 days with transforming growth factor-beta (TGF-beta), a cytokine that is rich in tumor microenvironments and a potent inducer of EMT. To evaluate the efficiency of our RIE-generated nanorough substrates for capturing EMT and non-EMT cells from blood specimens, capture assays were conducted for known quantities of EMT and non-EMT cells cells (n = 40 - 10,000) spiked in 500 μL lysed human blood (Figure 3-7). Target A549 cancer cells and background cells (leukocytes in lysed blood) were first labeled with CellTracker Green and Δ9-DiI, respectively, before they were mixed and used for 1-hr cell capture assays with nanorough glass surfaces (R_q = 150 nm).

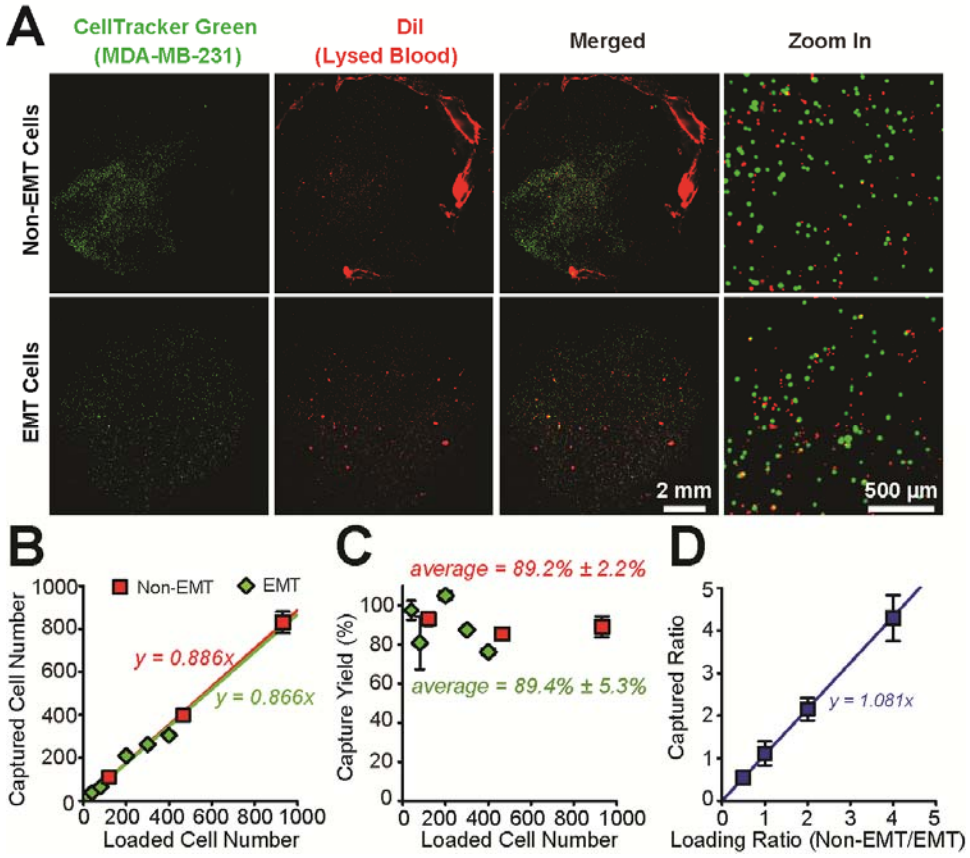

Figure 3-7 Capture of EMT and non-EMT lung cancer cells from lysed blood. (A) Representative fluorescence and merged microscopic images showing known quantities (10,000) of EMT and non-EMT lung cancer cells (A549) as indicated spiked in lysed blood captured on nanorough glass surfaces (R_q = 150 nm) 1 hr after cell seeding. Target lung cancer cells were labeled with CellTracker Green before spiked in lysed blood that was pre-stained with DiI. (B-C) Regression analysis of 1-hr capture efficiency for EMT and non-EMT cancer cells on nanorough (R_q = 150 nm) glass surfaces. In B-C, known quantities of cancer cells (n = 40 - 900) were spiked in 500 μL lysed blood as indicated. (D) Ratio of captured cell number of non-EMT and EMT cells on nanorough glass surfaces (R_q = 150 nm) as a function of the loading ratio. Results were obtained 1 hr after cell seeding. In D, a fixed number of EMT cancer cells (1,000) were mixed with non-EMT cells in lysed blood to achieve cell ratios from 1:0.5 to 1:4. Solid lines represent linear fitting. Error bars represent ± s.e.m. (n > 4).

As shown in Figure 3-7, high capture yields were achieved with nanorough glass surfaces for both EMT and non-EMT cells, even at low cancer cell concentrations. On average, capture yields were 89.4% ± 5.3% and 89.2% ± 2.2% for EMT and non-EMT cells spiked in lysed blood, respectively (Figure 3-7B&C). We further studied systematically the effect of admixtures of EMT cells with non-EMT cells on the efficiency of cancer cell capture on nanorough glass surfaces (R_q = 150 nm) by varying

the ratio of EMT and non-EMT cells from 1:0.5 to 1:4, with the EMT cell number fixed at 1,000 (Figure 3-7D). The 1-hr cell capture assay result showed that the capture yield was not affected strongly by the proportion of EMT or non-EMT cells (Figure 3-7D). Taken together, our results demonstrated that the nanorough glass surfaces permited cancer cell capture yield >89% within 1 hr of cell incubation, for both EMT and non-EMT cells.

3.3.3 Cell Adhesion Strength Measurements

Our results in Figure 3-5 & Figure 3-6 showed a significantly different levels of preference between cancer cells and PBMCs to adhere to nanorough glass surfces, which suggested an interesting possibility that adhesion strength of cancer cells might be affected by nanotopographic sensing, while adhesion of PBMCs might not be sensitive to nanotopographic cues. To examine this possibility, we developed a microfluidic channel using polydimethylsiloxane (PDMS) integrated with smooth (R_q = 1 nm) or nanorough (R_q = 100 nm) glass substrates for direct measurements of adhesion strength of cancer cells and PBMCs (see Appendix G for details; Figure 3-8A & Figure 3-9) [144]. A low density of cancer cells (MCF-7, MBA-MB-231 and PC3 cells) or PBMCs was seeded uniformly inside the microfluidic channel for 12 hrs before they were exposed to constant directional fluid shear (0.1 - 120 dyne cm^{-2}) for 5 min. The fractions of cancer cells and PBMCs remained adherent on smooth and nanorough substrates were quantified after their treatments with this sustained 5-min directional fluid shear [145]. Our data demonstrated that indeed, cancer cells attached on nanorough surfaces could withstand much greater fluidic shear stress than on the smooth surface, regardless of EpCAM

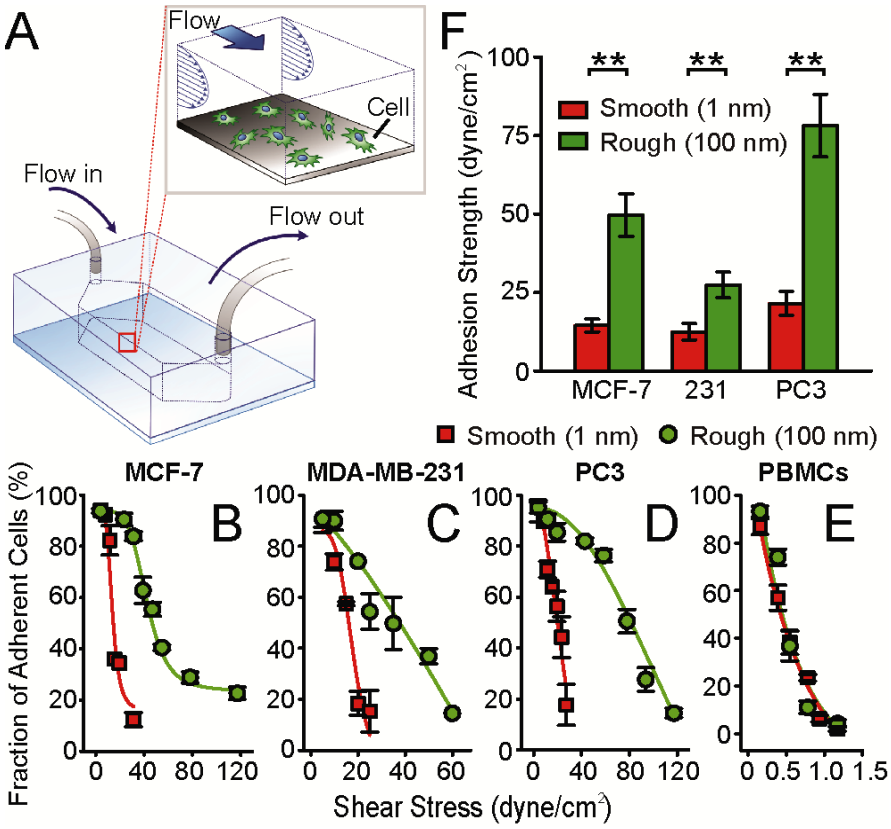

Figure 3-8 Effect of nanotopological sensing on cell adhesion strength. (A) Schematic of a microfluidic channel integrated with smooth or nanorough glass substrates for quantifications of cell adhesion strength. Insert shows adherent cancer cells in the channel under sustained directional fluid shear. (B-E) Fraction of MCF-7 (B), MBA-MB-231 (C), PC3 (D) and PBMCs (E) remained adherent on smooth (R_q = 1 nm) or nanorough (R_q = 100 nm) substrates after 5-min exposures to sustained directional fluid shear. Low densities of cancer cells or PBMCs were seeded into microfluidic channels and cultured for 12 hrs before PBS was flowed continuously along the channel to exert fluid shear stress on cells. (F) Adhesion strength of MCF-7, MBA-MB-231 and PC3 cells on smooth (R_q = 1 nm) or nanorough (R_q = 100 nm) substrates. Solid lines in B-E represent logistic (B-D) or exponential (E) fitting to guide eyes. Error bars represent ± s.e.m. (n = 4). Statistical analysis was performed by employing the Student's t-test. ** indicates $p < 0.01$.

expression on cancer cell surfaces (Figure 3-8B-D & Figure 3-9). Adhesion strength of cancer cells, defined as the fluidic shear stress at which 50% of cancer cells initially attached on glass surfaces would detach after exposed to fluid shear for 5 min [146], was significantly greater for cancer cells adhering on the nanorough surface than the smooth one (Figure 3-8F). As expected, adhesion strength of PBMCs to both smooth and nanorough glass surfaces was low, and they could easily be washed away even under a shear stress < 1 dyne cm^{-2}, consistent with our observation that most PBMCs were still

floating on both smooth and nanorough glass surfaces even after 12 hrs of incubation. Measurements of adhesion strength of cancer cells and PBMCs after 1 hr of incubation had been difficult, as most cells were still floating and not attach to glass surfaces, likely attributable to the confined microfluidic environment. Together, our results in Figure 3-8 demonstrated that nanotopographic surfaces could significantly enhance adhesion strength of cancer cells, regardless of their EpCAM expression. Adhesion of PBMCs to uncoated glass surfaces appeared to be not sensitive to nanotopographic cues.

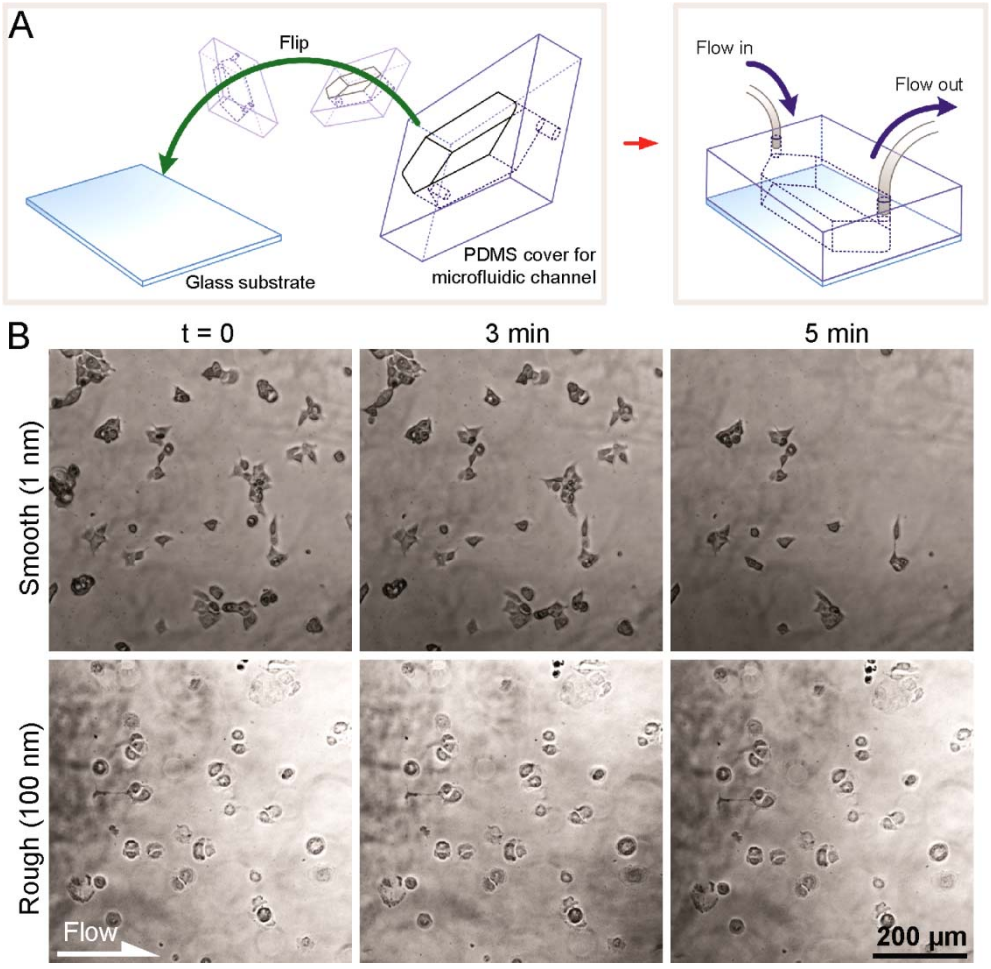

Figure 3-9 Microfluidic device for study of cell adhesion strength. (A) Schematic of fabrication process for the microfluidic channel for quantifications of cell adhesion strength. The microfluidic channel was fabricated in PDMS using soft lithography and was bound to smooth and nanorough glass substrates using the oxygen plasma-assisted PDMS bonding process. (B) Representative phase images showing temporal sequences of adherent MCF-7 cells detaching from the smooth (R_q = 1 nm; top) and nanorough (R_q = 100 nm; bottom) glass surfaces under a constant fluid shear stress of 12.5 dyne cm^{-2}.

3.3.4 Nanotopological Sensing through Focal Adhesions

To investigate the possible mechanotransductive mechanism for nanotopographic sensing of cancer cells, we examined focal adhesions (FAs) of EpCAM+ MCF-7 and EpCAM- MDA-MB-231 cells plated as single cells on both smooth and nanorough glass surfaces. Published data indicate that integrin-mediated FA signaling, critical for many cellular functions and strongly dependent on their nanoscale molecular arrangement and dynamic organization, may play an important role in regulating cellular mechanosensitivity to nanotopography [147]. After 24 hrs in culture, both MDA-MB-231 (Figure 3-10) and MCF-7 (Figure 3-11) cells exhibited distinct FA formation and organization on the smooth and nanorough glass surfaces, as characterized by immunofluorescence staining of vinculin, a FA protein.

On smooth glass surfaces where R_q = 1 nm, mature and prominent vinculin-containing FAs formed primarily on the periphery of both cancer cells. By comparison, on nanorough surfaces with R_q = 150 nm, both MDA-MB-231 and MCF-7 cells exhibited randomly distributed, punctate FAs of small cross-sections throughout the entire cell spread area. Morphometric analysis of cell populations showed that on nanorough glass surfaces, both MDA-MB-231 and MCF-7 cells had smaller mean cell spread area and single FA area and less total number of FAs and total FA area per cell than on the smooth surface (Figure 3-10B-E & Figure 3-11B-E). The molecular arrangement and dynamic organization of integrin-mediated FAs of both cancer cells appeared sensitive and responsive to local presentation of nanotopographical cue and hence might result in their distinct adhesion behaviors on nanorough surfaces as demonstrated in this work.

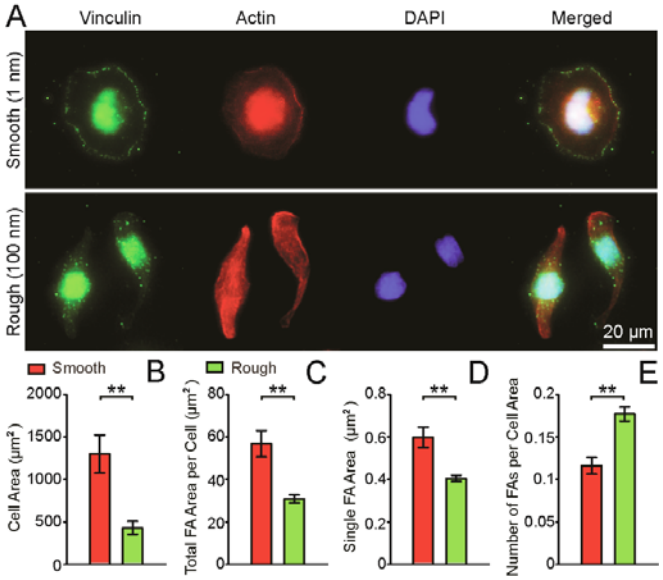

Figure 3-10 Effect of nanotopological sensing on FA formation of MDA-MB-231 cells. (A) Representative immunofluorescence images of MDA-MB-231 cells adherent on smooth (R_q = 1 nm) and nanorough (R_q = 100 nm) glass surfaces after 24 hr of culture. Cells were co-stained for nuclei (DAPI; *blue*), actin (*red*), and vinculin (*green*). (B-E) Cell area (B), total FA area per cell (C), average single FA area (D) and number of FAs per cell area (FA density; E) of MDA-MB-231 cells adherent on smooth (R_q = 1 nm) and nanorough (R_q = 100 nm) glass surfaces after 24 hr of culture. Error bars represent ± s.e.m. (n > 30). Statistical analysis was performed by employing the Student's *t*-test. ** indicates $p < 0.01$.

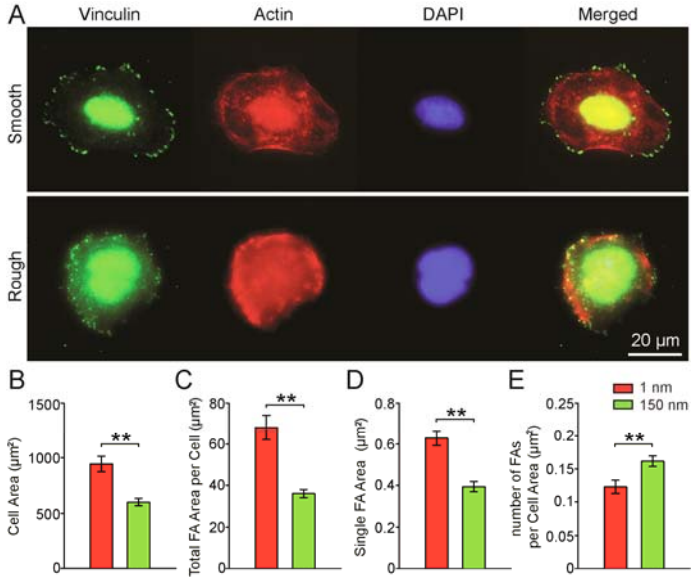

Figure 3-11 Effect of nanotopological sensing on FA formation of MCF-7 cells. (A) Representative immunofluorescence images of MCF-7 cells adherent on smooth (R_q = 1 nm) and nanorough (R_q = 100 nm) glass surfaces after 24 hr of culture. Cells were co-stained for nuclei (DAPI; *blue*), actin (*red*), and vinculin (*green*). (B-E) Cell area (B), total FA area per cell (C), average single FA area (D) and number of FAs per cell area (FA density; E) of MCF-7 cells adherent on smooth (R_q = 1 nm) and nanorough (R_q = 100 nm) glass surfaces after 24 hr of culture. Error bars represent ± s.e.m. (n > 20). Statistical analysis was performed by using the Student's *t*-test. ** indicates $p < 0.01$.

3.3.5 Microfluidics-based CTC Capture Chip for *in vivo* Study

In the last section, a simple yet effective strategy has demonstrated for highly sensitive and specific capture of different types of cancer cells using RIE-generated nanorough glass surfaces. Based on the nanorough glass surface, a CTC capture chip combining nanorough glass substrate with a microfluidic chamber was futher developed for capture of CTCs with improved capture performance (Figure 3-12).

The microfluidic CTC capture platform includes three components: a nanorough glass substrate, a PDMS microfluidic chamber, and a polyacrylate holder sandwiching the PDMS chamber and the glass substrate. The glass substrate has dimensions of 50 mm × 76 mm and an effective nanoroughed region of 44 mm × 56 mm. The PDMS microfluidic chamber with a height of 400 μm, width of 44 mm and width of 56 mm was produced by soft-lithography using a replicate on a silicon mold. A holder composed of two pieces of polyacrylate plates was home-machined to sandwich the PDMS microfluidic chamber and the glass substrate. The PDMS microfluidic chamber was aligned onto the patterned glass substrate. Then the holder can sandwich these two parts by screws at the sides of plastic plates. Two through-holes were drilled on the top plastic plate with a good alignment to the inlet and outlet holes of the PDMS microfluidic chamber, thus allowing convenience connection of tubings to the microfluidic channel of the chip. The complete assembly is capable of enduring back pressure of about 10 psi on the tested fluid samples without leaking. Such a microfluidic setting can lead to a significant enhancement in cell–substrate contact frequency compared to a simple nanorough glass substrate, hence improve the CTC capture yield and throughout.

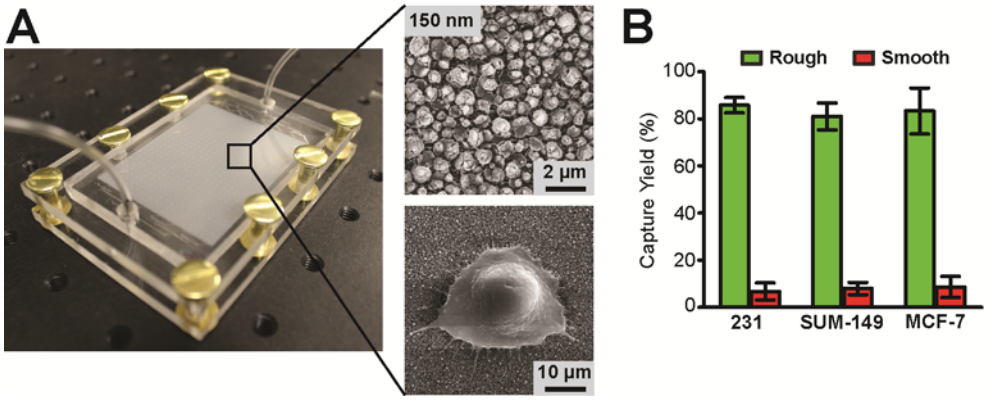

Figure 3-12 Microfluidic chip for capture of CTCs. (A) The left image shows a photo of a representative microfluidic CTC capture chip. The right images shows SEM images of the nanotough surface (top, R_q = 150 nm) and cancer cells captured on the nanotough surface. (B) Cell capture yield of MCF-7, MBA-MB-231 and SUM-149 cells on smooth (R_q = 1 nm) or nanorough (R_q = 150 nm) substrates. Error bars represent ± standard error of the mean (s.e.m; n = 4).

The microfluidic CTC capture chip including a nanorough substrate (R_q = 150 nm) and a microfluidic chamber achieved high capture yields for MBA-MB-231 (83.3% ± 9.8%), SUM-149 cells (80.9% ± 5.7%) and MCF-7 (85.7% ± 3.2%) within 30 min of capture time for 1 mL sample. In distinct contrast, only 6.7% MDA-MB-231, 8.0% SUM-149 and 8.6% MCF-7cells were captured in microfluidic chip with a bare smooth glass surfaces (R_q = 1 nm) over the same period of time.

Since the discovery of CTCs, most of the investigative efforts have been focused on their clinical application in terms of prognosis and monitoring response to therapy. To date, very few studies assessed the functional significance of CTCs in terms of their role in the clinical manifestation of tumor metastasis. CTCs have been found in patients both with and without metastatic disease [118, 148]. A recent survey by ASCO concluded that only a proportion of patients with detectable CTCs will go on to develop overt metastasis with a 5-10 year follow up [149]. This clearly indicates that qualitative assessment of CTCs and understanding their functional relevance to EMT and clinical manifestation of metastasis is essential for improving their clinical potential. Using well-defined cell

lines in xenogeneic as well as syngeneic mouse models, we have examed the functional relevance of CTCs with respect to the tumor progression and metastasis capability using our newly developed CTC capture chip.

First, we identified CTCs that spontaneously intravasated into the circulation from orthotopic tumor xenografts of human breast cancer cells. To generate tumor xenografts, 1×10^6 MDA-MB-231 or SUM-149 breast cancer cells were injected orthotopically into left inguinal mammary fat pad of each female Ncr nude mouse (Taconic; 5–6 week old) [150].

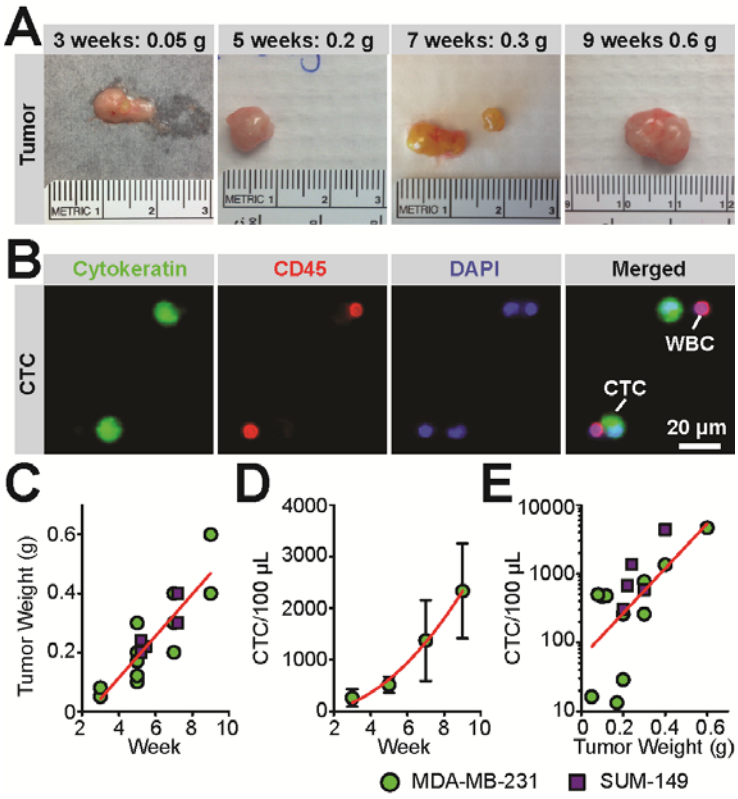

Figure 3-13 Capture of CTCs from mice with breast cancer xenografts. (A) Reprenstitive photos of MDA-MB-231tumor xenografts. (B) Representative immunofluorescence images of captured CTCs from mice with MDA-MB-231tumor xenografts. Cells were co-stained for nuclei (DAPI; *blue*), cytokeratin (*green*), and CD45 (*red*). (C-E) Serial analysis of temporal changes in CTC during tumor progression. Tumor volume (C) and recovered CTC quantity (D) from mice with MDA-MB-231 and SUM-149 tumor xenografts increase over time. The recovered CTC quantity coralated with the tumor weight (E). Mice were implanted with orthotopic tumor xenografts of MDA-MB-231 or SUM-149 human breast cancer cells. Approximately, 0.5-1 mL blood samples were obtained via cardiac puncture from mice anesthetized with 1.5% isoflurane.

At each time point, small volume (0.5–1 mL) blood samples were collected from each mouse by puncture of the left ventricle for CTC capture experiments when animals were euthanized for tumor burden. In the experiments, CTCs were successfully identified from all the mice with tumor xenografts (n = 16). Numbers of CTCs ranged from 10 to 10,000 cells/100 μL blood increased significantly over a 9-week period during tumor progression, corresponding with an increase in tumor weight/volume of the primary tumor (Figure 3-13).

To determine the functional relevance of CTCs with respect to the metastasis capability, we further applied the CTC capture chip to a syngeneic lung cancer mouse model. Two well-defined mouse lung cancer cell lines (344SQ and 393P) with different metastasis capability were used sub-cutaneously implanted in C57BL6 mice to generate tumor allografts (Taconic). The mouse 344SQ lung cancer cells have high metastatic potential, while the mouse 393P cells are metastasis-incompetent [151]. The 344SQ cells undergo metastasis when implanted sub-cutaneously (spontaneous metastasis) or through tail vein (experimental metastasis), but 393P does not metastasize at all by both routes [151]. Using our CTC capture platform, CTCs were detected in all 6 mice using metastatic 344SQ cell line, but only idenfied CTCs from 2 out of 4 mice uing the metastasis-incompetent 393P cell line (Figure 3-14). Similar to the result from the xenograft mouse model, the number of CTCs strongly corelated to the tumor volume of the primary tumor (Figure 3-14). More CTCs were identified from mice with large tumors and no CTCs were captured from blood samples collected from mice without tumor xenografts (Figure 3-14B & C). More interestingly, the number of captured CTCs is also corresponding to the metastasis capability. Overall, significantly higher number of

CTCs was identified from mice implanted with tumor allografts of lung cancer cells with high metastasis capability (344SQ) than that from the mice using a metastasis-incompetent cell line (393P). This distinct CTC kinetics between the two compartments indicated a strong relationship between CTCs and metastasis.

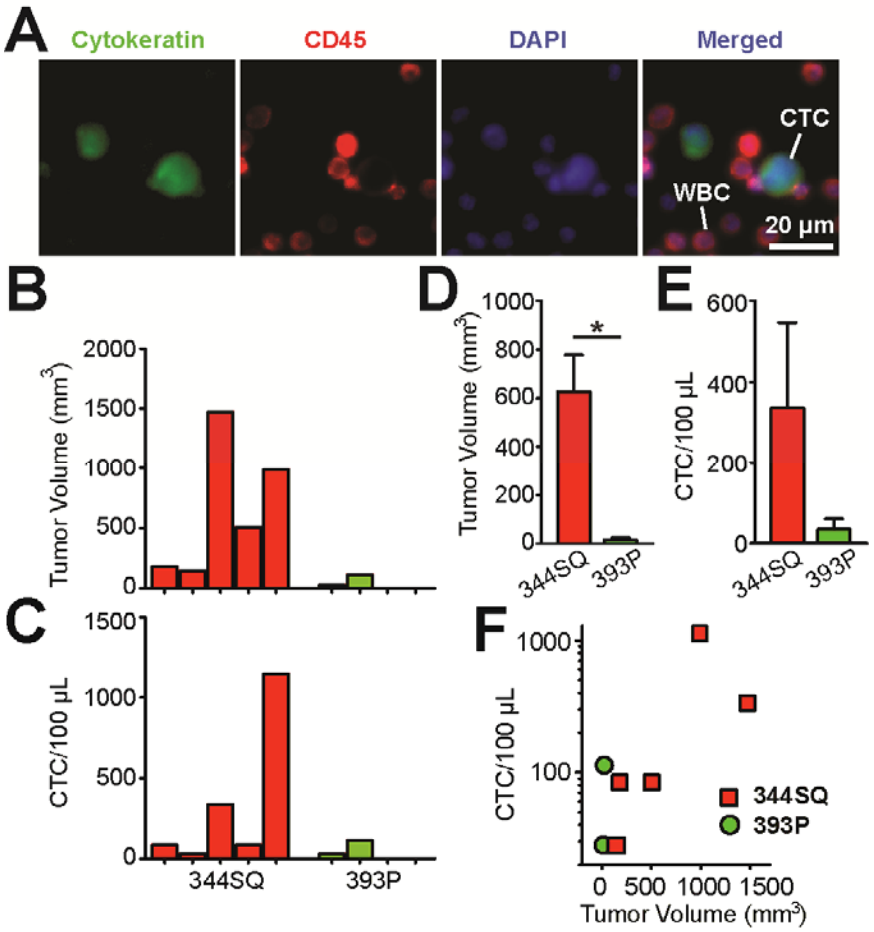

Figure 3-14 Capture of CTCs from mice with lung cancer allografts. (A) Representative immunofluorescence images of captured CTCs from mice with 344SQ lung tumor allografts. Cells were co-stained for nuclei (DAPI; *blue*), cytokeratin (*green*), and CD45 (*red*). (B-F) Serial analysis of CTC in mice with 344SQ and 393P lung tumor allografts. (B) Tumor volume and (C) recovered CTC quantity from individual mouse with 344SQ and 393P lung tumor allografts. (D) Average tumor volume and (E) average recovered CTC quantity from mice with 344SQ and 393P lung tumor allografts. (F) The recovered CTC quantity coralated with the tumor weight. Mice were implanted with tumor allografts of 344SQ or 393P lung tumor cells. Approximately, 0.4-1 mL blood samples were obtained via cardiac puncture from mice anesthetized with 1.5% isoflurane. The mouse 344SQ lung cancer cells have high metastatic potential, while the mouse 393P lung cancer cells are metastasis-incompetent. Error bars represent ± standard error of the mean (s.e.m; $n > 4$). Statistical analysis was performed by using the Student's *t*-test. * indicates $p < 0.05$.

3.4 Conclusion

In summary, a simple yet effective strategy was demonstrated for highly sensitive and specific capture of different types of cancer cells using nanorough glass surfaces. Our cancer cell capture strategy uniquely utilized the differential adhesion preference of cancer cells to nanorough surfaces when compared to normal blood cells and thus did not depend on their physical size or surface protein expression, a significant advantage as compared to other existing CTC capture techniques. Our cancer cell capture strategy is applicable to many different cancer cell types regardless of EpCAM expression and EMT process, can potentially provide a promising solution to study intratumor phenotypic heterogeneity at the single-cell level using patient CTCs for diagnostics and therapy [152, 153]. Exploiting the differential adhesion preference of cancer cells for nanorough surfaces when compared to normal blood cells is a promising strategy to achieve their efficient capture at very low costs and is expected to lead to better isolation and enrichment strategies for live CTCs from cancer patient's blood specimens, critical for informative analysis of CTCs and for accurate diagnosis, therapeutic choices, and prognosis and for fundamental understanding of cancer metastasis.

Chapter 4

Biophysical Phenotyping of Inflammatory Breast Cancer Stem Cells

4.1 Introduction

Increasing evidence indicates that cancer cells with stem cell-like properties, termed 'cancer stem cells' (CSCs), have the potential for self-renewal, differentiation, and tumorigenicity and play a major role in cancer recurrence and metastasis [154-156]. CSCs have been shown to initiate tumorigenesis in numerous cancer types [157-159], and recent studies have begun to define a role for CSCs in cancer metastasis as well [32, 160-162]. CSCs have been characterized on the basis of their expression of particular surface markers [163, 164] - such as CD133 and CD44 - and also on the basis of cell adhesion molecules [165], cytoprotective enzymes (*e.g.* aldehyde dehydrogenase, ALDH) [166], and drug-efflux pumps (*e.g.* ABC transporters) [167]. CSCs, defined as the high ALDH-expressing subpopulation, have been shown to play a role in inflammatory and aggressive breast cancers [32]. Inflammatory breast cancer (IBC) is the most lethal form of breast cancer with 20 - 30% of patients presenting with metastasis at initial diagnosis [30, 31]. Although RhoC GTPase and anaplastic lymphoma kinase (ALK) are implicated in the

IBC phenotype, the underlying detailed mechanisms that allow IBC to be so aggressively metastatic from its inception are still under study. In order to advance the field, an understanding of the physical attributes of CSCs that underlie their ability to execute the multiple events of metastases is important and has not been previously undertaken.

Here we analyzed both the intrinsic functional capabilities of IBC's CSC compartment as well as these cells' inherent biophysical properties that make them capable of early metastasis, essentially from the tumor's inception. During metastatic progression, cancer cells encounter complex biophysical environments consisting of different degrees of extracellular matrix (ECM) cross-linking [168], a differing ECM topology [169-171], mechanical heterogeneity within the ECM [170, 172, 173], as well as being exposed to shear flow and interstitial pressure [174-176]. In response, metastatic cancer cells must acquire unique biophysical characteristics in order to navigate through this dynamic microenvironment to reach and proliferate in distant sites. As CSCs are believed to play critical roles in metastasis, it is highly possible that CSCs too will develop biophysical properties - such as increased deformability and decreased adhesion strength - necessary to traverse this environment and be capable, for example, of repopulating tumor masses following treatment.

Cell deformability (*i.e.* compliance under an applied load) has been postulated to play key roles in cancer cell invasiveness [174, 177-180]. Cytoskeletal changes have been suggested to underlie mechanical differences observed in invasive cancer cells, consistent with a process of selection for cells that are able to squeeze into vessels by traversing walls (intravasate) [174, 181, 182]. Many studies have demonstrated a significantly higher degree of cell deformability for both cancer cell lines and primary

tumors when compared to normal epithelial cells [177-179]. In the case of breast and ovarian cancers, the subpopulation of cancer cells with increased cell deformability has been shown to have a more malignant phenotype compared to stiffer cells [177, 183]. Cell traction force is another key mechanical factor that has previously been shown to mediate cell functions (*e.g.* migration, adhesion, and proliferation) as well as mechanotransduction [136, 184-186]. Therefore, cell traction forces may also be involved in cancer progression.

Previous studies have convincingly established the usefulness of biophysical characteristics for identifying more aggressive cancer cells in a label-free manner that is independent of current immunohistological methods [174, 177, 181, 182, 187, 188]. Given that IBC is the most aggressive and metastatic breast cancer, we sought to utilize quantitative techniques to characterize the IBC CSC compartment using a panel of assays to specifically profile the functional as well as biophysical characteristics of CSCs at the single-cell level. Such comprehensive, multiparametric phenotypic profiling of CSCs can provide useful insights into the qualities of IBC CSCs that increase their aggressiveness and propensity for tumorigenesis and metastasis as well as allow for studies of novel therapeutic interventions targeting CSCs functions.

4.2 Results and Discussion

4.2.1 Functional Phenotyping of IBC CSCs.

High activity of ALDH within tumors has been associated with a poor prognosis in many cancers including breast [32, 164, 189, 190], lung [191, 192], liver [193], colon

[166, 194], pancreatic [195], ovarian [196], head and neck [197], and prostate [198] cancer. ALDH is a superfamily of detoxifying enzymes responsible for metabolizing a wide variety of intracellular aldehydes and plays an important role in multiple biological activities, including drug resistance, cell differentiation, and oxidative metabolism [199-201]. ALDH expression has been used as a predictive marker of CSCs for breast cancer [164, 189, 190, 202] – including IBC [32] – and ALDH expression has proven to be more predictive than other established markers such as CD44+ / CD24- for identification of breast CSCs, as it has been shown that ALDH can identify cells with a greater resistance to chemotherapy [203, 204].

In this study, breast CSCs with high ALDH enzymatic activity were isolated from an IBC cell line, SUM149, using an ALDEFLOUR assay (Figure 4-1B; See Appendix I8 for details) [189]. SUM149 cells were stained for ALDH using the ALDEFLOUR reagent and sorted by flow cytometry. ALDEFLUOR treated cells quenched with the ALDH inhibitor diethylaminobenzaldehyde (DEAB) were used to set the ALDEFLUOR-positive FACS gate, containing less than 0.1% of DEAB-treated cells (Figure 4-1B). SUM149 cells above this 0.1% fluorescence threshold were sorted as ALDH-positive (ALDH+). ALDH negative (ALDH-) cells were sorted as the bottom percentage of cells that corresponded to the ALDH+ percentage (*i.e.* if 3.5% of cells were ALDH+, then the bottom 3.5% of cells were gated for the ALDH- population).

We performed comprehensive profiling to study functional phenotypes of ALDH+ IBC CSCs. First, the ratio of ALDH+ CSCs in the SUM149 cell line was quantified across multiple sortings to establish reliability (>20). The proportion of ALDH+ cells in the SUM149 cell line was between 1 - 7%, with an average of 3.93% ±

1.84%, similar to what has been reported previously [32]. Interestingly, the ALDH+ CSC population maintained a dynamic equilibrium in the SUM149 cell line. In a purified ALDH+ population, the percentage of ALDH+ cells gradually decreased from 100% to the normal level (3 - 5%) for SUM149 cells over 3-5 days, presumably by cell differentiation. Thus, the ALDH+ compartment was able to recapitulate the heterogeneity of the parent cell population by maintaining an almost constant percentage of ALDH+ CSCs, consistent with previously reported results [32, 205, 206].

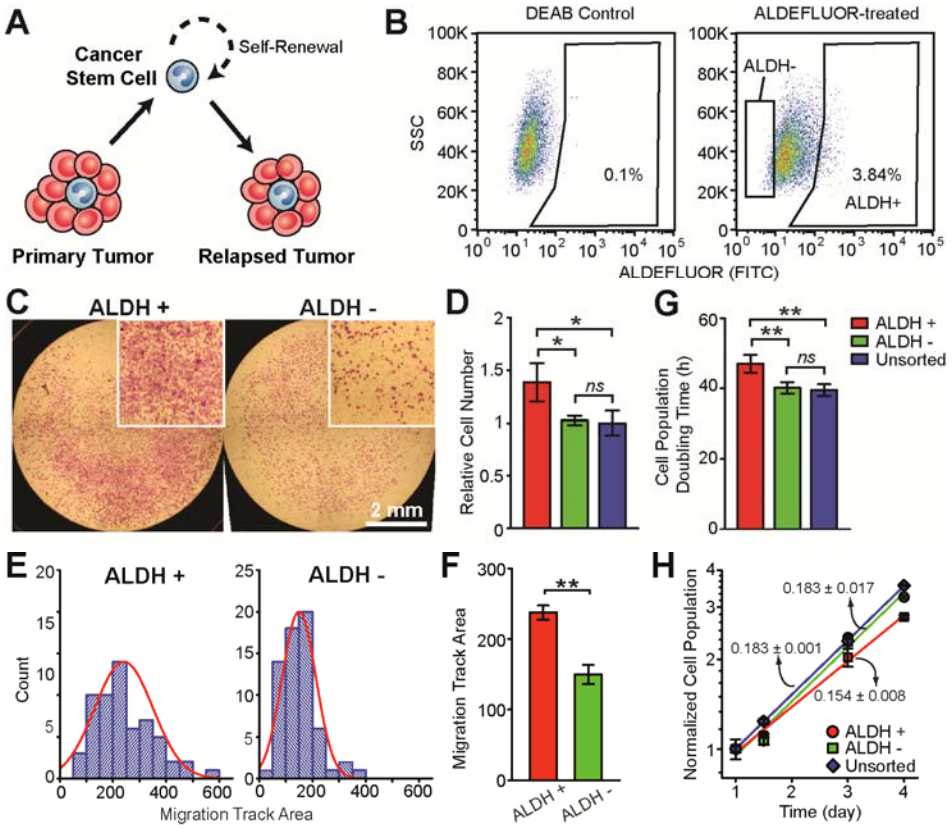

Figure 4-1 Functional phenotyping of IBC CSCs. (A) Concept of cancer stem cells. (B) Representative ALDEFLUOR analysis for SUM149 cells by FACS. Negative control samples (*left*) pre-treated with DEAB inhibitor were used to ensure identification of ALDH+ and ALDH- cells (*right*). (C&D) Representative images (C) and quantitative data (D) from *in vitro* invasion assays performed for ALDH+ and ALDH- SUM149 cells using the Biocoat Matrigel Invasion Chambers. In C, invading cells were fixed with formaldehyde before stained with 1% crystal violet. (E&F) Distribution (E) and average (F) migration track area for single ALDH+ and ALDH- SUM149 cells measured by the Cellomics Cell Motility kit. (G&H) Cell population doubling time (G) and normalized cell population as a function of culture time (H) determined using the MTT Cell Proliferation Assay Kit. For D, F, G, and H, error bars represent ± standard error of the mean (s.e.m.; $n = 4$). p-values were calculated using the student's t-test; *ns* ($p > 0.05$), * ($p < 0.05$), and ** ($p < 0.01$).

To study the tumorigenic and metastatic potential of ALDH+ IBC CSCs, *in vitro* invasion, migration, and proliferation assays were conducted. *In vitro* invasion assays were performed using the Biocoat Matrigel Invasion Chamber (See Appendix I9 for details) to examine the ability of cancer cells to invade through a Matrigel membrane under a serum gradient, mimicking the basement membrane invasion process in cancer metastasis. As shown in Figure 4-1C&D, ALDH+ IBC CSCs were more invasive compared to the ALDH- population and the unsorted SUM149 control.

To examine cell motility, the Cellomics Cell Motility kit was utilized to measure the migration area of ALDH+ and ALDH- cells (See Appendix I7 for details). Each sorted cell type (ALDH+ and ALDH-) was plated in equal densities in 3 -5 wells of a 96-well plate that had previously been coated with blue fluorescent microbeads. After 24 hr of incubation, the area a cell migrated is represented by the negative space in the microbead carpet that has been pushed away or phagocytosed by the cell. This cell motility assay demonstrated a significantly higher motility for ALDH+ than ALDH- cells (Figure 4-1E&F), suggesting a more aggressive and motile phenotype for ALDH+ IBC CSCs.

To evaluate the growth rates of ALDH+ and ALDH- cells, these populations were quantified and compared with unsorted SUM149 controls using MTT assays (See Appendix I10 for details). Cell populations of flow-sorted ALDH+ and ALDH- cells and unsorted SUM149 controls were measured at 24 hr, 36 hr, 72 hr, and 96 hr post sorting. As shown in Figure 4-1G&H, ALDH+ cells had a slower growth rate and significantly longer cell doubling time compared to ALDH- cells and unsorted control cells. This

slower growth rate for ALDH+ cells suggests that the IBC CSCs can maintain a semi-quiescent or slowly-cycling state, similar to the behavior of many adult stem cell types.

4.2.2 Cell Deformability Measurements

Our invasion assays demonstrated that ALDH+ cells had a greater capability to migrate through confined physical spaces, a process that necessitates significant cell shape and cytoskeleton changes. Thus, we hypothesized that there would be a concomitant difference in cell deformability between ALDH+ and ALDH- cells. Furthermore, at a key step in the metastatic cascade, cell deformability has been postulated to play a key role in invasion through the basement membrane [181, 182]. To explore potential differences in cell deformability between the ALDH+ IBC CSCs and ALDH- subpopulations, we utilized a microfluidics-based deformability microcytometer especially designed for highly-sensitive, high-throughput and label-free quantification of cell deformability at the single-cell level.

The microfluidic deformability microcytometer was made of PDMS and contained an array of identical funnel-shaped, long confining microchannels that served to automatically direct and trap individual live cancer cells within each channel (Figure 4-2A; See Appendix I11 for details). The microchannel walls were pre-coated with Pluronic-127, a hydrophilic non-ionic surfactant, so that friction between the cell and the channel wall would be negligible. Within the deformability microcytometer, differential hydrodynamic pressure acting on individual cancer cells gradually pushes the cell down the funnel and, ultimately, the motion of the cell stops and the cell is trapped due to confining space of the funnel-shaped channel. For inert microfluidic channels where cell

trapping is dictated by steric interactions between cancer cells and the channel wall, the penetration length (L) of an individual cancer cell into the channel is completely determined by its cell volume and cell deformability (Figure 4-2A&B). Thus, the cell deformability of each cancer cell can be calculated (See Appendix I11 for details) based upon known or measured parameters including pressure, cell volume, and the penetration length L (or the distance d between the position where the cell started to deform and the final trapped position in the channel).

We quantified the cell deformability of both ALDH+ and ALDH- SUM149 cells using the deformability microcytometer, with results showing that under the same differential hydrodynamic pressure across the confining microchannels, the average penetration length L of ALDH+ IBC CSCs was significantly greater than that of ALDH- cells, while the cell diameters of both populations were comparable (Figure 4-2C&D). This suggested a greater deformability of ALDH+ IBC CSCs than ALDH- cells. We further performed correlative studies using single cell data for cell deformability and cell diameter. Our analysis in Figure 4-2E showed no strong correlation between cell deformability and cell diameter for either ALDH+ or ALDH- cells, suggesting that cell deformability is an intrinsic biophysical property regardless of cell size. Interestingly, deformability of ALDH+ cells was distributed across a relatively higher range than ALDH- cells (Figure 4-2E&F), pointing to a potential inherent propensity and ability of ALDH+ IBC CSCs to more readily undergo the necessary cytoskeletal rearrangement to intravasate across the basement membrane during invasion. Together, our data show that the small population of IBC CSCs possesses a greater degree of cell deformability than normal breast cancer cells.

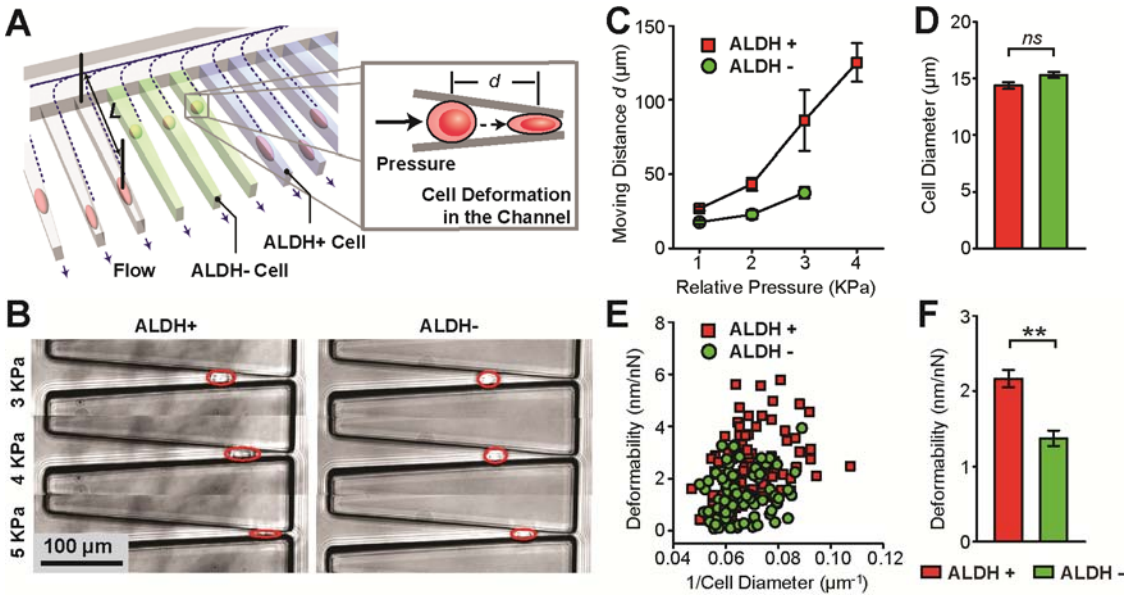

Figure 4-2 Cell deformability measurements for IBC CSCs. (A) Schematic of microfluidic deformability microcytometer for single cell deformability measurements. (B&C) Representative images (B) and quantitative data (C) showing differential penetrating distances for ALDH+ and ALDH- SUM149 cells in the deformability microcytometer under different pressures as indicated. (D) Average cell diameter of ALDH+ and ALDH- SUM149 cells. (E) Cell deformability plotted as a function of cell diameter. Each data point represents an individual cell. (F) Average cell deformability of ALDH+ and ALDH- SUM149 cells. For C, D, and F, error bars represent ± s.e.m ($n > 100$). *p*-values were calculated using the student *t*-test; *ns* ($p > 0.05$) and ** ($p < 0.01$).

4.2.3 Cell Adhesion Strength Characterization

We conducted adhesion assays for SUM149 breast cancer cells to evaluate their ability to make stable physical contact with surfaces (Figure 4-3A&B). Three groups of SUM149 cancer cells - sorted ALDH+ cells, ALDH- cells, and an unsorted control – were seeded at the same density as single cells in polystyrene 48-well cell culture plates. Three hours after cell seeding, floating cells were removed, and adherent cancer cells were stained with Calcein AM for visualization. Fluorescence images of stained cancer cells in the entire sample area were taken for quantification of the adhesion rate, defined as the ratio of the number of cells adhered to the surface to the total number of cells initially seeded per sample. Quantitative analysis revealed that ALDH+ cells had a much

lower adhesion rate compared to both the ALDH- population and unsorted control (Figure 4-3B). On average, the adhesion rate after 3 hr of cell seeding was 25.6% for ALDH+ cells, while for ALDH- cells and unsorted control cells the adhesion rates were 60.6% and 52.0%, respectively.

Our results in Figure 4-3A&B demonstrating a significant difference in the adhesion properties of ALDH+ and ALDH- cancer cells suggested the possibility that adhesion strength of cancer cells might similarly be correlated with ALDH expression as was cell deformability. To examine specifically the possibility of the IBC CSC compartment consisting of intrinsically less adherent cells, we developed a microfluidic cell adhesion assay for direct measurements of the adhesion strength of cancer cells (Figure 4-3C; see Appendix G for details). A low density of ALDH+ or ALDH- IBC cells was seeded uniformly inside the microfluidic channel for 12 hr before they were exposed to constant directional fluid shear (0.1 - 320 dyne cm^{-2}) for 3 min. We quantified the fraction of cancer cells remaining adherent in the microfluidic channel after exposure to this sustained 3-min directional fluid shear. Our data demonstrated that indeed, the ALDH+ IBC CSCs that adhered to the microfluidic channel were only capable of withstanding much lower fluidic shear stresses than the ALDH- cells (Figure 4-3D&E). The adhesion strength of cancer cells, defined as the fluidic shear stress at which 50% of cancer cells initially adherent on the microfluidic channel detach after exposed to shear, was significantly lower for ALDH+ IBC CSCs than ALDH- cells (Figure 4-3F). Together, our results in Figure 4-3 demonstrated that adhesive properties could be quantitatively delineated and correlated with the ALDH-defined IBC CSC

population in the SUM149 cell line. In summary, ALDH+ IBC cells had a decreased ability to adhere to a substrate and overall decreased adhesion strength.

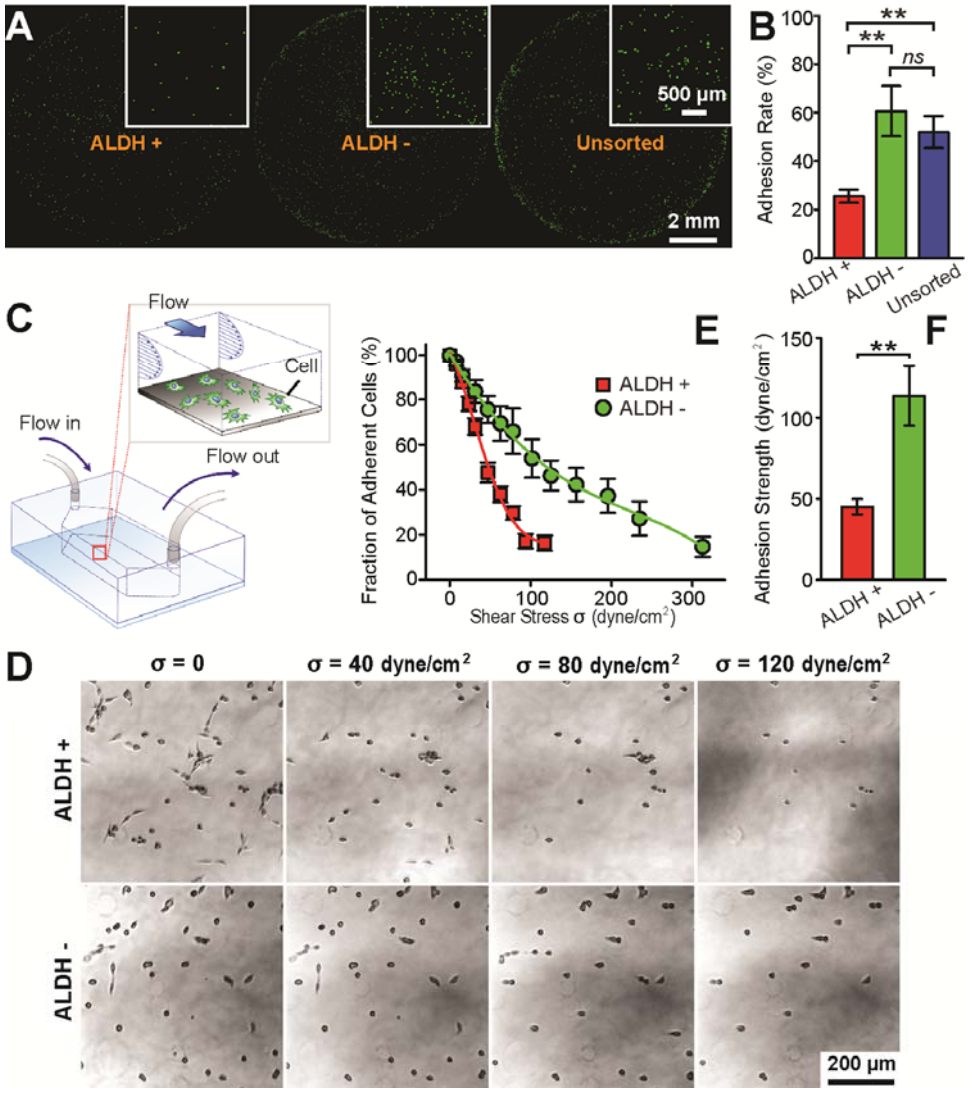

Figure 4-3 Cell adhesion strength characterization. (A&B) Representative fluorescence images (A) and quantified adhesion rate (B) of ALDH+, ALDH-, and unsorted SUM149 cells adhering to polystyrene 48-well cell culture plates 3 hr after cell seeding. Cells were stained with Calcein AM for visualization and enumeration. (C) Schematic of a microfluidic channel for quantification of cell adhesion strength. Insert shows adherent cancer cells in the channel under sustained directional fluid shear. (D) Representative brightfield images showing temporal sequences of ALDH+ and ALDH- SUM149 cells detaching from the microfluidic channel under increased fluid shear stress. (E) Fraction of ALDH+ and ALDH- SUM149 cells remaining adherent in the microfluidic channel after 3-min exposures to sustained directional fluid shear. Low densities of cancer cells were seeded into microfluidic channels and cultured for 12 hr before PBS was flowed continuously along the channel to exert fluid shear stress on cells. Solid lines represent logistic curve fitting. (F) Adhesion strength of ALDH+ and ALDH- SUM149 cells. For B, E, and F, error bars represent ± s.e.m. (n = 4). p-values were calculated using the student t-test; *ns* ($p > 0.05$) and ** ($p < 0.01$).

4.2.4 Cell Deformability

The difference seen in cell adhesion properties between ALDH+ IBC CSCs and ALDH- cells implicated an involvement of actin cytoskeleton (CSK) and integrin-mediated focal adhesions that tether the actin CSK to the extracellular matrix. To investigate this hypothesis, we utilized an array of PDMS microposts as subcellular live-cell force sensors to quantify intracellular CSK contractile forces (Figure 4-4; see Appendix H for details) [207-209]. This PDMS micropost array consists of hexagonally spaced, vertical, elastomeric posts fabricated using replica molding with PDMS from microfabricated silicon masters (Figure 4-4A). After adhesive proteins are coated on the post tips using microcontact printing, cells are able to adhere, spread out, and exert contractile forces that deflect the underlying posts (Figure 4-4A-D). Each post, therefore, functions as a cantilever and force sensor, capable of measuring local cellular traction force exerted at the post tip [207-209].

We performed quantitative analysis of cell morphology and CSK contractility of SUM149 cells with the PDMS micropost array (Figure 4-4E&F). Our results revealed that the total cell traction force was significantly less for ALDH+ cells compared to ALDH- ones Figure 4-4G). Previous studies have demonstrated that cell traction force generation can be confounded by a cell's footprint area [136, 186, 207]. To exclude the possibility that the decreased cell traction force for ALDH+ CSCs was simply caused by a variance in cellular area, we quantified cell spread area for SUM149 cells. Our results in Figure 4-4H showed no significant difference in cell spread area between ALDH+ and ALDH- cells. To further investigate the role of cell spread area in the generation of traction forces, we analyzed the total traction force of each cell normalized by its spread

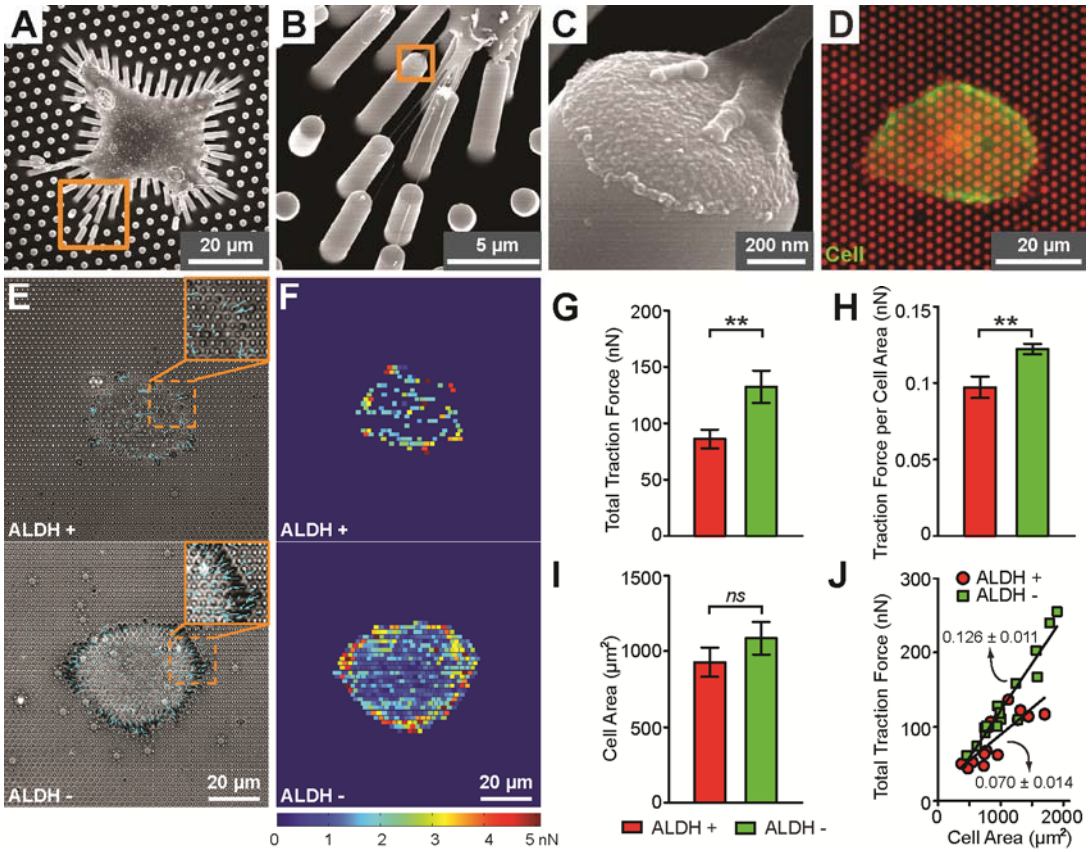

Figure 4-4 Quantification of cell traction force. (A-D) Representative SEM (A-C) and immunofluorescence (D) images showing single SUM149 cells adherent on the PDMS micropost array. In D, the single SUM149 cell was stained with fluorophore-labeled phalloidin for visualization of actin filaments (*green*). The underlying PDMS posts were labeled with DiI for visualization. (E&F) Phase (E) and colorimetric (F) maps showing subcellular traction forces exerted by single ALDH+ (*top*) and ALDH- (*bottom*) SUM 149 cells on the PDMS microposts. (G-J) Quantitative analysis of cell morphology and traction force. G-I plot total traction force per cell (G), total cell spread area (H), and traction force per cell area (I) for single ALDH+ and ALDH- cells. Data represents the means ± s.e.m ($n > 15$). *p*-values were calculated using the student *t*-test; *ns* ($p > 0.05$) and ** ($p < 0.01$). (J) Total traction force per cell as a function of cell spread area. Each data point represents an individual cell. Data trends in J are plotted using linear least square fitting (black lines), with slope values ± s.e.m indicated.

area (traction force per cell area), with results showing that the average traction force per cell area was lower for ALDH+ IBC CSCs compared to ALDH- SUM149 cells (Figure 4-4I). Hence, these results indicate that the smaller traction forces exerted by ALDH+ IBC CSCs *vs.* ALDH- cells are not linked to differences in cell spread area, but to other inherent cellular differences between the two populations. Consistent with previous reports though [136, 186, 207], within the same group of cells (ALDH+ or ALDH-) the

correlative plot (Figure 4-4J) of single-cell data of total traction force and cell spread area did show a strong linear correlation of increasing traction force with cell spread area. However, the slope of the linear correlation between the traction force and cell spread area was substantially less for ALDH+ cells than for ALDH- cells (0.13 nN μm^{-2} *vs.* 0.07 nN μm^{-2}), again indicating distinct biophysical properties of ALDH+ and ALDH- cells. Our traction force study in conjunction with the adhesion strength results indicate that ALDH+ and ALDH- cells have differential biophysical properties with the ALDH+ IBC CSCs being less adherent and exerting less contractile force. This may help explain the metastatic potential difference between the ALDH+ and ALDH- populations. Cells that are prone to forming strong connections with their surrounding ECM (ALDH- cells) may be less likely to successfully migrate away from the primary tumor [210].

4.3 Conclusion

CSCs as defined through specific marker expression methods, have been shown to initiate tumorigenesis, have the capacity to self-renew, and initiate cancer metastasis in many cancer types. Although identification of CSCs through marker expression helps separate and define the CSC compartment, it does not directly provide information on how or why this cancer cell subpopulation is more metastatic or tumorigenic. IBC is the most aggressive and lethal form of breast cancer with two-thirds of patients presenting with axillary lymph node involvement and up to one-third of patients having distant metastases at initial diagnosis [30, 31]. Why IBC is so much more aggressive and metastatic than other breast cancers though is not definitively known. Previous studies have identified ALDH+ IBCs as key mediators of tumorigenesis and metastasis, and they

are negatively correlated with survival [32]; however, the how and why have been left unstudied. In this study, we comprehensively profiled the functional as well as biophysical characteristics of IBC CSCs at the single-cell level using multiple microengineered tools and traditional *in vitro* studies to delineate the live cell phenotypic characteristics of the model of the most metastatic breast cancer subtype.

Characterizing the functional behaviors of IBC CSCs such as cell migration, growth, adhesion, invasion, self-renewal, and differentiation is a direct approach to describe and understand IBC CSCs based upon their intrinsic properties, thus paving the way to determine therapeutic approaches to this most lethal subpopulation within IBC. Distinct biophysical properties of IBC CSCs such as cell deformability, adhesion strength, and traction force provide physical insights into why IBC has an enhanced propensity to metastasize compared to other breast cancers. Such multiparametric cellular phenotypic profiling of CSCs can provide critical insight into the characteristics of these cells and their biomechanical adaptation for cancer metastasis, opening the door for the standardization of studies to potentially prognosticate the probability of metastatic growth and/or of therapies that target a tumor's unique biophysical signature associated with IBC CSCs.

Chapter 5

Nanotopography-mediated Mechanoseing of Human Embryonic Stem Cells

5.1 Introduction

Human embryonic stem cells (hESCs) have great potentials for future cell-based therapeutics. However, their mechanosensitivity to biophysical signals from the cellular microenvironment is not well characterized. In their physiological niche, stem cells are challenged by both soluble biochemical cues and insoluble physical stimuli from the microenvironment [211, 212]. At the frontier of cell-microenvironment interactions, cell-extracellular matrix (ECM) interfaces are composed of structural units of nanometer length scale, which thus enable the regulation of stem cell fates by extracellular nanotopographical cues along with other physical factors [213-216]. For example, *in vivo* ECM is enriched with hierarchical fibers/fibrils consisting of filamentous proteins such as collagen, elastin, fibronectin, vitronectin, and laminin, which present adhesive ligands on a structured landscape with spatially organization of characteristic dimensions from a few nanometers to hundreds of nanometers [217]. The helical surface

topographical periodicity of individual ECM (e.g., collagen I) fibrils is also an operative physical cue that could dictate stem cell differentiation [218]. In direct contact with the ECM, the cell membrane is also rich of adhesive molecules and protrusive structures with characteristic lengths of nanometers. For instance, integrins, the transmembrane receptors directly linking the ECM ligands to the intracellular adaptor proteins and actin cytoskeleton (CSK), are on the dimension of 20~50 nm [213, 219], and the nanoscale filopodia ("nanopodia") has also been shown in the cellular probing of extracellular fine nanotopographical features [220]. Therefore, the symphony between the extracellular nanotopographical cues and the nanoscale architecture of cell-ECM adhesions initiates unique mechanotransduction processes, resulting in the regulation of a multitude of cell behaviors, such as adhesion, morphology, proliferation, gene expression, self-renewal and differentiation [147, 216, 221-226].

Due to their potential roles as important regulators of stem cell fates in the niche, the extracellular nanotopography recently attracts much attention from bioengineers in an effort to leverage the stem cell mechanobiology and fate control using synthetic nanotopograhical biomaterials for future tissue engineering and regenerative medicine [217, 224]. Recent reports have shown that the nanoscale surface topography plays a critical role in regulating survival, proliferation and differentiation of various types of adult multipotent stem cells [227-231]. For example, human mesenchymal stem cells (hMSCs) cultured on nanoscale gratings on PDMS surfaces tend to align and elongate their actin cytoskeleton (CSK) and nuclei along the nanogratings [229]. Likewise, gene profiling and immunostaining of these hMSCs demonstrate a significant up-regulation of neuronal markers when cultured on the nanogratings, as compared to unpatterned flat

controls [229]. Recent published reports have also demonstrated that the nanoscale disorder in a nanopit array can stimulate osteogenesis of hMSCs in the absence of osteogenic supplements [228], while another study from the same group verifies that the perfectly ordered arrays of nanopits support long-term maintenance of hMSC phenotype and multipotency [231].

Only in the last few years has experimental evidence begun to emerge showing that pluripotent stem cells such as embryonic stem cells (ESCs) are sensitive to the cell-ECM physical interactions [232-238], including their intrinsic sensitivity to the nanoscale surface topography [237, 238]. These early findings have promoted significant interest from the developing fields of functional tissue engineering and regenerative medicine, as ESCs are able to replicate themselves (self-renewal) while retaining their ability to give rise to any type of specialized cell in the adult body (pluripotency) [239-241] and as such, hESCs are a promising cell source for disease modeling [242, 243], drug screenings [244-246] and future cell-based therapeutics to treat degenerative human diseases such as diabetes mellitus and trauma such as spinal cord injury [247-250].

To date, the existing work on regulation of ESC behaviors using nanotopography has focused on their neurogenic differentiation with regularly arranged nanoscale surface structures. For example, it has been shown that the electrospun fibrous scaffolds can not only enhance differentiation of mouse ESCs (mESCs) into specific neural lineages, but also promote and guide the neurite outgrowth [237]. More recently, nanoscale ridge/groove pattern arrays generated on polyurethane acrylate (PUA) surfaces are shown to induce morphological changes and differentiation of hESCs into a neuronal lineage without treatment with differentiation-inducing biochemical agents [238].

However, all the aforementioned work on nanotopography for stem cells has largely relied on complex and expensive nanofabrication techniques, such as electron beam and nanoimprint lithography, to generate nanoscale surface structures to regulate cell-ECM interactions. Further, it is still largely unknown to what extent such synthetic regular nanoscale structures can mimic the intrinsic random nanoscale topology associated with the *in vivo* cellular microenvironment. Using our RIE-generated nanorough glass surfaces, we explored the nanoscale surface roughness as a potent physical signal in the cellular microenvironment to regulate a diverse array of hESC behaviors, including their morphology, cell adhesion, self-renewal, and fate [135]. As an example of the regulation effect of the nanotopography cue on hESCs, we demonstrated using the nanorough glass surfaces for promoting motor neuron differention. In order to bring current mechanistic understanding of stem cell mechanobiology into the context of nanotopography-regulated fate control, a few important mechanosensing and mechanotransduction mechanisms are discussed that have been implicated in the cellular responsiveness to extracellular nanotopography. Finally, we will also discuss some speculations regarding how these mechanotransduction events converge with classical signal transduction pathways to control stem cell fates.

5.2 Nanotopological Sensing of hESCs

5.2.1 Functional Responses of hESC to the Nanotopographic Cue

Using the nanorough glass substrates described above, we first examined functional responses of hESCs to different levels of nanoroughness, including their

morphology, adhesion, proliferation and clonal expansion, and differentiation. Here, all glass substrates were pre-coated with vitronectin (5 µg/mL) by adsorption to support long-term self-renewal of hESCs as reported by others [251]. Using AFM, we confirmed that the RMS roughness R_q of the smooth and nanorough glass surfaces did not significantly change before and after vitronectin coating (Figure 5-1A&B). To further confirm that the density of the adsorbed vitronectin on the glass surfaces was independent of the nanoroughness R_q of the glass surface, control assays were performed. Using fluorophore-labeled proteins, no apparent difference in fluorescence intensity was observed between glass surfaces of different nanoroughness R_q, indicating constant protein densities on the glass surfaces (Figure 5-1C&D).

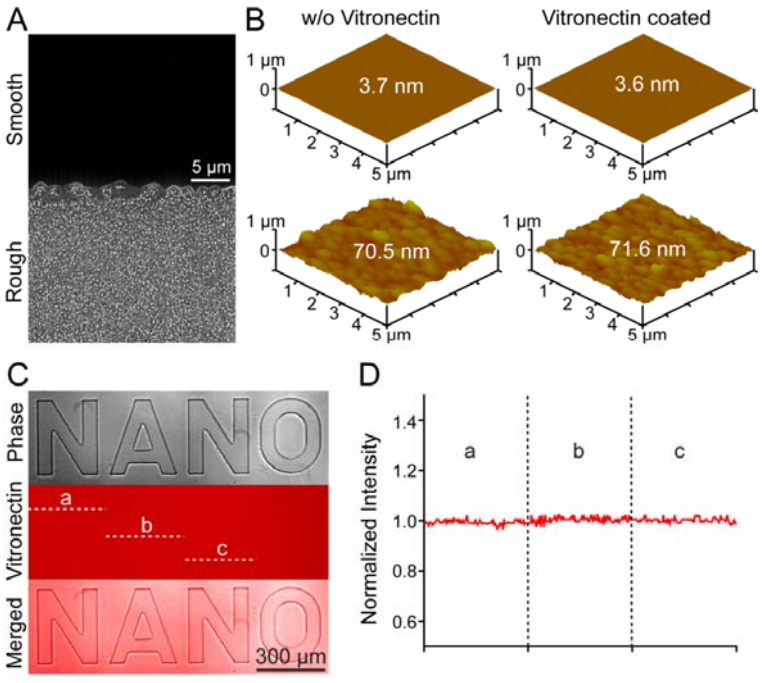

Figure 5-1 Surface analysis of the nanorough glass. (A) Top-view SEM image showing a patterned glass surface with smooth (top) and nanorough (bottom) regions on the same substrate as indicated. (B) AFM topographs of the smooth and nanorough regions of the glass substrate shown in A with (right) or without (left) vitronectin coating. The values of the RMS roughness R_q were indicated on the topographs. (C) Phase-contrast (top), immunofluorescence (middle), and merged (bottom) images of a glass surface patterned with nanorough letters (NANO). The patterned glass surface was coated uniformed with vitronectin (5 µg/mL). A fluorescence conjugated antibody was used for visualization of vitronectin. (D) Normalized fluorescence intensity along the three dashed lines (a-c) shown in C.

First, hESCs demonstrated significant adhesion selectivity between different levels of nanoroughness on the glass surfaces. For example, after 48 hr of culture on a glass surface patterned with square-shaped, smooth islands surrounded by nanorough surfaces, hESCs selectively adhered to, and aggregated on, the smooth islands where R_q = 1 nm, but not on the nanorough areas where R_q = 70 nm (Figure 5-2A). During this selective adhesion and aggregation process, hESCs retained their stemness, as evidenced by their positive expression of *Oct*3/4 (*Oct*3/4+), a transcription factor and a hallmark of undifferentiated hESCs (Figure 5-2A). Interestingly, spontaneously differentiated hESCs, which would loose their expression of *Oct*3/4 (*Oct*3/4-), did not show any adhesion preference to either the smooth or nanorough surfaces, and *Oct*3/4- hESCs would randomly distribute on the patterned glass substrate (Figure 5-2B).

We quantified the cell adhesion rate, defined as the ratio of number of cells adhered to the glass surface to the total number of cells initially seeded, of single *Oct*3/4+ hESCs plated on glass substrates with different values of R_q. Our results showed that 24 hr after cell seeding, *Oct*3/4+ hESCs at the single cell level had a strong tendency to adhere to smooth glass surfaces with smaller R_q (Figure 5-2C). In contrast, *Oct*3/4+ hESCs adhered less to surfaces with an increasing R_q. Both phenomena were consistent regardless of treatment with or without Y27632, a Rho-Associated Coil Kinase (ROCK) inhibitor used to enhance survival of single fully-dissociated hESCs (Figure 5-2C).

The effect of topological sensing of hESCs on their self-renewal and stemness maintenance was also investigated. In the experiments, *Oct*3/4+ hESCs were seeded at a low density (5×10^3 cells/cm^2) on both smooth (R_q = 1 nm) and nanorough (R_q = 150 nm) glass surfaces and cultured for 7 d. Subsequently, cells were fixed and stained with 4',6-

diamidino-2-phenylindole (DAPI) to identify nuclei and fluorescent-labeled antibodies for *Oct*3/4 (Figure 5-2F). Quantification of *Oct*3/4+ hESCs as a function of R_q showed a higher percentage of *Oct*3/4+ cells (93.6%) on the smooth glass surface (R_q = 1 nm) as compared to cells seeded on nanorough surfaces (41% and 36.6% for R_q = 70 nm and 150 nm, respectively; Figure 5-2D). Thus, our results indicated that the smooth glass surface was conductive for self-renewal and maintenance of hESC stemness in long-term culture, while the nanorough glass surfaces resulted in a large portion of hESCs undergoing spontaneous differentiation thus loosing their pluripotency (Figure 5-2D&F).

To investigate the extent to which nanoscale topological cues could affect proliferation of hESCs, small clusters of undifferentiated hESCs were seeded on glass substrates with different values of R_q (1, 70 and 150 nm). Phase-contrast microscopic images of hESC colonies were taken 1, 2, and 3 days after cell seeding for these different glass substrates. The colony sizes were analyzed using these colony images with the image analysis software ImageJ to calculate the cell population doubling time. hESCs proliferated more rapidly with a shortened cell population doubling time of 41 hr on the smooth glass surface (R_q = 1 nm) as compared to cells on the RIE-generated nanorough surfaces, on which the cell population doubling time was 71 hr for R_q = 70 nm and 77 hr for R_q = 150 nm (Figure 5-2E&G). Together, these results confirmed that the nanotopological cue on the RIE-generated glass surface to which hESCs adhered could provide a potent regulatory signal that affects a diverse array of hESC behaviors including cell morphology, adhesion, proliferation and self-renewal.

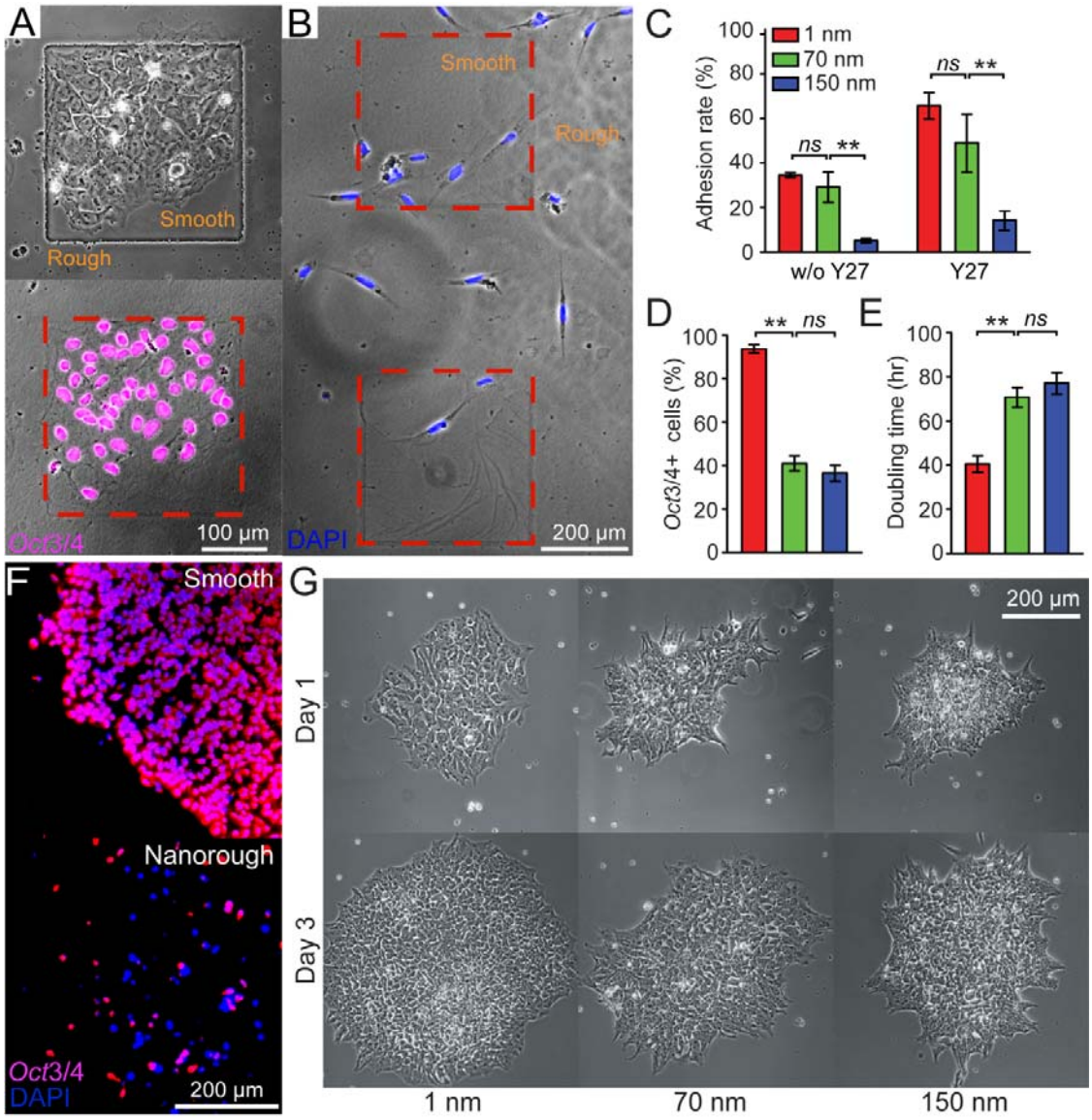

Figure 5-2 Functional responses of hESCs to the nanoroughness on glass. (A) Representative phase-contrast (top) and merged (bottom) microscopic images showing *Oct*3/4+ hESCs selectively attached and aggregated on the smooth region (R_q = 1 nm) of a patterned nanorough glass substrate. (B) Representative merged microscopic image showing *Oct*3/4- hESCs randomly distributed on a patterned nanorough glass surface without showing a preference for either smooth or nanorough areas. For A & B, the nanorough regions of the glass substrate had a RMS R_q of 70 nm. Cells were cultured 48 hr after initial cell seeding and co-stained with DAPI for nuclei (*blue*) and *Oct*3/4 (*red*). (C) Adhesion rate of single hESCs after 24 hr of culture on glass substrates with different levels of nanoroughness. Cells were treated with or without Y27632 (Y27) as indicated. Error bars represent ± standard error of the mean (s.e.m, n = 3). (D) Percentage of *Oct*3/4+ hESCs on the glass substrates with different levels of nanoroughness as indicated, after culture for 7 days. Error bars represent ± s.e.m (n = 3). (E) Doubling time of hESCs on the glass substrates with different levels of nanoroughness as indicated. Error bars represent ± s.e.m (n = 20). For C-E, *ns* ($P > 0.05$) and ** ($P < 0.01$) (Student's t-test). (F) Representative immunofluorescence images of hESCs cultured for 7 days on both the smooth (R_q = 1 nm; top) and nanorough (R_q = 150 nm; bottom) glass substrates. The cells were co-stained for *Oct*3/4 (*red*) and nuclei (DAPI; *blue*). (G) Representative phase-contrast microscopic images of hESC colonies on smooth (R_q = 1 nm; left) and nanorough (R_q = 70 and 150 nm; middle and right) glass substrates after culture of 1 day (top) and 3 days (bottom).

5.2.2 Topological Sensing by FAs, CSK Structure, and Cell-cell Contacts

The molecular mechanism for topological sensing by adherent cells remains largely undetermined, yet existing evidence from different cell types has suggested the involvement of integrin-mediated focal adhesion (FA) signaling [252]. Integrins mediate cell adhesion to the ECM and contribute to cell-matrix signaling by activating intracellular tyrosine kinase and phosphatase signaling to elicit downstream biochemical signals important for regulation of gene expression and stem cell fate. Importantly, integrin-mediated FA signaling is closely related to its molecular arrangement and dynamic organization, which can be affected directly by local nanotopological cues [252].

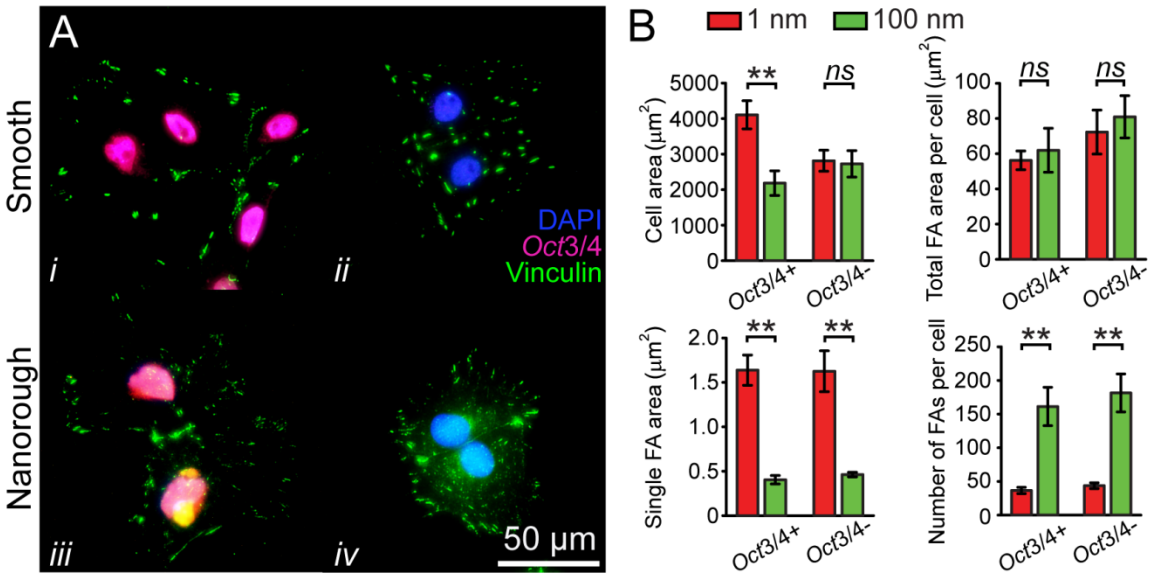

Figure 5-3 Foacal adheiosn analysis of hESCs to nanoroughness. (A) Representative immunofluorescence images of *Oct*3/4+ (*i* & *iii*) and *Oct*3/4- (*ii* & *iv*) hESCs on smooth (R_q = 1 nm) and nanorough (R_q = 100 nm) glass substrates after 48 hr of culture. Cells were co-stained for nuclei (DAPI; *blue*), *Oct*3/4 (*red*), and vinculin (*green*). (B) Bar graphs showing quantitative results of cell spread area (top left), total FA area per cell (top right), average single FA area (bottom left), and number of FAs per cell (bottom right) for *Oct*3/4+ and *Oct*3/4- hESCs cultured on glass substrates with different levels of nanoroughness as indicated. Error bars represent ± s.e.m (n = 50). *ns* ($P > 0.05$), ** ($P < 0.01$); Student's t-test.

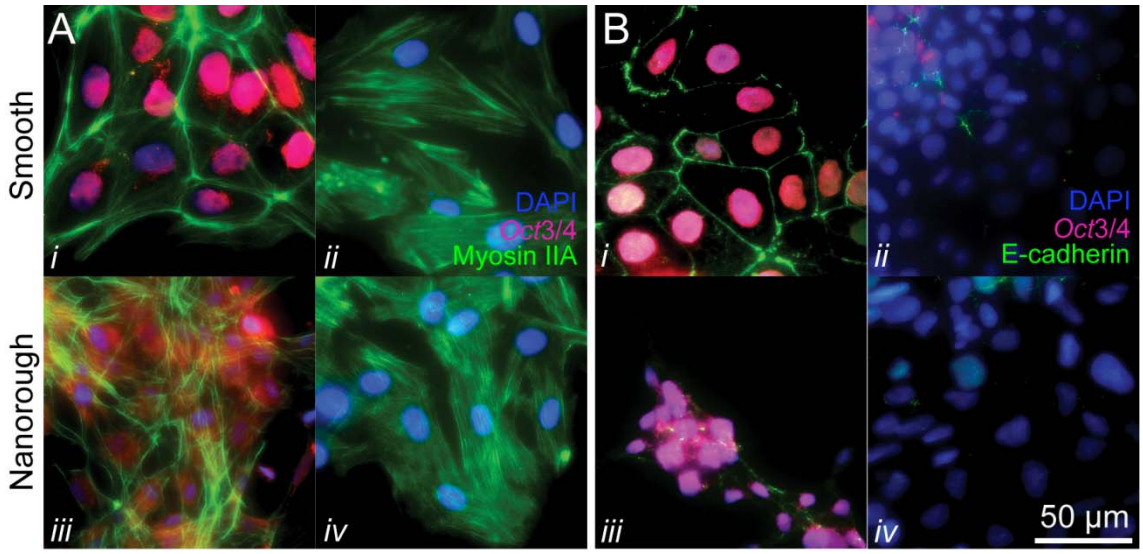

Figure 5-4 Nanotopography reugulates hESC myosin IIA and E-cadherin. Representative immunofluorescence images of *Oct*3/4+ (*i* & *iii*) and *Oct*3/4- (*ii* & *iv*) hESCs on smooth (R_q = 1 nm) or nanorough (R_q = 100 nm) glass surfaces after culture of 48 hr. The cells were co-stained for nuclei (DAPI; *blue*), *Oct*3/4 (*red*), and myosin IIA (A; *green*) or E-cadherin (B; *green*).

To investigate the likely involvement of integrin-mediated FA formation in regulating topological sensing of hESCs, we examined FA formation of single hESCs plated on nanorough glass surfaces. After 48 hr of culture, single hESCs exhibited distinct FA formations and organizations on the smooth and nanorough glass surfaces, as characterized by immunofluorescence staining of vinculin, a FA protein. On smooth glass surfaces, where R_q = 1 nm, vinculin-containing FAs formed primarily on the periphery of undifferentiated hESCs (*Oct*3/4+) but distributed randomly throughout the whole cell spread area of differentiated cells (*Oct*3/4-) (Figure 5-3A). However, on the nanorough surface where R_q = 100 nm, both *Oct*3/4+ and *Oct*3/4- hESCs exhibited randomly distributed, punctate FAs of small areas throughout the entire cell spread area (Figure 5-3A). Morphometric analysis of cell populations suggested that on the smooth glass surface, *Oct*3/4- hESCs had a smaller mean cell spread area than *Oct*3/4+ hESCs, and the nanorough surface resulted in both *Oct*3/4+ and *Oct*3/4- hESCs having a small

mean cell spread area comparable to *Oct*3/4- hESCs on the smooth glass surface. Furthermore, our results indicated that both *Oct*3/4+ and *Oct*3/4- hESCs on the nanorough surface formed FAs of smaller areas but with a greater density as compared with the cells on the smooth surface (Figure 5-3B). Collectively, our results indicated that the nanotopography significantly affected the molecular arrangement, formation and distribution of FAs in hESCs (Figure 5-3).

Previous studies have suggested that non-muscle myosin IIA (NMMIIA)-dependent CSK contractility is a key mediator of the mechano-sensing and -transduction processes in different types of stem cells [233, 253-255]. For hESCs, recent studies show that the NMMIIA-mediated CSK contractility plays a critical role in regulating hESC survival and cloning efficiency by controlling E-cadherin-mediated intercellular adhesion of hESCs [255-258]. Thus, we hypothesized that a feedback regulation and mechanical-biochemical integration involving FA, NMMIIA, and E-cadherin might be engaged in topological sensing of hESCs by their cross-regulation of intercellular adhesion and cell-ECM interactions (Figure 5-3 & Figure 5-4).

To examine this possibility, we examined NMMIIA (Figure 5-4A) and E-cadherin (Figure 5-4B) expressions in hESCs plated on both the smooth (R_q = 1 nm) and nanorough (R_q = 100 nm) glass substrates after 48 hr of culture, by co-staining the cells with *Oct*3/4 and DAPI. Subcellular organizations of NMMIIA and E-cadherin were distinct between *Oct*3/4+ and *Oct*3/4- hESCs on the smooth surface, where *Oct*3/4+ hESCs demonstrated strong expressions of NMMIIA and E-cadherin concentrating and co-localizing on the cell-cell contacts, while *Oct*3/4- cells displayed a random distribution of NMMIIA throughout the whole cell spread area and a low expression level for E-

cadherin. Interestingly, regardless of the *Oct*3/4 expression levels, hESCs adhered to the nanorough surface demonstrated a random distribution of NMMIIA throughout the entire cells and a weak expression of E-cadherin, similar to *Oct*3/4- hESCs adhered on the smooth surface, suggesting that topological sensing and functional regulation by hESCs might involve the functional interplay between the mechanosensory components of FA, NMMIIA, and E-cadherin.

We further performed western blot analysis of full-length E-cadherin, vinculin, NMMIIA, focal adhesion kinase (FAK; a kinase involved in regulating FA signaling), *Oct*3/4, and *β*-actin (as a housekeeping control protein) in *Oct*3/4+ hESCs plated on smooth (R_q = 1 nm) and nanorough (R_q = 100 nm) glass substrates after 24 hr and 48 hr of culture. Our result suggested that for both time points, the total amount of vinculin, NMMIIA, and FAK did not change between cells plated on smooth and nanorough surfaces (Figure 5-5). However, expression of E-cadherin was clearly down-regulated for hESCs plated on the nanorough surfaces as compared to cells on the smooth substrates, consistent with the immunostaining results shown in Figure 5-4. Combining together the results in Figure 5-3 and Figure 5-5, it appeared that nanotopography might regulate hESC behaviors through its direct effect on the local molecular arrangement and formation of FAs that might in turn regulate the spatial organization of NMMIIA-mediated CSK contractility and thus the E-cadherin-mediated intercellular adhesion of hESCs, even though the total expression levels of FA proteins such as vinculin and NMMIIA might not be significantly affected by nanotopography. It was highly likely that E-cadherin-mediated cell-cell contacts of hESCs might serve as the downstream

mediator to convert the nanotopographic signal through FAs and CSK contractility to regulate downstream gene expression and fate decisions of hESCs (Figure 5-6).

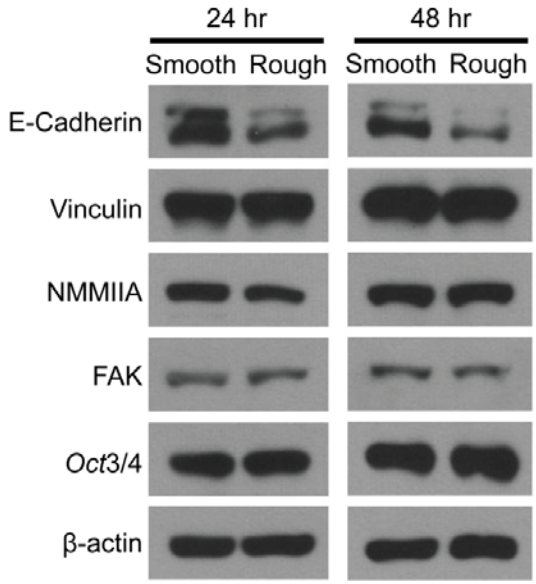

Figure 5-5 Western blot analysis of full-length E-cadherin, vinculin, NMMIIA, focal adhesion kinase (FAK), *Oct*3/4, and *β*-actin in *Oct*3/4+ hESCs plated on smooth (R_q = 1 nm) and nanorough (R_q = 100 nm) glass substrates after 24 hr (left) and 48 hr (right) of culture.

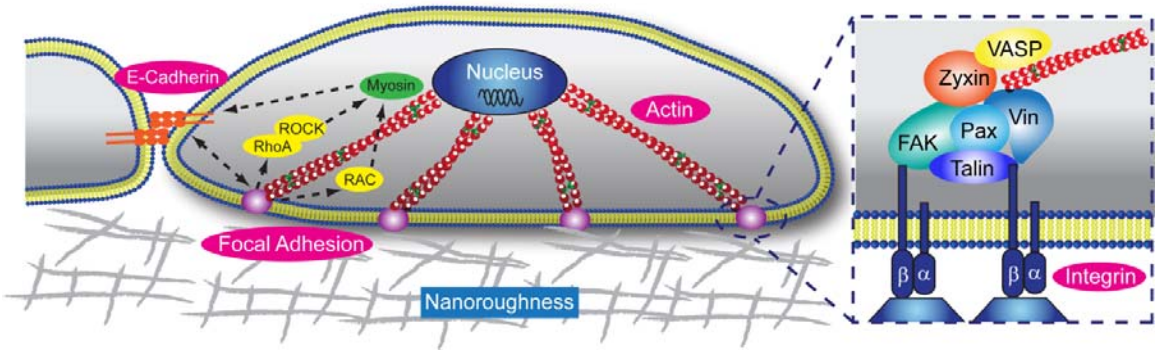

Figure 5-6 Schematic showing a feedback regulation and mechanical-biochemical integration involving FA, NMMIIA, and E-cadherin engaged in the topological sensing of hESCs by their cross-regulation of intercellular adhesion and cell-ECM interactions. Focal adhesion kinase (FAK), talin, paxillin (Pax), vinculin, zyxin, and vasodilator-stimulated phosphoprotein (VASP) are mechanosensitive proteins contained in the FA plague.

5.2.3 Nanotopographic Cue for Cell Separation

As discussed in the last section, hESCs showed higher adheiosn preference to the smooth surfaces. Contrariously, NIH/3T3 fibroblasts attached preferentially to the patterned nanorough islands and spread to conform to the different geometries of the nanorough islands (Figure 5-7A-C). The adhesion selectivity of NIH/3T3 fibroblasts to the patterned nanorough islands was about 91% (Figure 5-7B), suggesting the patterned nanoroughness could serve as an effective means to control the adhesion location and cell shape or spread area of NIH/3T3 cells. In addition, when a high density of single NIH/3T3 fibroblasts were seeded on a glass surface patterned with large nanorough islands, the cells attached and aggregated to the patterned nanorough islands to form cell colonies that conformed to the different geometries of the nanorough islands (Figure 5-7D). Thus, the adhesion response of NIH/3T3 fibroblasts to nanotopography was completely contrary to that of hESCs (Figure 5-2), indicating cell-type specificities in cellular responses to nanotopography. The cell-type specific preference to adhere to either smooth or nanorough surfaces provided an opportunity to spatially separate different cell types for cell co-culture applications. To explore this prospect, a mixture of hESCs and NIH/3T3 fibroblasts were cultured on a patterned nanorough glass substrate containing an array of nanorough strips separated by smooth regions. The cell adhesion and separation on the patterned surface after co-culturing the cells for 48 hr was examined, showing that hESCs and NIH/3T3 fibroblasts selectively attached and autonomously segregated to the smooth and nanorough regions, respectively (Figure 5-7E). Quantitative analysis suggested a superior cell segregation efficiency for hESCs and NIH/3T3 cells using the patterned nanorough surfaces, as 87% of the cells adhered

on the smooth regions of the glass surface were hESCs, while on the nanorough regions 97% of cells were NIH/3T3 fibroblasts (Figure 5-7F).

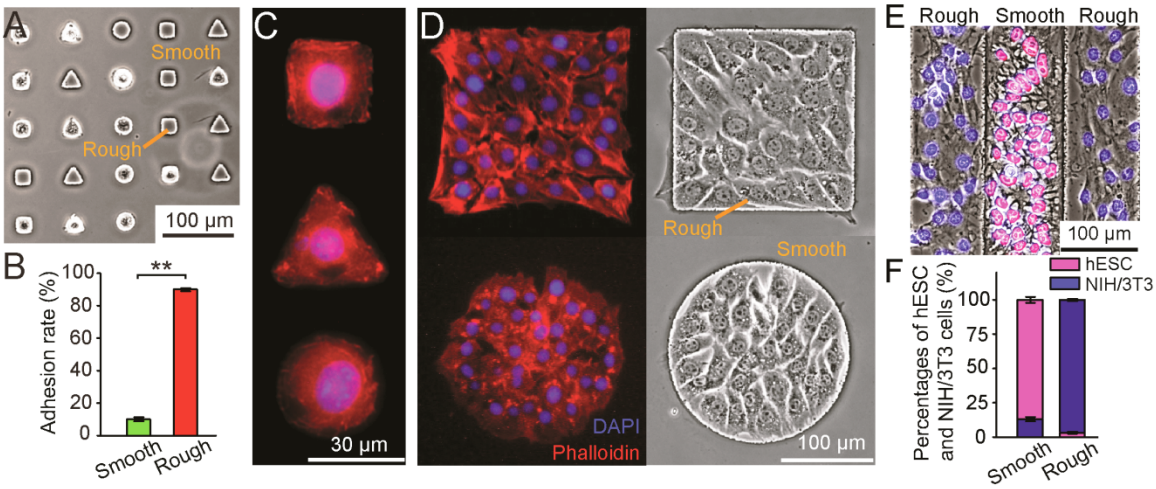

Figure 5-7 Study of nanotopographic cue for cell separation. (A) Phase-contrast microscopic image of single NIH/3T3 fibroblasts adhered on patterned nanorough islands (R_q = 70 nm) on a glass substrate 4 hr after initial cell seeding. (B) Bar graph showing the cell adhesion rate of single NIH/3T3 fibroblasts on the smooth surface (R_q = 1 nm) and the patterned nanorough islands (R_q = 70 nm) of a glass substrate. Error bars represent ± s.e.m. (n = 30). ** (P < 0.01); Student's t-test. (C) Immunofluorescence image showing single NIH/3T3 fibroblasts attaching and conforming to nanorough islands (R_q = 70 nm) of different geometries on the glass surface. The cells were fixed and stained 4 hr after initial cell seeding. (D) Immunofluorescence (left) and phase-contrast (right) microscopic images of clusters of NIH/3T3 fibroblasts selectively attaching and conforming to nanorough islands (R_q = 70 nm) of different geometries on the glass surface. The images were taken 24 hr after initial cell seeding. For C & D, cells were co-stained with DAPI (*blue*) and phalloidin (*red*) for visualization of nuclei and actin microfilaments, respectively. (E) Merged microscopic image showing co-cultured *Oct*3/4+ hESCs and NIH/3T3 fibroblasts spatially self-segregating on a patterned nanorough glass surface after 48 hr of culture. Cells were fixed and stained for nuclei (DAPI, *blue*) and *Oct*3/4 (*red*). The smooth and nanorough regions on the glass surface had RMS R_q of 1 nm and 70 nm, respectively. (F) Bar graph showing percentages of hESCs and NIH/3T3 fibroblasts located on the smooth (R_q = 1 nm) and nanorough (R_q = 70 nm) regions of the patterned nanorough glass substrate after culture of 48 hr. Error bars represent ± s.e.m (n = 3).

5.3 Nanotopography-mediated Neuron Differention of hESCs

Human pluripotent stem cells (hPSCs) including hESCs and induced pluripotent stem cells (hiPSCs) are a promising source of differentiated cells for developmental studies, cell transplantation, disease modeling, and drug testing. However, their widespread use even for intensely studied cell types like spinal motor neurons (MNs) is hindered by poorly defined culture conditions, protracted differentiation and low yield

and purity of existing protocols for *in vitro* differentiation. Current hPSC-based MN differentiation protocols also rely extensively on soluble morphogens such as sonic hedgehog (SHH) and retinoic acid (RA) acting as ventralization and caudalization factors to direct MN differentiation. Given that during development of human embryonic brain, extensive cellular morphogenesis occurs with embryonic cells experiencing dynamic modulations of extracellular physical signals, it is likely that insoluble physical signals such as nanotopograhy, which has been overlooked in existing stem cell reseearch, may be important for differentiation and functional maturation of neural subtypes from hESCs.

In this work, we sought to investigate if the intrinsic mechanosensitive properties of hESCs to nanotopography could be leveraged to improve derivation of functional spinal MNs. Using the RIE-generated nanorough glass surfacces, we first examined whether substrate nanoroughness could influence neural induction of hESCs. Single undifferentiated hESCs were seeded in growth media at a high density (20,000 cells cm-2) on glass surfaces with varied surface roughness (Rq = 1, 100 and 200 nm) and being pre-coated with vitronectin that is supportive for hESC self-renewal [251]. After 24 hr, hESCs were switched from growth media to neural induction media containing dual Smad inhibitors, SB 431542 (SB, a TGF-β inhibitor) and LDN 193189 (LDN, a BMP4 inhibitor), and allowed to differentiate for a total of 8 d (Figure 5-8A). Combined treatments with dual Smad inhibitors can greatly increase efficiency of neural induction of hESCs [259]. Neural induction was monitored by expression of Pax6, an early marker of neuroectodermal differentiation. On nanorough surfaces, Pax6+ neuroepithelial cells (NEs) appeared as early as day 2, and the percentage of NEs rose quickly and reached

94.5% by day 8 (Figure 5-8 & Figure 5-9). In distinct comparison, on smooth glasses Pax6+ NEs started to appear only at day 4 and constituted only 32.2% of total cells at day 8 (Figure 5-8 & Figure 5-9). At the same time, we also observed the stem cell pluripotency marker Oct3/4 was downregulated significantly more on the nanorough surfaces at the early stage of the neural induction than that on the smooth ones (Figure 5-8D & Figure 5-9A). We further analyzed temporal expressions of pluripotency (OCT4

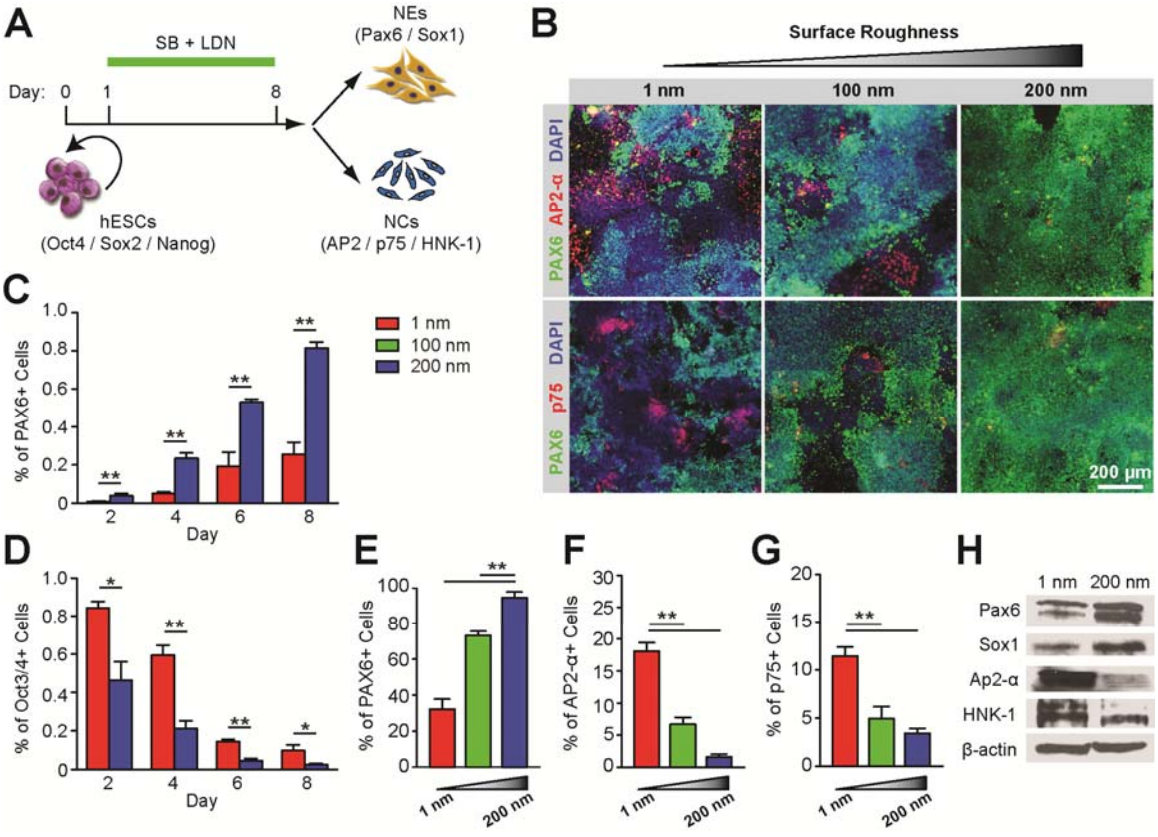

Figure 5-8 Nanorough substrates promoted neuroepithelial conversion while inhibiting neural crest differentiation of hESCs in a BMP4 dependent manner. (a) Schematic diagram showing experimental design of neural induction of hESCs. hESCs were cultured for 8 d in neural induction media containing dual Smad inhibitors, SB 431542 (SB, 10 μM) and LDN 193189 (LDN, 100 nM). (b) Representative immunofluorescence images showing Pax6+ NEs and NCs (AP2+ or p75+) derived from hESCs after 8 d of culture on glass surfaces with different surface roughness (R_q = 1, 100, 200 nm). (c-d) Bar graphs showing percentage of Pax6+ NEs (c) and Oct3/4+ hESCs (d) on smooth (R_q = 1 nm) and nanorough (R_q = 200 nm) glass surfaces at day 2, 4, 6, and 8. (e-g) Bar plots showing percentages of $Pax6^+$ NEs (e), AP+ NCs (f) and p75+ NCs (g) derived from hESCs at day 8 as a function of surface roughness. (h) Western blotting showing expression levels of Pax6, Sox1, Ap2-α and HNK-1 for hESCs cultured for 8 d on smooth (R_q = 1 nm) and nanorough (R_q = 200 nm) glass surfaces. Data represents means ± s.e.m with n = 3. P-values were calculated using Student's t-test. *, $P < 0.05$; **, $P < 0.01$.

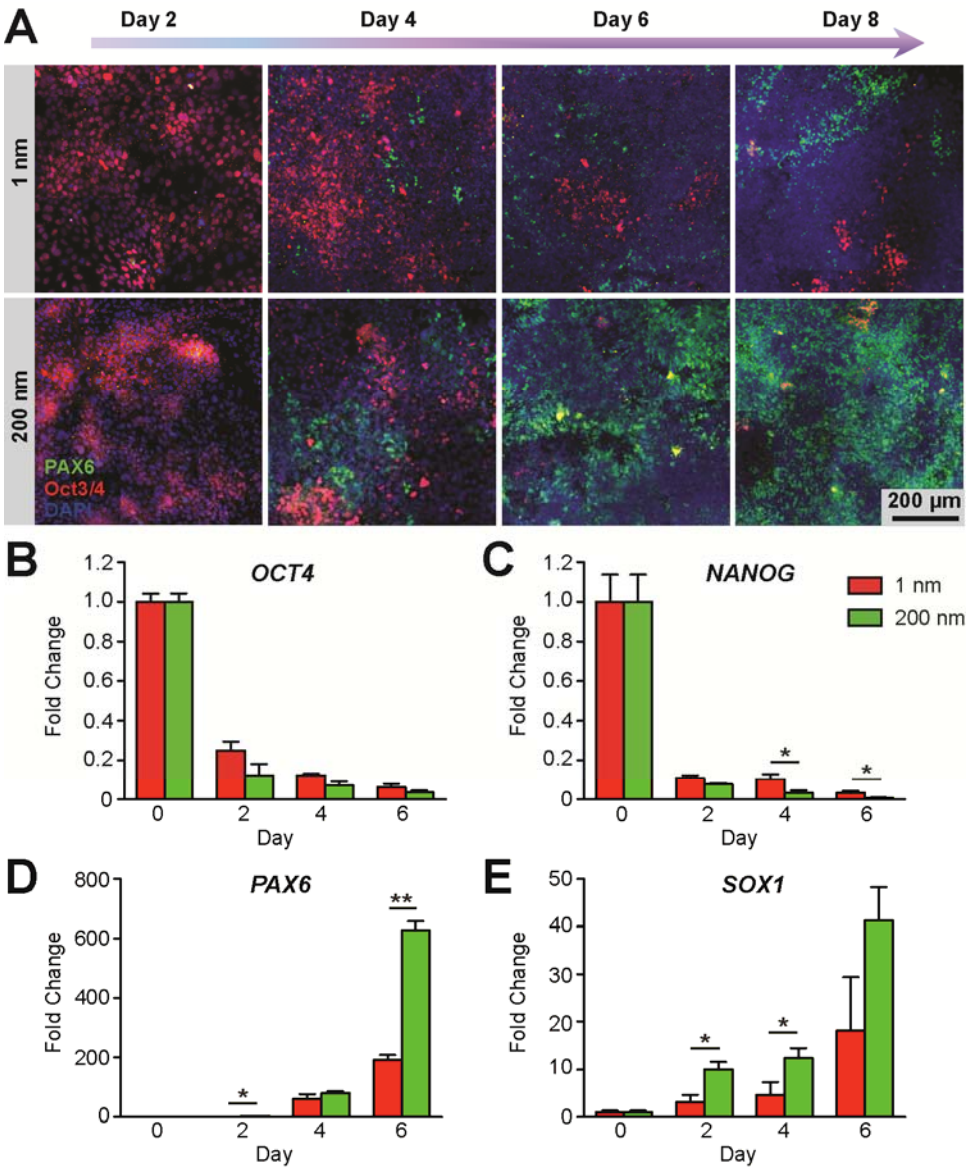

Figure 5-9 Temporal expressions of pluripotency and neuroectodermal markers during neural induction of hESCs. (a) Representative immunofluorescence images showing $Pax6^{+}$ NE cells derived from hESCs cultured in neural induction media at day 2, 4, 6 and 8 on smooth (R_q = 1 nm) and nanorough (R_q = 200 nm) glass surfaces. (b-e) RT-qPCR for temporal expressions of pluripotency (*OCT4* and *NANOG*; b&c) and neuroectodermal (*PAX6* and *SOX1*; d&e) markers during neural induction of hESCs. hESCs were cultured in neural induction media on smooth (R_q = 1 nm) and nanorough (R_q = 200 nm) glass surfaces. *NANOG, a* gene associated with pluripotency, decreased more significantly since day 4 on nanorough as compared to smooth ones. Genes associated with neural lineages, including *PAX6* and *SOX1*, both showed greater levels of expression on nanorough surfaces since day 2 when compared to those from smooth surfaces. The earliest neural markers expressed in our culture system were *SOX1*, preceding induction of *PAX6*, consistent with previous studies using dual Smad inhibitors. Expression level of each gene was normalized to data from undifferentiated hESCs. Data represents means ± s.e.m with at least three biological replicates and three technical replicates. *P*-values were calculated using two-side unpaired student *t*-test. *, $P < 0.05$; **, $P < 0.01$.

and NANOG) and neuroectodermal (PAX6 and SOX1) genes using quantitative real-time PCR with results confirming that nanorough surfaces could accelerate disruption of the transcriptional circuitry that maintains pluripotency of hESCs while simultaneously promoting neuroectodermal gene expressions (Figure 5-9). Our screening assay using glass surfaces with varied surface roughness (Rq = 1, 100, 200 nm) further revealed a strong corelation between the surface roughness and neural induction efficiency (Figure 5-9B&E). A glass surface with surface roughness of 200 nm showed a potent effect on neural induction, whereas smooth surfaces (Rq = 1 nm) did not.

Consistent to results reported previously [259], treatment of hESCs with dual Smad inhibitors led to not only Pax6+ NEs but also Pax6- cells co-expressing neural crest cell (NC) markers, including AP2, p75 and HNK-1 (Figure 5-8). At day 8, 18.0% and 14.4% cells were AP2+ and p75+ on smooth glasses (Rq = 1 nm), respectively. Strikingly, only 1.6% and 3.4% cells were AP2+ and p75+ on nanorough surfaces (Rq = 200 nm) (Figure 5-8D). Immunoblot analysis confirmed greater expressions of Pax6 and Sox1 (a neuroectodermal transcription factor) but low expression of AP2 and HNK-1 for hESCs at day 8 on nanorough surfaces (Rq = 200 nm) than cells on smooth glasses (Rq = 1 nm) (Figure 5-8H). We further examined whether caudalized NEs derived from nanorough surfaces could be specified into spinal MNs in the presence of the ventralization factor purmorphamine (Pur), using oligodendrocyte transcription factor 2 (Olig2) as a MN marker. When NEs were cultured continuously for another 8 d in the presence of Pur and RA, 58.5% cells on nanorough surface (R_q = 200 nm) emerged as Olig2+, whereas only 11.2% cells became Olig2+ on smooth glasses (R_q = 1 nm) (Figure 5-10).

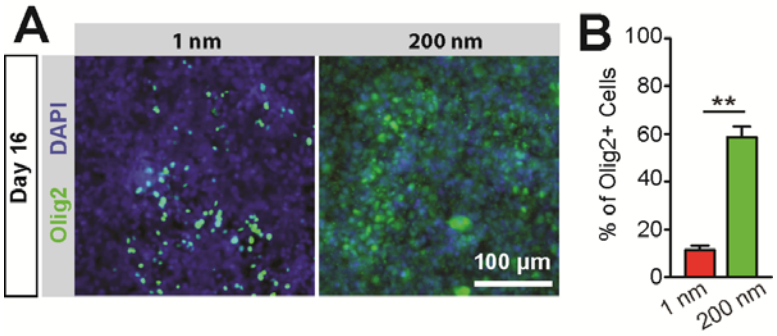

Figure 5-10 Nanorough surfaces promoted motor neuron (MN) specification of hESC-derived neural epithelial cells (NEs). (b) Representative immunofluorescence images and (c) bar plots showing percentages of Olig2^{+} MN progenitor cells derived from hESCs at day 16 on smooth (R_q = 1 nm) and nanorough (R_q = 200 nm) glass surfaces. hESCs were cultured on glass surfaces in neural induction media containing dual Smad inhibitors SB and LDN for 8 d before switched to MN differentiation media containing purmorphamine (Pur), basic fibroblast growth factor (bFGF), and retinoic acid (RA) for another 8 d. Olig2 is a transcription factor expressed by motor neuron progenitors at the pMN domain of the ventral neural tube. Data represents means ± s.e.m with n = 3. P-values were calculated using two-side unpaired student t-test. **: $P < 0.01$.

In summary, combining dual Smad inhibition with nanotopographic cue, here we achieved accelerated high-yield and -purity generation of NEs and spinal MNs from hESCs. Nanorough glass substrats are fully defined substrates that can be easily mass-produced for large-scale hESC culture. Our results further showed that just like many other human adult stem cells [254, 260, 261], hPSCs are intrinsic mechanosensitive, and surface topography can serve as an *in vitro* extracellular switch to direct the NE *vs.* NC lineage decisions. Thus, it is tempting to speculate that physical properties of *in vivo* ECM may serve as a "physical trigger" to work synergistically with soluble morphogens to direct neural plate specification during primary neurulation.

5.4 Mechanisms of Cellular Responses to Nanotopography: a Hypothetical Core Axis of Stem Cell Mechanotransduction

In the past decade, much effort has been directed to study the behaviors of stem cells in the presence of nanotopographic cues and successfully demonstrated the significant potential of nanotopographical biomaterials in stem cell-based tissue engineering. However, the underlying molecular mechanisms governing these processes remain elusive. Two most challenging questions are: how do stem cells sense matrix nanotopography and how is the topographical signal transduced and integrated into intracellular signaling pathways? Hereby, we discuss some common yet prominent mechanosensing machineries possibly involved in nanotopographic sensing with the focus on their operational mechanisms as well as functions in the context of cellular mechanotransduction. We will discuss how signaling pathways downstream of these mechanosensing machineries might relay the extracellular mechanical signals such as the nanotopography through a hypothetical axis composed of potential cytoplasmic transducers, cytoskeletal integrators and transcriptional actuators, which might provide a route map for future study and understanding of nanotopography-sensitive stem cell mechanobiology.

5.4.1 Plasma Membrane-associated Mechanosensors and Cytoplasmic Transducers

Playing a pivotal role in initiating and organizing cell-ECM adhesions, integrins are heterodimeric transmembrane proteins composed of an α and a β subunit. Currently,

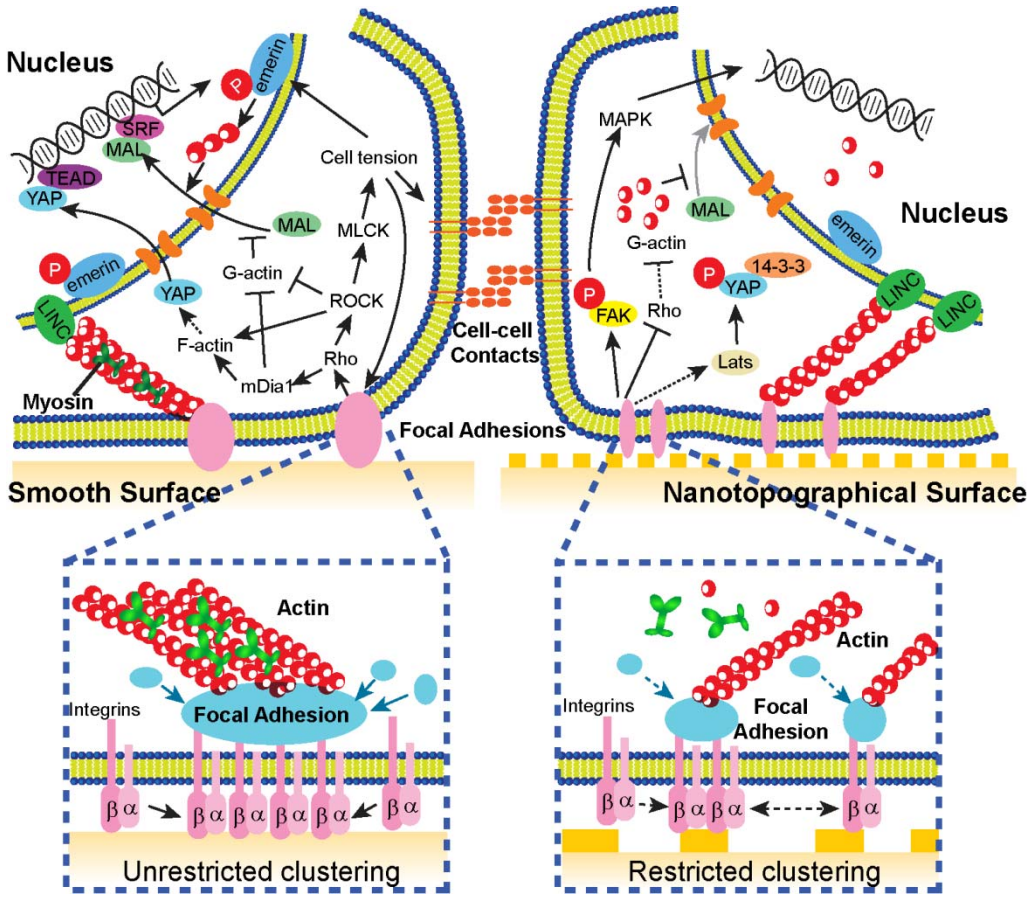

Figure 5-11 Potential mechanotransduction mechanisms in cellular responsiveness to nanotopographical biomaterials. (*left*) On smooth surfaces, integrins could undergo free lateral recruitment and ligation with ECM proteins, and thus cluster and form mature, stable focal adhesions together with the unhindered recruitment of FA adaptor proteins. This process initiates signals from plasma membrane, enhancing RhoA activity, which further promoting cell tension (through ROCK-MLCK) as well as stress fiber formation (through ROCK and mDia). Cell tension, as an important mediator of mechanotransduction, could provide positive feedback to the focal adhesions and cell-cell contacts. In addition, cell tension could also induce phosphorylation of emerin, a nuclear envelope-located protein, and thus initiate nuclear mechanotransduction through enhanced nuclear actin polymerization and subsequent nuclear translocation of MAL, a transcription co-factor of SRF. In the meantime, prominent stress fibers formed in cells on smooth surfaces could promote the nuclear translocation of YAP/TAZ, a transcription co-factor of TEAD. Nuclear shuttling of SMAD 2/3 (R-SMAD), the transcription factor downstream of TGFβ signaling, is also controlled by YAP/TAZ translocation. (*right*) On nanotopographical surfaces, although integrins could still freely diffuse laterally, the nanoscale surface features restrict the ligation of additional integrins to the ECM proteins, which further restrict successful recruitment and clustering of integrins and other focal adhesion proteins, resulting in smaller, less stable FAs. Such process disrupts the activation of RhoA and therefore limits the formation of stress fibers and might induce high cytoplasmic G-actin level, which inhibits the nuclear translocation of MAL and thus SRF signaling. In addition, nanotopography was found to induce high phosphorylation level of FAK, which could further connect MAPK signaling pathways to stem cell fate regulation. Last but not the least, compromised stress fibers and FAs on nanotopographical substrates could potentially intersect with Hippo/YAP pathway by enhancing YAP/TAZ phosphorylation via either Lats-dependent or –independent mechanisms, resulting in cytoplasmic retention of YAP/TAZ.

there are 24 known integrin heterodimers that are constituted by different combinations of 18 α and 8 β subunits, hosting a wide range of differential sensing to external chemical and mechanical cues [262-265]. For human pluripotent stem cells in particular, it has been found that human ESCs express a broad range of integrins including α_1, α_2, α_3, α_5, α_6, α_7, α_{11}, α_V, α_E, and β_1, β_2, β_3, β_5, β_6 integrins, while human iPSCs were found expressing in majority α_5, α_6, α_V, β_1, and β_5 integrins, with variations among different cell lines [266-268].

The first step cells make to probe the ECM is mediated by the "inside-out" and "outside-in" bidirectional regulation of integrin-ligand binding [269-271]. Specifically, the binding of intracellular adaptor protein talin to the cytoplasmic domain of integrin induces conformational change of integrin's extracellular domain and endows high affinity to bind corresponding ECM ligands. In return, the firm binding of integrin to ECM ligand activates the clustering of integrins through their intracellular domains and thus further recruitment of both adaptor and signaling proteins. In the early stage of integrin-mediated cell-ECM adhesion (also known as "nascent adhesion"), the key components include adaptor proteins talin and paxillin and tyrosine kinases such as focal adhesion kinase (FAK) and Src family kinases [272, 273].

Although intracellular force has been shown to be dispensable for the formation of nascent adhesions [274], as long as there remains intact binding between talin head domain and integrin, the early formation of cell-ECM adhesions has been found sensitive to the spacing of external ECM ligands. As the size of the head of an integrin heterodimer consisting of an α subunit and a β subunit is approximately 20 nm in diameter [213], a nanometer scale variation in substrate topography could potentially

result in a significant change in the clustering of integrins and adaptor proteins which in turn initiates signal transduction controlling stem cell fates (Figure 5-11). Results reported by multiple groups confirmed that successful integrin clustering requires a spacing between individual ECM ligands smaller than a threshold value of 50-70 nm, and too sparse distribution of individual ligands inhibited lateral crosslinking between integrins [275-278]. Interestingly, by simply clustering individual ECM ligands into oligomer nanopatterns, it could promote the cell-ECM adhesions and cell spreading without changing the overall ligand density, suggesting a critical role of nanoscale organization of integrins in the control of cell behaviors [279]. Given such sensitivity of integrin clustering to the spacing and local organization of ECM ligands, the myriad of cellular behaviors found responsive to the nanotopography might result from the sensitivity of FAs to nanoscale surface features that apply spatial restrictions on integrin clustering. In particular, as the nanoscale islands in many nanotopographical biomaterials are usually of a dimension of tens or hundreds of nanometers, they might limit the clustering of integrin and recruitment of FA proteins for morphological maturation (Figure 5-11). Although originally found in somatic cell lines, such regulation mechanism has been confirmed in dictating stem cell adhesions and phenotypes as well. For examples, results from different independent studies [135, 214, 218, 230, 280, 281] all suggested a threshold size around 50-70 nm for surface nanotopographical features that allowed clustering of integrins into the nearly closest packing and resulting in optimal integrin activation and FA maturation in stem cells.

During the maturation of nascent adhesions to focal adhesions (FAs), the recruitment of critical force-bearing adaptor proteins such as vinculin, α-actinin and

zyxin provides the indispensable connection to actomyosin contractile fibrils and the transmission of intracellular forces onto the adhesion complex through a positive-feedback loop (Figure 5-11) [272, 282-291]. The force-dependent FA maturation has long been thought to be responsive to extracellular nanotopography along with other physical cues such as substrate rigidity [225, 285, 286]. Recently, a few interesting studies revealed several mechanisms by which nanoscale cues regulate different aspects of FA maturation. In a recent study from the Sutherland group, it was found that nanoscale fibronectin islands of diameter 100-800 nm and inter-island distance about 300-500 nm in average strictly confined the FAs onto individual islands, which prevented FAs from further enhancement of recruitment and thus morphological maturation [292]. Interestingly, by using vitronectin nanopatterns instead, they found unhindered FA morphological maturation mediated by the "bridging" between individual nanoislands, which was found to be facilitated by adaptor proteins such as vinculins and zyxins but not integrins. Although such bridging effect has been also implicated in earlier study by Coyer et al. [293], the abovementioned results for the first time suggested a differential role of ECM ligands in the determination of FA morphological maturation in response to nanoscale surface features. Interestingly, a very recent study also from the Sutherland group found that unlike the morphological maturation, the recruitment of adaptors proteins (e.g., vinculin, α-actinin, and myosin IIa) *per se*, which was commonly associated with mature FAs and named the "biochemical maturation" of FAs, was not inhibited by nanoscale confinements of corresponding ECM ligands on 100-300 nm fibronectin nanopatterns [294]. This result clearly distinguished the nano-confined FAs from nascent adhesions in terms of their core biochemical compositions, even though

they share a similar nanometer length scale. Importantly, this study revealed it was the morphological maturation, instead of the biochemical maturation, that played a critical role in dictating the epidermal stem cell differentiation [294]. It implicated that the stability of FAs accompanying with the morphological maturation might hold the key to the nanotopography-driven stem cell fate regulation. This proposition was in line with earlier study by Kulangara et al., wherein the downregulation of zyxin – the force-dependent adaptor protein sustaining FA stability – was observed on 350 nm nanogratings [295]. Nonetheless, how both FA morphological and biochemical maturations might play roles in general nanotopography-sensing and fate control of different types of stem cells is worth of further investigations, which should also take the FA-related mechanotransduction signaling pathways into consideration, as we will discuss in following.

As an important mechanosensor, integrin-mediated cell-ECM adhesions relay the topographical cues from ECM to intracellular signaling networks since its early stage. A very important signaling axis serving as cytoplasmic transducers of extracellular mechanical signals at downstream of cell-ECM adhesions is the FAK-Src signaling pathway [272, 296, 297]. Activated by integrin ligation, FAK is recruited to cell-ECM adhesion. Binding of FAK to integrin activates FAK through autophosphorylation on Y397. Further phosphorylation on FAK is completed by the binding to Src family proteins to integrin and FAK. Together, FAK and Src relay the signals from integrins to control Rho GTPase activities through, for instance, FAK/p190RhoGEF/RhoA, FAK/p190RhoGAP/RhoA and Grb2/SOS/Rac pathways [296]. It also controls the MAPK signaling pathways that govern cell proliferation, apoptosis and differentiation,

through FAK/Ras/Raf/MEK/ERK, Fyn/Shc/Grb2/SOS/Ras, and p38 MAPK pathways [298-301]. Although it has been found that nanotopographical substrates promoted FAK phosphorylation[302], given the dual, opposite effects of FAK on RhoA activation [296, 303, 304] (e.g., activation through p190RhoGEF [305, 306] and inactivation via p190RhoGAP [307, 308], respectively), it remains an open question that whether the high FAK phosphorylation induced by nanotopographical substrate would result in high or low Rho activity. Given their roles identified in previous studies, other signaling downstream of integrin and FAK activation, such as the PI3K/Akt pathway [309] and TGFβ/SMAD [310] pathway might also have potential roles in nanotopography-sensitive mechanotransduction and stem cell mechanobiology through regulation of cell proliferation, self-renewal and differentiation [259, 311, 312]. Further studies are needed to verify whether these signaling axes were actively regulated during the nanotopography-sensing by early cell-ECM adhesions and how.

The maturation of FAs, along with the activation of its adaptor proteins as well as the cell tension, relays the extracellular mechanical signals further into another signaling axis intersecting with cell-ECM adhesions – the RhoA-ROCK pathway originating from G-protein coupled receptor (GPCR) signaling [313-316]. As a prominent mechanotransduction pathway, RhoA-ROCK signaling axis not only relays signals from integrin-mediated cell-ECM adhesions, but also forms a feedback loop in control of several mechanosensors. As induced partly by the integrin/FAK activation, the activity of Rho family proteins, such as RhoA, could further activates two critical effectors - ROCK and mDia - that regulate the structural quality of filamentous actin cytoskeleton and the contractile activity of non-muscle myosin II motor proteins. Specifically, ROCK

serves a dual function on enhancing both actin polymerization and cell tension generation, through LIM kinase-driven inhibition of cofilin (an actin severing protein) and myosin light chain kinase (MLCK)-driven non-muscle myosin II activity, respectively. In the meantime, mDia performs its role mainly in promoting actin polymerization by enhancing the activity of profilin (an actin polymerizing protein) [313]. These downstream effects could then feedback to the maturation of cell-ECM adhesions and further enhance their roles in Rho activation. As a hallmark of activated RhoA-ROCK signaling, the non-muscle myosin II-driven cell tension has been found compromised on nanotopographical substrates in one of our recent studies [136]. However, it is still unclear that if such nanotopography-sensitive cell tension was regulated through repressed RhoA-ROCK signaling, which calls for further studies.

In addition to the integrin-mediated cell-ECM adhesions, another group of plasma membrane-associated mechanosensors is the cell-cell contact mediated by cadherins in a calcium-dependent manner [266]. Well-known cadherins include E-cadherin, N-cadherin and VE-cadherin, which are commonly seen in epithelial, neural and vascular endothelial tissues, respectively [317]. Here, we will briefly discuss in focus the E-cadherin given its prevalence and importance in pluripotent stem cells, as well as the recent evidence demonstrating its sensitivity to nanotopography [135, 266].

Unlike integrin, E-cadherin *per se* is not known for its force-dependent activation and clustering. Instead, E-cadherins recruit intracellular β-catenin upon Ca-mediated homophilic ligation within cell-cell contacts. β-catenin subsequently recruit both p120-catenin and α-catenin and then connect to actin cytoskeleton [318, 319]. However, the direct E-cadherin/β-catenin/α-catenin/actin linkage was demonstrated very unstable, if

ever possible, and no complex containing all four components has been isolated from cells [318, 319]. Interestingly, a recent study found that mechanical force is required for robust and stable connection from E-cadherin to actin cytoskeleton via the force-driven recruitment of vinculin by α-catenin [320]. As a direct force-sensor, α-catenin unfolded under intracellular force possibly transmitted through its transient connection with actomyosin contractile fibrils, exposing a cryptic domain for vinculin binding. As an important force-sensitive adaptor protein, the recruitment of vinculin substantiated the stability of E-cadherin-mediated adhesions under force through further lateral recruitment and mechanical linkage to actin cytoskeleton [321]. The positive-feedback loop suggested by recent studies between mechanical force and E-cadherin-mediated cell-cell contact [322-324] is reminiscent of that in FA maturation, supporting the identity of cell-cell contacts as an important plasma-membrane associated mechanosensor. In the light of these discoveries, α-catenin in cell-cell contact shares a similar role as talin in cell-ECM adhesions, initiating force-dependent development and maturation of adhesion complex [291]. In fact, more and more crosstalk between cell-cell contacts and cell-ECM adhesions through either physical interconnection or intracellular signaling has been found in recent years [325-332].

Such similarity and connection between cell-cell contacts and cell-ECM adhesions raise an interesting question: whether extracellular nanotopography could impose its regulations beyond the cell-ECM boundary to control the cell-cell interactions. Interestingly, as discussed above, we found that nanotopographical substrates with random roughness of characteristic sizes about 100 nm disrupted E-cadherin-mediated cell-cell contacts while promoting spontaneous differentiation of human ESCs [135].

Along with this observation and the notion of crosstalk between cell-cell and cell-ECM adhesions, it was not surprising to observe and understand that flat substrates preferentially induced prominent, stable cell-ECM adhesions, while small and instable FAs were mainly found on nanorough surfaces that rendered less accessible surfaces for cell adhesion and spreading [136]. Similar effect of nanotopography on FA morphology was also reported recently by the Dalby group [333]. Taken together, it implicated that the regulation by extracellular nanotopography might reach far deep into the cell through mechanosensing and mechanotransduction axes involving cell-ECM adhesions, cell-cell contacts and their interactions.

5.4.2 Cytoskeletal Integrators

As a cellular architecture physically anchored to both cell-ECM and cell-cell adhesions, and also an effector directly downstream of RhoA-ROCK signaling axis, the integrity of actin cytoskeleton, especially the formation of contractile actin stress fibers, serves as a critical integrator of a multitude of extracellular mechanical signals [334]. Given recent reports that disorganized F-actin cytoskeleton as well as compromised contractility was observed in cells cultured on nanorough substrates [135], we are particularly intrigued by the possibility that F-actin might serve as a cytoskeletal integrator of nanotopography-driven signaling in cell mechanotransduction. Herein we will briefly discuss the current understanding of the role of F-actin in cell mechanotransduction, which might help lay down the foundation for future exploration of the mechanisms of cellular responses to nanotopography.

Recently, Hippo/YAP pathway, which was originally discovered in studies on regulations of cell growth and organ size, has been found as a downstream effector of the quality, dynamics as well as the intrinsic contractility of F-actin cytoskeleton, which has been thought as a potent regulator of stem cell mechanotransduction by integrating various upstream mechanical inputs and leading them to a convergent downstream signaling hub [335-340]. Interestingly, experimental evidence accumulated in past years started to implicate an emerging pattern in the mechanical regulation of Hippo/YAP pathway: extracellular mechanical cues (e.g., rigid substrate, external stretch, large cell size) promoting stable cell adhesions were all found enhancing the formation of prominent F-actin cytoskeleton and resulting in high nuclear YAP activity, while those cues (e.g., soft substrate and small cell size) demonstrated destabilizing cell adhesions were found compromising the integrity and robustness of F-actin and resulting in low YAP activity and dominant cytoplasmic YAP retention due to the association with 14-3-3 proteins [335, 336]. Such a role of F-actin cytoskeleton as potent mechanical signal integrator has been supported by recent studies in both 2D and 3D contexts on a myriad of cellular behaviors and functions [336]. Further, the convergent signaling through F-actin to suppress YAP activity has also been shown important in regulating motor neuronal differentiation of human ESCs on soft substrates in our recent study [223].

In addition to the Hippo/YAP pathway, the integrity and polymerization of actin cytoskeleton has also been implicated in the regulation of SRF (serum response factor) signaling [341, 342]. In particular, the enhanced polymerization of cytoplasmic actin monomers (G-actin) has been found to release MAL, a transcription co-factor, from its association with G-actin and thus to initiate the nuclear translocation of MAL, resulting

in elevated SRF signaling. For example, large cell size that elevated the cytoplasmic G-actin level has been found to inhibit SRF signaling as well as the differentiation of epidermal stem cells [341].

Combining these observations with my recent observation of disorganized, compromised F-actin cytoskeleton in human ESCs cultured on nanotopographical substrates [135], we speculate that nanotopography might either activate F-actin damage-dependent Hippo pathway and suppress nuclear YAP activity, or inhibit the nuclear translocation of MAL and the subsequent SRF signaling (**Fig. 8**). Yet, how Hippo/YAP and/or MAL/SRF signaling might play roles in stem cell fate determination in response to nanotopography has not been addressed so far, to which the answer likely depends on stem cell sources and species as well. This question calls careful future studies.

5.4.3 Nuclear Mechanosensors and Transcriptional Actuators

Although deeply embedded within a cell, the nucleus is an emerging, active mechanosensor as suggested by recent researches [343, 344]. As the most important mechanical components of the nucleus, the nuclear lamina that is mainly composed of intermediate filament proteins lamin A and C endows significant mechanical stiffness to the nucleus, and lamin A/C has been demonstrated critical for cell mechanotransduction and transcription regulation through signaling molecules such as MAL, emerin and F-/G-actin [212, 343, 345-347]. In contrast, nuclei of embryonic stem cells that lack lamin A/C have been shown to be extremely soft and the emergence of lamin A/C has been proposed as an embryonic stem cell differentiation marker [348]. Counterintuitively, nucleus is also not just an isolated DNA factory. Through its connection to cellular

cytoskeleton via KASH and SUN domain proteins (together also known as the LINC – linker of nucleoskeleton and cytoskeleton – complex) across the nuclear envelope as well as perinuclear adaptor proteins like nesprin and plectin, the nuclear lamina right underneath the inner membrane of nuclear envelope is structurally integrated into the cellular mechanical signaling network of actin filaments, microtubules and intermediate filaments [343, 349, 350]. Along with the abovementioned candidate mechanotransduction mechanisms potentially functioning in cellular responses to nanotopography, we are particular interested in the question that if the cell nucleus could serve an unexpected role in mechano-responsive stem cell fate regulation. Herein, we will review recent reports revealing several nuclear structures as distinct mechanosensors, and discuss a few possible transcriptional actuators that might lead the nanotopography-driven mechanotransduction to its culmination.

Using a cysteine shot gun technique in combination with *in vitro* shear force application [351], the Discher group has identified a group of proteins, including nuclear lamin A, that change their conformations and expose cryptic hydrophobic domains under unfolding forces [352]. Although such direct force-sensitive conformational change was not seen in nuclear lamin under physiological conditions, they did observed a clear scaling relation between nuclear lamin expression and *in vivo* ECM rigidity, suggesting a potential link between rigidity-sensitive cytoskeletal contractility and force-dependent nuclear lamin A functions [352]. This work also implicated that nuclear mechanical stiffness, as mainly endowed by lamin A/C, might scale with extracellular matrix rigidity, and this was recently confirmed by nanoindentation study conducted by Liu and colleagues [353]. Recently, Poh et al. have found that an intact linkage between

cytoskeleton and nucleoskeleton could transmit integrin-mediated twisting forces from cytoplasm membrane to Cajal bodies in the nucleus and thus directly dissociate the coilin and SMN protein complexes [354]. Furthermore, transmission of cytoskeletal stress within the actin stress fibers and microtubules has also been found critical for mediating the long-distance force-sensing, which potentially involves the nucleus [350, 355]. In addition, cell shape has also been used as an external regulator of nuclear mechanics to probe the mechanisms of nuclear mechanosensing. By confining cells to high-aspect ratio morphology, the nuclear shape changed according at a loss of volume. At high nucleus aspect ratio, the significant distortion of nucleus has been observed to result in prominent chromatin condensation, indicating that the mechanical deformation of nucleus might be a direct mechanosensor that controls the chromatin structures and apoptosis [356].

In a very recent study, direct experimental evidence has been provided that an inner membrane-located protein, emerin, was a force-sensor and underwent force-driven phosphorylation [357]. Using isolated nuclei, this study demonstrated nuclear stiffening in response to external cyclic pulling forces, mimicking the cytoskeletal tension exerted upon nucleoskeleton. They found it was driven by the recruitment of lamin A/C by Src-mediated tyrosine-phosphorylated emerins under tension. Similar tension-dependent emerin phosphorylation has also been found sensitive to the rigidity of the cell-culture substrate and the mechanical force applied through integrin ligation, respectively. Although we are still at the beginning of understanding the mechanosensing in nucleus, all these discoveries above strongly suggested cell nucleus as a potent mechanosensor through multifaceted mechanisms such as direct force transmission, nucleus shape

distortion, nuclear lamina protein expression and phosphorylation. We envision the study on nuclear mechanosensing and mechanobiology will initiate a new, active research field in addition to the ones established on cytoplasmic mechanosensing mechanisms.

To the best of our knowledge, the study of nuclear mechanics in the context of stem cells sensing extracellular nanotopography has been rare. Although it was found that nanotopography could induce nuclei deformation [358, 359], quantification of the mechanical forces on the nucleus in intact cells has not yet been demonstrated. Recently, the Dalby group has also reported mechanosensitive chromosomal repositioning in response to disordered nanopit arrays, wherein extracellular nanotopography posed chromosome 1 closer to the nuclear membrane during human MSC osteogenesis, and increased the mean inter-territory distance of chromosome 1 in the meantime [360]. They have also found that the position of gene regulation along the chromosome was sensitive to substrate nanotopography [361], and subsequently identified that the nanotopography-enhanced gene regulation concentrated towards the telomeric end of the chromosome, where osteogenesis-regulated genes also clustered [360]. Yet, the direct connection between the nanotopography and chromosomal repositioning as well as gene regulation remains elusive. Taken together, it raises an intriguing question that whether the topography-sensitive nuclear deformation and nuclear mechanical forces could initiate corresponding changes in nucleus stiffness and nuclear structure rearrangement, and how it might relate to stem cell fate determination. It calls for further studies.

Recently, a few mechanosensitive nuclear actuators that relay extracellular mechanical signals to control the transcriptional activity and gene expression in the nucleus have been revealed. As a nuclear transcription co-factor, YAP could bind to

transcription factors TEAD and also co-translocate SMAD 2/3 (regulatory SMAD, R-SMAD) to the nucleus, thus relaying the cytoplasmic mechanotransductive signals to transcriptional control machineries [223, 362-364]. As regulator of pro-survival and pro-proliferation effectors, YAP activity has always been found correlated with pro-survival and pro-proliferation extracellular mechanical cues [365]. However, stem cell differentiation seems requiring either Hippo-dependent or -independent suppression of YAP activity, and it is still unclear what might fill in the transcriptional control position previously occupied by YAP [363, 366]. In principle, we reckoned that extracellular mechanical cues that induced the suppression of YAP might either stimulate or inactivate other transcriptional actuators in the same time, which eventually could determine the fate of stem cells. In the light of the altered F-actin cytoskeleton observed on nanotopographical substrates, and the newly emergent role of cytoskeleton-nucleoskeleton interaction and nuclear forces in regulating nucleoskeletal structures, chromatin structures and nuclear lamina protein expression and phosphorylation, we speculate that future studies on nuclear mechanotransduction might help us find the end link on the signaling axis through which substrate nanotopography controls stem cell fate. In fact, the expression of emerin in nucleus and the requirement of lamin A/C for its correct localization to nuclear membrane has recently been found playing an important role in MAL/SRF signaling [347, 367]. In particular, emerin promoted nuclear actin polymerization that in turn inactivated MAL nuclear export and thus promoted the transcriptional activity of MAL. In addition, high level of emerin phosphorylation has also been found correlated with cells cultured on rigid substrate and high level of nuclear YAP localization and activity [357]. Mechanical tension through nesprin-1 onto isolated

nuclei was also found to induce RhoA activation in nucleus, although its exact role in transcriptional control remains unclear [357]. To date, how these mechanisms might be involved in cellular responsiveness to substrate nanotopography is elusive. In the near future, studies on the nanotopography-sensitivity of nuclear deformation, nuclear envelope mechanics, lamin A/C expression, nuclear lamina protein expression and phosphorylation, and nuclear transcription activation might help to validate our hypothesis regarding this end game of the mechanotransduction in stem cells (Figure 5-11).

5.5 Conclusion

Stem cells are promising cell sources for the future tissue engineering and regenerative therapies. The current challenge faced by stem cell engineering mainly has to do with the large-scale, long-term maintenance and high-specificity, high-yield, directed differentiation towards clinically relevant lineages. Advances in nanotechnology and materials science could help leverage the regulation of stem cell fates and function via microenvironmental physical factors such as the nanotopographical cues to enhance the performance of synthetic biomaterials in future stem cell engineering.

In this chapter, a state of the art nanofabrication method was discussed for generating nanotopographical biomaterials for regulating stem cell fates and function. The proposed synthetic nanotopographical biomaterial has been successfully applied to control various phenotypes of hESCs, such as adhesion, migration, morphology and proliferation, and eventually in determining transcriptional activities and fates. By designing nanotopographical features mimicking *in vivo* stem cell niches, a diverse

toolbox of nanotopographical biomaterials have enabled either long-term maintenance or directed lineage commitment of different types of stem cells including hESCs, producing promising solutions for clinical regenerative treatments. Although successful as it is as proof of concept, the stationary nanotopographical biomaterials alone might not be sufficiently satisfactory for meeting all the criteria set by the demanding clinical applications. Soluble and insoluble biochemical cues, dynamic control of topographical features, as well as the *in vitro* co-culture of cells that share a common stem cell niche *in vivo*, have also been demonstrated to play in synergy with physical cues in regulating stem cell fates [211, 212, 368-372]. In future, the design and fabrication of nanotopographical biomaterials might need to be integrated with multifunctional biochemical modifications and even spatiotemporal patterning for simultaneously controlling multiple aspects of *in vitro* stem cell microenvrionment and fine tuning the specific terminal lineage commitment of stem cells at a large scale, eventually delivering the promise of stem cells to the regenerative medicine.

In order to shed light on our knowledge of stem cell biology and development, as well as to further improve the performance of nanotopography-driven stem cell fate regulation and fully realize the virtually unlimited potential of stem cells, it is also important to understand better the mechanosensing and mechanotransduction mechanisms underlying the cellular responses to extracellular nanotopography. In this chapter, I summarized a few key mechanosensing and mechanotransduction mechanisms that have been implicated, although not completely proven, to play important roles in the regulation of stem cell fates via nanotopographical biomaterials. Based on the current understanding of stem cell mechanobiology, I also proposed a few speculations regarding

how different mechanosensitive signaling events might eventually be integrated and converge onto several core mechanotransduction axes, which constitute the "chain of commands" from extracellular nanotopography to nuclear gene expression. Future studies on the nanotopography-responsive mechanotransduction might have to involve molecular mechanosensors, transducers, integrators and actuators residing in different cellular compartments and organelles. Elucidating the interconnections between each links in cell mechanotransduction remains another major challenge that needs to be addressed in the near future.

Looking into the future, the ultimate success of stem cell engineering will be the *in vivo* demonstrations of functional engraftment and tissue regeneration. A multidisciplinary approach merging stem cell biology, materials science, biomedical engineering and nanotechnology will be the most promising route towards the eventual realization of clinical stem cell therapies.

Chapter 6

Conclusions and Future Work

6.1 Summary

Taking advantage of state-of-art nanotechnologies and fabricating fascinating functional biomaterials, we can address numerous important problems in fundamental biology as well as clinical applications in disease diagnosis and treatment. My doctoral research, therefore, has focused upon developing microengineered functional biomaterials and integrated microfluidics for biomedical applications in systems immunology, cancer biology and stem cell-based regenerative medicine.

6.1.1 Integreted Microfluidics for Functional Immunophenotyping

Developments of reliable, multiplexed biosensing techniques permitting simultaneous characterization of functional status of different subpopulations of immune cells is an exciting emerging concept that holds great promise not only for unraveling the pathogenesis of different immune diseases but also for translating the newly available therapeutic options into optimal personalized treatments. To address this need, my

doctoral dissertation has centered on developing integrated microfluidic immunophenotyping device that could achieve rapid and efficient isolation, enrichment, stimulation and functional immunophenotyping of subpopulations of immune cells directly from blood specimens. This intgergated MIPA device enabled us to achieve rapid and sensitive on-chip immunophenotyping assays for subpopulations of immune cells isolated directly from minute quantities of blood samples [8]. The MIPA device could achieve high capture yield (> 90%) and excellent capture purity (> 97%) for subpopulations of immune cells from blood samples. For quantitative immunosensing, the MIPA device utilizes a commercially available homogenous chemiluminescence technique, the "AlphaLISA", which does not require any washing or blocking step, greatly shortening the total assay time and enhancing the dynamic range for analyte detection. Owing to the miniaturized on-chip microfluidic environment, the MIPA device can achieve highly sensitive cellular immunophenotyping with 20-fold fewer cells as compared to standard whole-blood stimulation assay to assess functional status of patient immune system. The total assay time of the MIPA device, including immune cell isolation and enrichment, stimulation and in situ detection of cytokines secreted by immune cells only need 4 hours, which is 6 times faster than that of whole-blood stimulation assay using conventional ELISA. The MIPA device can provide a very high sensitivity for cytokine measurement, about 75 pg mL^{-1}, which is comparable to ELISA. As a proof-of-concept of the importance of the new platform, we have applied this newly developed microfluidic technologies to address the critical need for an accurate measurement of the immune status in patients. We have applied this innovative microfluidics-based immunomonitoring technology to identify the incidence of

immunoparalysis and determine its predictive power for post-operative infections in pediatric patients undergoing cardiac surgery with cardiopulmonary bypass. Such an innovative tool will allow comprehensive and systems-level immunomonitoring to define and characterize the "immune status" of healthy individuals and patients, critical for clinical interventions and managements of patients with immune system disorders.

6.1.2 Nanoroughened Surfaces for Capture of Circulating Tumor Cells

Nanotechnologies including advanced nanofabrication and functional nanomaterials have provided new opportunities for many biological and medical applications. My doctoral study has leveraged novel nanofabrication techniques to develop synthetic nanotopographical biomaterial to address specifically these broad challenges in understanding the CTC biology. We introduced a simple yet effective microfabrication strategy for precise control and patterning of the local nanoroughness on glass surfaces using photolithography and RIE which are well-established processes used in semiconductor microfabrication. Incorporating this nanotopographic surface into a microfluidic platform, we have proven a new approach that can efficiently isolate, enrich, and rapidly perform informative molecular and cellular analysis of live CTCs at the single-cell level. Our method uniquely utilized the differential adhesion preference of cancer cells to nanorough surfaces when compared to normal blood cells and thus did not depend on their physical size or surface protein expression, a significant advantage as compared to other existing CTC capture techniques. Our CTC capture chip, which includes the nanotopographical glass substrate and a microfluidic mixing chamber, can

provide a superior performance for efficient and non-invasive capture of rare and viable CTCs from blood.

It is well known that EMT process of tumor cells, a process by which epithelial cells lose their cell polarity and cell-cell adhesion, and gain migratory and invasive properties to become mesenchymal cells, is essential for the initiation of metastasis for cancer progression. However, most current EpCAM-antibody based CTC isolation methods can only isolate cancer cells with high expression of EpCAM (epithelial-like cells) and may loss the mesenchymal-like CTCs, hence precluding the capabilities for studying the crucial EMT process. Because our CTC capture chip captures CTCs not based on cancer surface makers, it had been proven to be able to capture both epithelial-like and mesenchymal-like cancer cells, particularly suitable for study the role of CTCs in EMT and metastasis.

Furthermore, we have unitized the new CTC detection technology to monitor and study the CTCs in mouse xenograft as well as allograft models in *vivo*, hence provide the foundation for studies of molecular regulation of CTCs in cancer and CTCs as biomarker for therapeutic efficacy. So far, studies of CTCs in metastasis have been limited by the inability to repetitively monitor CTCs in cancer patients. Previous studies of CTCs in endogenous mouse models though have provided insightful understandings of metastasis, there is still a big gap between findings from endogenous mouse models and clinical interpretation in human. In order to fill this technical gap, developing our own human cancer cell based murine xenograft models specific for CTCs becomes particularly important. Adapting existing technology used to serially assay CTCs in human for studies in mice would allow for direct translation to clinical investigations and permit

early development of ‘‘companion’’ diagnostic assays for targeted therapies in mouse models of cancer. Theirfor, we have performed serial analysis of temporal changes in CTCs in mouse xenograft as well as allograft models of breast and lung cancer during tumor progression and response to therapy in living mice. We have demonstrated strong correlations in CTC quantity, the tumor volume and the cancer metastatic capability, hence revealed the pathophysiological role of CTCs in cancer metastasis. Togethor, this new CTC capture technology for isolation of CTCs will allow informative analysis of live CTCs for accurate diagnosis and prognosis of cancer and help understand the crucial early metastatic process of cancer and hopefully discover new targets or phenotypes in the CTCs that can aid in the design of more effective molecular treatments.

6.1.3 Biophysical Phenotyping of Inflammatory Breast Cancer Stem Cells

Cancer stem cells have been proven to initiate tumorigenesis and are the primary population of cells responsible for cancer metastasis in numerous cancer types [32, 157-162]. Within IBC, the ALDH+ population has been shown to represent the tumorigenic and metastatic subpopulation [32], but detailed studies characterizing the IBC CSC’s mechanical properties were lacking. ALDH expression is also negatively correlated with survival outcome [32], thus we postulated that the ALDH+ CSCs of IBC would exhibit distinct biomechanical properties that would help explain their extremely aggressive metastatic behavior. In order to more specifically ascertain and potentially explain the mechanical basis for the aggressive behavior of IBC CSC’s, we undertook novel

experiments and engineered devices targeted at quantitatively defining cells' mechanical properties.

This biophysical characterization of ALDH+ IBC CSCs revealed distinct biophysical properties that might mechanistically explain the functional differences seen between the IBC CSCs and non-CSC population. These biophysical properties included a greater cell deformability, weaker adhesion strength, and less cellular traction force. This unique profile of biophysical characteristics associated with ALDH+ IBC CSCs could help explain how CSCs are better adapted than non-CSCs to successfully navigate through their dynamic microenvironment in the metastatic process.

In the first step of the metastatic cascade, decreased adhesion of IBC CSCs, as demonstrated by their lower measured adhesion strength, might indicate why these cells are able to migrate away from the primary tumor. The strongly adherent ALDH- cells might not be able to overcome their attachment, which is further supported by ALDH- cells' reduced migration capacity in our *in vitro* studies. Additionally, IBC CSCs, a highly metastatic cell population, showed significantly lower traction forces compared to their non-CSC counterparts, suggesting inherent differences in cell force generation correlated with aggressiveness. In the next steps of the metastatic cascade, migrating cancer cells must invade through the basement membrane and squeeze through endothelial cell tight junctions during intravasation and extravasation. As measured in our assays, the greater capacity for deformation of ALDH+ cells suggests significant plasticity towards cytoskeletal changes or reorganization and underlying mechanical differences in IBC CSCs. This may account in part for their invasive capability to more successfully transit through a confining biophysical microenvironment. Cell

deformability may thus be used as a label-free biophysical marker for identification and understanding of other CSCs in future studies. Together, the biophysical profiling of IBC CSCs has provided comprehensively delineation of the live cell phenotypic characteristics of the model of the most metastatic breast cancer subtype, and yields a new understanding of IBC's metastatic properties and how they might develop and be targeted for therapeutic interventions.

6.1.4 Nanotopography-mediated Mechanoseing of Human Embryonic Stem Cells

Stem cells are critical players during development, tissue regeneration, and healthy homeostatic cell turnover, and they are an important driving force for the developing fields of functional tissue engineering and regenerative medicine owing to their self-renewal capacity and pluripotency. *In vivo*, local tissue structure defines stem cell environment and therefore regulate stem cell functions. Stem cells interact with and interrogate their surroundings at the nanometer length scale. Therefore novel biomaterials that can encode specific nanoscale biological cues (*e.g.*, mechanical signals, and/or adhesive and soluble factor gradients) offer unique opportunities for engineering stem cell functions. My doctoral research, therefore, is oriented toward developing synthetic nanoscale *ex vivo* stem cell microenvironment to direct hESC behaviors, and further employing them to identify the unique mechano-sensitive and -responsive properties of stem cells and the effect of the physical aspects of the local cellular microenvironment on regulating stem cell behaviors. On this purpose, we have developed synthetic nanotopographical materials to direct stem cell behaviors, and

further employing them to identify the extrinsic nanotopographical cue and their downstream signaling pathways that regulate stem cell functions [135]. My study demonstrated that hESCs were intrinsically sensitive to the nanoscale topological cues on the substrate and the nanotopography cue could provide a potent regulatory signal over different hESC behaviors, including cell morphology, adhesion, proliferation, clonal expansion, self-renewal and fate. In this work, we have futher investigate if and how the intrinsic mechanosensitive properties of hESCs to nanotopography could be leveraged to improve derivation of functional spinal MNs. Combining dual Smad inhibition with nanotopographic cue, we have achieved accelerated high-yield and -purity generation of NEs and spinal MNs from hESCs. Nanorough glass substrats are fully defined substrates that can be easily mass-produced for large-scale hESC culture. Our results further showed that just like many other human adult stem cells [254, 260, 261], hESCs are intrinsic mechanosensitive, and surface topography can serve as an *in vitro* extracellular switch to direct the NE *vs.* NC lineage decisions. The mechanism study indicated that topological sensing of hESCs might include feedback regulation involving mechanosensory integrin-mediated cell-matrix adhesion, cell cytoskalten reorganization and cell-cell interactions. Together, our stem cell studies have highlighted the important role of nanotopographic cue in stem cell microenvironment to direct hESC behaviors that are desirable for functional tissue engineering and regenerative medicine.

6.2 Future Work

6.2.1 Integreted Microfluidic Immunophenotyping Device for Multiplexed Detection

In my doctoral research, a microfluidics-based immunophenotyping device has been developed for functional cellular immunophenotyping of the immune status of patients with immue disorders. Yet, the proposed MIPA device currently only permits measurement of one cytokine from one type of immue cell subpopulation. Continued progress in many fields ranging from fundamental biological to patient care critically hinges on the availability of specific, reliable assay systems capable of multiplex detection from a single sample (multiplexed cell-secreted cytokine detection from multiple immue cell subpopulations). Therefore, to address this critical technical need, contining research could be performed to establish a highly integrated, automated microfluidic immunomonitoring technology to achieve rapid, accurate and multiplexed detection of multiple cytokines secreted from different types of immune cell subpopulations from blood specimens.

For example, based on our first-generation MIPA device, we can develop a fully integrated and automatic second-generation MIPA device that can achieve isolation 3 subpopulations of immune cells (CD14+ monocytes, CD4+ and CD8+ T-cells) from human blood specimen and parallel stimulation and detection of multiple cytokines (TNF-α, IL-6, IL-10, and IFN-γ) secreted from these subpopulations of immune cells (Figure 6-1). I select CD14+ monocytes, CD4+ and CD8+ T-cells as the immune effector cells as they are reported as major subpopulations involved in the response of the

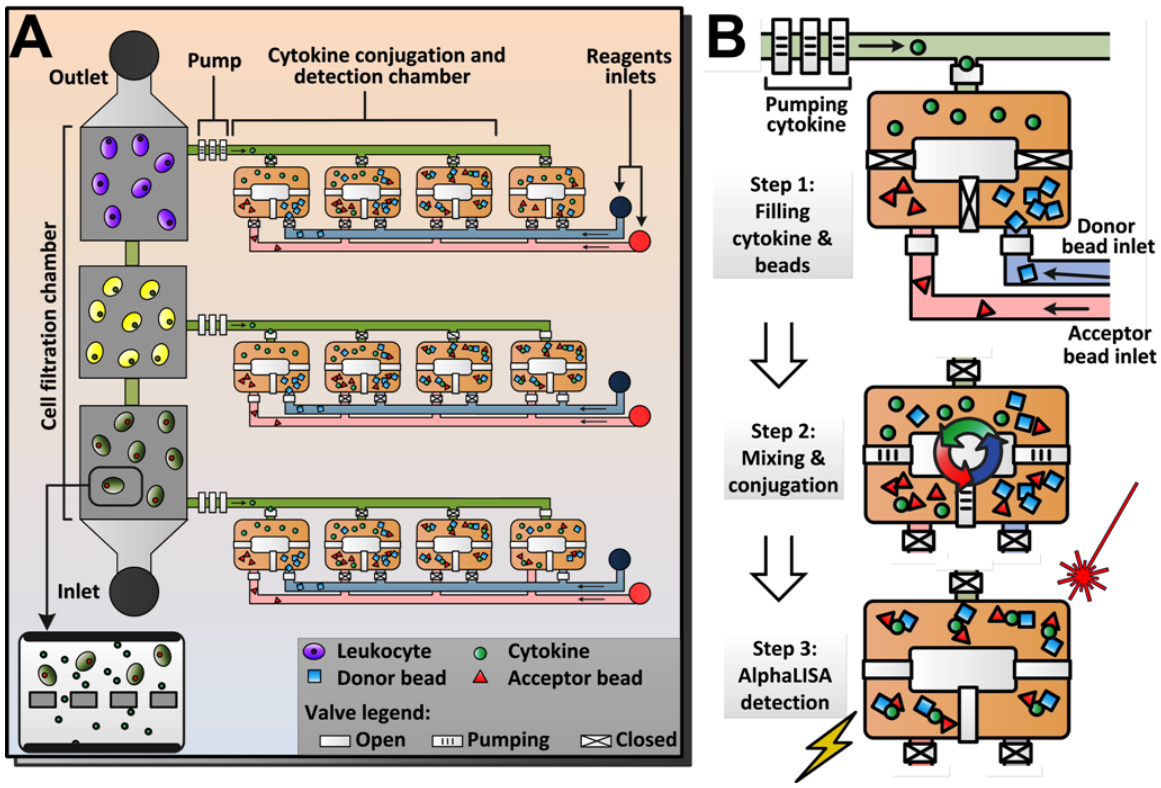

Figure 6-1 Concept of new microfluidic device for multiplexed cellular immunophenotyping. (A) 2nd generation MIPA device for parallel detection of multiple cytokines secreted from immune cells. (B) Sequential operation steps for immunosensing.

immune system to inflammatory stimuli, such as CPB [373-375]. The selected panel of these four inflammatory cytokines has also been reported to yield positive, predictive values indicating the development of organ damage [376] and bacterial infections [377].

The new device will integrate an array of 3 independent first-generation MIPA units for isolation of different tpes of subpopulations of immune cells (Figure 6-1A). Each cell isolation unit includes a PDMS microfiltration membrane (PMM) for cell isolation. The new integrated MIPA device, when combined with different-sized antibody-conjugated microbeads targeting different surface proteins, could provide an effective solution for isolation and enrichment of multiple subpopulations of immune cells (CD14+ monocytes, CD4+ and CD8+ T-cells) simultaneously from blood

specimens. To achieve quantitative parallel detections of multiple cytokines secreted from each isolated subpopulation of immune cells with AlphaLISA, each MIPA unit will have a microfluidic interconnect channel that fluidically connecting an array of 4 cytokine conjugation and detection chambers to the main cell filtration chamber (Figure 6-1A). Each array of the cytokine conjugation and detection chambers will be used for multi-detection of the 4 types of cytokines. After LPS (for monocytes) or PMA (for T-cells) stimulation and incubation, cytokines secreted by the isolated cells will be delivered along each of the interconnect channels using microfluidic pumps integrated in the MIPA device. The reagent loading (i.e., AlphaLISA detection beads), mixing, and conjugation will be accomplished sequentially by modulating the on/off states of integrated microfluidic valves (Figure 6-1B). The new integrated device is automatically controlled by microfluidic valves that are actuated using an external air pneumatic actuation controller connected to a LabView software-installed personal computer.

The sophisticated device structure incorporating a large number of microfluidic pumps and valves warrants a careful design and validation to achieve efficient analyte transport and reagent mixing. We should carefully design these microfluidic components and their arrangement using the commercial finite-element method (FEM) software (COMSOL 4.2a Multiphysics) and experimentally validate their performance. After developing new deivce, we will then repeat our assays (similar to Chapter 2) to carefully examine the capture efficiency and purity for immune cell subpopulations as a function of the PMM through-hole size, porosity, flow rate and total sample volume, and to establish the standard curve for detection of all proposed cytokines by AlphaLISA and correlate the concentration values between AlphaLISA and ELISA measurements.

The new parallel functional immunophenotyping assay device are expected to simultaneously measure cell secretion of 4 cytokines, while reducing the entire assay time down to about 2 hrs, a nearly 10-fold reduction in time compared to the standard whole blood assay using ELISA. Based on our preliminary results charactering the limit of detection (LOD) in Chapter 2, we expect the sensitivity of our assays to be sufficiently high and in the range of tens of pg/mL, comparable to that of ELISA.

In Chapter 2, we have performed preliminary study using the MIPA device to measure TNF-α secretion from monocytes to identify immunoparalyzed children following CPB. However, a potential limitation is the possibility that monocytes may not be the key/only predictor of immunoparalysis. The incomplete understanding of the pathophysiology of immunoparalysis leaves the possibility that even though monocyte deactivation is extensively characterized in immunoparalysis, functional testing of other subpopulations of leukocytes may better predict immunoparalysis. In this case, I believe the development of the new multiplexed device has a distinct advantage as it allows us to immunophenotype different subpopulations of immune cells simultaneously and to design subsequent studies to determine the contribution of immune cell subpopulations in the event that CD14+ monocytes do not most accurately identify immunoparalyzed patients.

With new multiplexed device, we may futher perform real-time immunophenotyping of pediatric patients following CPB using the MIPA device to identify immunoparalyzed patients and determine its predictive power for post-operative infections. Immunoparalysis in children following CPB has a highly predictable incidence (~20%) and increases the likelihood of developing a post-operative infection

[114, 378]. These studies argue for a real-time platform that provides clinicians this patient-specific information across a variety of cohorts.

The incidence and time course of immunoparalysis as well as data on development of infections from any patient along with the functional status of the subpopulations of immune cells (CD14+ monocytes, CD4+ and CD8+ T-cells) will be collected and analyzed in relationship to the individual patient's immunophenotype (dichotomized as immunoparalyzed or non-immunoparalyzed). To immunophenotype the enrolled patients, patient blood will be collected right before the CPB, on the post-operative days 1, 3, 5, 7, and then every 7 days until patient discharge from the ICU. Concentrations of TNF-α, IL-6, IL-10, and IFN-γ measured using the new device for the subpopulations will be compared and correlated with the results generated using the standard whole blood assay. Based on previous studies using whole blood assay [11], immunoparalysis is defined as TNF-α production of less than 200 pg/mL. Patients will be first dichotomized as immunoparalyzed or non-immunoparalyzed using this value from the standard whole blood assay. Receiver operator curves (ROC) will then be generated to determine the cutoff values of these multiple cytokines for identifying patients as immunoparalyzed using the new MIPA device for the subpopulations of immune cells. Next, more samples from patients enrolled in the study will be used to validate the cutoff values established from the first cohort of 40 patients. Test characteristics including sensitivity, specificity, positive and negative predictive values will be determined on this validation cohort and further be compared between the two immune monitoring methods (i.e., the new multiplexed microfludic device for leukocyte subpopulations and the standard whole blood assay). Additional clinical data, including

development of an infection from any source, length of stay in the ICU, length of stay in hospital, and mortality will be collected and correlated with the immunophenotype determined by both methods discussed above.

In addition to the immunophenotyping of pediatric patients following CPB, the new technology can be applied as general tool for many different immune diseases. For example, we may use the new immunophenotyping technology to define post-operative infections in the same manner as the SPECS Study: as culture positive infections, knowing that patients can develop infections and sepsis without positive cultures. To address this concern, patients will also be followed daily to determine if the care team starts or alters antibiotics. Once there is a change in antibiotic administration, the care team will be contacted to determine the rational for starting/altering antibiotics. Factors leading to the decision to starting/altering antibiotics will be recorded, and patients will also be classified as presumed infection. Using this approach, while the primary analysis will be conducted with the primary outcome as culture positive infections, a secondary analysis could be performed with presumed infections.

6.2.2 Biophysical and Molulular Characteristical Study of CTCs

Dissemination of cancer cells from primary tumor in the form of metastasis in distant organs is responsible for 90% of cancer-related deaths, representing over 500,000 people dying every year in the United States alone. Consequently, metastases are among the most important biological problems to address in cancer research. Although a cellular link between the primary malignant tumor and the peripheral metastases has been established in the form of CTCs in peripheral blood, a major challenge remains in

deciphering the biology of this very unique cellular population, and ultimately, improving our systems level understanding of "how cancer spreads and kills". Despite the clinical and pathophysiological importance of CTCs, the current molecular and cellular understanding of CTCs is extremely poor, largely owing to the fact that current techniques to isolate and characterize these rare cells are limited by low yield and purity, complex techniques, and expensive proprietary equipments, compounded by yielding little phenotypic and molecular information about the CTCs themselves. As such, there is still little knowledge about characteristics of CTCs such as timing of CTC release from primary tumors, their heterogeneity and molecular and cellular properties, and the degree to which they are representative of either primary or metastatic tumor deposits. During my doctoral study, I have successfully developed a nanotopographical-material-based microfluidic platform for efficient and non-invasive capture of rare and viable CTCs from blood [29]. This pioneer work fulfills the critical need for isolation of rare CTCs and made informative analysis of live CTCs possible. In my future research, I will leverage the novel CTC isolation technique and develop new functional biomaterials and engineering platforms for comprehensive study of cancer metastases and characterizations of CTCs, to provide new knowledge for cancer pathophysiology and more effective techniques for personalized therapy.

First, I plan to perform comprehensive study of the biomechanical properties of CTCs. Recent studies have shown that malignant phenotype, metastatic potential, and tissue tropism of cancer cells are correlated with their mechanical properties (such as deformability) [379, 380]. Thus, biomechanical properties of CTCs might serve as a specific diagnostic marker for cancer. To approach this window of opportunity, I will

develop a microfabricated Cell-Mechanical-Phenotyping (CMP) chip for efficient trapping and high-throughput, highly-sensitive, and label-free quantification of cell size, deformability and expression levels of surface receptors of live single CTCs. In this research, I will quantify and compare the deformation responses of CTCs with normal cancer cells and healthy human epithelial cells under various pressures in an array of V-shaped trapping channels, in order to determine the specific mechanical characteristics of CTCs, including the cell shape, size distribution and stiffness. The internal walls of the trapping channels can be functionalized with different antibodies against specific surface receptors of cancer cells. As such, the expression levels of target surface receptors can be measured based on the immunoaffinities of the trapped cancer cells to channel wall. I hypothesize that my experimental results will potentially reveal distinct mechanical properties (ex. higher mechanical deformability) of CTCs from the normal cancer cells and healthy human epithelial cells. In addition, functional and phenotypic variation among individual single cells, or single-cell functional heterogeneity, is a common feature for tumor cells. Thus, quantitative functional analysis of cancer cells down to a single-cell resolution is required for a precise characterization of CTCs. Comprehensive study of the biomechanical properties and expression levels of different surface receptors of live single CTCs using this novel CMP-chip will for the first time provide us a complete pattern of the mechanical and biochemical phenotypes of CTCs at single cell level, hence pinpoint specific diagnostic markers for cancer. This microfluidics-based platform can serve as a comprehensive and standardized monitoring platform to define and characterize the "mechanophenotype" of healthy individuals and cancer patients before, during, and after targeted therapies thus provides new knowledge of cancer

pathophysiology, critical for developing better, more effective interventions for personalized therapy.

In addition to the study on biomechanical properties of CTCs, I will explore the potential correlations in CTC quantity in patient blood, the tumor volume and the time course of the anti-cancer treatments, hence reveal the pathophysiological role of CTCs in cancer metastasis. I will utilize our recent developed nanomaterial-based CTC-capture chip to monitor serial changes in CTC quantity, and the tumor size in cancer (ex. breast or lung cancer) patients using computed tomograms (CT scans). Additional clinical data, including development of a secondary tumor, length and type of anti-cancer treatment and overall survival will be collected and correlated with the temporal change of CTC quantity determined by my CTC-capture chip discussed above. I envision that monitoring the correlations in CTC quantity and the anti-cancer treatment response using the new engineering platform may ultimately be a powerful tool enabling accurate, early clinical decision-making.

Further, I will work closely with cancer specialist to perform fundamental study on molecular signaling in metastasis. I will perform RNA sequencing of isolated CTCs and identify possible candidate genes which are enriched in CTCs and important for metastasis. For example, I may pursue Wnt2 and Fn1, two known candidate genes important in oncogenesis [381], as potential prototypes of CTC-enriched transcripts and accordingly may identify candidate therapeutic targets to prevent the distal spread of cancer. Thus, through a combined using of both engineering tools and biological methods, we may generate an unbiased RNA sequencing profile for CTC-specific expression patterns. This CTC-specific RNA sequencing profile, which is in a urgent

need but currently unavailable, may provide opportunities to find extraordinary subpopulations of cancer cells such as metastasis-initiating cells (MICs) and cancer stem cells (CSCs) among CTCs. Overall, the comprehensive mechanical and molecular profiling of CTCs can help for broad screening of important cancer cell surface markers to search the crucial effective factors in metastasis and could be a paradigm of how advances in engineering tools boost development in medicine.

6.2.3 Blood-on-a-Chip for Point-of-Care Diagnosis

Blood is a treasure of information about the functional status of the whole body [105]. Every second of every day, blood is circulated around the body and takes the reasonability for a lot of critical living functions for human lives. Blood is a complex mixture of many different components including red blood cells, white blood cells, platelets and plasma, and each component play an important role in many live functions [105]. For example, red blood cells deliver oxygen from the lung to all parts of the body then pick up carbon dioxide and remove it from tissues and organs. White blood cells fight infection and play a major role in our immune system. Platelets help the blood clotting process by gathering at the site of an injury and prevent a blood leaking. Plasma is the liquid portion of the blood, a mixture of water, sugar, fat, protein, and salts. The main job of the plasma is to transport blood cells throughout body along with nutrients, waste products, clotting factors, hormones and proteins that help maintain the body a proper working function. In a circumstance of disease such as cancer, we may find abnormal components like rare CTCs in the blood which is indicator of a possible formation of tumor in the body [10, 12, 120]. As a result, blood harbors a massive

amount of information about the functioning of all tissues and organs in the body. Blood cells constantly die and replaced by new ones, and the plasma components such as hormones and proteins are continuously refreshed when blood circulated throughout the body. Whenever occurred an abnormal or dysfunction of any tissues and organs in the body, there will be an instant reflection in the change of the blood component. As such, by analysis of blood we can gain not only the massive amount of but also the freshest information about the status a disease. In addition to its massive information blood can provide, drawing blood is one of the most convenient diagnosis approaches in current clinical practice, hence it enables broad potential biomedical applications for numerous disease diagnosis. As such, blood sample processing and analysis are of great importance for both medical and science applications, and hold a central role in the diagnosis of many physiologic and pathologic conditions, such as immune system dysfunction and cancer. However, tapping into this wealth of information, for clinical and scientific applications, requires not only the understanding of the biology involved but also adequate technologies. Yet, current available sample preparation procedures for blood analysis involve handling multiple steps prone to introducing artifacts, whereas analysis methods commonly require skilled technicians and well-equipped, expensive laboratories.

Recent advances in microfluidics and microfabrication have made possible miniaturization and integration of biosample preparative and analytical techniques on a single chip to enable rapid, sensitive, and multiplexed high-throughput on-chip cell-based assays. Some of these microfluidic tools have been demonstrated as promising technologies with integrated cell trapping and analysis functionalities and a minimum

sample requirement to achieve rapid functional phenotyping analysis of immune cells [67, 70] or CTCs [117, 123, 124] directly isolated from blood within one lab-on-a-chip-type device. Therefore my future research will focus on developing promising microfluidic technologies with integrated cell trapping and analysis functionalities and a minimum sample requirement to achieve rapid functional phenotyping analysis of immune cells, red blood cells, platelets or CTCs directly isolated from blood within one lab-on-a-chip-type device. These types of "blood-on-a-chip" devices are extremely attractive for blood analysis and disease diagnosis.

One good example is new microfluidic chip for point-of-care diagnosis of human immunodeficiency virus (HIV) infection / acquired immumunodeficiency syndrome (AIDS). HIV/AIDS is a severe human immune disease caused by human immunodeficiency virus [382, 383]. It is one of the most destructive pandemics in the world, causing more than 1.8 million deaths per year [383]. Currently, the major HIV diagnosis method is called the antibody test. In this test, HIV antigens are used to capture HIV antibodies in the person's serum. However, most HIV patients will not develop a detectable antibody level until 30 days after infection. Another simpler yet less accurate diagnosis method is WBC count test, especially CD4+ T-cell number counting [33]. CD4+ T-cell is the major leukocyte attacked by HIV, the cell number typically drops below 200 cells/μL when the HIV infection occurs. As a result, the absolute counts of CD4+ T cells and the ratio of CD4+ / CD8+ T cells are commonly used as indicators of the onset of the AIDS and as benchmarks for the initiation of antiviral therapy to treat AIDS. Currently, most of the above well-established diagnosis methods require sophisticate expensive instruments and specifically trained technicians to perform the

tests. However, most patients who suffer from HIV usually live in the developing countries with limited medical resources. Therefore, to make HIV diagnosis more accessible and efficient, I will develop a portable microfluidic platform to measure CD4+/CD8+ T-cell numbers in human blood.

We can utilize our PDMS surface micromachining technique to generate PDMS-based HIV-test device consists of two cell isolation units and each contains a PDMS microfiltration membrane (PMM) with array of through holes for isolation and enumeration of CD4+ and CD8+ T-cells. Similar to our MIPA platform, for isolation and purification of CD4+ and CD8+ T-cells from blood specimens, I will employ a combined use of the PMMs in the device and antibody-conjugated polystyrene microbeads. Using the biotin-streptavidin conjugation chemistry, polystyrene microbeads can be coated with antibodies against cell surface antigens that are specific to the desired subpopulation of immune cells (CD4+ or CD8+ T-cells). When mixed with a blood specimen for 15-30 min, the microbeads could selectively capture desired CD4+ or CD8+ T-cells by recognizing and binding covalently to the CD4 or CD8 surface proteins of the cells. Owing to their significant physical size increase after captured by microbeads (diameter of 15μm), when the blood sample is passing through the PMM, the desired subpopulation of immune cells could be easily isolated and regularly retained on the PMM in the through holes, while the other blood cells including undesired immune cells and erythrocytes (red blood cells) would be eluded through the PMM. For a point-of-care test, the numbers of CD4+ or CD8+ T-cells can be easily counted under an optical microscope due to transparency of PDMS-based device. Hence, this point-of-care HIV-test device does not require sophisticate instruments and specifically trained

technicians to perform the tests, particularly suitable for HIV diagnosis in developing countries. Because of the simplicity and miniaturization of the chip, I expect to provide a simple, economic and fast (entire assay time < 20 min) solution for diagnosis of HIV/AIDS using minutes of blood sample (down to 5 μL/test).

Another blood-on-a-chip prototype we may pursue is high-throughput RBC-Deformability chip for diagnosis of malaria. Malaria is the most deadly parasitic disease threatening 200 million people worldwide and causing nearly one million annual deaths [384]. Researches have demonstrated that red blood cell (RBC) deformability plays a major role in the pathogenesis of malaria [385]. Healthy human RBCs have exceptional deformability enabling them to pass capillaries that are smaller than the diameter of RBCs, which is of crucial importance to both macro and microcirculation. The most severe human malaria parasite, Plasmodium falciparum, invades and develops within RBCs, and transitions through morphologically distinct ring, trophozoite and schizont stages during the 48 hour maturation period within the RBC. While ring stage parasite-infected RBCs are less deformable than uninfected RBCs by only several-fold, late (trophozoite and schizont) stage parasite-infected RBCs are stiffer by a factor of up to 50 or more. Therefore, measurement of the RBC deformability is one of the most efficient ways of diagnosis of malaria. To address this critical need, we can develop a "RBC-Deformability chip" for high-throughput, highly-sensitive, and label-free characterization of RBC deformability at single cell level. Specifically, RBC deformability measurement is made when single RBCs flow through a V-shaped constriction channel that is marginally smaller than RBCs' diameters. Under a fixed pressure, the RBC deformability is simply determined by the penetrating length of the RBC into the

constriction channel. For high-throughput measurement, the RBC-Deformability chip includes an array of constriction channels (up to 10^4) that permits measurement of thousands of RBCs simultaneously. A computer-assisted scanning system will be developed to record the positions of the trapped cells and convert them into the final cell deformability profile. Together, this microfluidics-based RBC-Deformability chip will offer for new solution for diagnosis of malaria and clearly is a prototype of blood-on-a-chip for blood analysis and disease diagnosis.

6.3 Conclusions

Numerous exciting topics exist at the interface between biology and micro/nanotechnology. Taking advantage of state-of-art micro/nanotechnologies and fabricating fascinating functional biomaterials, my doctoral research have addressed numerous important problems in fundamental biology as well as clinical applications in disease diagnosis and treatment. Examples include new micro/nanoengineered functional biomaterials and integreted biosystems for biomedical applications in systems immunology, cancer biology and stem cell-based regenerative medicine. I envision that these interdisciplinary researchs can potentially provid new and better solotions for wide range investigation of the interactions of biological entities (from nanoscale biomolecules to micron-sized mammalian cells) with the micro/nanoscale microenvironment and high throughput quantitative micro/nanoscale analysis of molecular and cellular functions. Finally, I expect that these novel micro/nanoengineered functional biomaterials and biosystems will not only permit advances in engineering but also greatly contribute to improving human health.

Appendix A

Fabrication of MIPA Device

A.1 Silicon Wafer Cleaning

1. Piranha clean (H_2SO_4: H_2O_2 = 1: 1) for 10 min and BHF dip for 1 min.
2. DI water rinse for 10 min and air dry the wafer.
3. Dehydration bake on hotplate for 120°C, 5 min

A.2 Microfluidic Channel Mold Fabrication

1. Photoresist Patterning

a) Spin coat 3 μm SPR220 photoresist and softbake at 110°C for 3min, manually or using ACS 200 cluster tool.

b) Expose the photoresist using MA/BA-6 Mask Aligner (Exposure intensity ~20J/s) for 10s.

c) Develop the exposed photoresist using AZ 300 Developer for 30s, manually or using ACS 200 cluster tool.

2. Plasma Etching

Etch silicon using deep reactive ion-etching (DRIE; Deep Silicon Etcher, STS; Recipe-LNF Pegasus Recipe 1; Etch rate ~ 5μm/min).

3. Silicon Surface Silanization

a) O_2 Plasma activate the Silicon mold surface for 2 min (Plasma Cleaner PDC-001, Harrick Plasma: O_2, 80W, 250 mT, 5min), right before silanization.
b) Silanize the Silicon mold using 100µl of Silane (tridecafluoro- 1, 1, 2, 2,-tetrahydrooctyl)-1-trichlorosilane (United Chemical Technologies) for 1 hr under vacuum in a desiccator.

A.3 PDMS Microfiltration Membrane Fabrication

1. Silicon Surface Silanization

c) O_2 Plasma activate the Silicon wafer surface for 2 min (Plasma Cleaner PDC-001, Harrick Plasma: O_2, 80W, 250 mT, 5min), right before silanization.
d) Silanize the Silicon wafer using 100µl of Silane (tridecafluoro- 1, 1, 2, 2,-tetrahydrooctyl)-1-trichlorosilane (United Chemical Technologies) for 1 hr under vacuum in a desiccator.

2. PDMS Precursor Preparation

a) Mix the Sylgard 184 base and curing agent in ratio of 10: 1.
b) Degas in vacuum desiccator for ~30 min.
c) Spin Coating of the PDMS Membrane
d) Spin coat PDMS precursor at 500 rpm for 10 s (spread) followed by 7200 rpm for 30 s (spin) for a 10 µm membrane.
e) Bake the wafer overnight at 60°C before further processing.

4. Photoresist Patterning

a) O_2 Plasma activate the PDMS membrane surface for 5-10 min (Plasma Cleaner PDC-001, Harrick Plasma: O_2, 80W, 250 mT, 5min), right before photoresisit spin-coating to allow a uniform photoresist coating.
b) Spin coat AZ 9260 photoresist at 500 rpm for 10 s (spread) followed by 2400 rpm for 30 s (spin; 10 µm).
c) Soft bake the wafer with photoresist in an oven at 80°C for 10 min and cool down to room temperature slowly (~20 min).

d) Expose the photoresist to the pattern using a MA/BA-6 Mask Aligner/Bond (Exposure intensity ~20J/s) for 50s.
e) Develop the exposed wafer using AZ 400K developer (Ratio of Developer: Water = 1:4) for ~2 min. Visually inspect the developed wafer very carefully.

5. Plasma Etching of PDMS

a) The patterned wafer is then processed with reactive ion etching (RIE; LAM 9400) using SF_6 and O_2 gas mixtures to transfer patterns from patterned photoresist to the underlying PDMS layer. Recipe: gas (SF_6 (90 sccm) and O_2 (6 sccm)), chamber pressure (0.67 Pa), bias voltage (100 V), RF power (500 W), PDMS etching rate 1 μm/min and photoresist etching rate 0.5 μm/min.
b) Remove the photoresist in PR2000 solution for 5 min, rinse and wash the sample with water and dry the sample with N_2 gun.
c) Bake the sample overnight in a oven at 60°C to let the PDMS recover.

A.4 Device Assembly

1. PDMS Precursor Preparation

a) Mix the Sylgard 184 base and curing agent in ratio of 10: 1.
b) Degas in vacuum desiccator for ~30 min.

2. PDMS Soft Lithography

a) Place the silanized silicon mold in a Petri dish.
b) Pour PDMS precursor over mold, ~1 mm thick (bottom chamber); ~4 mm thick (top chamber).
c) Degas in vacuum desiccator for ~30 min.
d) Bake PDMS in a furnace overnight at 60°C before further processing.
e) Cut and peel the PDMS chambers from silicon mold.

3. Inlet Fabrication

a) Dice and separate the individual PDMS devices.

b) Punch the inlet hole (diameter 1 mm) through the top chamber PDMS using a Biopsy Punch.

4. Bonding of the Membrane with PDMS Top chamber

a) O_2 plasma activate the PDMS membrane and PDMS chamber (top) with microchannel facing upwards in a plasma cleaner (Plasma Cleaner PDC-001, Harrick Plasma: O_2, 80W, 250 mT) for 2 min.
b) Align and bond the top chamber (microchannels facing down) to the membrane.
c) Bake the bonded device in an oven at 90ºC for 5min.
d) Cut the membrane boundaries using a scalpel and gently peel off bonded membrane from the silicon wafer.

5. Outlet Fabrication

In a symmetrically opposite end of the inlet, punch an outlet hole (diameter 1 mm) through the PDMS top chamber and the membrane using a Biopsy Punch.

6. Bonding of the PDMS Bottom Chamber with Cover Glass Substrate

a) O_2 plasma activate a cover glass substrate (No. 1, 18 x 18mm, thickness 150µm and the PDMS bottom chamber, with microchannel facing downwards, in a Plasma Cleaner for 2 min.
b) Bond the bottom chamber (microchannels facing up) to the cover glass substrate.
c) Bake the bonded part in an oven at 90ºC for 5min.

7. Bonding of the PDMS Top Chamber with Membrane to Bottom Chamber

a) O_2 plasma activate the top chamber with the membrane and PDMS bottom chamber on cover glass substrate, with membrane and bottom chamber microchannel facing upwards, in a Plasma Cleaner for 2 min.
b) Align and bond the top chamber with membrane to the bottom chamber.
c) Bake the bonded device in an oven at 90ºC for 5min.
d) Seal the device on the sides to prevent potential flow leakage with PDMS precursor and cure the PDMS in an oven at 90ºC for 1 hr.

Appendix B

Capture of Subpopulations of Immune Cells Using Surface Functionalized Microbeads

B.1 Surface Functionalization of Microbeads with Biotinylated Antibody

1. Vortex the streptavidin-coated microbead suspension (Bangs Lab; diameter 15 μm, supplied at 1% solids) for 20s before use.
2. Wash microbeads 2-3 times. To do the washing, dilute an aliquot of Microbeads with DI water at a 1:10 *v/v* ratio. Centrifuge the diluted microbead suspension at 3000 rpm for 10 min. After washing the microbeads, resuspend the final pellet in 10X PBS (0.1 M PBS, pH 7.4) to a concentration of 0.05% solids (0.5 mg/mL).
3. To this solution, add biotinylated antibody to the washed microbeads suspension. The protein concentration will have to be optimized based on the binding capacity of the microbeads. For example, 200 μL streptavidin-coated microbead suspension (Bangs Lab; diameter 15 μm, supplied at 1% solids) should be diluted in 4 mL 10X PBS (final concentration 300,000 bead/mL) after washing. Then 160 μL biotinylated anti-CD14 anitbody (Invitrogen) should be mixed with the 4 mL diluted microbead suspension.
4. Incubate and mix the solution with a roller mixer (Invitrogen) at 15 rpm at room temperature for 30-40 min.

5. Wash the functionalized microbeads 3 times. To do the washing, dilute the surface functionalized microbead suspension with DI water at a 1:10 *v/v* ratio. Centrifuge the diluted microbead suspension at 3000 rpm for 10 min. After washing the microbeads, resuspend the final pellet to a required concentration in cell culture medium for the following cell isolation. For storage, resuspend the antibody-coated beads in10X PBS to desired storage concentration (often 0.5 mg/mL).

B.2 Capture of Subpopulations of Immune Cells Using Surface Functionalized MicroBeads

1. Mix the surface functionalized microbeads with lysed blood at a optimized bead : cell ratio. For commercial available s-pluriBead (pluriSelect GmbH, Leipzig, Gemany; diameter 32 μm), use 40 μl bead suspension per 1ml lysed blood (10^6 target cells) in 2mL tube (bead: target cell = 1: 3). For the above prepared microbeads (Bangs Lab; diameter 15 μm), bead : target cell = 1 : 2.
2. Incubate and mix the solution with a roller mixer (Invitrogen) at 15 rpm at room temperature for 30-60 min to capture targeted cells.

Appendix C

Human Blood Specimen Collection and Processing

C.1 Human Blood Specimen Collection

Human blood specimens were obtained from healthy donors and collected into the vacutainer containing ethylenediaminetetraacetic acid (EDTA) according to the standard protocol. Human blood specimens were processed and assayed within 6 hrs after blood collection.

C.2 Lysis of Red Blood Cell from Blood

1. Add Lysis Buffer (eBioscience, San Diego, CA) to whole blood at a 10:1 *v/v* ratio.
2. Incubate for 10 minutes at room temperature (no more than 15 minutes).
3. Add 20-30 mL PBS to stop lysis.
4. Spin the cells at 300xg at for 10min, then resuspend the PBMCs in cell culture media to the original volume.
5. Quantify the white blood cell concentration by hemocytometer or flow cytometry.

Note: In general a small number of residual red cells do not interfere with the following assays. However, if required, a second round of lysis can be performed.

Appendix D

AlphaLISA Protocol

D.1 Standard Curve Calibration

1. Analyte Standard Dilution

a) Preparation of 1X AlphaLISA Immunoassay Buffer: Add 2 mL of 10X AlphaLISA Immunoassay Buffer to 18 mL DI H_2O.

b) Preparation of analyte (e.x. human TNF-α) standard dilutions: Reconstitute lyophilized human TNF (0.1 μg) in 100 μL DI H_2O (1 μg/mL) and then the analyte is series diluted1X AlphaLISA Immunoassay Buffer to 10,000 - 1 pg/mL.

2. AlphaLISA Beads Preparation (Prepare just before use)

a) Prepare 10X Acceptor beads + Biotinylated Antibody MIX (250 μg/mL /25 nM): Add 2.5 μL of 5 mg/mL Acceptor beads and 2.5 μL of 500 nM biotinylated antibody to 47.5 μL of 1X AlphaLISA Immunoassay Buffer.

b) Prepare 10X Streptavidin-Donor beads (800 μg/mL): Keep the beads under subdued laboratory lighting. Add 8 μL of 5 mg/mL SA-Donor beads to 42 μL of 1X AlphaLISA Immunoassay Buffer.

3. Assay Loading Procedure in 384-well Microplate:

a) Add 20 μL analyte with various concentrations into a well of a 384-well microplate.

b) Add 2.5 uL 10X Acceptor beads + Biotinylated Antibody MIX (250 μg/mL /25 nM) to each well to achieve a final concentration of 40 ug/mL for Accept beads and 4 nM for Biotinylated Antibody.

c) Incubate 60 min at at 37°C and 5% CO_2.

d) Add 2.5 uL 800 µg/mL Strepatividin-Donor Beads (80 µg/mL final)

e) Incubate 30 min at 37°C and 5% CO_2.

c) Read using PHERAstar MicroPlate Reader (BMG)

D.2 MIPA Device Measurement

1. MIPA Device Preparation

a) Apply O_2 Plasma to activate the top surface of the MIPA device for 2 min to make the top PDMS surface hydrophilic.

b) Add 50uL Pluronics or RPMI cell culture media on the inlet and outlet of MIPA device and put it in the vacuum pump to degas. Slightly reduce the pressure and reintroduce the gas for two times. The device should fill with RPMI without bubble inside.

2. Preparation of Cell Stimuli (Prepare just before use)

a) Preparation of LPS for monocytes: Add 1mg LPS powder into 1mL RPMI media (1000 ug/mL). Dilute the LPS solution into 1000, 500, 100 ng/mL. Keep 1000 ug/mL LPS solution into -20C for future use.

b) Preparation of PMA/Ionomycin for T-cells: First, dilute 2 µl of PMA stock (5 mg/ml) in 200 µl of RPMI culture media to make a stock of 50 µg/ml (diluted PMA). Next, mix 2 µl of diluted PMA (final 50 ng /ml) and 2.7 µl of ionomycin (final 10 µg/ml) in 2 mL of culture media

3. AlphaLISA Beads Preparation: (Prepare just before use)

a) Prepare 10X Acceptor beads + Biotinylated Antibody MIX (250 µg/mL /25 nM): Add 2.5 µL of 5 mg/mL Acceptor beads and 2.5 µL of 500 nM biotinylated antibody to 47.5 µL of 1X AlphaLISA Immunoassay Buffer.

b) Prepare 10X Streptavidin-Donor beads (800 µg/mL): Keep the beads under subdued laboratory lighting. Add 8 µL of 5 mg/mL SA-Donor beads to 42 µL of 1X AlphaLISA Immunoassay Buffer.

4. Assay Loading Procedure in MIPA Device:

a) Inject required volume of cell sample (PBMCs or microbead captured subpopulation of immune cells such as monocytes, T-cells) through inlet using pipette to capture required number of target cells in MIPA device.

b) Inject 50 µL LPS (for monocytes or PBMCs) or PMA/Ionomycin (for T-cells or PBMCs) solution from the inlet using pipette 2-3 times to wash away unwanted cells (red blood cells, immune cells other than target subset) and file the MIPA device with stimulus. After stimulus loading, insert pipette tips into the inlet and outlet of the device to prevent evaporation and provide a shear stress free microenvironment for cell stimulation.

c) Incubate the MIPA device at 37°C and 5% CO_2 for 2 hr to stimulate the cells.

d) Then, remove the pipette tips inserted into the inlet and outlet of MIPA device. Add 2.5 uL 10X Acceptor beads + Biotinylated Antibody MIX (250 µg/mL /25 nM) using pipette from outlet to each device to achieve a final concentration of 40 ug/mL for Accept beads and 4 nM for Biotinylated Antibody in the device. After the loading, leave the pipette tip in outlet and insert another pipette tip in inlet to prevent evaporation. Fully mix the Acceptor beads and Biotinylated Antibody in the device by pipette from inlet and outlet a few times.

e) Incubate 60 min at 37°C and 5% CO_2.

f) Add 2.5 µL 10X Streptavidin Donor beads into device using the same method as described in 4d).

g) Incubate with the cells at 37°C and 5% CO_2 for 30 min.

h) Read AlphaLISA signal using customized optical setup.

D.3 Optical Setup for Detection of AlphaLISA Signal

In this setup, a 500 mW 680 nm laser diode (S-67-500C-100-H, Coherent, Clara, CA) was used as an excitation light to induce singlet oxygen from AlphaLISA donor beads. An electronic shutter (SmartShutter, Lambda SC, Shutter Instrument, Novato, CA) was placed in front of the laser to control the timing of laser pulse for excitation. The

laser light was guided into the inverted fluorescent microscope (Nikon Eclipse Ti-S, Nikon) and passed through the excitation filter (680/13nm BrightLine, Semrock, Rochester, New York) and dichroic mirror (ZT660dcspxr, Chroma, Bellows Falls, VT). The 2X objective (CFI Plan Achromat, N.A. = 0.06, Nikon) was used to focus the excitation light onto the device. After the excitation, the 615nm AlphaLISA emission signal, which passed through the dichroic mirror and the 660 nm shortpass filter (ET660SP, Chroma, Bellows Falls, VT), was then detected by an electron multiplying charge-coupled device (EMCCD) camera (Photometrics, Tucson, AZ). The microscopic analysis software (NIS-Element BR, Nikon) was used to synchronize the timing of shutter in front of laser and the opening time of the EMCCD. The software simultaneously counted the AlphaLISA emission signal intensity from the EMCCD during the measurement.

Appendix E

ELISA Protocol

E.1 Plate and Sample Preparation:

1. **Primary Antibody Immobilization**

   To prepare the ELISA plate, 100μL capture antibody is first prepared and immediately coated on the 96-well microplate. Then seal the plate and incubate it overnight at 4°C.

2. **Sample Pre-treatment**

   For LPS-stimulated cell sample solution, 500μL THP-1 cell solution of 2 x 10^5 cells/mL is first dispenseed into a 48-well microplate. Then, the THP-1 cells are stimulated with 50μL LPS (10-100ng/mL) solution and incubate for 4 hours at 37°C.

3. **Antibody Blocking**

   During the cell incubation, bring the 96-well microplate to room temperature for 30 min, then aspirate capture antibody solution and wash with wash buffer (0.05% Tween 20 in DPBS, pH 7.4) three times. Complete removal of liquid at each step is essential for good performance. For last wash, sit the wash buffer in wells for 1 minute. After the last wash, remove any remaining wash buffer by aspirating or by inverting the plate and blotting it against clean paper towels. After that, block plate by adding 300μL reagent diluent (1% BSA in PBS) to each well and incubate at room temperature on shaker for 1 hour. After the blocking step, repeat the aspiration/wash

steps for three times and incubate for 5 minutes for last wash. The plate is now ready for assay loading.

E.2 Assay Loading Protocol

1. **Sample Loading**

   Add 100μL LPS-stimulated THP-1 cell solution or standard TNF-α analyte (1-10000pg/mL, as a calibration curve) into the antibody-coated 96-well microplate. Then, cover the plate with an adhesive strip and incubate 2 hours at room temperature on shaker, following by aspiration/wash steps for three times.

2. **Detection Antibody Loading**

   Add 100μL detection antibody to each well incubating 2 hours at room temperature on shaker, following by aspiration/wash steps for three times.

3. **HRP/Substrate/Stop Solution Loading**

   Add 100μL streptavidin-HRP to each well for 20 minutes incubation at room temperature. Then, empty wells and wash five times with 200μL wash buffer. Then add 100μL substrate solution to each well and incubate for 20 minutes at room temperature. The reaction takes 8-10 minutes at room temperature. After that, add 50μL stop solution (sulfuric or phosphoric acid) to each well and gently tap the plate to ensure thorough mixing. Because the substrate and stop solution are both light sensitive, the plate should avoid directly placing under the light.

4. **ELISA Signal Reading**

   Finally, use a microplate reader (SpectraMax M2e, Molecular Device) to determine the optical density (OD) of each sample well. The reading wavelength range is set at 450-570 nm. The final OD is the subtracted readings at 540 nm or 570 nm from the readings at 450 nm. This subtraction will correct optical imperfections of the 96-well microplate.

Appendix F

Fabrication and Characterization of Nanorough Glass Samples

F.1 Fabrication of Nanorough Glass Samples

1. Photoresist Patterning

a) Photoresist (SPR220, 3 μm) is first spin-coated on glass wafers (Borofloat 33, Plan Optik, Elsoff, Germany and softbake at 110°C for 3min, manually or using ACS 200 cluster tool.

b) Expose the photoresist using MA/BA-6 Mask Aligner (Exposure intensity ~20J/s) for 10s.

c) Develop the exposed photoresist using AZ 300 Developer for 30s, manually or using ACS 200 cluster tool.

Note: The Photoresist Patterning step can be skipped if no patterning required and unifroem roughness will be generated on the glass surface.

2. Plasma Etching

a) The patterned glass wafer was then processed with RIE (LAM 9400, Lam Research, Fremont, CA) for different periods of time to generate different levels of the nanoscale surface roughness (R_q = 1 - 150 nm) on the exposed regions of the glass wafer, where the photoresist had previously been developed and dissolved. The RIE processing condition used in this work was: SF_6 (8 sccm), C_4F_8 (50 sccm), He (50 sccm), Ar (50 sccm), chamber pressure (1.33 Pa), bias

voltage (100 V), and radio frequency power (500 W). The resulting RIE glass etch rate was about 50 nm/min. For un-patterned nanorough glass samples, bare glass wafers were directly processed with RIE using the same RIE condition as described above.

b) After the RIE process, photoresist is striped using solvents (SPR2000), and the glass wafer was rinsed using distilled water and air dried.
c) The glass wafers were cut into small pieces (e.x. 2 cm × 2 cm) using dicing saw (ADT7100; Advanced Dicing Technologies Ltd., Yokneam, Israel).

F.2 Surface Characterization Using Atomic Force Microscopy

Nanoroughness of the glass or PDMS surfaces was measured at room temperature with atomic force microscopy (Veeco NanoMan Atomic Force Microscope; Digital Instruments Inc., Santa Barbara, CA) using a non-contact, tapping mode and standard Si tapping mode AFM tips. The AFM scan size was set as 10 μm × 10 μm with a scan rate of 1 Hz. The resulting map of the local surface height was represented using AFM topographs. The nanoroughness of each sample was characterized using the root mean square (RMS) roughness R_q of the local surface height over the whole sample area scanned by AFM. The initial surface roughness R_q of unprocessed bare glass wafer and PDMS surface characterized by AFM was about 1 nm and 0.5 nm, respectively.

F.3 Anti-EpCAM Antibody Coating

Glass Surfaces are functionalized with anti-EpCAM antibodies using avidin-biotin chemistry.

1. O_2 plasma treatment for the glass substrates for 1-2min.
2. The glass substrates are modified with 4% (v/v) 3-mercaptopropyl trimethoxysilane (Sigma-Aldrich) in ethanol at room temperature for 30-45 min.
3. Rinse and wash with ethanol.

4. The glass surfaces are then treated with N-ymaleimidobutyryloxy succinimide ester (GMBS, 1 mM or 0.28%; Thermo Fisher Scientific, Rockford, IL) in ethanol for 15 min.
5. Rinse with PBS.
6. The glass surfaces are treated with 10 μg/ml Neutravidin (Thermo Fisher Scientific) in PBS at room temperature for 30 min, leading to immobilization of Neutravidin onto GMBS.
7. The glass surfaces were rinsed with PBS to remove excess free avidin.
8. Add biotinylated anti-EpCAM antibody (R&D Systems, Minneapolis, MN) at a concentration of 10 μg/ml in PBS with 1% (w/v) bovine serum albumin (BSA; Equitech-Bio Inc, Kerrville, TX) and 0.09% (w/v) sodium azide (Sigma-Aldrich) to the glass surfaces and allow to react for 15–30 min
9. The glass substrates are washed with PBS, air dried and stored at ambient temperature for up to three weeks till later use.

Appendix G

Cell Adhesion Strength Measurement Protocol

G.1 Fabrication of PDMS Microfluidic Channels for Cell Adhesion Strength Measurements

G.1.1 Fabrication of Silicon Mold for the Microfluidic Channels

1. Photoresist Patterning

a) Spin coat 3 μm SPR220 photoresist and softbake at 110°C for 3min, manually or using ACS 200 cluster tool.

b) Expose the photoresist using MA/BA-6 Mask Aligner (intensity ~20J/s) for 10s.

c) Develop the exposed photoresist using AZ 300 Developer for 30s, manually or using ACS 200 cluster tool.

2. Plasma Etching

Etch silicon using DRIE (Deep Silicon Etcher, STS; Etch rate ~ 5μm/min).

3. Silicon Surface Silanization

a) O_2 Plasma activate the Silicon mold surface for 2 min (Plasma Cleaner PDC-001, Harrick Plasma: O_2, 80W, 250 mT, 5min), right before silanization.

b) Silanize the Silicon mold using 100μl of Silane (tridecafluoro- 1, 1, 2, 2,-tetrahydrooctyl)-1-trichlorosilane (United Chemical Technologies) for 1 hr under vacuum to facilitate subsequent release of the PDMS from the mold.

G.1.2 Fabrication of the Microfluidic Channels

1. PDMS Precursor Preparation

a) Mix the Sylgard 184 base and curing agent in ratio of 10: 1.

b) Degas in vacuum desiccator for ~30 min.

2. PDMS Soft Lithography

a) Place the silanized silicon mold in a Petri dish.

b) Pour PDMS precursor over mold about 3-5 mm thick.

c) Degas in vacuum desiccator for ~30 min.

d) Bake PDMS in a furnace overnight at 60°C before further processing.

e) Cut and peel off the fully cured PDMS microfluidic channels from silicon mold.

3. Inlet and Outlet Fabrication

a) Dice and separate the individual PDMS devices.

b) Punch the inlet and outlet hole (diameter 0.75 mm) through the PDMS using a Biopsy Punch.

4. Bonding of the PDMS Microfluidic Channels with Glass Substrates

a) O_2 plasma activate glass substrates and the PDMS microfluidic channels with microchannel facing upwards in a plasma cleaner (Plasma Cleaner PDC-001, Harrick Plasma: O_2, 80W, 250 mT) for 2 min.

b) Align and bond the microfluidic channels facing to the glass substrates.

c) Bake the bonded device in an oven at 90ºC for 5 min.

Note: For nanorough glass substrates, a device holder composed of two pieces of polyacrylate plates was home-machined to sandwich the PDMS channel and the nanorough glass substrate using screws at the four corners of the polyacrylate plates. Two through-holes were drilled on the top polyacrylate plate to align with the inlet and outlet holes of the PDMS microfluidic channel, thus allowing a convenience connection of tubings to the microfluidic channel. The complete assembly using polyacrylate plates to hold the PDMS microfluidic channel could endure a back pressure of about 50 psi without leaking.

G.2 Cell Adhesion Strength Measurements

1. Cancer cells (MCF-7, MBA-MB-231, PC3 cells or SUM149) in growth media are first injected into the microfluidic channel by pipette and the cells are allowed to adhere to the bottom glass substrate in an incubator for 12 hrs. An optimized cell loading density (1×10^6 cells mL^{-1}) should be used to ensure a uniform seeding of single cells on the substrate.
2. The microfluidic channel is then connected to a syringe pump.
3. To remove floating cells before cell adhesion strength measurements, PBS is flowed into the channel with a very low flow rate (10 μL min^{-1} for 1 min, then 30 μL min^{-1} for 1 min).
4. Then increase the flow rate to a designated value (50-1500 μL min^{-1}) and maintained constant for 5 min to exert a constant directional fluid shear stress on cells. During the assay, detachment of cells is monitored with the Carl Zeiss Axio Observer Z1 microscope using a 10× objective (0.3 NA; EC Plan NEOFLUAR®; Carl Zeiss MicroImaging). Phase-contract images are recorded at 10 sec intervals for a total period of 5 min.
5. The numbers of adherent cells on glass substrates before and after their treatments with this sustained 5-min directional fluid shear are then quantified from the recorded microscope images using ImageJ (National Institutes of Health, Bethesda, MD).
6. The fluidic shear stress (τ_0) exerted on cells is calculated using the equation $\tau_0 = (6\mu Q) / (WH^2)$, where μ is the viscosity of culture media (~10^{-3} Pa s), Q is the flow rate, and W and H are the microfluidic channel width and height, respectively. Adhesion strength of cells is defined as the fluidic shear stress at which 50% of cells initially attached on glass surfaces would detach after exposed to fluid shear for 5 min.

Appendix H

PDMS Micropost Array for Cellular Traction Force Measurement

H.1 Fabrication of PDMS Micropost Array

H.1.1 Fabrication of Silicon Mold for the PDMS Micropost Array

1. Photoresist Patterning

a) Spin coat 3 μm SPR220 photoresist and softbake at 110°C for 3min, manually or using ACS 200 cluster tool.

b) Expose the photoresist using GCA AS200 AutoStep Aligner.

c) Develop the exposed photoresist using AZ 300 Developer for 30s, manually or using ACS 200 cluster tool.

2. Plasma Etching

Etch silicon using DRIE (Deep Silicon Etcher, STS; Etch rate ~ 5μm/min).

3. Silicon Surface Silanization

a) O_2 Plasma activate the Silicon mold surface for 2 min (Plasma Cleaner PDC-001, Harrick Plasma: O_2, 80W, 250 mT, 5min), right before silanization.

b) Silanize the Silicon mold using 100μl of Silane (tridecafluoro- 1, 1, 2, 2,-tetrahydrooctyl)-1-trichlorosilane (United Chemical Technologies) for 4 hr under vacuum to facilitate subsequent release of the negative PDMS mold.

H.1.2 Fabrication of Negative PDMS Mold

1. PDMS Precursor Preparation

a) Mix the PDMS precursor with base and curing agent in ratio of 10: 1.

b) Degas in vacuum desiccator for ~30 min.

2. PDMS Soft Lithography

a) Place the silanized silicon mold in a Petri dish.

b) Pour PDMS precursor over mold about 3 mm thick.

c) Degas in vacuum desiccator for ~30 min.

d) Fully cure the PDMS in a furnace at 110ºC for 30 min.

e) Peel off the fully cured negative PDMS mold from the silicon mold, and the excessive PDMS is trimmed using a razor blade.

3. Silanization of Negative PDMS Mold

a) O_2 Plasma activate the negative PDMS mold for 2 min (Plasma Cleaner PDC-001, Harrick Plasma: O_2, 80W, 250 mT, 5min), right before silanization.

b) Silanize the Silicon mold using 100µl of Silane (tridecafluoro- 1, 1, 2, 2,-tetrahydrooctyl)-1-trichlorosilane (United Chemical Technologies) for 24 hr under vacuum to facilitate subsequent release of the PDMS micropost array from the negative PDMS mold.

c) Dice and separate the individual negative PDMS molds.

H.1.3 Fabrication of PDMS Micropost Array

1. PDMS Precursor Preparation

a) Mix the PDMS precursor with base and curing agent in ratio of 10: 1.

b) Degas in vacuum desiccator for ~30 min.

2. PDMS Soft Lithography

a) Pour PDMS precursor over the negative PDMS mold.

b) Degas in vacuum desiccator for ~10 min.

c) A 25 cm × 25 cm cover glass, which served as the substrate for the PDMS micropost array, is then placed on top of the negative PDMS mold.
d) Fully cure the PDMS in a furnace at 110ºC for 40 hr.
e) Peel off the fully cured PDMS micropost array from the negative PDMS mold, and the excessive PDMS is trimmed using a razor blade.
f) Sonicate the PDMS microposts in 100% ethanol for 30 s to regenerated freestanding PDMS microposts which may be collapsed in the peeling process.
g) Dry-release the PDMS micropost array with liquid CO_2 using the critical point dryer.

H.2 Surface Functionalization of PDMS Micropost Array

H.2.1 Fabrication of PDMS Stamps for Microcontact Printing

1. Mix the PDMS precursor with base and curing agent in ratio of 30: 1.
2. Pour PDMS precursor in a Petri dish about 3 mm thick.
3. Degas in vacuum desiccator for ~30 min.
4. Fully cure the PDMS in a furnace at 110ºC for 30 min.
5. Dice and PDMS into individual PDMS stamps (5mm × 5 mm) with flat surface.

H.2.2 Microcontact Printing

1. Ink the flat 30:1 PDMS stamp with fibronectin (BD Biosciences, San Jose, CA) at a saturating concentration of 50 mg mL^{-1} in distilled water for 1 hr at room temperature.
2. The PDMS stamp is then thoroughly rinsed with distilled water and blown dry with nitrogen gas.
3. In parallel, the PDMS micropost array is treated with ultraviolet (UV) ozone (UV-ozone cleaner; Jelight, Irvine, CA) for 7 min to ionize the PDMS surface and thus facilitate transfer of ECM molecules from the stamp to the PDMS micropost tops.

4. The fibronectin-coated PDMS stamp is then gently placed in conformal contact with the PDMS micropost array for 10s to complete the protein transfer process.
5. To utilize the PDMS micropost array for live-cell traction force measurements, the PDMS microposts are stained by rinsing in a 5 μg/mL 1,1′-dioleyl-3,3,3′,3′-tetramethylindocarbocyanine methanesulfonate (Δ^9-DiI; Invitrogen) solution.
6. Rinse wash with distilled water.
7. Pluronics F127 NF dissolved in PBS (0.2%, *w*/*v*; BASF, Ludwigshafen, Germany) is then adsorbed to the PDMS surface for 1 hr at room temperature to prevent protein adsorption to nonfunctionalized portions of the PDMS micropost array.
8. Rinse wash with distilled water.

H.3 Quantification of Cellular Traction Force

Cell traction forces are quantified as described as follows. In brief, phase-contrast images of live cells and fluorescence images of Δ^9-DiI stained PDMS microposts underlying the cells are taken at the focal plane passing through the top surface of the posts with a 40× objective on the Zeiss Observer Z1 microscope attached with the AxioCam camera. The microscope is enclosed in the Carl Zeiss XL S1 environmental chamber to maintain the experimental environment at 37°C and 5% CO_2. Images are then analyzed with a custom-developed MATLAB program to calculate the deflection δ of the post centroid from its ideal position determined by the free and undeflected posts, which is then converted to the horizontal traction force f using the expression $f = K\delta$, where K is the nominal spring constant of the PDMS micropost calculated from the *Euler-Bernoulli* beam theory.

Appendix I

General Cell Related Assays

I.1 Cell Culture and Reagents

THP-1 cells (ATCC, Manassas, VA) are cultured in the cell growth medium (RPMI-1640, ATCC, Manassas, VA) supplemented with 0.05 mM 2-mercaptoethanol (Invitrogen, Carlsbad, CA) and 10% (*v*/*v*) heat-inactivated fetal bovine serum (FBS; Atlanta Biological, Atlanta, GA). Cells are maintained at 37^{o}C with 5% CO_2 and 100% humidity and passaged every two days.

NIH/3T3 mouse embryonic fibroblasts (ATCC, Manassas, VA) are maintained in a growth medium consisting of high-glucose Dulbecco's modified Eagle's medium (DMEM; Invitrogen, Carlsbad, CA) supplemented with 10% bovine serum (Atlanta Biological, Atlanta, GA), 100 μg mL^{-1} L-glutamine, 100 units mL^{-1} penicillin, and 100 μg mL^{-1} streptomycin. Fresh 0.25% trypsin-EDTA in phosphate *buffered* saline (PBS) is used to re-suspend NIH/3T3 cells. NIH/3T3 cells are seeded at a low density (3,000 cells/cm^2) in the growth medium onto the glass or PDMS surfaces.

hESCs (H9; WiCell, Madison, WI) are cultured on a feeder-free synthetic polymer coating (PMEDSAH) [386, 387] with the Human-Cell-Conditioned Medium (hCCM, GlobalStem, Rockville, MD) at 37ºC in 5% CO_2. hESC colonies are observed every 24 hr using a Leica stereomicroscope (Leica Microsystems Inc, Buffalo Grove, IL). Differentiated cells are removed mechanically using a sterile pulled-glass pipette. The culture medium is replaced every 24 hr. Cultures are passaged every 4-7 days.

Hela and MCF-7 cells (ATCC, Manassas, VA) are maintained in growth media consisting of high-glucose Dulbecco's modified Eagle's medium (DMEM; Invitrogen, Carlsbad, CA) supplemented with 10% fetal bovine serum (Atlanta Biological, Atlanta, GA), 0.5 μg mL^{-1} Fungizone (Invitrogen), 5 μg mL^{-1} Gentamicin (Invitrogen), 100 units mL^{-1} penicillin, and 100 μg mL^{-1} streptomycin. PC-3 and MDA-MB-231 cells are cultured in growth media (RPMI-1640, ATCC) supplemented with 10% fetal bovine serum (Atlanta Biological), 0.5 μg mL^{-1} Fungizone (Invitrogen), 5 μg mL^{-1} Gentamicin (Invitrogen), 100 units mL^{-1} penicillin, and 100 μg mL^{-1} streptomycin. SUM149 cells are cultured in growth media (Ham's F-12 w/L-glutamine, Fisher Scientific, Hanover Park, IL) supplemented with 5% fetal bovine serum (Atlanta Biological), 0.5 μg mL^{-1} Fungizone (Invitrogen), 5 μg mL^{-1} Gentamicin (Invitrogen), 5 μg mL^{-1} Insulin (Sigma-Aldrich, St. Louis, MO), 1 μg mL^{-1} Hydrocortisone (Sigma-Aldrich), 50 units mL^{-1} penicillin, and 50 μg mL^{-1} streptomycin. Cells are maintained at 37ºC with 5% CO_2 and 100% humidity. Fresh 0.25% trypsin-EDTA in phosphate buffered saline (PBS) is used to re-suspend cells.

I.2 SEM Specimen Preparation

Cells are washed three times with 50 mM Na-cacodylate buffer (pH 7.3; Sigma-Aldrich, St. Louis, MO), fixed for 1 hr with 2% glutaraldehyde (Electron Microscopy Sciences, Hatfield, PA) in 50 mM Na-cacodylate buffer, and dehydrated in a graded series of ethanol concentrations through 100% over a period of 1.5 hr. Dehydration in 100% ethanol is performed three times. Dehydrated samples are then dried with liquid CO_2 using a super critical point dryer (Samdri®-PVT-3D, Tousimis, Rockville, MD). Samples are mounted on stubs, sputtered with gold palladium, observed and photographed under SEM (Hitachi SU8000 Ultra-High Resolution SEM; Hitachi High Technologies America, Inc., Pleasanton, CA).

I.3 EdU Cell Proliferation Assay

For the EdU cell proliferation assay, cells are first starved at confluence in the growth medium supplemented with 0.5% bovine serum (Invitrogen) for 48 hr to synchronize cell cycle before trypsinization. Synchronized cells are re-plated on the glass substrates and recovered in the complete growth medium for 12 to 24 hr, and are then exposed to 4 μM 5-ethynyl-2′-deoxyuridine (EdU; Invitrogen) in the growth medium for 8 hr. Cells are then fixed with 3.7% formaldehyde (Electron Microscopy Science) in PBS, permeabilized with 0.3% Triton X-100 (Roche Applied Science, Indianapolis, IN) in PBS, blocked with 10% goat serum, and stained with Alexa Fluor 488 conjugated azide targeting the alkyne groups in EdU that is incorporated in newly synthesized DNA. Cells are co-stained with Hoechst 33342 (Invitrogen) to visualize cell nucleus.

I.4 Immunofluorescence Staining

In brief, cells were incubated in an ice-cold cytoskeleton buffer (50 mM NaCl, 150 mM sucrose, 3 mM $MgCl_2$, 1 μg ml^{-1} aprotinin, 1 μg ml^{-1} leupeptin, and 1 μg ml^{-1} pepstatin) for 1 min, and then permeabilized for 1 min in the cytoskeleton buffer supplemented with 0.5% Triton X-100. Detergent-extracted cells were fixed with 4% paraformaldehyde in PBS for 30 min, washed with PBS, incubated with 10% goat serum (Invitrogen) for 1 hr, incubated with a primary antibody to vinculin produced in mouse (Sigma-Aldrich) for 1 hr, and stained with Alexa Fluor 488 conjugated goat anti-mouse IgG secondary antibody (Invitrogen) for 1 hr. Alexa Fluor 555 conjugated phalloidin (Invitrogen) and DAPI were used to visualize F-actin and nucleus, respectively.

In brief, cells are incubated in an ice-cold cytoskeleton buffer (50 mM NaCl, 150 mM sucrose, 3 mM $MgCl_2$, 1 μg mL^{-1} aprotinin, 1 μg mL^{-1} leupeptin, and 1 μg mL^{-1} pepstatin) for 1 min and then permeabilized with 0.5% Triton X-100 (Roche Applied Science, Indianapolis, IN) in the cytoskeleton buffer for 1 min. Detergent-extracted cells are fixed with 4 % paraformaldehyde (Electron Microscopy Sciences) in PBS for 30 min and washed three times with PBS. The fixed cells are then incubated with 10% goat serum

(Invitrogen) for 1 hr and then primary antibodies for 1 hr and Alexa Fluor 488, 555 or 647 conjugated IgG secondary antibodies for 1 hr. Alexa Fluor 555 conjugated phalloidin (Invitrogen) and 4',6-diamidino-2-phenylindole (DAPI; Invitrogen) are add with secondary antibodies for visualization of actin microfilaments and nucleus, respectively. After each incubation steps, cells are washed with PBS 2-3 times.

I.5 Quantitative Analysis of Cell Spread Area and Focal Adhesion

In brief, immunofluorescence images of actin CSK and vinculin are obtained using epi-fluorescence microscopy (Carl Zeiss Axio Observer Z1 Carl Zeiss MicroImaging, Thornwood, NY) equipped with a thermoelectrically-cooled monochrome CCD camera (AxioCam camera; Carl Zeiss MicroImaging) and a 40× objective (0.75 NA; EC Plan NEOFLUAR®; Carl Zeiss MicroImaging). Images are captured using the Axiovision Software (Carl Zeiss MicroImaging) and processed using custom-developed MATLAB programs (Mathworks, Natick, MA). To determine the cell spread area, the Canny edge detection method is used to binarize the actin fibers and FAs in the images, and then image dilation, erosion, and fill operations were used to fill in the gaps between the white pixels in the images. The resultant white pixels are summed to quantify cell spread area. To quantify FA number and area, the grayscale vinculin image is thresholded to produce a black and white FA image from which the white pixels, representing FAs, are counted and summed.

I.6 Quantitative Analysis of Cell Migration

Timelapse microscopy experiments are performed for cell migration assays. Individual cells are chosen at random, and their phase-contract images are recorded with 5-min intervals for a total period of 20 hr with the Carl Zeiss Axio Observer Z1 microscope using a 10× objective (0.3 NA; EC Plan NEOFLUAR®; Carl Zeiss MicroImaging). The microscope is enclosed in an enviromental chamber (XL S1

chamber; Carl Zeiss MicroImaging) to maintain the experimental environment at 37°C and 5% CO_2. Cell migration trajectories and speeds are determined from the recorded microscope images using ImageJ (National Institutes of Health, Bethesda, MD) and the manual object tracking plug-in MTrackJ (developed by Dr. E. Meijering, Biomedical Imaging Group of Rotterdam, University Medical Center of Rotterdam, Netherlands).

I.7 Cell Motility Assay

The Cellomics Cell Motility kit (Thermo Scientific, Waltham, MA) was used to determine cell motility. According to the manufacturer's protocol, single cell suspensions were plated in three wells of a 96-well plate that had previously been coated with blue fluorescent microbeads. After 24 hr of incubation, the area a cell migrated was represented by the negative space in the microbead carpet that was pushed away or phagocytosed by the cell. Cells were then fixed, and the migration tracks were imaged using fluorescence microscopy with an Olympus DP26 single chip color CCD camera and an Olympus IX-51 inverted microscope (Olympus, Center Valley, PA). To quantify cell motility, the whole sample surface area was imaged and the image processing software ImageJ (National Institutes of Health, Bethesda, MD) was then used to determine the migration track area of each cell.

I.8 ALDEFLUOR Assay

The ALDEFLUOR assay was performed using the ALDEFLOUR Kit (Stemcell Technologies, Vancouver, Canada) according to the manufacturer's instructions[189]. Briefly, ALDEFLUOR treated cells quenched with ALDH inhibitor diethylaminobenzaldehyde (DEAB) were used to set the ALDEFLUOR-positive FACS gate, which we defined as a gate containing less than 0.1% of DEAB-treated cells. Cells treated with ALDEFLUOR alone were then sorted by FACS and used for downstream experiments. SUM149 cells above this fluorescence threshold were sorted as ALDH+ and the bottom matching percentage was sorted as ALDH-.

I.9 Cancer Cell Invasion Assay

In vitro invasion was assayed using the Biocoat Matrigel invasion chamber (BD Biosciences, San Jose, CA). Cells were plated in triplicate in the top portion of the invasion chamber in serum-free medium with 5% serum growth medium in the bottom chamber to induce invasion through the Matrigel membrane. After 24 hr of incubation, non-invading cells were removed from the top chamber with a cotton swab, and invading cells were fixed with formaldehyde and stained with 1% crystal violet. Matrigel membranes were then removed and de-stained in 10% acetic acid, and an VersaMax optical density reading (Molecular Devices, Sunnyvale, CA) of the acetic acid was taken at 590 nm. In some experiments, Matrigel membranes stained with crystal violet were imaged with invaded cells manually counted.

I.10 Cell Proliferation Assay

Cell proliferation rates were quantified using an MTT Cell Proliferation Assay Kit (Life technologies, Grand Island, NY). Cells were sorted by FACS and plated in triplicate onto 96-well plates. MTT staining and a subsequent optical density reading (Molecular Devices VersaMax) at 590 nm were carried out at 24 hr, 36 hr, 72 hr, and 96 hr post sorting.

I.11 Cell Deformability Measurement

The cell deformability was measured using a PDMS-based microfluidic deformability microcytometer developed in our lab (fabrication process is similar to Appendix G1). The deformability microcytometer contains an array of funnel-shaped long confining microchannels that trap individual live cancer cells in each channel for single cell deformability measurement. Each channel has a length of 300 μm, a height of 30 μm, a width at the wide end (entry) of 30 μm and a width at the narrow end of 4 μm. The

channel wall is pre-coated with Pluronic-127 (Sigma) for 30 min such that friction between the cell and the channel wall can be neglected. Single cancer cells in suspension are first loaded into the channel using a pressure pump (ELVESYS, Paris, French) under low pressure (0.1-0.5 kPa). The differential pressure acting on cancer cells will gradually push the cells down the funnel, and ultimately the motion of cancer cells will stop due to the confining channel and the cells will be trapped in place. After the cell trapping, the loading pressure is gradually increased in steps (0.5 kPa for each step) to push the cell further into the channel. The trapped cells will have different deformation under different pressure. For inert microfluidic channels where cell trapping is dictated by steric interactions of cancer cells with the confining channel, the penetration length (L) of individual cancer cells into the confining channel will be purely determined by cell size and deformability. Thereby, the single cell deformability can be calculated based on model equation $Deformability = 16.9 \times d \times (A \times \Delta P)^{-1}$, where ΔP is the change of the flow pressure, d is the penetrating length under the pressure change, and A is the projective area of the cell. Cell volume V is calculated as $V = (4 \times A \times \pi^{-1})^{-1/2}$. During the assay, deformed cells were monitored with the Carl Zeiss Axio Observer Z1 microscope using a 10× objective (0.3 NA; EC Plan NEOFLUAR®; Carl Zeiss MicroImaging). Phase-contrast images were recorded. The penetration length (L) and the longitudinal and lateral diameters (D_{long} and D_{lat}) of each cell for each pressure were quantified from the recorded microscope images using ImageJ (National Institutes of Health, Bethesda, MD) to calculate the projective area of the cell $A \approx 0.25\pi \times D_{long} \times D_{lat}$.

I.12 Western Blot Analysis

Whole cell lysates are prepared from cells, separated on 7.5% SDS-polyacrylamide gel and transferred to PVDF membranes. The membranes are incubated with 5% milk in PBS for 1 hr and then incubated with primary antibodies overnight at 4ºC. Primary antibodies used in this thesis are as follows: mouse anti-NMMIIA (1:1000; Abcam, Cambridge, MA), mouse anti-E-cadherin (1:1000; Invitrogen, Carsbad, CA), mouse anti-vinculin (1:1000; Sigma-Aldrich, St. Louis, MO), mouse anti-FAK (1:500; BD

Biosciences, San Diego, CA), rabbit anti-Oct4 (1:2000; Santa Cruz, Santa Cruz, CA), and rabbit anti-β-actin (1:1000; Cell Signaling, Danvers, MA). Blots are incubated with peroxidase-coupled secondary antibodies (Promega, Madison, WI) for 1 hr, and protein expression is detected with SuperSignal West Pico Chemiluminescent Substrate (Thermo Scientific, Rockford, IL).

References

[1] R. S. Hotchkiss and I. E. Karl, "The pathophysiology and treatment of sepsis," *New England Journal of Medicine,* 348, 138-50, 2003.

[2] G. Monneret, F. Venet, A. Pachot, and A. Lepape, "Monitoring immune dysfunctions in the septic patient: a new skin for the old ceremony," *Molecular Medicine,* 14, 64-78, 2008.

[3] J. S. Boomer, K. To, K. C. Chang, O. Takasu, D. F. Osborne, A. H. Walton*, et al.*, "Immunosuppression in patients who die of sepsis and multiple organ failure," *Journal of the American Medical Association,* 306, 2594-605, 2011.

[4] T. T. Cornell, L. Sun, M. W. Hall, J. G. Gurney, M. J. Ashbrook, R. G. Ohye*, et al.*, "Clinical implications and molecular mechanisms of immunoparalysis after cardiopulmonary bypass," *Journal of Thoracic and Cardiovascular Surgery,* 2011.

[5] T. M. Clay, A. C. Hobeika, P. J. Mosca, H. K. Lyerly, and M. A. Morse, "Assays for monitoring cellular immune responses to active immunotherapy of cancer," *Clinical Cancer Research,* 7, 1127-35, 2001.

[6] R. A. Seder, P. A. Darrah, and M. Roederer, "T-cell quality in memory and protection: implications for vaccine design," *Nature Reviews Immunology,* 8, 247-58, 2008.

[7] W. Chen, R. H. Lam, and J. Fu, "Photolithographic surface micromachining of polydimethylsiloxane (PDMS)," *Lab on a Chip,* 12, 391-5, 2012.

[8] N. T. Huang, W. Chen, B. R. Oh, T. T. Cornell, T. P. Shanley, J. Fu*, et al.*, "An integrated microfluidic platform for in situ cellular cytokine secretion immunophenotyping," *Lab on a Chip,* 12, 4093-101, 2012.

[9] W. Chen, N. T. Huang, B. Oh, R. H. Lam, R. Fan, T. T. Cornell*, et al.*, "Surface-micromachined microfiltration membranes for efficient isolation and functional immunophenotyping of subpopulations of immune cells," *Advanced Healthcare Materials,* 2, 965-75, 2013.

[10] M. Yu, S. Stott, M. Toner, S. Maheswaran, and D. A. Haber, "Circulating tumor cells: Approaches to isolation and characterization," *Journal of Cell Biology,* 192, 373-382, 2011.

[11] K. Pantel, R. H. Brakenhoff, and B. Brandt, "Detection, clinical relevance and specific biological properties of disseminating tumour cells," *Nature Reviews Cancer,* 8, 329-340, 2008.

[12] M. Cristofanilli, G. T. Budd, M. J. Ellis, A. Stopeck, J. Matera, M. C. Miller*, et al.*, "Circulating tumor cells, disease progression, and survival in metastatic breast cancer," *New England Journal of Medicine,* 351, 781-791, 2004.

[13] D. F. Hayes, M. Cristofanilli, G. T. Budd, M. J. Ellis, A. Stopeck, M. C. Miller*, et al.*, "Circulating tumor cells at each follow-up time point during therapy of metastatic breast cancer patients predict progression-free and overall survival," *Clinical Cancer Research,* 12, 4218-4224, 2006.

[14] U. De Giorgi, V. Valero, E. Rohren, S. Dawood, N. T. Ueno, M. C. Miller*, et al.*, "Circulating tumor cells and [18F]fluorodeoxyglucose positron emission

tomography/computed tomography for outcome prediction in metastatic breast cancer," *Journal of Clinical Oncology,* 27, 3303-11, 2009.

[15] M. C. Liu, P. G. Shields, R. D. Warren, P. Cohen, M. Wilkinson, Y. L. Ottaviano*, et al.*, "Circulating tumor cells: a useful predictor of treatment efficacy in metastatic breast cancer," *Journal of Clinical Oncology,* 27, 5153-9, 2009.

[16] E. Botteri, M. T. Sandri, V. Bagnardi, E. Munzone, L. Zorzino, N. Rotmensz*, et al.*, "Modeling the relationship between circulating tumour cells number and prognosis of metastatic breast cancer," *Breast Cancer Research and Treatment,* 122, 211-217, 2010.

[17] A. Gradilone, G. Naso, C. Raimondi, E. Cortesi, O. Gandini, B. Vincenzi*, et al.*, "Circulating tumor cells (CTCs) in metastatic breast cancer (MBC): prognosis, drug resistance and phenotypic characterization," *Annals of Oncology,* 22, 86-92, 2011.

[18] J. Clark, G. Attard, S. Jhavar, P. Flohr, A. Reid, J. De-Bono*, et al.*, "Complex patterns of ETS gene alteration arise during cancer development in the human prostate," *Oncogene,* 27, 1993-2003, 2008.

[19] D. C. Danila, G. Heller, G. A. Gignac, R. Gonzalez-Espinoza, A. Anand, E. Tanaka*, et al.*, "Circulating tumor cell number and prognosis in progressive castration-resistant prostate cancer," *Clinical Cancer Research,* 13, 7053-8, 2007.

[20] J. S. de Bono, H. I. Scher, R. B. Montgomery, C. Parker, M. C. Miller, H. Tissing*, et al.*, "Circulating tumor cells predict survival benefit from treatment in metastatic castration-resistant prostate cancer," *Clinical Cancer Research,* 14, 6302-9, 2008.

[21] M. A. Leversha, J. Han, Z. Asgari, D. C. Danila, O. Lin, R. Gonzalez-Espinoza*, et al.*, "Fluorescence in situ hybridization analysis of circulating tumor cells in metastatic prostate cancer," *Clinical Cancer Research,* 15, 2091-7, 2009.

[22] T. Okegawa, K. Nutahara, and E. Higashihara, "Prognostic significance of circulating tumor cells in patients with hormone refractory prostate cancer," *Journal of Urology,* 181, 1091-7, 2009.

[23] S. L. Stott, R. J. Lee, S. Nagrath, M. Yu, D. T. Miyamoto, L. Ulkus*, et al.*, "Isolation and characterization of circulating tumor cells from patients with localized and metastatic prostate cancer," *Science Translational Medicine,* 2, 25ra23, 2010.

[24] S. Maheswaran, L. V. Sequist, S. Nagrath, L. Ulkus, B. Brannigan, C. V. Collura*, et al.*, "Detection of mutations in EGFR in circulating lung-cancer cells," *New England Journal of Medicine,* 359, 366-77, 2008.

[25] R. L. Katz, W. He, A. Khanna, R. L. Fernandez, T. M. Zaidi, M. Krebs*, et al.*, "Genetically abnormal circulating cells in lung cancer patients: an antigen-independent fluorescence in situ hybridization-based case-control study," *Clinical Cancer Research,* 16, 3976-87, 2010.

[26] S. J. Cohen, C. J. A. Punt, N. Iannotti, B. H. Saidman, K. D. Sabbath, N. Y. Gabrail*, et al.*, "Relationship of circulating tumor cells to tumor response, progression-free survival, and overall survival in patients with metastatic colorectal cancer," *Journal of Clinical Oncology,* 26, 3213-3221, 2008.

[27] C. A. Klein, "Parallel progression of primary tumours and metastases," *Nature Reviews Cancer,* 9, 302-312, 2009.
[28] C. L. Sawyers, "The cancer biomarker problem," *Nature,* 452, 548-52, 2008.
[29] W. Chen, S. Weng, F. Zhang, S. Allen, X. Li, L. Bao*, et al.*, "Nanoroughened surfaces for efficient capture of circulating tumor cells without using capture antibodies," *ACS Nano,* 7, 566-75, 2013.
[30] F. M. Robertson, M. Bondy, W. Yang, H. Yamauchi, S. Wiggins, S. Kamrudin*, et al.*, "Inflammatory breast cancer: the disease, the biology, the treatment," *CA: A Cancer Journal for Clinicians,* 60, 351-75, 2010.
[31] H. Yamauchi, W. A. Woodward, V. Valero, R. H. Alvarez, A. Lucci, T. A. Buchholz*, et al.*, "Inflammatory breast cancer: what we know and what we need to learn," *Oncologist,* 17, 891-9, 2012.
[32] E. Charafe-Jauffret, C. Ginestier, F. Iovino, C. Tarpin, M. Diebel, B. Esterni*, et al.*, "Aldehyde dehydrogenase 1-positive cancer stem cells mediate metastasis and poor clinical outcome in inflammatory breast cancer," *Clinical Cancer Research,* 16, 45-55, 2010.
[33] D. C. Douek, J. M. Brenchley, M. R. Betts, D. R. Ambrozak, B. J. Hill, Y. Okamoto*, et al.*, "HIV preferentially infects HIV-specific CD4+ T cells," *Nature,* 417, 95-8, 2002.
[34] G. Pantaleo and A. Harari, "Functional signatures in antiviral T-cell immunity for monitoring virus-associated diseases," *Nature Reviews Immunology,* 6, 417-23, 2006.
[35] W. H. Reece, M. Pinder, P. K. Gothard, P. Milligan, K. Bojang, T. Doherty*, et al.*, "A CD4(+) T-cell immune response to a conserved epitope in the circumsporozoite protein correlates with protection from natural Plasmodium falciparum infection and disease," *Nature Medicine,* 10, 406-10, 2004.
[36] A. Revzin, E. Maverakis, and H. C. Chang, "Biosensors for immune cell analysis-A perspective," *Biomicrofluidics,* 6, 21301-2130113, 2012.
[37] S. Gordon and P. R. Taylor, "Monocyte and macrophage heterogeneity," *Nature Reviews Immunology,* 5, 953-64, 2005.
[38] J. J. O'Shea, C. A. Hunter, and R. N. Germain, "T cell heterogeneity: firmly fixed, predominantly plastic or merely malleable?," *Nature Immunololgy,* 9, 450-3, 2008.
[39] S. M. Kaech and E. J. Wherry, "Heterogeneity and cell-fate decisions in effector and memory CD8+ T cell differentiation during viral infection," *Immunity,* 27, 393-405, 2007.
[40] F. Re and J. L. Strominger, "Heterogeneity of TLR-induced responses in dendritic cells: from innate to adaptive immunity," *Immunobiology,* 209, 191-8, 2004.
[41] P. Salgame, J. S. Abrams, C. Clayberger, H. Goldstein, J. Convit, R. L. Modlin*, et al.*, "Differing lymphokine profiles of functional subsets of human CD4 and CD8 T cell clones," *Science,* 254, 279-82, 1991.
[42] R. F. Siliciano, T. Lawton, C. Knall, R. W. Karr, P. Berman, T. Gregory*, et al.*, "Analysis of host-virus interactions in AIDS with anti-gp120 T cell clones: effect of HIV sequence variation and a mechanism for CD4+ cell depletion," *Cell,* 54, 561-75, 1988.

[43] R. S. Veazey, P. A. Marx, and A. A. Lackner, "The mucosal immune system: primary target for HIV infection and AIDS," *Trends in Immunology,* 22, 626-33, 2001.
[44] A. Harari, C. Cellerai, and G. Pantaleo, "Role of HIV-1-specific CD4 T cells," *Current Opinion in HIV and AIDS,* 1, 22-7, 2006.
[45] S. Romagnani, "Th1 and Th2 in human diseases," *Clinical Immunology and Immunopathology,* 80, 225-35, 1996.
[46] M. Clerici, F. T. Hakim, D. J. Venzon, S. Blatt, C. W. Hendrix, T. A. Wynn*, et al.*, "Changes in interleukin-2 and interleukin-4 production in asymptomatic, human immunodeficiency virus-seropositive individuals," *Journal of Clinical Investigation,* 91, 759-65, 1993.
[47] J. L. Flynn, J. Chan, K. J. Triebold, D. K. Dalton, T. A. Stewart, and B. R. Bloom, "An essential role for interferon gamma in resistance to Mycobacterium tuberculosis infection," *Journal of Experimental Medicine,* 178, 2249-54, 1993.
[48] A. Harari, V. Dutoit, C. Cellerai, P. A. Bart, R. A. Du Pasquier, and G. Pantaleo, "Functional signatures of protective antiviral T-cell immunity in human virus infections," *Immunology Review,* 211, 236-54, 2006.
[49] P. A. Bart and G. Pantaleo, "Immune-based interventions in HIV infection: doing the right studies, getting the right answers," *AIDS,* 20, 617-8, 2006.
[50] D. G. Remick, "Pathophysiology of sepsis," *American Journal of Pathology,* 170, 1435-44, 2007.
[51] T. J. Murphy, H. M. Paterson, J. A. Mannick, and J. A. Lederer, "Injury, sepsis, and the regulation of Toll-like receptor responses," *Journal of Leukocyte Biology,* 75, 400-7, 2004.
[52] J. Cohen, "The immunopathogenesis of sepsis," *Nature,* 420, 885-91, 2002.
[53] J. H. Cox, G. Ferrari, and S. Janetzki, "Measurement of cytokine release at the single cell level using the ELISPOT assay," *Methods,* 38, 274-82, 2006.
[54] M. Aidoo and V. Udhayakumar, "Field studies of cytotoxic T lymphocytes in malaria infections: implications for malaria vaccine development," *Parasitol Today,* 16, 50-6, 2000.
[55] M. R. Betts, J. P. Casazza, B. A. Patterson, S. Waldrop, W. Trigona, T. M. Fu*, et al.*, "Putative immunodominant human immunodeficiency virus-specific CD8(+) T-cell responses cannot be predicted by major histocompatibility complex class I haplotype," *Journal of Virology,* 74, 9144-51, 2000.
[56] F. Kern, I. P. Surel, N. Faulhaber, C. Frommel, J. Schneider-Mergener, C. Schonemann*, et al.*, "Target structures of the CD8(+)-T-cell response to human cytomegalovirus: the 72-kilodalton major immediate-early protein revisited," *Journal of Virology,* 73, 8179-84, 1999.
[57] A. A. Pathan, K. A. Wilkinson, R. J. Wilkinson, M. Latif, H. McShane, G. Pasvol*, et al.*, "High frequencies of circulating IFN-gamma-secreting CD8 cytotoxic T cells specific for a novel MHC class I-restricted Mycobacterium tuberculosis epitope in M. tuberculosis-infected subjects without disease," *European Journal of Immunology,* 30, 2713-21, 2000.
[58] S. Janetzki, D. Palla, V. Rosenhauer, H. Lochs, J. J. Lewis, and P. K. Srivastava, "Immunization of cancer patients with autologous cancer-derived heat shock

protein gp96 preparations: a pilot study," *International Journal of Cancer,* 88, 232-8, 2000.

[59] J. J. Lewis, S. Janetzki, S. Schaed, K. S. Panageas, S. Wang, L. Williams*, et al.*, "Evaluation of CD8(+) T-cell frequencies by the Elispot assay in healthy individuals and in patients with metastatic melanoma immunized with tyrosinase peptide," *International Journal of Cancer,* 87, 391-8, 2000.

[60] M. R. Betts, D. R. Ambrozak, D. C. Douek, S. Bonhoeffer, J. M. Brenchley, J. P. Casazza*, et al.*, "Analysis of total human immunodeficiency virus (HIV)-specific CD4(+) and CD8(+) T-cell responses: relationship to viral load in untreated HIV infection," *Journal of Virology,* 75, 11983-91, 2001.

[61] M. Catalfamo, C. Wilhelm, L. Tcheung, M. Proschan, T. Friesen, J. H. Park*, et al.*, "CD4 and CD8 T cell immune activation during chronic HIV infection: roles of homeostasis, HIV, type I IFN, and IL-7," *Journal of Immunology,* 186, 2106-16, 2011.

[62] A. M. Green, R. DiFazio, and J. L. Flynn, "IFN-gamma from CD4 T Cells Is Essential for Host Survival and Enhances CD8 T Cell Function during Mycobacterium tuberculosis Infection," *Journal of Immunology,* 190, 270-277, 2013.

[63] C. M. Rueda, N. D. Marin, L. F. Garcia, and M. Rojas, "Characterization of CD4 and CD8 T cells producing IFN-gamma in human latent and active tuberculosis," *Tuberculosis,* 90, 346-353, 2010.

[64] M. Azizia, J. Lloyd, M. Allen, N. Klein, and D. Peebles, "Immune Status in Very Preterm Neonates," *Pediatrics,* 129, e967-e974, 2012.

[65] R. S. Hotchkiss and S. Opal, "Immunotherapy for sepsis--a new approach against an ancient foe," *New England Journal of Medicine,* 363, 87-9, 2010.

[66] G. R. Bernard, J. L. Vincent, P. F. Laterre, S. P. LaRosa, J. F. Dhainaut, A. Lopez-Rodriguez*, et al.*, "Efficacy and safety of recombinant human activated protein C for severe sepsis," *New England Journal of Medicine,* 344, 699-709, 2001.

[67] R. Fan, O. Vermesh, A. Srivastava, B. K. Yen, L. Qin, H. Ahmad*, et al.*, "Integrated barcode chips for rapid, multiplexed analysis of proteins in microliter quantities of blood," *Nature Biotechnology,* 26, 1373-8, 2008.

[68] J. Wang, H. Ahmad, C. Ma, Q. Shi, O. Vermesh, U. Vermesh*, et al.*, "A self-powered, one-step chip for rapid, quantitative and multiplexed detection of proteins from pinpricks of whole blood," *Lab on a Chip,* 10, 3157-62, 2010.

[69] H. Zhu, G. Stybayeva, M. Macal, E. Ramanculov, M. D. George, S. Dandekar*, et al.*, "A microdevice for multiplexed detection of T-cell-secreted cytokines," *Lab on a Chip,* 8, 2197-205, 2008.

[70] J. C. Love, J. L. Ronan, G. M. Grotenbreg, A. G. van der Veen, and H. L. Ploegh, "A microengraving method for rapid selection of single cells producing antigen-specific antibodies," *Nature Biotechnology,* 24, 703-7, 2006.

[71] C. Ma, R. Fan, H. Ahmad, Q. Shi, B. Comin-Anduix, T. Chodon*, et al.*, "A clinical microchip for evaluation of single immune cells reveals high functional heterogeneity in phenotypically similar T cells," *Nature Medicine,* 17, 738-43, 2011.

[72] E. Stern, J. F. Klemic, D. A. Routenberg, P. N. Wyrembak, D. B. Turner-Evans, A. D. Hamilton*, et al.*, "Label-free immunodetection with CMOS-compatible semiconducting nanowires," *Nature,* 445, 519-22, 2007.

[73] T. Endo, S. Yamamura, K. Kerman, and E. Tamiya, "Label-free cell-based assay using localized surface plasmon resonance biosensor," *Analytica Chimica Acta,* 614, 182-9, 2008.

[74] H. Zhu, G. Stybayeva, J. Silangcruz, J. Yan, E. Ramanculov, S. Dandekar*, et al.*, "Detecting cytokine release from single T-cells," *Analytical Chemistry,* 81, 8150-6, 2009.

[75] Y. Liu, T. Kwa, and A. Revzin, "Simultaneous detection of cell-secreted TNF-alpha and IFN-gamma using micropatterned aptamer-modified electrodes," *Biomaterials,* 33, 7347-55, 2012.

[76] C. C. Czerkinsky, L. A. Nilsson, H. Nygren, O. Ouchterlony, and A. Tarkowski, "A solid-phase enzyme-linked immunospot (ELISPOT) assay for enumeration of specific antibody-secreting cells," *Journal of Immunological Methods,* 65, 109-21, 1983.

[77] Q. Han, N. Bagheri, E. M. Bradshaw, D. A. Hafler, D. A. Lauffenburger, and J. C. Love, "Polyfunctional responses by human T cells result from sequential release of cytokines," *Proceedings of the National Academy of Sciences of the United States of America,* 109, 1607-12, 2012.

[78] N. Varadarajan, D. S. Kwon, K. M. Law, A. O. Ogunniyi, M. N. Anahtar, J. M. Richter*, et al.*, "Rapid, efficient functional characterization and recovery of HIV-specific human CD8+ T cells using microengraving," *Proceedings of the National Academy of Sciences of the United States of America,* 109, 3885-90, 2012.

[79] A. Jin, T. Ozawa, K. Tajiri, T. Obata, S. Kondo, K. Kinoshita*, et al.*, "A rapid and efficient single-cell manipulation method for screening antigen-specific antibody-secreting cells from human peripheral blood," *Nature Medicine,* 15, 1088-92, 2009.

[80] Y. N. Xia and G. M. Whitesides, "Soft lithography," *Angewandte Chemie International Edition,* 37, 551-575, 1998.

[81] G. M. Whitesides, "The origins and the future of microfluidics," *Nature,* 442, 368-373, 2006.

[82] K. S. Ryu, X. F. Wang, K. Shaikh, and C. Liu, "A method for precision patterning of silicone elastomer and its applications," *Journal of Microelectromechanical Systems,* 13, 568-575, 2004.

[83] F. Y. Shih, B. R. Harkness, G. B. Gardner, J. S. Alger, M. R. Cummings, J. L. Princing*, et al.*, "Photopatternable silicone compositions for electronics packaging applications," in *Fifth International Conference on Electronic Packaging Technology, Proceedings*, 2003, 316-320.

[84] S. Desai, B. Taff, and J. Voldman, "A photopatternable silicone for biological applications," *Langmuir,* 24, 575-581, 2008.

[85] A. A. S. Bhagat, P. Jothimuthu, and I. Papautsky, "Photodefinable polydimethylsiloxane (PDMS) for rapid lab-on-a-chip prototyping," *Lab on a Chip,* 7, 1192-1197, 2007.

[86] J. C. Lotters, W. Olthuis, P. H. Veltink, and P. Bergveld, "The mechanical properties of the rubber elastic polymer polydimethylsiloxane for sensor

applications," *Journal of Micromechanics and Microengineering,* 7, 145-147, 1997.

[87] T. Scharnweber, R. Truckenmuller, A. M. Schneider, A. Welle, M. Reinhardt, and S. Giselbrecht, "Rapid prototyping of microstructures in polydimethylsiloxane (PDMS) by direct UV-lithography," *Lab on a Chip,* 11, 1368-1371, 2011.

[88] K. W. Meacham, R. J. Giuly, L. Guo, S. Hochman, and S. P. DeWeerth, "A lithographically-patterned, elastic multi-electrode array for surface stimulation of the spinal cord," *Biomedical Microdevices,* 10, 259-269, 2008.

[89] R. M. Diebold and D. R. Clarke, "Lithographic patterning on polydimethylsiloxane surfaces using polydimethylglutarimide," *Lab on a Chip,* 11, 1694-1697, 2011.

[90] N. Bowden, S. Brittain, A. G. Evans, J. W. Hutchinson, and G. M. Whitesides, "Spontaneous formation of ordered structures in thin films of metals supported on an elastomeric polymer," *Nature,* 393, 146-149, 1998.

[91] A. L. Thangawng, R. S. Ruoff, M. A. Swartz, and M. R. Glucksberg, "An ultra-thin PDMS membrane as a bio/micro-nano interface: fabrication and characterization," *Biomedical Microdevices,* 9, 587-595, 2007.

[92] S. J. Hwang, D. J. Oh, P. G. Jung, S. M. Lee, J. S. Go, J. H. Kim*, et al.*, "Dry etching of polydimethylsiloxane using microwave plasma," *Journal of Micromechanics and Microengineering,* 19, 2009.

[93] A. Plecis and Y. Chen, "Improved glass-PDMS-glass device technology for accurate measurements of electro-osmotic mobilities," *Microelectronic Engineering,* 85, 1334-1336, 2008.

[94] D. Bodas and C. Khan-Malek, "Hydrophilization and hydrophobic recovery of PDMS by oxygen plasma and chemical treatment - An SEM investigation," *Sensors and Actuators B-Chemical,* 123, 368-373, 2007.

[95] J. Garra, T. Long, J. Currie, T. Schneider, R. White, and M. Paranjape, "Dry etching of polydimethylsiloxane for microfluidic systems," *Journal of Vacuum Science & Technology A,* 20, 975-982, 2002.

[96] J. L. Arlett, E. B. Myers, and M. L. Roukes, "Comparative advantages of mechanical biosensors," *Nature Nanotechnology,* 6, 203-215, 2011.

[97] M. Bielefeld-Sevigny, "AlphaLISA immunoassay platform- the "no-wash" high-throughput alternative to ELISA," *Assay and Drug Development Technologies,* 7, 90-2, 2009.

[98] F. Poulsen and K. B. Jensen, "A luminescent oxygen channeling immunoassay for the determination of insulin in human plasma," *Journal of Biomolecular Screening,* 12, 240-7, 2007.

[99] K. P. Leister, R. Huang, B. L. Goodwin, A. Chen, C. P. Austin, and M. Xia, "Two High Throughput Screen Assays for Measurement of TNF-alpha in THP-1 Cells," *Current Chemical Genomics,* 5, 21-9, 2011.

[100] R. E. Guerkov, O. S. Targoni, C. R. Kreher, B. O. Boehm, M. T. Herrera, M. Tary-Lehmann*, et al.*, "Detection of low-frequency antigen-specific IL-10-producing CD4(+) T cells via ELISPOT in PBMC: cognate vs. nonspecific production of the cytokine," *Journal of Immunological Methods,* 279, 111-21, 2003.

[101] V. J. Hofman, M. I. Ilie, C. Bonnetaud, E. Selva, E. Long, T. Molina*, et al.*, "Cytopathologic detection of circulating tumor cells using the isolation by size of epithelial tumor cell method: promises and pitfalls," *American Journal of Clinical Pathology,* 135, 146-56, 2011.

[102] G. Vona, A. Sabile, M. Louha, V. Sitruk, S. Romana, K. Schutze*, et al.*, "Isolation by size of epithelial tumor cells : a new method for the immunomorphological and molecular characterization of circulatingtumor cells," *American Journal of Pathology,* 156, 57-63, 2000.

[103] S. Zheng, H. Lin, B. Lu, A. Williams, R. Datar, R. Cote*, et al.*, "3D microfilter device for viable circulating tumor cell (CTC) enrichment from blood," *Biomedical Microdevices,* 13, 203-213, 2011.

[104] Elżbieta Górska, Urszula Demkow, Roman Pińkowski, Barbara Jakubczak, Dorota Matuszewicz, Jolanta Gawęda*, et al.*, "Determination of monocyte count by hematological analyzers, manual method and flow cytometry in polish population," *Central European Journal of Immunology,* 31, 1-5, 2006.

[105] M. Toner and D. Irimia, "Blood-on-a-chip," *Annual Review of Biomedical Engineering,* 7, 77-103, 2005.

[106] S. M. Gilboa, J. L. Salemi, W. N. Nembhard, D. E. Fixler, and A. Correa, "Mortality Resulting From Congenital Heart Disease Among Children and Adults in the United States, 1999 to 2006," *Circulation,* 122, 2254-2263, 2010.

[107] J. H. Levy and K. A. Tanaka, "Inflammatory response to cardiopulmonary bypass," *The Annals of Thoracic Surgery,* 75, S715-20, 2003.

[108] K. L. Brown, D. A. Ridout, A. P. Goldman, A. Hoskote, and D. J. Penny, "Risk factors for long intensive care unit stay after cardiopulmonary bypass in children," *Critical Care Medicine,* 31, 28-33, 2003.

[109] W. Mrowczynski, M. Wojtalik, D. Zawadzka, G. Sharma, J. Henschke, R. Bartkowski*, et al.*, "Infection risk factors in pediatric cardiac surgery," *Asian Cardiovascular & Thoracic Annals,* 10, 329-33, 2002.

[110] J. M. Costello, D. A. Graham, D. F. Morrow, J. Morrow, G. Potter-Bynoe, T. J. Sandora*, et al.*, "Risk factors for surgical site infection after cardiac surgery in children," *Annals of Thoracic Surgery,* 89, 1833-41; discussion 1841-2, 2010.

[111] A. L. Allpress, G. L. Rosenthal, K. M. Goodrich, F. M. Lupinetti, and D. M. Zerr, "Risk factors for surgical site infections after pediatric cardiovascular surgery," *The Pediatric Infectious Disease Journal,* 23, 231-4, 2004.

[112] R. C. Bone, "Sir Isaac Newton, sepsis, SIRS, and CARS," *Critical Care Medicine,* 24, 1125-8, 1996.

[113] H. D. Volk, P. Reinke, and W. D. Docke, "Clinical aspects: from systemic inflammation to 'immunoparalysis'," *Chemical Immunology,* 74, 162-77, 2000.

[114] M. L. Allen, M. J. Peters, A. Goldman, M. Elliott, I. James, R. Callard*, et al.*, "Early postoperative monocyte deactivation predicts systemic inflammation and prolonged stay in pediatric cardiac intensive care," *Critical Care Medicine,* 30, 1140-5, 2002.

[115] M. W. Hall, N. L. Knatz, C. Vetterly, S. Tomarello, M. D. Wewers, H. D. Volk*, et al.*, "Immunoparalysis and nosocomial infection in children with multiple organ dysfunction syndrome," *Intensive Care Medicine,* 37, 525-32, 2011.

[116] J. Wynn, T. T. Cornell, H. R. Wong, T. P. Shanley, and D. S. Wheeler, "The host response to sepsis and developmental impact," *Pediatrics,* 125, 1031-41, 2010.
[117] S. Nagrath, L. V. Sequist, S. Maheswaran, D. W. Bell, D. Irimia, L. Ulkus*, et al.*, "Isolation of rare circulating tumour cells in cancer patients by microchip technology," *Nature,* 450, 1235-1239, 2007.
[118] K. Pantel, C. Alix-Panabieres, and S. Riethdorf, "Cancer micrometastases," *Nature Reviews Clinical Oncology,* 6, 339-351, 2009.
[119] M. S. Wicha and D. F. Hayes, "Circulating tumor cells: Not all detected cells are bad and not all bad cells are detected," *Journal of Clinical Oncology,* 29, 1-4, 2011.
[120] J. den Toonder, "Circulating tumor cells: the grand challenge," *Lab on a Chip,* 11, 375-377, 2011.
[121] S. J. Tan, R. L. Lakshmi, P. Chen, W.-T. Lim, L. Yobas, and C. T. Lim, "Versatile label free biochip for the detection of circulating tumor cells from peripheral blood in cancer patients," *Biosensors and Bioelectronics,* 26, 1701-1705, 2010.
[122] A. H. Talasaz, A. A. Powell, D. E. Huber, J. G. Berbee, K.-H. Roh, W. Yu*, et al.*, "Isolating highly enriched populations of circulating epithelial cells and other rare cells from blood using a magnetic sweeper device," *Proceedings of the National Academy of Sciences of the United States of America,* 106, 3970-3975, 2009.
[123] S. L. Stott, C.-H. Hsu, D. I. Tsukrov, M. Yu, D. T. Miyamoto, B. A. Waltman*, et al.*, "Isolation of circulating tumor cells using a microvortex-generating herringbone-chip," *Proceedings of the National Academy of Sciences of the United States of America,* 107, 18392-18397, 2010.
[124] S. Wang, K. Liu, J. Liu, Z. T. F. Yu, X. Xu, L. Zhao*, et al.*, "Highly efficient capture of circulating tumor cells by using nanostructured silicon substrates with integrated chaotic micromixers," *Angewandte Chemie International Edition,* 50, 3084-3088, 2011.
[125] S.-K. Lee, G.-S. Kim, Y. Wu, D.-J. Kim, Y. Lu, M. Kwak*, et al.*, "Nanowire Substrate-Based Laser Scanning Cytometry for Quantitation of Circulating Tumor Cells," *Nano Letters,* 12, 2697-2704, 2012.
[126] A. A. Adams, P. I. Okagbare, J. Feng, M. L. Hupert, D. Patterson, J. Göttert*, et al.*, "Highly efficient circulating tumor cell isolation from whole blood and label-free enumeration using polymer-based microfluidics with an integrated conductivity sensor," *Journal of the American Chemical Society,* 130, 8633-8641, 2008.
[127] J. Sekine, S. C. Luo, S. Wang, B. Zhu, H. R. Tseng, and H. H. Yu, "Functionalized conducting polymer nanodots for enhanced cell capturing: the synergistic effect of capture agents and nanostructures," *Advanced Materials,* 23, 4788-92, 2011.
[128] C. A. Bichsel, S. Gobaa, S. Kobel, C. Secondini, G. N. Thalmann, M. G. Cecchini*, et al.*, "Diagnostic microchip to assay 3D colony-growth potential of captured circulating tumor cells," *Lab on a Chip,* 12, 2313-6, 2012.
[129] J. P. Thiery, "Epithelial-mesenchymal transitions in tumour progression," *Nature Reviews Cancer,* 2, 442-454, 2002.

[130] C. L. Chaffer and R. A. Weinberg, "A perspective on cancer cell metastasis," *Science,* 331, 1559-1564, 2011.
[131] A. M. Sieuwerts, J. Kraan, J. Bolt, P. van der Spoel, F. Elstrodt, M. Schutte*, et al.*, "Anti-epithelial cell adhesion molecule antibodies and the detection of circulating normal-like breast tumor cells," *Journal of the National Cancer Institute,* 101, 61-66, 2009.
[132] I. Van der Auwera, D. Peeters, I. H. Benoy, H. J. Elst, S. J. Van Laere, A. Prove*, et al.*, "Circulating tumour cell detection: a direct comparison between the CellSearch System, the AdnaTest and CK-19/mammaglobin RT-PCR in patients with metastatic breast cancer," *British Journal of Cancer,* 102, 276-284, 2009.
[133] L. Yang, J. C. Lang, P. Balasubramanian, K. R. Jatana, D. Schuller, A. Agrawal*, et al.*, "Optimization of an enrichment process for circulating tumor cells from the blood of head and neck cancer patients through depletion of normal cells," *Biotechnology and Bioengineering,* 102, 521-534, 2009.
[134] K. Tkaczuk, O. Goloubeva, N. Tait, F. Feldman, M. Tan, Z.-P. Lum*, et al.*, "The significance of circulating epithelial cells in Breast Cancer patients by a novel negative selection method," *Breast Cancer Research and Treatment,* 111, 355-364, 2008.
[135] W. Chen, L. Villa-Diaz, Y. Sun, S. Weng, J. Kim, R. Lam*, et al.*, "Nanotopography influences adhesion, spreading, and self-renewal of human embryonic stem cells," *ACS Nano,* 6, 4094-4103, 2012.
[136] W. Chen, Y. Sun, and J. Fu, "Microfabricated nanotopological surfaces for study of adhesion-dependent cell mechanosensitivity," *Small,* 9, 81-9, 2013.
[137] E. Metwalli and C. G. Pantano, "Reactive ion etching of glasses: Composition dependence," *Nuclear Instruments and Methods in Physics Research Section B: Beam Interactions with Materials and Atoms,* 207, 21-27, 2003.
[138] P. W. Leech, "Reactive ion etching of quartz and silica-based glasses in CF4/CHF3 plasmas," *Vacuum,* 55, 191-196, 1999.
[139] D. Y. Choi, J. H. Lee, D. S. Kim, and S. T. Jung, "Formation of plasma induced surface damage in silica glass etching for optical waveguides," *Journal of Applied Physics,* 95, 8400-8407, 2004.
[140] R. Kalluri, "EMT: when epithelial cells decide to become mesenchymal-like cells," *Journal of Clinical Investigation,* 119, 1417-9, 2009.
[141] R. Kalluri and R. A. Weinberg, "The basics of epithelial-mesenchymal transition," *Journal of Clinical Investigation,* 119, 1420-8, 2009.
[142] R. Kalluri and E. G. Neilson, "Epithelial-mesenchymal transition and its implications for fibrosis," *Journal of Clinical Investigation,* 112, 1776-84, 2003.
[143] M. Yu, A. Bardia, B. S. Wittner, S. L. Stott, M. E. Smas, D. T. Ting*, et al.*, "Circulating breast tumor cells exhibit dynamic changes in epithelial and mesenchymal composition," *Science,* 339, 580-4, 2013.
[144] K. W. Kwon, S. S. Choi, S. H. Lee, B. Kim, S. N. Lee, M. C. Park*, et al.*, "Label-free, microfluidic separation and enrichment of human breast cancer cells by adhesion difference," *Lab on a Chip,* 7, 1461-1468, 2007.
[145] R. H. W. Lam, Y. B. Sun, W. Q. Chen, and J. P. Fu, "Elastomeric microposts integrated into microfluidics for flow-mediated endothelial mechanotransduction analysis," *Lab on a Chip,* 12, 1865-1873, 2012.

[146] N. D. Gallant, K. E. Michael, and A. J. Garcia, "Cell adhesion strengthening: Contributions of adhesive area, integrin binding, and focal adhesion assembly," *Molecular Biology of the Cell,* 16, 4329-4340, 2005.
[147] Y. Sun, C. S. Chen, and J. Fu, "Forcing Stem Cells to Behave: A Biophysical Perspective of the Cellular Microenvironment," *Annual Review of Biophysics,* 41, 519-542, 2012.
[148] K. Pantel and S. Riethdorf, "Pathology: are circulating tumor cells predictive of overall survival?," *Nature Reviews Clinical Oncology,* 6, 190-1, 2009.
[149] L. Harris, H. Fritsche, R. Mennel, L. Norton, P. Ravdin, S. Taube*, et al.*, "American Society of Clinical Oncology 2007 update of recommendations for the use of tumor markers in breast cancer," *Journal Clinical Oncology* 25, 5287-312, 2007.
[150] J. P. Eliane, M. Repollet, K. E. Luker, M. Brown, J. M. Rae, G. Dontu*, et al.*, "Monitoring serial changes in circulating human breast cancer cells in murine xenograft models," *Cancer Research,* 68, 5529-32, 2008.
[151] D. L. Gibbons, W. Lin, C. J. Creighton, Z. H. Rizvi, P. A. Gregory, G. J. Goodall*, et al.*, "Contextual extracellular cues promote tumor cell EMT and metastasis by regulating miR-200 family expression," *Genes & Development,* 23, 2140-51, 2009.
[152] D. L. Longo, "Tumor Heterogeneity and Personalized Medicine," *New England Journal of Medicine,* 366, 956-957, 2012.
[153] A. Marusyk, V. Almendro, and K. Polyak, "Intra-tumour heterogeneity: a looking glass for cancer?," *Nature Reviews Cancer,* 12, 323-334, 2012.
[154] T. Reya, S. J. Morrison, M. F. Clarke, and I. L. Weissman, "Stem cells, cancer, and cancer stem cells," *Nature,* 414, 105-11, 2001.
[155] M. R. Alison, S. Islam, and N. A. Wright, "Stem cells in cancer: instigators and propagators?," *Journal of Cell Science,* 123, 2357-68, 2010.
[156] C. T. Jordan, M. L. Guzman, and M. Noble, "Cancer stem cells," *New England Journal of Medicine,* 355, 1253-61, 2006.
[157] M. Al-Hajj, M. S. Wicha, A. Benito-Hernandez, S. J. Morrison, and M. F. Clarke, "Prospective identification of tumorigenic breast cancer cells," *Proceedings of the National Academy of Sciences of the United States of America,* 100, 3983-8, 2003.
[158] S. K. Singh, I. D. Clarke, M. Terasaki, V. E. Bonn, C. Hawkins, J. Squire*, et al.*, "Identification of a cancer stem cell in human brain tumors," *Cancer Research,* 63, 5821-8, 2003.
[159] A. T. Collins, P. A. Berry, C. Hyde, M. J. Stower, and N. J. Maitland, "Prospective identification of tumorigenic prostate cancer stem cells," *Cancer Research,* 65, 10946-51, 2005.
[160] H. Liu, M. R. Patel, J. A. Prescher, A. Patsialou, D. Qian, J. Lin*, et al.*, "Cancer stem cells from human breast tumors are involved in spontaneous metastases in orthotopic mouse models," *Proceedings of the National Academy of Sciences of the United States of America,* 107, 18115-20, 2010.
[161] P. C. Hermann, S. L. Huber, T. Herrler, A. Aicher, J. W. Ellwart, M. Guba*, et al.*, "Distinct populations of cancer stem cells determine tumor growth and metastatic activity in human pancreatic cancer," *Cell Stem Cell,* 1, 313-23, 2007.

[162] R. Pang, W. L. Law, A. C. Chu, J. T. Poon, C. S. Lam, A. K. Chow, *et al.*, "A subpopulation of CD26+ cancer stem cells with metastatic capacity in human colorectal cancer," *Cell Stem Cell,* 6, 603-15, 2010.
[163] L. Ricci-Vitiani, D. G. Lombardi, E. Pilozzi, M. Biffoni, M. Todaro, C. Peschle, *et al.*, "Identification and expansion of human colon-cancer-initiating cells," *Nature,* 445, 111-5, 2007.
[164] C. Ginestier, M. H. Hur, E. Charafe-Jauffret, F. Monville, J. Dutcher, M. Brown, *et al.*, "ALDH1 is a marker of normal and malignant human mammary stem cells and a predictor of poor clinical outcome," *Cell Stem Cell,* 1, 555-567, 2007.
[165] P. Dalerba, S. J. Dylla, I. K. Park, R. Liu, X. Wang, R. W. Cho, *et al.*, "Phenotypic characterization of human colorectal cancer stem cells," *Proceedings of the National Academy of Sciences of the United States of America,* 104, 10158-63, 2007.
[166] S. J. Dylla, L. Beviglia, I. K. Park, C. Chartier, J. Raval, L. Ngan, *et al.*, "Colorectal cancer stem cells are enriched in xenogeneic tumors following chemotherapy," *PLoS One,* 3, e2428, 2008.
[167] T. Teramura, K. Fukuda, S. Kurashimo, Y. Hosoi, Y. Miki, S. Asada, *et al.*, "Isolation and characterization of side population stem cells in articular synovial tissue," *BMC Musculoskeletal Disorders,* 9, 86, 2008.
[168] K. R. Levental, H. Yu, L. Kass, J. N. Lakins, M. Egeblad, J. T. Erler, *et al.*, "Matrix crosslinking forces tumor progression by enhancing integrin signaling," *Cell,* 139, 891-906, 2009.
[169] R. Jinka, R. Kapoor, P. G. Sistla, T. A. Raj, and G. Pande, "Alterations in Cell-Extracellular Matrix Interactions during Progression of Cancers," *International Journal of Cell Biology,* 2012, 219196, 2012.
[170] T. R. Cox and J. T. Erler, "Remodeling and homeostasis of the extracellular matrix: implications for fibrotic diseases and cancer," *Disease Models & Mechanisms,* 4, 165-78, 2011.
[171] F. Berthiaume, P. V. Moghe, M. Toner, and M. L. Yarmush, "Effect of extracellular matrix topology on cell structure, function, and physiological responsiveness: hepatocytes cultured in a sandwich configuration," *FASEB Journal,* 10, 1471-84, 1996.
[172] M. J. Paszek, N. Zahir, K. R. Johnson, J. N. Lakins, G. I. Rozenberg, A. Gefen, *et al.*, "Tensional homeostasis and the malignant phenotype," *Cancer Cell,* 8, 241-54, 2005.
[173] J. I. Lopez, I. Kang, W. K. You, D. M. McDonald, and V. M. Weaver, "In situ force mapping of mammary gland transformation," *Integrative Biology,* 3, 910-21, 2011.
[174] S. Kumar and V. M. Weaver, "Mechanics, malignancy, and metastasis: the force journey of a tumor cell," *Cancer Metastasis Reviews,* 28, 113-27, 2009.
[175] P. F. Davies, J. A. Spaan, and R. Krams, "Shear stress biology of the endothelium," *Annals of Biomedical Engineering,* 33, 1714-8, 2005.
[176] D. E. Ingber, "Mechanobiology and diseases of mechanotransduction," *Annals of Medicine,* 35, 564-77, 2003.

[177] V. Swaminathan, K. Mythreye, E. T. O'Brien, A. Berchuck, G. C. Blobe, and R. Superfine, "Mechanical stiffness grades metastatic potential in patient tumor cells and in cancer cell lines," *Cancer Research,* 71, 5075-80, 2011.
[178] S. Suresh, "Biomechanics and biophysics of cancer cells," *Acta Biomaterialia,* 3, 413-38, 2007.
[179] P. Katira, R. T. Bonnecaze, and M. H. Zaman, "Modeling the mechanics of cancer: effect of changes in cellular and extra-cellular mechanical properties," *Front in Oncology,* 3, 145, 2013.
[180] M. Lekka, K. Pogoda, J. Gostek, O. Klymenko, S. Prauzner-Bechcicki, J. Wiltowska-Zuber*, et al.*, "Cancer cell recognition--mechanical phenotype," *Micron,* 43, 1259-66, 2012.
[181] S. Byun, S. Son, D. Amodei, N. Cermak, J. Shaw, J. H. Kang*, et al.*, "Characterizing deformability and surface friction of cancer cells," *Proceedings of the National Academy of Sciences of the United States of America,* 110, 7580-5, 2013.
[182] D. Wirtz, K. Konstantopoulos, and P. C. Searson, "The physics of cancer: the role of physical interactions and mechanical forces in metastasis," *Nature Reviews Cancer,* 11, 512-22, 2011.
[183] W. W. Xu, R. Mezencev, B. Kim, L. J. Wang, J. McDonald, and T. Sulchek, "Cell Stiffness Is a Biomarker of the Metastatic Potential of Ovarian Cancer Cells," *Plos One,* 7, 2012.
[184] R. J. Pelham, Jr. and Y. Wang, "Cell locomotion and focal adhesions are regulated by substrate flexibility," *Proceedings of the National Academy of Sciences of the United States of America,* 94, 13661-5, 1997.
[185] D. A. Lauffenburger and A. F. Horwitz, "Cell migration: a physically integrated molecular process," *Cell,* 84, 359-69, 1996.
[186] S. Weng and J. Fu, "Synergistic regulation of cell function by matrix rigidity and adhesive pattern," *Biomaterials,* 32, 9584-93, 2011.
[187] C. T. Mierke, N. Bretz, and P. Altevogt, "Contractile forces contribute to increased glycosylphosphatidylinositol-anchored receptor CD24-facilitated cancer cell invasion," *The Journal of Biological Chemistry,* 286, 34858-71, 2011.
[188] C. M. Kraning-Rush, J. P. Califano, and C. A. Reinhart-King, "Cellular traction stresses increase with increasing metastatic potential," *PLoS One,* 7, e32572, 2012.
[189] D. T. Rosenthal, J. Zhang, L. Bao, L. Zhu, Z. Wu, K. Toy*, et al.*, "RhoC impacts the metastatic potential and abundance of breast cancer stem cells," *PLoS One,* 7, e40979, 2012.
[190] A. K. Croker, D. Goodale, J. Chu, C. Postenka, B. D. Hedley, D. A. Hess*, et al.*, "High aldehyde dehydrogenase and expression of cancer stem cell markers selects for breast cancer cells with enhanced malignant and metastatic ability," *Journal of Cellular and Molecular Medicine,* 13, 2236-52, 2009.
[191] F. Jiang, Q. Qiu, A. Khanna, N. W. Todd, J. Deepak, L. X. Xing*, et al.*, "Aldehyde Dehydrogenase 1 Is a Tumor Stem Cell-Associated Marker in Lung Cancer," *Molecular Cancer Research,* 7, 330-338, 2009.

[192] D. Ucar, C. R. Cogle, J. R. Zucali, B. Ostmark, E. W. Scott, R. Zori, *et al.*, "Aldehyde dehydrogenase activity as a functional marker for lung cancer," *Chemico-Biological Interactions,* 178, 48-55, 2009.
[193] S. Ma, K. W. Chan, T. K. W. Lee, K. H. Tang, J. Y. H. Wo, B. J. Zheng, *et al.*, "Aldehyde dehydrogenase discriminates the CD133 liver cancer stem cell populations," *Molecular Cancer Research,* 6, 1146-1153, 2008.
[194] J. E. Carpentino, M. J. Hynes, H. D. Appelman, T. Zheng, D. A. Steindler, E. W. Scott, *et al.*, "Aldehyde Dehydrogenase-Expressing Colon Stem Cells Contribute to Tumorigenesis in the Transition from Colitis to Cancer," *Cancer Research,* 69, 8208-8215, 2009.
[195] Z. A. Rasheed, J. Yang, Q. Wang, J. Kowalski, I. Freed, C. Murter, *et al.*, "Prognostic significance of tumorigenic cells with mesenchymal features in pancreatic adenocarcinoma," *Journal of the National Cancer Institute,* 102, 340-51, 2010.
[196] I. A. Silva, S. M. Bai, K. McLean, K. Yang, K. Griffith, D. Thomas, *et al.*, "Aldehyde Dehydrogenase in Combination with CD133 Defines Angiogenic Ovarian Cancer Stem Cells That Portend Poor Patient Survival," *Cancer Research,* 71, 3991-4001, 2011.
[197] Y. C. Chen, Y. W. Chen, H. S. Hsu, L. M. Tseng, P. I. Huang, K. H. Lu, *et al.*, "Aldehyde dehydrogenase 1 is a putative marker for cancer stem cells in head and neck squamous cancer," *Biochemical and Biophysical Research Communications,* 385, 307-313, 2009.
[198] C. van den Hoogen, G. van der Horst, H. Cheung, J. T. Buijs, J. M. Lippitt, N. Guzman-Ramirez, *et al.*, "High aldehyde dehydrogenase activity identifies tumor-initiating and metastasis-initiating cells in human prostate cancer," *Cancer Research,* 70, 5163-73, 2010.
[199] M. Magni, S. Shammah, R. Schiro, W. Mellado, R. Dalla-Favera, and A. M. Gianni, "Induction of cyclophosphamide-resistance by aldehyde-dehydrogenase gene transfer," *Blood,* 87, 1097-103, 1996.
[200] Y. Luo, K. Dallaglio, Y. Chen, W. A. Robinson, S. E. Robinson, M. D. McCarter, *et al.*, "ALDH1A isozymes are markers of human melanoma stem cells and potential therapeutic targets," *Stem Cells,* 30, 2100-13, 2012.
[201] V. Vasiliou, A. Pappa, and T. Estey, "Role of human aldehyde dehydrogenases in endobiotic and xenobiotic metabolism," *Drug Metabolism Reviews,* 36, 279-99, 2004.
[202] E. Charafe-Jauffret, C. Ginestier, and D. Birnbaum, "Breast cancer stem cells: tools and models to rely on," *BMC Cancer,* 9, 202, 2009.
[203] P. Marcato, C. A. Dean, D. Pan, R. Araslanova, M. Gillis, M. Joshi, *et al.*, "Aldehyde Dehydrogenase Activity of Breast Cancer Stem Cells is Primarily Due to Isoform ALDH1A3 and Its Expression is Predictive of Metastasis," *Stem Cells,* 29, 32-45, 2011.
[204] T. Tanei, K. Morimoto, K. Shimazu, S. J. Kim, Y. Tanji, T. Taguchi, *et al.*, "Association of breast cancer stem cells identified by aldehyde dehydrogenase 1 expression with resistance to sequential Paclitaxel and epirubicin-based chemotherapy for breast cancers," *Clinical Cancer Research,* 15, 4234-41, 2009.

[205] P. B. Gupta, C. M. Fillmore, G. Jiang, S. D. Shapira, K. Tao, C. Kuperwasser, *et al.*, "Stochastic state transitions give rise to phenotypic equilibrium in populations of cancer cells," *Cell,* 146, 633-44, 2011.
[206] C. L. Chaffer, I. Brueckmann, C. Scheel, A. J. Kaestli, P. A. Wiggins, L. O. Rodrigues, *et al.*, "Normal and neoplastic nonstem cells can spontaneously convert to a stem-like state," *Proceedings of the National Academy of Sciences of the United States of America,* 108, 7950-7955, 2011.
[207] J. Fu, Y. K. Wang, M. T. Yang, R. A. Desai, X. Yu, Z. Liu, *et al.*, "Mechanical regulation of cell function with geometrically modulated elastomeric substrates," *Nature Methods,* 7, 733-6, 2010.
[208] M. T. Yang, J. Fu, Y. K. Wang, R. A. Desai, and C. S. Chen, "Assaying stem cell mechanobiology on microfabricated elastomeric substrates with geometrically modulated rigidity," *Nature Protocols,* 6, 187-213, 2011.
[209] Z. Fan, Y. Sun, C. Di, D. Tay, W. Chen, C. X. Deng, *et al.*, "Acoustic tweezing cytometry for live-cell subcellular modulation of intracellular cytoskeleton contractility," *Scientific Reports,* 3, 2176, 2013.
[210] G. W. Brodland and J. H. Veldhuis, "The mechanics of metastasis: insights from a computational model," *PLoS One,* 7, e44281, 2012.
[211] R. M. Tenney and D. E. Discher, "Stem cells, microenvironment mechanics, and growth factor activation," *Current Opinion in Cell Biology,* 21, 630-635, 2009.
[212] T. Harada, J. Swift, J. Irianto, J. W. Shin, K. R. Spinler, A. Athirasala, *et al.*, "Nuclear lamin stiffness is a barrier to 3D migration, but softness can limit survival," *Journal of Cell Biology,* 204, 669-682, 2014.
[213] J. Takagi, B. M. Petre, T. Walz, and T. A. Springer, "Global conformational rearrangements in integrin extracellular domains in outside-in and inside-out signaling," *Cell,* 110, 599-11, 2002.
[214] J. Park, S. Bauer, K. von der Mark, and P. Schmuki, "Nanosize and vitality: TiO2 nanotube diameter directs cell fate," *Nano Letters,* 7, 1686-91, 2007.
[215] M. Crisan, S. Yap, L. Casteilla, C. W. Chen, M. Corselli, T. S. Park, *et al.*, "A perivascular origin for mesenchymal stem cells in multiple human organs," *Cell Stem Cell,* 3, 301-313, 2008.
[216] E. Kingham and R. O. Oreffo, "Embryonic and induced pluripotent stem cells: understanding, creating, and exploiting the nano-niche for regenerative medicine," *ACS Nano,* 7, 1867-81, 2013.
[217] H. N. Kim, A. Jiao, N. S. Hwang, M. S. Kim, D. H. Kang, D. H. Kim, *et al.*, "Nanotopography-guided tissue engineering and regenerative medicine," *Advanced Drug Delivery Reviews,* 65, 536-558, 2013.
[218] R. K. Das, O. F. Zouani, C. Labrugere, R. Oda, and M. C. Durrieu, "Influence of nanohelical shape and periodicity on stem cell fate," *ACS Nano,* 7, 3351-61, 2013.
[219] M. Dalby, N. Gadegaard, and R. Oreffo, "Harnessing nanotopography and integrin-matrix interactions to influence stem cell fate," *Nature materials,* 13, 558-569, 2014.
[220] L. E. McNamara, T. Sjostrom, K. Seunarine, R. D. Meek, B. Su, and M. J. Dalby, "Investigation of the limits of nanoscale filopodial interactions," *Journal of Tissue Engineering,* 5, 2014.

[221] I. R. Lemischka and K. A. Moore, "Stem cells - Interactive niches," *Nature,* 425, 778-779, 2003.
[222] A. Spradling, D. Drummond-Barbosa, and T. Kai, "Stem cells find their niche," *Nature,* 414, 98-104, 2001.
[223] Y. Sun, K. M. A. Yong, L. G. Villa-Diaz, X. Zhang, W. Chen, R. Philson*, et al.*, "Hippo/YAP-mediated rigidity-dependent motor neuron differentiation of human pluripotent stem cells," *Nature Materials,* In press, 2014.
[224] D. H. Kim, P. P. Provenzano, C. L. Smith, and A. Levchenko, "Matrix nanotopography as a regulator of cell function," *Journal of Cell Biology,* 197, 351-360, 2012.
[225] F. Guilak, D. M. Cohen, B. T. Estes, J. M. Gimble, W. Liedtke, and C. S. Chen, "Control of stem cell fate by physical interactions with the extracellular matrix," *Cell Stem Cell,* 5, 17-26, 2009.
[226] K. C. Wu, C. L. Tseng, C. C. Wu, F. C. Kao, Y. K. Tu, E. C. So*, et al.*, "Nanotechnology in the regulation of stem cell behavior," *Science and Technology of Advanced Materials,* 14, 2013.
[227] E. K. Yim, R. M. Reano, S. W. Pang, A. F. Yee, C. S. Chen, and K. W. Leong, "Nanopattern-induced changes in morphology and motility of smooth muscle cells," *Biomaterials,* 26, 5405-13, 2005.
[228] M. J. Dalby, N. Gadegaard, R. Tare, A. Andar, M. O. Riehle, P. Herzyk*, et al.*, "The control of human mesenchymal cell differentiation using nanoscale symmetry and disorder," *Nature Materials,* 6, 997-1003, 2007.
[229] E. K. F. Yim, S. W. Pang, and K. W. Leong, "Synthetic nanostructures inducing differentiation of human mesenchymal stem cells into neuronal lineage," *Experimental Cell Research,* 313, 1820-1829, 2007.
[230] S. Oh, K. S. Brammer, Y. S. J. Li, D. Teng, A. J. Engler, S. Chien*, et al.*, "Stem cell fate dictated solely by altered nanotube dimension," *Proceedings of the National Academy of Sciences of the United States of America,* 106, 2130-2135, 2009.
[231] R. J. McMurray, N. Gadegaard, P. M. Tsimbouri, K. V. Burgess, L. E. McNamara, R. Tare*, et al.*, "Nanoscale surfaces for the long-term maintenance of mesenchymal stem cell phenotype and multipotency," *Nature Materials,* 10, 637-644, 2011.
[232] S. Saha, L. Ji, J. J. de Pablo, and S. P. Palecek, "TGF beta/Activin/Nodal pathway in inhibition of human embryonic stem cell differentiation by mechanical strain," *Biophysical Journal,* 94, 4123-4133, 2008.
[233] F. Chowdhury, S. Na, D. Li, Y. C. Poh, T. S. Tanaka, F. Wang*, et al.*, "Material properties of the cell dictate stress-induced spreading and differentiation in embryonic stem cells," *Nature Materials,* 9, 82-88, 2010.
[234] N. D. Evans, C. Minelli, E. Gentleman, V. LaPointe, S. N. Patankar, M. Kallivretaki*, et al.*, "Substrate Stiffness Affects Early Differentiation Events in Embryonic Stem Cells," *European Cells & Materials,* 18, 1-14, 2009.
[235] F. Chowdhury, Y. Li, Y.-C. Poh, T. Yokohama-Tamaki, N. Wang, and T. S. Tanaka, "Soft substrates promote homogeneous self-renewal of embryonic stem cells via downregulating cell-matrix tractions," *Plos One,* 5, e15655, 2010.

[236] Y. Mei, K. Saha, S. R. Bogatyrev, J. Yang, A. L. Hook, Z. I. Kalcioglu*, et al.*, "Combinatorial development of biomaterials for clonal growth of human pluripotent stem cells," *Nature Materials,* 9, 768-778, 2010.
[237] J. W. Xie, S. M. Willerth, X. R. Li, M. R. Macewan, A. Rader, S. E. Sakiyama-Elbert*, et al.*, "The differentiation of embryonic stem cells seeded on electrospun nanofibers into neural lineages," *Biomaterials,* 30, 354-362, 2009.
[238] M. R. Lee, K. W. Kwon, H. Jung, H. N. Kim, K. Y. Suh, K. Kim*, et al.*, "Direct differentiation of human embryonic stem cells into selective neurons on nanoscale ridge/groove pattern arrays," *Biomaterials,* 31, 4360-4366, 2010.
[239] J. A. Thomson, J. Itskovitz-Eldor, S. S. Shapiro, M. A. Waknitz, J. J. Swiergiel, V. S. Marshall*, et al.*, "Embryonic stem cell lines derived from human blastocysts," *Science,* 282, 1145-1147, 1998.
[240] R. Jaenisch and R. Young, "Stem cells, the molecular circuitry of pluripotency and nuclear reprogramming," *Cell,* 132, 567-582, 2008.
[241] G. Keller, "Embryonic stem cell differentiation: emergence of a new era in biology and medicine," *Genes & Development,* 19, 1129-1155, 2005.
[242] K. Saha and R. Jaenisch, "Technical challenges in using human induced pluripotent stem cells to model disease," *Cell Stem Cell,* 5, 584-595, 2009.
[243] A. Colman and O. Dreesen, "Pluripotent stem cells and disease modeling," *Cell Stem Cell,* 5, 244-247, 2009.
[244] L. L. Rubin, "Stem cells and drug discovery: The beginning of a new era?," *Cell,* 132, 549-552, 2008.
[245] C. W. Pouton and J. M. Haynes, "Embryonic stem cells as a source of models for drug discovery," *Nature Reviews Drug Discovery,* 6, 605-616, 2007.
[246] J. McNeish, "Embryonic stem cells in drug discovery," *Nature Reviews Drug Discovery,* 3, 70-80, 2004.
[247] G. Q. Daley and D. T. Scadden, "Prospects for stem cell-based therapy," *Cell,* 132, 544-548, 2008.
[248] D. Srivastava and K. N. Ivey, "Potential of stem-cell-based therapies for heart disease," *Nature,* 441, 1097-1099, 2006.
[249] O. Lindvall and Z. Kokaia, "Stem cells for the treatment of neurological disorders," *Nature,* 441, 1094-1096, 2006.
[250] C. Bordignon, "Stem-cell therapies for blood diseases," *Nature,* 441, 1100-1102, 2006.
[251] S. R. Braam, L. Zeinstra, S. Litjens, D. Ward-van Oostwaard, S. van den Brink, L. van Laake*, et al.*, "Recombinant Vitronectin Is a Functionally Defined Substrate That Supports Human Embryonic Stem Cell Self-Renewal via αVβ5 Integrin," *Stem Cells,* 26, 2257-2265, 2008.
[252] V. Vogel and M. Sheetz, "Local force and geometry sensing regulate cell functions," *Nature Reviews Molecular Cell Biology,* 7, 265-275, 2006.
[253] R. McBeath, D. M. Pirone, C. M. Nelson, K. Bhadriraju, and C. S. Chen, "Cell shape, cytoskeletal tension, and RhoA regulate stem cell lineage commitment," *Developmental Cell,* 6, 483-495, 2004.
[254] A. J. Engler, S. Sen, H. L. Sweeney, and D. E. Discher, "Matrix elasticity directs stem cell lineage specification," *Cell,* 126, 677-689, 2006.

[255] D. Li, J. X. Zhou, L. Wang, M. E. Shin, P. Su, X. H. Lei, *et al.*, "Integrated biochemical and mechanical signals regulate multifaceted human embryonic stem cell functions," *Journal of Cell Biology,* 191, 631-644, 2010.
[256] G. Chen, Z. Hou, D. R. Gulbranson, and J. A. Thomson, "Actin-myosin contractility is responsible for the reduced viability of dissociated human embryonic stem cells," *Cell Stem Cell,* 7, 240-248, 2010.
[257] M. Ohgushi, M. Matsumura, M. Eiraku, K. Murakami, T. Aramaki, A. Nishiyama, *et al.*, "Molecular pathway and cell state responsible for dissociation-induced apoptosis in human pluripotent stem cells," *Cell Stem Cell,* 7, 225-239, 2010.
[258] A. Walker, H. Su, M. A. Conti, N. Harb, R. S. Adelstein, and N. Sato, "Non-muscle myosin II regulates survival threshold of pluripotent stem cells," *Nature Communications,* 1, 71, 2010.
[259] S. Chambers, C. Fasano, E. Papapetrou, M. Tomishima, M. Sadelain, and L. Studer, "Highly efficient neural conversion of human ES and iPS cells by dual inhibition of SMAD signaling," *Nature Biotechnology,* 27, 275-280, 2009.
[260] P. M. Gilbert, K. L. Havenstrite, K. E. G. Magnusson, A. Sacco, N. A. Leonardi, P. Kraft, *et al.*, "Substrate elasticity regulates skeletal muscle stem cell self-renewal in culture," *Science,* 329, 1078-1081, 2010.
[261] J. Holst, S. Watson, M. S. Lord, S. S. Eamegdool, D. V. Bax, L. B. Nivison-Smith, *et al.*, "Substrate elasticity provides mechanical signals for the expansion of hemopoietic stem and progenitor cells," *Nature Biotechnology,* 28, 1123-1128, 2010.
[262] Schwartz, Martin, Ginsberg, and Mark, "Networks and crosstalk: integrin signalling spreads," *Nature Cell Biology,* 4, E65-E68, 2002.
[263] M. Arnaout, S. Goodman, and J.-P. Xiong, "Structure and mechanics of integrin-based cell adhesion," *Current Opinion in Cell Biology,* 19, 495-507, 2007.
[264] O. Rossier, V. Octeau, J.-B. Sibarita, C. Leduc, B. Tessier, D. Nair, *et al.*, "Integrins β1 and β3 exhibit distinct dynamic nanoscale organizations inside focal adhesions," *Nature Cell Biology,* 14, 1057-1067, 2012.
[265] H. Schiller, M.-R. Hermann, J. Polleux, T. Vignaud, S. Zanivan, C. Friedel, *et al.*, "β1- and αv-class integrins cooperate to regulate myosin II during rigidity sensing of fibronectin-based microenvironments," *Nature Cell Biology,* 15, 625-636, 2013.
[266] L. Li, S. A. L. Bennett, and L. S. Wang, "Role of E-cadherin and other cell adhesion molecules in survival and differentiation of human pluripotent stem cells," *Cell Adhesion & Migration,* 6, 59-70, 2012.
[267] Y. Meng, S. Eshghi, Y. J. Li, R. Schmidt, D. V. Schaffer, and K. E. Healy, "Characterization of integrin engagement during defined human embryonic stem cell culture," *FASEB Journal,* 24, 1056-1065, 2010.
[268] T. J. Rowland, L. M. Miller, A. J. Blaschke, E. L. Doss, A. J. Bonham, S. T. Hikita, *et al.*, "Roles of Integrins in Human Induced Pluripotent Stem Cell Growth on Matrigel and Vitronectin," *Stem Cells and Development,* 19, 1231-1240, 2010.
[269] R. Hynes, "Integrins: bidirectional, allosteric signaling machines," *Cell,* 2002.

[270] J. Qin, O. Vinogradova, and E. Plow, "Integrin bidirectional signaling: a molecular view," *PLoS biology,* 2, 2004.
[271] J. A. Askari, P. A. Buckley, A. P. Mould, and M. J. Humphries, "Linking integrin conformation to function," *Journal of Cell Science,* 122, 165-170, 2009.
[272] B. Geiger, J. Spatz, and A. Bershadsky, "Environmental sensing through focal adhesions," *Nature Reviews Molecular Cell Biology,* 10, 21-33, 2009.
[273] R. Zaidel-Bar and B. Geiger, "The switchable integrin adhesome," *Journal of Cell Science,* 123, 1385-1388, 2010.
[274] X. Zhang, G. Jiang, Y. Cai, S. Monkley, D. Critchley, and M. Sheetz, "Talin depletion reveals independence of initial cell spreading from integrin activation and traction," *Nature Cell Biology,* 10, 1062-1068, 2008.
[275] R. Glass, M. Möller, and J. Spatz, "Block copolymer micelle nanolithography," *Nanotechnology,* 14, 1153, 2003.
[276] M. Arnold, E. Cavalcanti-Adam, R. Glass, J. Blümmel, W. Eck, M. Kantlehner*, et al.*, "Activation of integrin function by nanopatterned adhesive interfaces," *Chemphyschem: A European Journal of Chemical Physics and Physical chemistry,* 5, 383-388, 2004.
[277] E. Cavalcanti-Adam, T. Volberg, A. Micoulet, H. Kessler, B. Geiger, and J. Spatz, "Cell spreading and focal adhesion dynamics are regulated by spacing of integrin ligands," *Biophysical Journal,* 92, 2964-2974, 2007.
[278] M. Schvartzman, M. Palma, J. Sable, J. Abramson, X. Hu, M. Sheetz*, et al.*, "Nanolithographic control of the spatial organization of cellular adhesion receptors at the single-molecule level," *Nano Letters,* 11, 1306-1312, 2011.
[279] G. Maheshwari, G. Brown, D. A. Lauffenburger, A. Wells, and L. G. Griffith, "Cell adhesion and motility depend on nanoscale RGD clustering," *Journal of Cell Science,* 113, 1677-1686, 2000.
[280] D. Khang, J. Choi, Y. M. Im, Y. J. Kim, J. H. Jang, S. S. Kang*, et al.*, "Role of subnano-, nano- and submicron-surface features on osteoblast differentiation of bone marrow mesenchymal stem cells," *Biomaterials,* 33, 5997-6007, 2012.
[281] A. J. Dulgar-Tulloch, R. Bizios, and R. W. Siegel, "Human mesenchymal stem cell adhesion and proliferation in response to ceramic chemistry and nanoscale topography," *Journal of Biomedical Materials Research Part A,* 90A, 586-594, 2009.
[282] M. ChrzanowskaWodnicka and K. Burridge, "Rho-stimulated contractility drives the formation of stress fibers and focal adhesions," *Journal of Cell Biology,* 133, 1403-1415, 1996.
[283] N. Balaban, U. Schwarz, D. Riveline, P. Goichberg, G. Tzur, I. Sabanay*, et al.*, "Force and focal adhesion assembly: a close relationship studied using elastic micropatterned substrates," *Nature Cell Biology,* 3, 466-472, 2001.
[284] A. Bershadsky, C. Ballestrem, L. Carramusa, Y. Zilberman, B. Gilquin, S. Khochbin*, et al.*, "Assembly and mechanosensory function of focal adhesions: experiments and models," *European Journal of Cell Biology,* 85, 165-173, 2006.
[285] C. Galbraith, K. Yamada, and M. Sheetz, "The relationship between force and focal complex development," *Journal of Cell Biology,* 159, 695-705, 2002.

[286] S. Moore, P. Roca-Cusachs, and M. Sheetz, "Stretchy proteins on stretchy substrates: the important elements of integrin-mediated rigidity sensing," *Developmental cell,* 19, 194-206, 2010.
[287] T. Lele, J. Pendse, S. Kumar, M. Salanga, J. Karavitis, and D. Ingber, "Mechanical forces alter zyxin unbinding kinetics within focal adhesions of living cells," *Journal of Cellular Physiology,* 207, 187-194, 2006.
[288] L. Gallegos, M. Ng, and J. Brugge, "The myosin-II-responsive focal adhesion proteome: a tour de force?," *Nature Cell Biology,* 13, 344-346, 2011.
[289] P. Oakes, Y. Beckham, J. Stricker, and M. Gardel, "Tension is required but not sufficient for focal adhesion maturation without a stress fiber template," *Journal of Cell Biology,* 196, 363-374, 2012.
[290] A. Carisey, R. Tsang, A. Greiner, N. Nijenhuis, N. Heath, A. Nazgiewicz*, et al.*, "Vinculin regulates the recruitment and release of core focal adhesion proteins in a force-dependent manner," *Current Biology,* 23, 271-281, 2013.
[291] A. del Rio, R. Perez-Jimenez, R. C. Liu, P. Roca-Cusachs, J. M. Fernandez, and M. P. Sheetz, "Stretching Single Talin Rod Molecules Activates Vinculin Binding," *Science,* 323, 638-641, 2009.
[292] J. Malmström, J. Lovmand, S. Kristensen, M. Sundh, M. Duch, and D. Sutherland, "Focal complex maturation and bridging on 200 nm vitronectin but not fibronectin patches reveal different mechanisms of focal adhesion formation," *Nano letters,* 11, 2264-2271, 2011.
[293] S. R. Coyer, A. Singh, D. W. Dumbauld, D. A. Calderwood, S. W. Craig, E. Delamarche*, et al.*, "Nanopatterning reveals an ECM area threshold for focal adhesion assembly and force transmission that is regulated by integrin activation and cytoskeleton tension," *Journal of Cell Science,* 125, 5110-5123, 2012.
[294] J. Gautrot, J. Malmström, M. Sundh, C. Margadant, A. Sonnenberg, and D. Sutherland, "The Nanoscale Geometrical Maturation of Focal Adhesions Controls Stem Cell Differentiation and Mechano-Transduction," *Nano letters,* In Press, 2014.
[295] K. Kulangara, Y. Yang, J. Yang, and K. W. Leong, "Nanotopography as modulator of human mesenchymal stem cell function," *Biomaterials,* 33, 4998-5003, 2012.
[296] S. Mitra, D. Hanson, and D. Schlaepfer, "Focal adhesion kinase: in command and control of cell motility," *Nature Reviews Molecular Cell Biology,* 6, 56-68, 2005.
[297] J. Seong, A. Tajik, J. Sun, J. L. Guan, M. J. Humphries, S. E. Craig*, et al.*, "Distinct biophysical mechanisms of focal adhesion kinase mechanoactivation by different extracellular matrix proteins," *Proceedings of the National Academy of Sciences of the United States of America,* 110, 19372-19377, 2013.
[298] D. D. Schlaepfer, S. K. Hanks, T. Hunter, and P. Vandergeer, "Integrin-Mediated Signal-Transduction Linked to Ras Pathway by Grb2 Binding to Focal Adhesion Kinase," *Nature,* 372, 786-791, 1994.
[299] S. Y. Hong, Y. M. Jeon, H. J. Lee, J. G. Kim, J. A. Baek, and J. C. Lee, "Activation of RhoA and FAK induces ERK-mediated osteopontin expression in mechanical force-subjected periodontal ligament fibroblasts," *Molecular and Cellular Biochemistry,* 335, 263-272, 2010.

[300] K. K. Wary, A. Mariotti, C. Zurzolo, and F. G. Giancotti, "A requirement for caveolin-1 and associated kinase Fyn in integrin signaling and anchorage-dependent cell growth," *Cell,* 94, 625-634, 1998.
[301] R. Aikawa, T. Nagai, S. Kudoh, Y. Z. Zou, M. Tanaka, M. Tamura*, et al.*, "Integrins play a critical role in mechanical stress-induced p38 MAPK activation," *Hypertension,* 39, 233-238, 2002.
[302] B. K. K. Teo, S. T. Wong, C. K. Lim, T. Y. S. Kung, C. H. Yap, Y. Ramagopal*, et al.*, "Nanotopography Modulates Mechanotransduction of Stem Cells and Induces Differentiation through Focal Adhesion Kinase," *ACS Nano,* 7, 4785-4798, 2013.
[303] D. A. Hsia, S. K. Mitra, C. R. Hauck, D. Streblow, J. A. Nelson, D. Ilic*, et al.*, "Differential regulation of cell motility and invasion by FAK," *Journal of Cell Biology,* 160, 753-767, 2003.
[304] D. D. Schlaepfer, S. K. Mitra, and D. Ilic, "Control of motile and invasive cell phenotypes by focal adhesion kinase," *Biochimica Et Biophysica Acta-Molecular Cell Research,* 1692, 77-102, 2004.
[305] J. B. Zhai, H. Lin, Z. Y. Nie, J. H. Wu, R. Canete-Soler, W. W. Schlaepfer*, et al.*, "Direct interaction of focal adhesion kinase with p190RhoGEF," *Journal of Biological Chemistry,* 278, 24865-24873, 2003.
[306] B. Rico, H. E. Beggs, D. Schahin-Reed, N. Kimes, A. Schmidt, and L. F. Reichardt, "Control of axonal branching and synapse formation by focal adhesion kinase," *Nature Neuroscience,* 7, 1059-1069, 2004.
[307] J. D. Hildebrand, J. M. Taylor, and J. T. Parsons, "An SH3 domain-containing GTPase-activating protein for Rho and Cdc42 associates with focal adhesion kinase," *Molecular and Cellular Biology,* 16, 3169-3178, 1996.
[308] X. D. Ren, W. B. Kiosses, D. J. Sieg, C. A. Otey, D. D. Schlaepfer, and M. A. Schwartz, "Focal adhesion kinase suppresses Rho activity to promote focal adhesion turnover," *Journal of Cell Science,* 113, 3673-3678, 2000.
[309] H. Xia, R. S. Nho, J. Kahm, J. Kleidon, and C. A. Henke, "Focal adhesion kinase is upstream of phosphatidylinositol 3-kinase/Akt in regulating fibroblast survival in response to contraction of type I collagen matrices via a beta(1) integrin viability signaling pathway," *Journal of Biological Chemistry,* 279, 33024-33034, 2004.
[310] J. Du, X. Chen, X. Liang, G. Zhang, J. Xu, L. He*, et al.*, "Integrin activation and internalization on soft ECM as a mechanism of induction of stem cell differentiation by ECM elasticity," *Proceedings of the National Academy of Sciences of the United States of America,* 108, 9466-9471, 2011.
[311] L. Armstrong, O. Hughes, S. Yung, L. Hyslop, R. Stewart, I. Wappler*, et al.*, "The role of PI3K/AKT, MAPK/ERK and NF kappa beta signalling in the maintenance of human embryonic stem cell pluripotency and viability highlighted by transcriptional profiling and functional analysis," *Human Molecular Genetics,* 15, 1894-1913, 2006.
[312] A. M. Singh, D. Reynolds, T. Cliff, S. Ohtsuka, A. L. Mattheyses, Y. H. Sun*, et al.*, "Signaling Network Crosstalk in Human Pluripotent Cells: A Smad2/3-Regulated Switch that Controls the Balance between Self-Renewal and Differentiation," *Cell Stem Cell,* 10, 312-326, 2012.

[313] K. Burridge and K. Wennerberg, "Rho and Rac take center stage," *Cell,* 116, 167-179, 2004.
[314] A. Mammoto, S. Huang, K. Moore, P. Oh, and D. E. Ingber, "Role of RhoA, mDia, and ROCK in cell shape-dependent control of the Skp2-p27(kip1) pathway and the G(1)/S transition," *Journal of Biological Chemistry,* 279, 26323-26330, 2004.
[315] K. Bhadriraju, M. Yang, S. Alom Ruiz, D. Pirone, J. Tan, and C. Chen, "Activation of ROCK by RhoA is regulated by cell adhesion, shape, and cytoskeletal tension," *Experimental Cell Research,* 313, 3616-3623, 2007.
[316] C. Guilluy, V. Swaminathan, R. Garcia-Mata, E. T. O'Brien, R. Superfine, and K. Burridge, "The Rho GEFs LARG and GEF-H1 regulate the mechanical response to force on integrins," *Nature Cell Biology,* 13, 722-727, 2011.
[317] J. Halbleib and W. Nelson, "Cadherins in development: cell adhesion, sorting, and tissue morphogenesis," *Genes & Development,* 20, 3199-3214, 2006.
[318] S. Yamada, S. Pokutta, F. Drees, W. I. Weis, and W. J. Nelson, "Deconstructing the cadherin-catenin-actin complex," *Cell,* 123, 889-901, 2005.
[319] F. Drees, S. Pokutta, S. Yamada, W. J. Nelson, and W. I. Weis, "alpha-catenin is a molecular switch that binds E-cadherin-beta-catenin and regulates actin-filament assembly," *Cell,* 123, 903-915, 2005.
[320] S. Yonemura, Y. Wada, T. Watanabe, A. Nagafuchi, and M. Shibata, "alpha-Catenin as a tension transducer that induces adherens junction development," *Nature Cell Biology,* 12, 533-542, 2010.
[321] Q. le Duc, Q. Shi, I. Blonk, A. Sonnenberg, N. Wang, D. Leckband*, et al.*, "Vinculin potentiates E-cadherin mechanosensing and is recruited to actin-anchored sites within adherens junctions in a myosin II-dependent manner," *Journal of Cell Biology,* 189, 1107-1115, 2010.
[322] D. E. Conway, M. T. Breckenridge, E. Hinde, E. Gratton, C. S. Chen, and M. A. Schwartz, "Fluid Shear Stress on Endothelial Cells Modulates Mechanical Tension across VE-Cadherin and PECAM-1," *Current Biology,* 23, 1024-1030, 2013.
[323] Z. Liu, J. Tan, D. Cohen, M. Yang, N. Sniadecki, S. Ruiz*, et al.*, "Mechanical tugging force regulates the size of cell-cell junctions," *Proceedings of the National Academy of Sciences of the United States of America,* 107, 9944-9949, 2010.
[324] S. Huveneers, J. Oldenburg, E. Spanjaard, G. van der Krogt, I. Grigoriev, A. Akhmanova*, et al.*, "Vinculin associates with endothelial VE-cadherin junctions to control force-dependent remodeling," *Journal of Cell Biology,* 196, 641-652, 2012.
[325] Q. Tseng, E. Duchemin-Pelletier, A. Deshiere, M. Balland, H. Guillou, O. Filhol*, et al.*, "Spatial organization of the extracellular matrix regulates cell-cell junction positioning," *Proceedings of the National Academy of Sciences of the United States of America,* 109, 1506-1511, 2012.
[326] J. Tsai and L. Kam, "Rigidity-Dependent Cross Talk between Integrin and Cadherin Signaling," *Biophysical Journal,* 96, L39-L41, 2009.
[327] A. F. Mertz, Y. L. Che, S. Banerjee, J. M. Goldstein, K. A. Rosowski, S. F. Revilla*, et al.*, "Cadherin-based intercellular adhesions organize epithelial cell-

matrix traction forces," *Proceedings of the National Academy of Sciences of the United States of America,* 110, 842-847, 2013.
[328] V. Maruthamuthu, B. Sabass, U. S. Schwarz, and M. L. Gardel, "Cell-ECM traction force modulates endogenous tension at cell-cell contacts," *Proceedings of the National Academy of Sciences of the United States of America,* 108, 4708-4713, 2011.
[329] C. M. Nelson, D. M. Pirone, J. L. Tan, and C. S. Chen, "Vascular endothelial-cadherin regulates cytoskeletal tension, cell spreading, and focal adhesions stimulating RhoA," *Molecular Biology of the Cell,* 15, 2943-2953, 2004.
[330] A. Jasaitis, M. Estevez, J. Heysch, B. Ladoux, and S. Dufour, "E-cadherin-dependent stimulation of traction force at focal adhesions via the Src and PI3K signaling pathways," *Biophysical journal,* 103, 175-184, 2012.
[331] G. Weber, M. Bjerke, and D. DeSimone, "Integrins and cadherins join forces to form adhesive networks," *Journal of cell science,* 124, 1183-1193, 2011.
[332] M. Fukata and K. Kaibuchi, "Rho-family GTPases in cadherin-mediated cell-cell adhesion," *Nature Reviews Molecular Cell Biology,* 2, 887-897, 2001.
[333] P. Tsimbouri, N. Gadegaard, K. Burgess, K. White, P. Reynolds, P. Herzyk*, et al.*, "Nanotopographical Effects on Mesenchymal Stem Cell Morphology and Phenotype," *Journal of Cellular Biochemistry,* 115, 380-390, 2014.
[334] C. DuFort, M. Paszek, and V. Weaver, "Balancing forces: architectural control of mechanotransduction," *Nature Reviews Molecular Cell Biology,* 12, 308-319, 2011.
[335] S. Dupont, L. Morsut, M. Aragona, E. Enzo, S. Giulitti, M. Cordenonsi*, et al.*, "Role of YAP/TAZ in mechanotransduction," *Nature,* 474, 179-183, 2011.
[336] M. Aragona, T. Panciera, A. Manfrin, S. Giulitti, F. Michielin, N. Elvassore*, et al.*, "A Mechanical Checkpoint Controls Multicellular Growth through YAP/TAZ Regulation by Actin-Processing Factors," *Cell,* 154, 1047-1059, 2013.
[337] K. I. Wada, K. Itoga, T. Okano, S. Yonemura, and H. Sasaki, "Hippo pathway regulation by cell morphology and stress fibers," *Development,* 138, 3907-3914, 2011.
[338] B. G. Fernandez, P. Gaspar, C. Bras-Pereira, B. Jezowska, S. R. Rebelo, and F. Janody, "Actin-Capping Protein and the Hippo pathway regulate F-actin and tissue growth in Drosophila," *Development,* 138, 2337-2346, 2011.
[339] L. Sansores-Garcia, W. Bossuyt, K. I. Wada, S. Yonemura, C. Y. Tao, H. Sasaki*, et al.*, "Modulating F-actin organization induces organ growth by affecting the Hippo pathway," *EMBO Journal,* 30, 2325-2335, 2011.
[340] C. Yang, M. W. Tibbitt, L. Basta, and K. S. Anseth, "Mechanical memory and dosing influence stem cell fate," *Nature Materials,* 13, 645-52, 2014.
[341] J. T. Connelly, J. E. Gautrot, B. Trappmann, D. W. M. Tan, G. Donati, W. T. S. Huck*, et al.*, "Actin and serum response factor transduce physical cues from the microenvironment to regulate epidermal stem cell fate decisions," *Nature Cell Biology,* 12, 711-718, 2010.
[342] G. Schratt, U. Philippar, J. Berger, H. Schwarz, O. Heidenreich, and A. Nordheim, "Serum response factor is crucial for actin cytoskeletal organization and focal adhesion assembly in embryonic stem cells," *Journal of Cell Biology,* 156, 737-750, 2002.

[343] P. Isermann and J. Lammerding, "Nuclear Mechanics and Mechanotransduction in Health and Disease," *Current Biology,* 23, R1113-R1121, 2013.
[344] G. V. Shivashankar, "Mechanosignaling to the Cell Nucleus and Gene Regulation," *Annual Review of Biophysics,* 40, 361-378, 2011.
[345] J. Lammerding, C. Schulze, T. Takahashi, S. Kozlov, T. Sullivan, R. D. Kamm*, et al.*, "Defective nuclear mechanics and mechanotransduction in larnin A/C null cells," *Circulation,* 108, 289-289, 2003.
[346] J. Lammerding, P. C. Schulze, T. Takahashi, S. Kozlov, T. Sullivan, R. D. Kamm*, et al.*, "Lamin A/C deficiency causes defective nuclear mechanics and mechanotransduction," *Journal of Clinical Investigation,* 113, 370-378, 2004.
[347] C. Y. Ho, D. E. Jaalouk, M. K. Vartiainen, and J. Lammerding, "Lamin A/C and emerin regulate MKL1-SRF activity by modulating actin dynamics," *Nature,* 497, 507-511, 2013.
[348] J. D. Pajerowski, K. N. Dahl, F. L. Zhong, P. J. Sammak, and D. E. Discher, "Physical plasticity of the nucleus in stem cell differentiation," *Proceedings of the National Academy of Sciences of the United States of America,* 104, 15619-15624, 2007.
[349] M. L. Lombardi, D. E. Jaalouk, C. M. Shanahan, B. Burke, K. J. Roux, and J. Lammerding, "The Interaction between Nesprins and Sun Proteins at the Nuclear Envelope Is Critical for Force Transmission between the Nucleus and Cytoskeleton," *Journal of Biological Chemistry,* 286, 26743-26753, 2011.
[350] N. Wang, J. Tytell, and D. Ingber, "Mechanotransduction at a distance: mechanically coupling the extracellular matrix with the nucleus," *Nature Reviews Molecular Cell Biology,* 10, 75-82, 2009.
[351] C. P. Johnson, H. Y. Tang, C. Carag, D. W. Speicher, and D. E. Discher, "Forced unfolding of proteins within cells," *Science,* 317, 663-666, 2007.
[352] J. Swift, I. Ivanovska, A. Buxboim, T. Harada, P. Dingal, J. Pinter*, et al.*, "Nuclear lamin-A scales with tissue stiffness and enhances matrix-directed differentiation," *Science,* 341, 1240104, 2013.
[353] H. Liu, J. Wen, Y. Xiao, J. Liu, S. Hopyan, M. Radisic*, et al.*, "In Situ Mechanical Characterization of the Cell Nucleus by Atomic Force Microscopy," *ACS Nano,* 8, 3821-3828, 2014.
[354] Y. C. Poh, S. P. Shevtsov, F. Chowdhury, D. C. Wu, S. Na, M. Dundr*, et al.*, "Dynamic force-induced direct dissociation of protein complexes in a nuclear body in living cells," *Nature Communications,* 3, 2012.
[355] S. Na, O. Collin, F. Chowdhury, B. Tay, M. X. Ouyang, Y. X. Wang*, et al.*, "Rapid signal transduction in living cells is a unique feature of mechanotransduction," *Proceedings of the National Academy of Sciences of the United States of America,* 105, 6626-6631, 2008.
[356] M. Versaevel, T. Grevesse, and S. Gabriele, "Spatial coordination between cell and nuclear shape within micropatterned endothelial cells," *Nature Communications,* 3, 671, 2012.
[357] C. Guilluy, L. D. Osborne, L. Van Landeghem, L. Sharek, R. Superfine, R. Garcia-Mata*, et al.*, "Isolated nuclei adapt to force and reveal a mechanotransduction pathway in the nucleus," *Nature Cell Biology,* 16, 376-381, 2014.

[358] K. J. Chalut, K. Kulangara, M. G. Giacomelli, A. Wax, and K. W. Leong, "Deformation of stem cell nuclei by nanotopographical cues," *Soft Matter,* 6, 1675-1681, 2010.
[359] J. M. Dang and K. W. Leong, "Myogenic induction of aligned mesenchymal stem cell sheets by culture on thermally responsive electrospun nanofibers," *Advanced Materials,* 19, 2775-2779, 2007.
[360] P. M. Tsimbouri, K. Murawski, G. Hamilton, P. Herzyk, R. O. C. Oreffo, N. Gadegaard*, et al.*, "A genomics approach in determining nanotopographical effects on MSC phenotype," *Biomaterials,* 34, 2177-2184, 2013.
[361] M. J. Dalby, N. Gadegaard, P. Herzyk, D. Sutherland, H. Agheli, C. D. W. Wilkinson*, et al.*, "Nanomechanotransduction and interphase nuclear organization influence on genomic control," *Journal of Cellular Biochemistry,* 102, 1234-1244, 2007.
[362] X. Varelas, R. Sakuma, P. Samavarchi-Tehrani, R. Peerani, B. M. Rao, J. Dembowy*, et al.*, "TAZ controls Smad nucleocytoplasmic shuttling and regulates human embryonic stem-cell self-renewal," *Nature Cell Biology,* 10, 837-848, 2008.
[363] T. Mammoto, A. Mammoto, and D. Ingber, "Mechanobiology and Developmental Control," *Annual Review of Cell and Developmental Biology,* 29, 27-61, 2013.
[364] J. S. Mo, H. W. Park, and K. L. Guan, "The Hippo signaling pathway in stem cell biology and cancer," *EMBO Reports,* 15, 642-656, 2014.
[365] S. Piccolo, M. Cordenonsi, and S. Dupont, "Molecular Pathways: YAP and TAZ Take the Centerstage in Organ Growth and Tumorigenesis," *Clinical Cancer Research,* 19, 4925-4930, 2013.
[366] G. Halder, S. Dupont, and S. Piccolo, "Transduction of mechanical and cytoskeletal cues by YAP and TAZ," *Nature Reviews Molecular Cell Biology,* 13, 591-600, 2012.
[367] C. Baarlink, H. C. Wang, and R. Grosse, "Nuclear Actin Network Assembly by Formins Regulates the SRF Coactivator MAL," *Science,* 340, 864-867, 2013.
[368] M. Kabiri, M. Soleimani, I. Shabani, K. Futrega, N. Ghaemi, H. H. Ahvaz*, et al.*, "Neural differentiation of mouse embryonic stem cells on conductive nanofiber scaffolds," *Biotechnology Letters,* 34, 1357-1365, 2012.
[369] T. I. Chao, S. Xiang, C. S. Chen, W. C. Chin, A. J. Nelson, C. Wang*, et al.*, "Carbon nanotubes promote neuron differentiation from human embryonic stem cells," *Biochemical and Biophysical Research Communications,* 384, 426-30, 2009.
[370] I. Sridharan, T. Kim, and R. Wang, "Adapting collagen/CNT matrix in directing hESC differentiation," *Biochemical and Biophysical Research Communications,* 381, 508-12, 2009.
[371] J. Kim, H. N. Kim, K. T. Lim, Y. Kim, S. Pandey, P. Garg*, et al.*, "Synergistic effects of nanotopography and co-culture with endothelial cells on osteogenesis of mesenchymal stem cells," *Biomaterials,* 34, 7257-7268, 2013.
[372] M. Guvendiren and J. A. Burdick, "Stem Cell Response to Spatially and Temporally Displayed and Reversible Surface Topography," *Advanced Healthcare Materials,* 2, 155-164, 2013.

[373] U. Grundmann, H. Rensing, H. A. Adams, S. Falk, O. Wendler, N. Ebinger*, et al.*, "Endotoxin desensitization of human mononuclear cells after cardiopulmonary bypass: role of humoral factors," *Anesthesiology,* 93, 359-69, 2000.
[374] D. M. Nguyen, D. S. Mulder, and H. Shennib, "Effect of cardiopulmonary bypass on circulating lymphocyte function," *The Annals of thoracic surgery,* 53, 611-6, 1992.
[375] P. Gessler, R. Pretre, C. Burki, V. Rousson, B. Frey, and D. Nadal, "Monocyte function-associated antigen expression during and after pediatric cardiac surgery," *The Journal of thoracic and cardiovascular surgery,* 130, 54-60, 2005.
[376] J. Y. Wang, X. L. Wang, and P. Liu, "Detection of serum TNF-alpha, IFN-gamma, IL-6 and IL-8 in patients with hepatitis B," *World Journal of Gastroenterology,* 5, 38-40, 1999.
[377] C. A. Ray, R. R. Bowsher, W. C. Smith, V. Devanarayan, M. B. Willey, J. T. Brandt*, et al.*, "Development, validation, and implementation of a multiplex immunoassay for the simultaneous determination of five cytokines in human serum," *Journal of Pharmaceutical and Biomedical Analysis,* 36, 1037-1044, 2005.
[378] T. T. Cornell, L. Sun, M. W. Hall, J. G. Gurney, M. J. Ashbrook, R. G. Ohye*, et al.*, "Clinical implications and molecular mechanisms of immunoparalysis after cardiopulmonary bypass," *The Journal of thoracic and cardiovascular surgery,* 143, 1160-1166 e1, 2012.
[379] G. Y. Lee and C. T. Lim, "Biomechanics approaches to studying human diseases," *Trends Biotechnol,* 25, 111-8, 2007.
[380] A. Fritsch, M. Hockel, T. Kiessling, K. D. Nnetu, F. Wetzel, M. Zink*, et al.*, "Are biomechanical changes necessary for tumour progression?," *Nature Physics,* 6, 730-732, 2010.
[381] M. Yu, D. T. Ting, S. L. Stott, B. S. Wittner, F. Ozsolak, S. Paul*, et al.*, "RNA sequencing of pancreatic circulating tumour cells implicates WNT signalling in metastasis," *Nature,* 487, 510-3, 2012.
[382] K. A. Sepkowitz, "AIDS--the first 20 years," *N Engl J Med,* 344, 1764-72, 2001.
[383] UNAIDS, "UNAIDS 2011 World AIDS Day report," 2011.
[384] G. M. Nayyar, J. G. Breman, P. N. Newton, and J. Herrington, "Poor-quality antimalarial drugs in southeast Asia and sub-Saharan Africa," *Lancet Infect Dis,* 12, 488-96, 2012.
[385] B. M. Cooke, N. Mohandas, and R. L. Coppel, "The malaria-infected red blood cell: structural and functional changes," *Adv Parasitol,* 50, 1-86, 2001.
[386] L. G. Villa-Diaz, H. Nandivada, J. Ding, N. C. Nogueira-De-Souza, P. H. Krebsbach, K. S. O'Shea*, et al.*, "Synthetic polymer coatings for long-term growth of human embryonic stem cells," *Nature Biotechnology,* 28, 581-583, 2010.
[387] H. Nandivada, L. G. Villa-Diaz, K. S. O'Shea, G. D. Smith, P. H. Krebsbach, and J. Lahann, "Fabrication of synthetic polymer coatings and their use in feeder-free culture of human embryonic stem cells," *Nature Protocols,* 6, 1037-43, 2011.